Dissertation zur Erlangung des Doktorgrades

der Fakultät für Chemie und Pharmazie

der Ludwig-Maximilians-Universität München

Biocompatible Nanocarriers for Drug Delivery Applications

Lisa Wehl (geborene Haddick)

aus

Münster, Deutschland

2023

Erklärung

Diese Dissertation wurde im Sinne von § 7 der Promotionsordnung vom 28. November 2011 von Herrn Prof. Dr. Thomas Bein betreut.

Eidesstattliche Versicherung

Diese Dissertation wurde eigenständig und ohne unerlaubte Hilfe bearbeitet.

München, den 25.09.2023 Lisa Wehl

Lisa Wehl

Dissertation eingereicht am 07.08.2023

1. Gutachter: Prof. Dr. Thomas Bein

2. Gutachterin: Ass.-Prof. Dr. Hanna Engelke

Mündliche Prüfung am 11.09.2023

“ Träume dir dein Leben schön

und mach aus diesen Träumen eine Realität.“

Marie Curie

Danksagung

Viele Herausforderungen haben auf mich gewartet, während der Arbeit an und beim Zusammenschreiben der Doktorarbeit. Eine davon war definitiv diese Danksagung. Mich haben viele Menschen auf der Reise meiner akademischen Laufbahn begleitet, unterstützt, inspiriert und motiviert. Ich möchte euch allen gebührend Danke sagen, ohne dass ihr euch durch einen langweiligen und endlosen Text quälen müsst.

Deshalb in aller Kürze, aber trotzdem mit der größten Wertschätzung: Danke!

Danke an alle Personen, die mich fachlich betreut haben. Ich habe auf so vielen Gebieten unglaublich viel dazu gelernt. Mein besonderer Dank geht an Thomas Bein, meinen Doktorvater, einfach für „alles“ und vor allem für die Möglichkeit, ein Teil deines bemerkenswerten Arbeitskreises zu sein. Auch an Hanna Engelke vielen Dank. Ich bin tief beeindruckt von deinem fachlichen Wissen und deiner positiven Einstellung. Liebe Karin, auch an dich vielen Dank für das Teilen deiner unglaublich großen Erfahrung auf eine professionelle und gleichzeitig fast mütterliche Art. Auch an Stefan Wuttke ein großes Dankeschön, für einen tollen Start in den AK Bein während meiner Masterarbeit.

Danke an alle meine Doktorand:innen und PostDoc Kollegen, dass ihr diese Zeit zu etwas so Besonderem gemacht habt!!!

Ich möchte mich auch bei allen Personen bedanken, die auf organisatorischer Ebene an der Doktorarbeit beteiligt waren - danke Tina Reuther für alles was das Labor anging. Liebe Corinna, vielen Dank. Und zwar nicht nur für den ganzen Bürokratie-Kram sondern für noch viel mehr. Auch an Markus Döblinger und Steffen Schmidt, als fester, zuverlässiger Bestandteil dieses Arbeitskreises ein großes Dankeschön.

An alle meine Praktikant:innen und Kooperationspartner:innen ein riesiges Dankeschön für die tatkräftige Unterstützung und den wertvollen fachlichen Beitrag zu dieser Arbeit.

Für ein gesundes mentales Mindset danke ich meinen Freunden und vor allem meiner Familie, für die nie enden wollende Liebe, Unterstützung, Aufmunterung und Ablenkung. Ein besonderes Dankeschön an Mama und Papa! Lieber Michi, es gibt keine Worte dafür, wie dankbar ich dir bin, dass du diesen wundervollen Wahnsinn mit mir zusammen gelebt hast – to be continued.

Abstract

Nanotechnology has revolutionized the field of drug delivery by enabling the design and development of targeted and multifunctional nanocarrier systems. Nanoparticles have been engineered to become 'smart' agents to overcome the limitations of free molecular therapeutics. They can improve the stability and solubility of the cargos they encapsulate, facilitate transport across membranes, and prolong circulation times, thereby improving safety and efficacy. Advanced nanoparticle designs have incorporated complex architectures, stimuli-responsive components, and targeting agents to improve drug delivery, using controlled synthesis strategies. In this context, many different nanoparticles have been investigated including liposomes, carbon nanotubes, quantum dots, polymers, gold or silver nanoparticles, mesoporous silica nanoparticles (MSN), cyclodextrin-based nanocarriers, dendrimers, and micelles. These nanoparticles have effectively delivered a wide range of therapeutic agents, including chemotherapy drugs, proteins, vaccines, immunoadjuvants, and nucleic acids, aiming to provide novel and effective therapeutic opportunities. In recent years, researchers have concentrated their efforts on the development and optimization of nanosystems, which has led to tremendous advancements in creating multiple formulations and nanocarriers that are being utilized in various clinical applications. However, notably, many these systems still suffer from poor clinical translation and the number of nanomedicines available to patients is still drastically below expectations in this field for several reasons. This is partially due to the incomplete understanding of the fundamental behavior of nanocarriers in the (human) body and their physico-chemical properties. There still exist multiple concerns regarding nanocarriers, e.g. concerning the biodegradability of drug carriers. This shows that there is still a great need for further research on this topic to gain more insights into the behavior of these complex materials in the biological and medical context and to further improve drug delivery systems.

This thesis aims to contribute to a better understanding of nanoparticles for drug delivery applications. Striving to investigate and improve nanotechnology, this work focuses on the development of novel biodegradable nanoagents and the modification of a well-established delivery platform to tailor it for targeted delivery of RNA as anti-cancer agent. Systematic studies were conducted to investigate the influence of the particle size effect and the type of nanocarrier on delivery efficiency.

The first part of this thesis summarizes the results of research concerning the synthesis and degradation behavior of novel mesoporous magnesium phosphate-citrate nanoparticles (MPCs) (Chapter 3) as well as novel cyclodextrin-based nanoparticles (Chapter 4). These nanoparticles are both constructed from biogenic precursors, resulting in biocompatible and biodegradable carrier systems. The impact of the synthesis conditions, especially on the colloidal stability, was investigated for both nanoparticle systems. Magnesium phosphate (MgP) based materials provide attractive features for biomedical applications, because the human body possesses mechanisms to degrade MgP materials and therefore the risks of side effects are small. We show that chelating with citric acid in the synthesis process enables the formation of colloidal nanoparticles that are small in size and colloidally stable. To achieve a high loading capacity for drugs, a surfactant template was employed during synthesis to implement mesoporosity, resulting in the first reported mesoporous magnesium-phosphate citrate material for drug delivery applications. The crosslinked β-cyclodextrin (β-CD) nanoparticles consist specifically of β-CD units that were covalently crosslinked by carbonyl linkages using carbonyldiimidazol (CDI) and were colloidally stabilized via PEGylation (β-CD-CDI-PEG). β-CD is a naturally occurring, cone-shaped molecule, and a variety of hydrophobic guest molecules can be encapsulated in its non-polar cavity, making it a promising candidate for drug delivery applications. The crosslinking creates additional voids for guest encapsulation in the nanoparticle structure. We show exemplarily the drug delivery potential of MPCs and β-CD-

CDI-PEG using different model cargos, including the chemotherapeutic agent methotrexate (MTX) and the fluorescent Hoechst dye, respectively. We demonstrate a stable retention of cargo at neutral pH for both carrier systems, and in contrast, an efficient stimuli-responsive release at acidic pH.

To implement the gained knowledge and to explore the potential of the described nanocarriers as drug delivery systems, a comparative study was conducted in the following chapter where the delivery efficiencies of three different types of porous nanoparticles are examined (Chapter 5). MSN, the newly developed crosslinked cyclodextrin carriers (β-CD-CDI-PEG), and mesoporous MPCs were used to deliver Necrosulfonamide (NSA) to both mouse and human macrophages. NSA is known to suppress the inflammatory response of immune cells, such as macrophages, which is induced by the release of mediators of inflammation, e.g. the cytokines interleukin (IL)-1β and IL-18, through pores in the plasma membrane formed by the oligomerized protein gasdermin D (GSDMD). NSA is an effective GSDMD inhibitor and represents a promising therapeutic agent in GSDMD-dependent inflammatory diseases. A significant (undesired) cytostatic effect was observed in a macrophage cell line when exposed to free NSA. Notably, the impact on cell growth was considerably lower when NSA was administered using nanoparticle carriers. Functional assays, measuring the extracellular IL-1β concentration, showed the strongest suppressive effect on human macrophages when using the crosslinked cyclodextrin carriers for NSA delivery, followed by MSN. In contrast, MPCs completely blocked the metabolic activity in macrophages when loaded with NSA. This study demonstrates the potential of porous nanoparticles for the effective delivery of hydrophobic drugs to macrophages in order to suppress inflammatory responses.

The final part of this thesis addresses the development of a series of MSN with different particle sizes ranging from 60 to 160 nm to investigate the particle-size-dependent delivery of microRNA (miRNA) as anti-cancer agent. Intracellular delivery of miRNA offers the

possibility to mediate the process of RNA interference in order to suppress cancer-related genes as targets of cancer therapy. MSN were efficiently tailored to make them specifically suitable for miRNA delivery including a positively charged core for adsorption of the fragile miRNA cargo, and negatively charged particle surface which enables the linkage of a designed block copolymer. The latter was intended to function as gate keeper and simultaneously as endosomal escape agent, and can be covalently bound to a targeting ligand. To exclusively study the particle size effect on targeted miRNA delivery, the series of functionalized MSN covers a broad size range but still provides comparable properties for each sample, including surface chemistry, surface charge, pore size and miRNA concentration. Here we show that good gene-silencing and antitumoral effects are obtained when miRNA is delivered by the largest MSN particles in this sequence, due to the fastest cellular internalization.

In summary, we have established the synthesis of two new nanocarrier systems to expand the spectrum of powerful biocompatible nanoparticles with great potential for drug delivery applications. Furthermore, systematic studies helped to establish a better understanding of the complex mechanisms and nanocarrier behavior in the field of drug delivery. Implementing these materials as ‘talented’ carrier systems even further and adding comparative studies to close the gap of knowledge will ultimately facilitate the translation of scientific nanomedicine into clinical applications.

Table of contents

CHAPTER 1

Introduction

1. Introduction

1.1. Nanotechnology in Biomedicine – Definition, History and Examples

The field of nanoscience deals with the study of structures and materials at the nanoscale. Technology which utilizes nanoscience in applications to manipulate and control matter is called nanotechnology.[1] The prefix ‘nano’ comes from the Greek term for ‘dwarf’ and refers to materials with characteristic sizes in the 10^{-9} m range - one billionth of a meter. The common definition of the nanoscale ranges from 1-100 nm. The upper limit of the definition is vague since most nanomaterials do not change their size-dependent properties at a cut-off of 100 nm. This has led to different definitions in industry, governments, and standard organizations, where some authors expanded the upper limit potentially beyond 100 nm.[2-3] Sizes between 10-200 nm are especially preferred for nanocarriers for drug delivery applications.

Nanotechnology, as we know it today, is a relatively recent development in science and technology. However, nanoparticles have accompanied mankind throughout its history, dating back as far as ancient Roman times where gold nanoparticles were used to stain glass for decorative purposes. The term "nanotechnology" was first used in the 1970s but the history of nanotechnology goes back much further than that, with roots in 19th-century scientific discoveries and technological innovations.

A key figure in the history of nanotechnology was Michael Faraday, who studied the preparation and properties of colloidal suspensions of gold nanoparticles with their unique optical and electronic properties in the 1850s. Faraday demonstrated how gold nanoparticles produce differently-colored solutions under certain lighting conditions.[4] With his discoveries he laid the groundwork for modern colloid chemistry.

Another pioneer in the field was Richard Zsigmondy, who won the Nobel Prize in Chemistry in 1925 for his work on colloids. Zsigmondy developed techniques for measuring the size and shape of small particles, including gold nanoparticles, using light scattering methods.[5]

In the 1950s, the physicist Richard Feynman gave a famous lecture at the California Institute of Technology in which he discussed the potential of manipulating and controlling matter at the atomic and molecular level. This lecture, titled 'There's Plenty of Room at the Bottom', is often cited as the birth of modern nanotechnology.[6] Feynman's ideas laid the foundation for the development of nanotechnology as a field of research in the decades that followed.

The era of modern nanotechnology began in the 1980s and 1990s, when advances in microscopy, e.g. by scanning tunneling microscopy (STM)[7-8], atomic force microscopy[9-10], and other techniques made it possible to study and manipulate materials at the nanoscale. These techniques paved the way for the development of new materials with unprecedented properties and functions. Hence, in 1985, almost at the same time as Binnig and Rohrer received the Nobel Prize in Physics "for their design of the STM", one of the first carbon nanomaterials, fullerenes, were discovered. Fullerenes are spherical, cage-like carbon molecules discovered by Harry Kroto, Richard Smalley and Robert Curl.[11] In the following years several further carbon nanomaterials were discovered, including carbon nanotubes[12] as cylindrical carbon molecules with high strength, thermal conductivity, and electrical conductivity, as well as single-layer graphene[13] as a two-dimensional material, and carbon dots[14] with small sizes below 10 nm. Overall, the discovery of carbon nanomaterials has opened up new opportunities for materials science, electronics, energy, and biomedicine.

In the decades that followed, researchers made significant advances in the field of nanotechnology. Recently, several studies have emphasized the huge potential that nanotechnologies offer in biomedicine for the diagnosis and therapy of many human diseases.[15-

[20] In this regard, bio-nanotechnology, also called nanomedicine, is considered by many experts to be one of the most intriguing fields of application for nanoscience and will be the focus of this thesis.

Today, nanomedicine has branched out in numerous different directions. It can be used for the synthesis and application of targeted drug delivery systems, cancer therapeutics, diagnostic tools, and medical implants to name only a few. Recently, nanotechnology gained a lot of attention when it showed its potential in medicine with the development of the SARS/CoV2 mRNA vaccine.[21] The Pfizer-BioNTech and Moderna vaccines use messenger RNA (mRNA) molecules encapsulated within lipid nanoparticles to stimulate an immune response against the virus.[22] The World Health Organization has estimated that over one million lives were saved by this vaccination across Europe alone.[23-24]

An example of successful modern nanotechnology in cancer therapeutics is Abraxane®, the anti-cancer drug Paclitaxel as an albumin-bound nanoparticle formulation for the treatment of metastatic breast, pancreatic and lung cancer.[25] The nanoformulation enhances transendothelial transport into the tumor site.[26]

A popular diagnostic tool in biomedicine is the lateral flow assay (LFA), for example, commonly used as urine diagnostic pregnancy test. The principle is based on antibodies conjugated to the surface of gold nanoparticles which can bind to specific target molecules. This binding causes a visible color change, indicating the presence or absence of the target molecule.[27] Gold nanoparticle-based LFAs have furthermore been successfully used for the rapid diagnosis of a wide range of diseases, including HIV[28]and COVID-19[29].

Drug delivery is another key application of nanomedicine. Over the last decades the research concerning drug delivery has increased dramatically, as shown by the high number of publications on this topic. Nowadays, there exist over 300,000 publications with the keyword

‘drug delivery’ in scientific collections such as the Web of Science. To understand the tremendous developments and the huge interest generated by this field, it is necessary to take a closer look at the advantages, potential and limitations of drug delivery.

1.2. Nanocarriers for Drug Delivery Applications

Drug delivery is one of the most significant applications of nanotechnology in medicine. Researchers are exploring the use of nanocarriers or nanoparticles to deliver cargos to specific targets in the body, such as cancer cells or diseased tissues. Drug delivery systems can help to overcome limitations of the direct pharmaceutical use of molecular drugs while improving their therapeutic efficacy. They can have advantages over conventional therapies, thereby providing new therapeutic opportunities for a large number of agents that cannot be used effectively as conventional formulations, e.g., when oral administration cannot be used effectively due to poor bioavailability of a given drug. The main purpose of using nanobiotechnology in drug delivery is to increase the concentration and lifetime of a drug in the diseased site and decrease its concentration in normal cells, thereby enhancing the therapeutic effect.

Since the beginning of nanomedicine, the majority of nanomedicine research has almost exclusively focused on tumor-targeting drug delivery.[30-31] Therefore, the advantages of drug delivery systems in contrast to conventional therapy will be discussed in the context of anti-tumor treatment while giving additional examples and explanations of other innovative approaches and applications.

Conventional cancer therapy consists of surgery, chemotherapy and radiation-treatment. At present, most patients encounter multiple challenges during treatment, including severe side effects and drug resistance. Many potent anti-cancer drugs face solubility issues because they are too hydrophobic for direct use. Furthermore, they are unspecific, exhibiting a lack of selectivity. The encapsulation of the drug inside suitable nanocarriers can overcome limitations regarding the solubility and improve bioavailability. Moreover, some nanoparticles are even capable of performing two functions and simultaneously assuming diagnostic functions, like

tumor imaging, in addition to the delivery of therapeutic drugs. This is referred to as theranostic, a combination of therapeutic and diagnostics.

However, drug delivery systems face demanding issues for successful and safe use as nanocarriers. Multiple factors need to be considered in a sensible design strategy for drug delivery. Design considerations should include the composition of the nanocarrier core, the cargo, targeting ligands, stimulation–responsive triggers for specific site release of cargo, and expected therapeutic outcomes among others.[32-33]

Nanocarrier core

Beginning with the choice of nanocarrier core for an efficient drug delivery, the drug loading capacity should be high. Therefore, the nanocarrier has to be able to encapsulate, bind or adsorb the drug. Several nanosized materials were introduced as nanocarriers for drug delivery applications. They include liposomes, carbon nanotubes, quantum dots, polymers, gold or silver nanoparticles, mesoporous silica nanoparticles, cyclodextrin-based nanocarriers, dendrimers, micelles, etc.[34-35] Figure 1.1 schematically depicts several constructs used as drug delivery systems for targeting cancer.

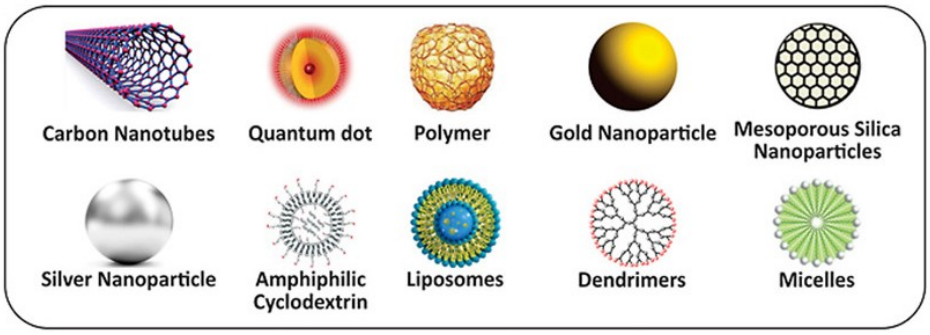

Figure 1.1: Nanocarriers for drug delivery applications. Modified from reference[35].

Carbon nanotubes are one type of nanocarrier that has been explored for drug delivery.[36] These tubes are extremely strong and have a high surface area, which makes them a potentially attractive option for carrying drugs. Quantum dots are another type of nanocarrier with a small size that comprise a semiconductor core and are useful for detection, monitoring and localized treatments in the body.[37] Polymers are commonly used as nanocarriers due to their biocompatibility, versatility and ability to encapsulate a wide range of drugs. Polymeric nanoparticles can be made from synthetic[38] or natural[39-40] polymers, and may be used to encapsulate drugs without chemical modification. Polymers can also be used to design polymer-drug conjugates as nanocarriers.[41]

Gold[42] or silver[43] nanoparticles are also frequently used as nanocarriers because they have unique optical and electronic properties that make them useful for imaging and tracking applications. They can also be functionalized with specific targeting molecules to enhance drug delivery to specific cells or tissues. Dendrimers are highly branched, nanoscale molecules that can be designed to carry drugs and targeting molecules. They offer a high degree of control over their size and shape, making them an attractive option for drug delivery.[44-45] Micelles are another type of nanocarrier that are formed from amphiphilic molecules and can encapsulate hydrophobic drugs for targeted delivery.[46-48] Mesoporous silica nanoparticles (MSN) have a high surface area and tunable pore sizes. Both the core and the shell of the MSN can be functionalized for tailoring the nanocarrier characteristics for specific applications and cargos.[49-50] Cyclodextrin (CD)-based nanocarriers are also useful for drug delivery, as they can encapsulate hydrophobic drugs to enhance bioavailability and protect the drug from degradation.[51]

The latter two nanocarriers, MSN and CD-based nanocarriers, were explored in this thesis and their potential for drug delivery as well as their unique properties and wide range of applications will be discussed in the following chapters.

Beside this, there exist special cases including metal organic frameworks[52-53] and metal phosphate-based nanoparticles which have both been successfully used as nanocarriers. Metal phosphate-based nanoparticles will also be described in more detail in chapter 1.2.2.

Different synthetic routes, architectures and physicochemical properties yield multiple different nanosized materials, each of them with their own advantages and disadvantages regarding different aspects of drug delivery. Overall, the use of nanocarriers for drug delivery holds great promise for improving the efficacy and safety of drug therapies. However, more research is needed to fully understand the potential benefits and risks of these systems and ultimately control their properties.

Cargo

Nanoparticles can be loaded with a variety of cargos for drug delivery in cancer therapy, including chemotherapeutic drugs, proteins (enzymes), antibody drugs, nucleic acids, immunoadjuvants and imaging agents (Figure 1.2). The choice of cargo depends on the specific therapeutic goals, the disease type, and the intended mode of action.

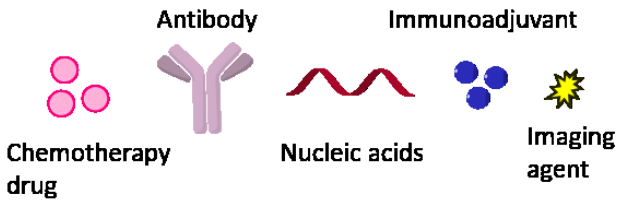

Figure 1.2: Examples of cargos used for anti-cancer drug delivery.

Small-molecule chemotherapeutic drugs, e.g., paclitaxel, doxorubicin (DOX) and cisplatin can be delivered to improve their pharmacokinetics, biodistribution, and therapeutic efficacy.

Encapsulation, surface adsorption, or chemical conjugation can be used to load these drugs into nanoparticles. Since many anticancer drugs are hydrophobic, the loading process is often based on hydrophobic adsorption. This involves adsorbing the drug or cargo onto the surface of the nanoparticle through hydrophobic interactions.

Larger molecules such as proteins can be loaded into nanoparticles, e.g., for the delivery of the active enzymes into cancer cells that catalyze reactions within living systems.[54] This can induce cell-death for cancer treatment and has shown to be an efficient combination cancer therapy when combined with DOX delivery.[55] Enzymes represent large cargos and require large pores or appropriate molecular interactions for the successful adsorption/encapsulation.[56] Another approach is the covalent conjugation of enzymes into the structure of polymeric nanoparticles[57].

Efficient therapeutic anti-cancer strategies can be performed with the delivery of antibodies, for example immune checkpoint inhibitors[58]. Immune checkpoint inhibitors can inhibit immunosuppressive molecules, which provide cancer cells with a mechanism to escape elimination through the immune system. Inhibiting these molecules successfully activates the immune system to fight cancer. To date, various drug delivery platforms have also been developed to improve the bioavailability, delivery convenience, and reduced toxicity towards an increased therapeutic efficacy of antibodies.[59] Antibodies, such as trastuzumab, can be delivered through the design of antibody-based nanoparticles[60-61] or through antibody encapsulation in nanosystems like liposomes or polymers[62].

Nucleic acids, such as small interfering RNA (siRNA) or messenger RNA (mRNA), can be encapsulated within nanoparticles for gene therapy[63] or RNA interference (RNAi) therapy.[64-65] These nanoparticles can be designed to target specific genes or pathways involved in carcinogenesis and metastasis.[66] RNA molecules are fragile: they show limited stability in serum, suffer from rapid blood clearance, off-target effects, and poor cellular uptake, and may

activate immune responses.[67-69] Therefore, they need to be protected and specifically delivered inside target cells to reach their full therapeutic potential. Delivery by nanocarriers can ensure that the therapeutic RNA can function inside target cells without eliciting unwanted immune responses. Electrostatic adsorption is commonly used for the loading of negatively charged nucleic acids into nanocarriers.[70]

For the delivery of immunoadjuvants, e.g., toll-like receptor agonists, the cargo can be encapsulated or adsorbed within nanoparticles to augment or potentiate the immune response against cancer cells. These nanoparticles can be used in cancer immunotherapy to activate the immune system and induce antitumor immunity.[71] While for most cargos a tumor-targeted delivery is needed, the delivery of the toll-like receptor (TLR) 7/8 agonist resiquimod[72] was achieved through delivery to the lymph nodes. MSN were equipped with biotin-avidin caps to obtain a tailor-made pH-responsive drug carrier system which ensures tight binding of resiquimod without premature release. By taking advantage of the dendritic cells which phagocytose foreign elements including nanocarriers and bring them to the lymph nodes, it was possible to initiate an immune response.[73] The MSN significantly improved the pharmacokinetic profile of resiquimod in mice, increasing the drug's half-life 6-fold while also reducing systemic exposure.

Overall, the choice of cargo as well as the loading method depends on the cargo properties, the nanoparticle properties, the therapeutic application as well as the desired drug release profile.

Surface functionalization: Targeting ligands

In the context of tumor-targeted drug delivery, there are two main ways to target cancer cells using nanocarriers: passive targeting and active targeting. Figure 1.3 depicts a schematic representation of passive and active tumor targeting.

Passive targeting refers to the accumulation of nanoparticles in tumors due to the unique features of tumor tissues, such as leaky blood vessels and impaired lymphatic drainage. These features allow nanoparticles to accumulate in the tumor tissue more than in normal tissues, leading to a higher drug concentration in the tumor area. This phenomenon is known as the 'enhanced permeability and retention (EPR) effect' and takes advantage of the natural differences in blood vessels between normal and tumor tissues to achieve selective drug delivery.[74-75] In general, nanoparticles with a size range of 10-200 nm are considered to be the most suitable for passive targeting.[34, 76] Nanoparticles within this size range can extravasate through the leaky blood vessels surrounding the tumor tissue and accumulate in the tumor through the EPR effect. The optimal size of nanoparticles depends on several factors, including the tumor type, the location of the tumor, and the route of administration. It is known that nanoparticles with smaller sizes are rapidly cleared by renal filtration, while larger particles can be trapped in the liver and spleen, leading to reduced accumulation in the tumor tissue.[77] Within this size range, it is expected that nanoparticles exhibit longer circulation times in the blood, due to their ability to avoid recognition and clearance by the immune system. In addition to size, several other properties can influence their circulation time in the blood, including particle shape and surface charge and coating. It has been shown that PEGylation of particles can achieve or improve this effect.[78]

However, passive delivery via the EPR effect takes place in an unspecific way and varies from patient to patient. The effect generally offers only a modest increase in accumulation inside the tumor compared with critical normal organs.[79]

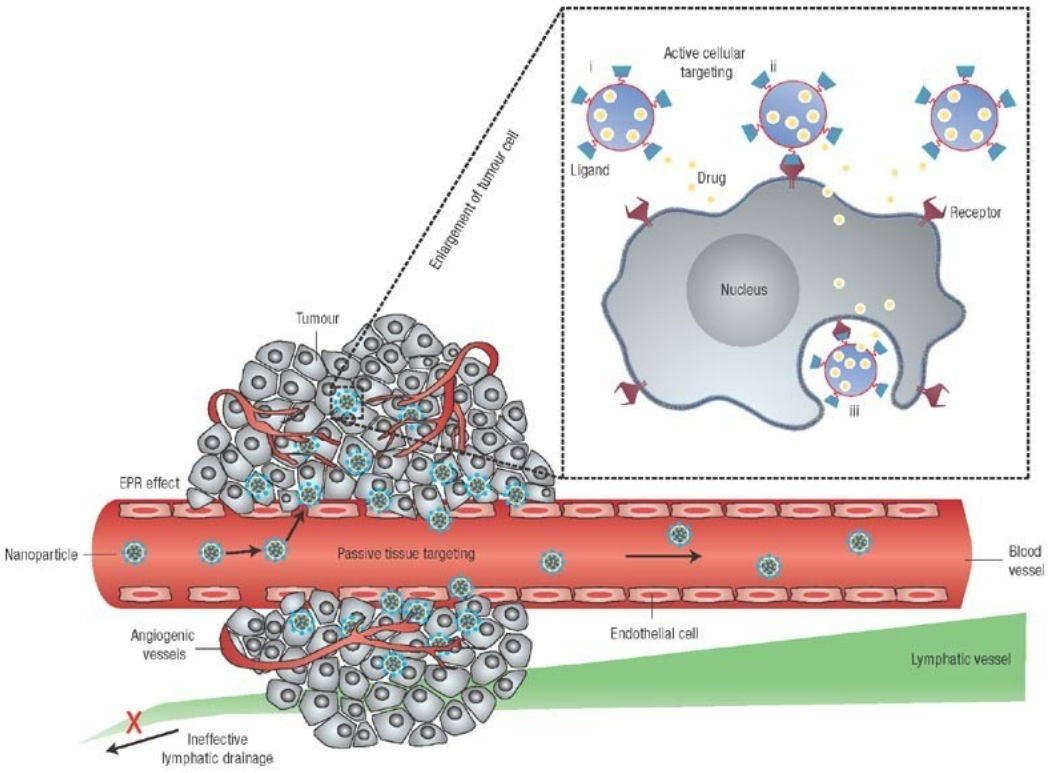

Figure 1.3: Schematic representation of passive and active cellular targeting (inset). Nanocarriers are shown as discs and can accumulate passively inside tumor tissue through the EPR effect. Active targeting can be achieved by presenting targeting ligands at the surface of the nanocarrier. Thus, the cargo can be released (i) extracellularly, (ii) in a sustained way from a depot or reservoir in the form of the nanocarrier attached to the cell membrane or (iii) intracellularly after uptake.[34]

Because of this, great efforts have been made towards active targeting. Active targeting involves attaching specific targeting molecules to the surface of nanoparticles that interact specifically with antigens or receptors that are either uniquely expressed or overexpressed on the tumor cells relative to normal tissues. Active targeting is more selective than passive targeting because it relies on the interaction between the targeting molecule and its specific receptor on the cancer cell's surface.[80]

In 1906 Paul Ehrlich dreamed of the idea of the ‘magic bullet’: a hypothetical drug that could selectively target and destroy diseased cells in the body without harming healthy cells. He envisioned a drug that would be able to recognize and bind specifically to a disease-causing agent, such as a bacterium or a cancer cell, and deliver a lethal dose of medication directly to the target site while sparing healthy cells.[81]

At the time, Ehrlich's vision of the ‘magic bullet’ was largely based on the use of chemical compounds, such as drugs and synthetic molecules, to target specific cells. However, with the advent of modern nanotechnology, nanomedicine has made significant strides in recent years towards realizing Ehrlich's vision of the ‘magic bullet’ by developing a range of nanoscale targeted drug delivery systems.

Methods of active targeting can range from the attachment of an antibody for a specific cell surface protein to the use of a synthetic targeting moiety.[82-83] At the moment, multiple ligand-targeted nanoparticle formulations for preferential cancer cell binding are in the early stages of investigation in clinical trials.[80] MESOMIR 1 is one example which is a nonliving bacterial minicell targeting the epidermal growth factor receptor (EGFR) with EGFR antibodies as targeting ligands.[84] EGFR belongs to the tyrosine kinase receptor family and is present in the epithelial cell membrane. Mutations in the epidermal growth factor occur in various cancer types. When EGFR is overexpressed, binding of endogenous ligands, including the epidermal growth factor (EGF), stimulates the growth and progression of tumors. In cancer therapy EGFR is currently considered an important target, aiming to achieve the synergistic effects of inhibition of receptor activation through binding of EGF as well as achieving targeted drug delivery (Figure 1.4).[85]

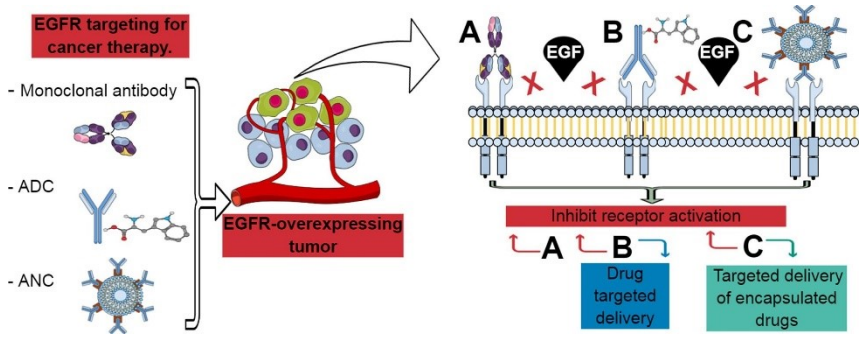

Figure 1.4: Targeting of EGFR-overexpressing tumors can be achieved through monoclonal antibodies, antibody-drug conjugates (ADC) or antibody-nanoparticle conjugates (ANC). Upon administration, the binding to EGFR inhibits the activation of the receptor by EGF binding and ADC and ANC targeted delivery of drugs.[85]

Drug Release Mechanisms

Stimuli-responsive drug delivery refers to the ability of nanoparticles to release their cargo in response to specific environmental cues or external stimuli. The idea behind stimuli-responsive drug delivery is to design nanocarriers that can remain stable and intact until they reach the target site, at which point the nanocarriers collapse/degrade or experience stimuli-responsive pore opening caused by some physical or chemical change to the carrier material, followed by the release of the cargo either intracellularly or extracellularly in a controlled manner to achieve optimal therapeutic efficacy.[86]

There are several types of stimuli that can trigger the release of drugs from nanoparticles, including pH, temperature[87], oxidation potential[88], light[89], magnetic field[90], and enzymatic activity[91]. The most commonly used stimuli are pH and temperature, as they are easily controlled and the latter can be readily manipulated *in vivo* e.g., via magnetic heating. In pH-responsive drug delivery systems, nanoparticles are designed to respond to changes in the acidity of the surrounding environment. Different organs, tissues and cellular compartments have different pH values, which makes the pH value a suitable stimulus for controlled drug release.[92] The pH values in tumors and inflammatory tissues are lower than those in blood and

normal tissues (≈7.4), and the acidic cellular environments exhibit even lower pH values, e.g. endosomes (pH ≈5.5–6.0) and lysosomes (pH ~4.5–5.0).[93] For example, the research groups of Fraser Stoddart and Jeffrey Zink have extensively studied the development of pH-responsive systems using cyclodextrins as macrocyclic gatekeepers on MSN. The systems typically consist of a monolayer of β-CD rings positioned selectively around the orifices of the pores of the nanoparticles. The cylindrical β-CD cavities could be used as closable openings, while conjugates can be moved in and out responding to pH levels like nanopistons (Figure 1.5).[94] This stimuli-responsive release worked for small cargo molecules (e.g. 2,6-naphthalenedisulfonic acid disodium). For larger cargo molecules (e.g. rhodamine B), the whole β-CD rings could be severed from the surface, releasing the large cargo molecules at acidic pH.[94-95]

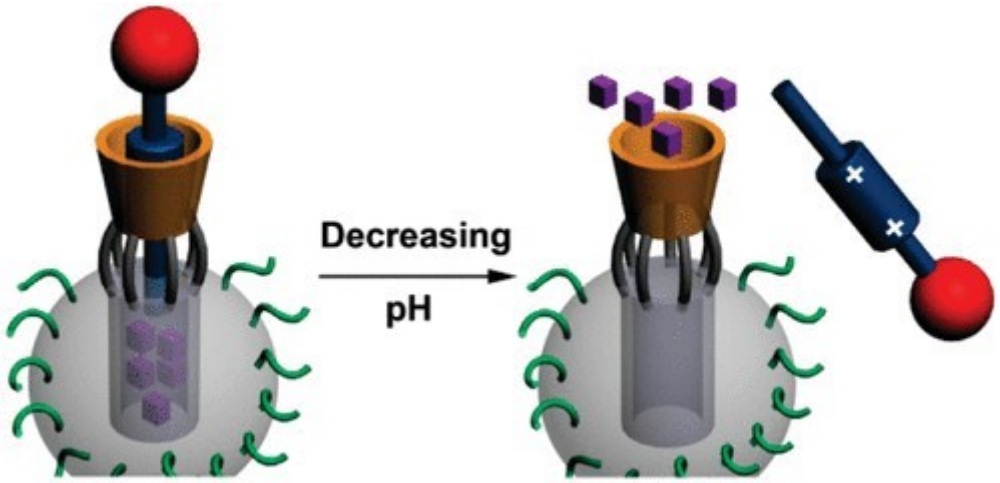

Figure 1.5: Schematic representation of nanopistons as gate keepers. Reprinted with permission from reference [94]. Copyright 2010 American Chemical Society.

Overall, stimuli-responsive drug delivery systems offer a promising approach to improve the efficacy and safety of drug delivery by providing more precise control over drug release.

Toxicity Profile

The use of nanocarriers for cancer therapy is a rapidly evolving field and researchers face multiple challenges in the design and synthesis of drug-loading nanocarriers. Reliable and reproducible safety assessments are required, as the safety of consumer products quickly became a topic of concern in society.[96] There are several regulatory frameworks in place to ensure the safety of nanoparticles. The United States Food and Drug Administration (FDA) is one such regulatory body that oversees the approval of nanocarriers for use in cancer therapy.

For example, before a nanocarrier can be approved by the FDA, it must go through a rigorous testing process to ensure its safety and efficacy. The FDA considers several factors, including the toxicity, pharmacokinetics and biodistribution of the nanoparticles.[97]

Biocompatibility and biodegradability of vehicles is a prerequisite for non-toxicity to animals and humans. The attraction of biodegradable nanoparticles centers on the principle of enhanced bioavailability of drugs through uptake, followed by degradation and disappearance of the vehicle from the system. A careful selection of precursors is therefore necessary. Furthermore, the synthesis conditions can play a role in the degradation behavior of nanoparticles.[98] For example, in a conclusive study of our group, the biodegradability of MSN at low concentrations was addressed in relation to their synthesis conditions (acidic, neutral, or basic pH) and their functionalization. The synthesis conditions determine the silica network connectivity while co-condensation with functional groups ‘interrupted’ the silica building blocks. Both predominantly determined the dissolution rate of MSN at low concentrations (Figure 1.6).

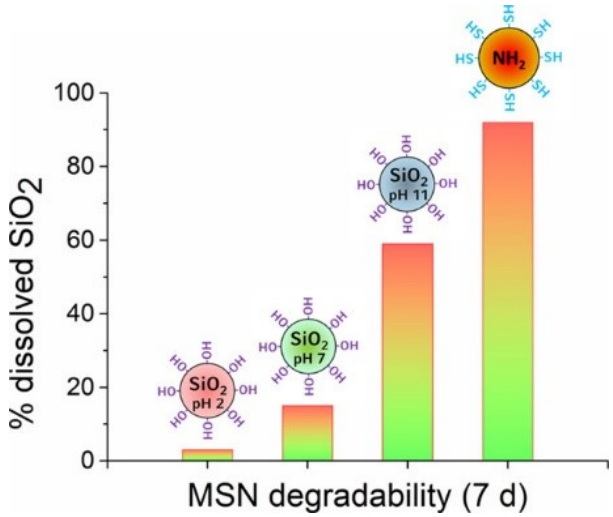

Figure 1.6: Comparison of the dissolution rate of MSN at low concentrations in dependence of their synthesis conditions or their functionalization. Reprinted with permission from reference [98]. Copyright 2019 American Chemical Society.

Then, during the design phase of the nanocarrier, it is necessary to conduct toxicity studies to further determine the safety of vehicles. These studies should evaluate the potential toxicity of the nanoparticles *in vitro* and *in vivo* and provide information on the dose-response relationship and the potential for adverse effects. Toxicity studies *in vitro* mostly involve cell viability assays, conducted via the measurement of metabolic activity. Interestingly, calcium phosphate-citrate nanoparticles are composed of completely biogenic, non-toxic calcium, phosphate, and citrate and the particles are not toxic to healthy cells either before endosomal release or after their degradation. However, as a composite they show an enormous potential to selectively kill cancer cells without involvement of inherently toxic drugs. The mechanism behind the selective killing might be the result of a high intracellular release of Ca^{2+} and citrate which induce apoptosis only in cancerous cells due to their altered metabolic activity.[99] More details can be found in Chapter 1.2.2.

For toxicity studies *in vivo,* it is important to carefully evaluate the biodistribution of nanoparticles used in drug delivery to ensure that they reach their intended targets and do not

cause harm to other tissues or organs, e.g. liver or spleen. Understanding the interactions between drug delivery vehicles and biological systems *in vivo* is essential for evaluating nanocarriers' safety and developing better nanomedicine. Interactions between nanocarrier and proteins, e.g. immediate formation of a protein corona, can occur when nanoparticles are administered or exposed to biological systems.[100] Protein corona formation can depend on the surface of the nanocarrier, e.g. differences occur when coated or non-coated carriers are considered.[101]

All of these aspects have to be carefully evaluated when nanocarriers are designed for drug delivery.

1.1.1. **Mesoporous Silica Nanoparticles**

Mesoporous silica nanoparticles (MSN) are a type of material that have a large surface area and a well-defined porous structure with a pore size in the range of about 2-50 nm.[102-103] MSN are composed of silica, which is a fairly biocompatible and non-toxic material, and they have been extensively studied as a drug delivery system due to their unique properties.[95]

MSN can be synthesized using a sol-gel process, which involves the hydrolysis and condensation of a silica precursor to form a solid silica network. There are multiple different synthesis routes which are based on the formation of surfactant micelles that serve as a template for the formation of a silica network.

The general steps involved in MSN synthesis are as follows:

1. Silica precursor: A silica precursor such as tetraethyl orthosilicate (TEOS) is mixed with a solvent.
2. Surfactant: A surfactant, for example cetyltrimethylammonium bromide (CTAB) is added to the mixture to form micelles, which act as a template for the formation of the mesoporous structure.
3. Stabilization: The mixture is stirred or sonicated to stabilize the micelles and prevent them from coalescing.
4. Hydrolysis and condensation: An acidic or basic catalyst is added to the mixture to induce the hydrolysis and condensation of the silica precursor, forming a silica network around the micelles.
5. Calcination / acid wash: To remove the surfactant, the as-synthesized product is washed and then subjected to either high-temperature calcination or acid wash, resulting in a mesoporous silica structure.

The parameters involved in the synthesis process can be optimized to control the size, shape and pores of the MSN. For example, the type and concentration of the surfactant can affect the size and shape of the MSN as well as their pore size and the degree of ordering of the mesoporous structure. The surfactant template can form either lamellar (g=1), cylindrical (g=1/2), or spherical (g=1/3) micellar structures and can be described using the surfactant packing parameter g. This model predicts molecular self-assembly in surfactant solutions.[104] The surfactant packing parameter is defined as:

$$g = \frac{V}{al} \tag{1.1}$$

Surfactant packing parameter g: V: Volume of the hydrophobic chain of the organic template, a: surface interface (cross-section area at head) of surfactant, l: length of the hydrophobic chain of the surfactant.

The first material synthesis reported by the Mobil researchers (designated as MCM-41) was a significant breakthrough in the field of materials science, as it represented a new class of ordered mesoporous materials with well-defined pore sizes and large surface areas (700–1500 m^2/g). The base-hydrolysed synthesis with TEOS as precursor and CTAB as cationic surfactant led to micrometer-sized particles with hexagonally ordered mesopores.[105-106] The successful synthesis of MCM-41 demonstrated the potential of using surfactant templates to control the formation of mesoporous silica materials and has laid the groundwork for controlling the morphology of the particles by manipulating the pH during synthesis[107], by adding cosolvents[108], or by adjusting the surfactant concentration.[109] In subsequent work, the synthesis of MSN was targeted, however, many synthesis approaches suffered from agglomeration issues. Some attempts to circumvent these issues, e.g., by dilution of the reaction, resulted in large reaction volumes with low product yields.[110-112] To overcome this hurdle, we developed a synthesis route which employs the chelating base triethanolamine (TEA).[113] TEA can act as a basic catalyst, enabling the use of lower pH values in synthesis, and as a complexing agent for silica-based species. This could increase the hydrolysis rate and affect the nucleation of MSNs to

achieve smaller particle sizes and a narrower size distribution and to avoid particle agglomeration.[113]

To date, systematic studies exist investigating the impact of experimental parameters on the particle sizes of MSNs, e.g. stirring rate, TEA concentration, and reaction temperature. Some of the results are visualized in Figure 1.7.[114-115]

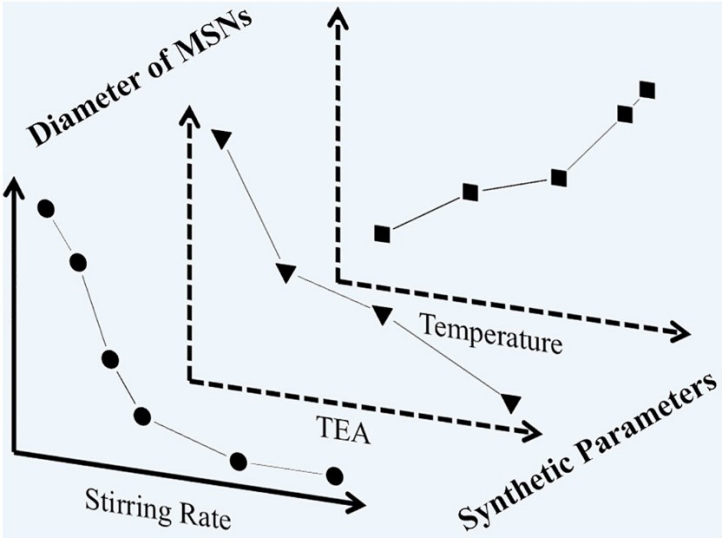

Figure 1.7: Impact of synthetic parameters on the resulting diameters of MSN.[114]

In addition, functional groups can be incorporated into the walls of the MSN during the synthesis. There are generally two possible ways to introduce organic functionalities into the silica framework: post-synthesis grafting and co-condensation. In post-synthesis grafting, MSN are first synthesized without any functional groups (except the naturally occurring silanol groups) on their surface or pores. After synthesis, the MSN are functionalized by adding a functional molecule such as a silane coupling agent, e.g. by either soaking or grinding the MSN in a solution or powder containing the functional molecule. In some cases, it has been found that materials functionalized via this grafting method can contain an inhomogeneous surface coverage of organic functional groups.[116]

Co-condensation functionalization is another approach where the functional groups are incorporated into the MSN during synthesis. In this method, a functional molecule, normally

an organotrialkoxysilane, is mixed with the silica precursor (often TEOS) before the MSN are synthesized. During synthesis, the functional molecule is co-condensed with the silica precursor and incorporated into the silica structure.[116]

MSN can be functionalized in a spatially controlled manner, gaining access to core-shell nanoparticles. The core of MSN can be functionalized to optimally control the interactions between cargo and host to achieve very high loading and release efficiencies. On the other hand, the shell can be differently functionalized to enable the attachment of targeting ligands, endosomal escape agents or different capping systems. Bifunctional core-shell MSN can be obtained by a site-selective delayed co-condensation synthesis approach, developed in our group (Figure 1.8).[117]

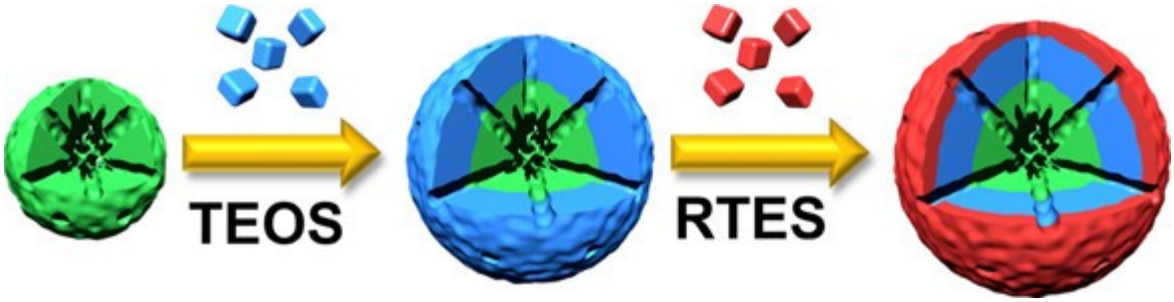

Figure 1.8: Site-selective delayed co-condensation approach for creating bifunctional MSNs. In a first step, co-condensation with a specific functionalization forms the core of the MSN (green). An unfunctionalized middle layer completes the growth of the nanoparticle (blue) by addition of TEOS to the reaction mixture. Finally, the addition of another organotriethoxysilane (RTES, R represents an organic moiety, red) forms the differently functionalized shell of the MSN. Reprinted with permission from reference [118]. Copyright 2014 American Chemical Society.

Overall, the above characteristics make MSN a promising family of materials that meets many of the requirements for a successful drug delivery vehicle.[118] The size-dependent delivery of antitumoral miRNA using MSN was investigated in Chapter 6.

1.1.2. **Metal Phosphate-based Nanoparticles**

Metal phosphate-based nanoparticles are a class of materials that have shown promise in drug delivery applications due to their biocompatibility, biodegradability and ability to encapsulate and protect drugs from degradation.[119] Among different metal ions used to form these nanoparticles, calcium is preferred. One advantage of using calcium in metal phosphate-based nanoparticles is its biocompatibility. Calcium is a naturally occurring element in the human body, making it a safe and biocompatible option for drug delivery.[120]

Crystalline hydroxyapatite and amorphous calcium phosphate are two types of calcium phosphate-based materials that have been extensively studied for medical and biological applications. The use of calcium-based metal phosphates for medical applications can be traced back to the discovery of crystalline hydroxyapatite in 1920.[121] Hydroxyapatite is the main mineral component of bone and teeth and has been extensively used for bone repair and regeneration.[122]

Amorphous calcium phosphate has been investigated for use in drug delivery, gene therapy, and tissue engineering applications. Due to their strong affinity for binding nucleic acids[123-124] and therapeutic drugs, promising results were generated using calcium phosphate nanoparticles for drug delivery.[125] Furthermore, it is hypothesized that after entering the cells, calcium phosphate nanoparticles would de-assemble at low pH in the endosome, which would cause endosome swelling and bursting to release the entrapped cargo to ensure an efficient drug delivery.[126] Therefore, considering the use of calcium phosphate nanoparticles in advanced drug delivery systems seems to be very attractive.

There are various synthesis strategies for these materials, but the most common method involves wet-chemical precipitation from aqueous solutions.[127] In this process, calcium and phosphate ions are mixed together to form a supersaturated solution. Calcium phosphate

nanoparticles can then easily be precipitated. Synthesis strategies can be altered for co-precipitation with various regulators or stabilizers to prevent rapid nucleation and disordered growth. Furthermore, the precipitation kinetics of calcium phosphates can be controlled with organic complexing agents, such as ethylenediamine tetraacetic acid or citric acid.[128-129] The established method of complexing metal ions with hydroxycarboxylic acids to slow down kinetics[130] was employed for an easy synthesis route of amorphous calcium-phosphate-citrate nanoparticles (CPC), developed by Schirnding et al. in our group.[99]

If the metal is changed from calcium to magnesium, and magnesium-phosphate-citrate nanoparticles (MPCs) are obtained, the properties of the nanoparticles are different. Magnesium is also a biocompatible metal but it has different chemical and physical properties compared to calcium. However, similar to calcium phosphate, amorphous magnesium phosphate is used as part of state-of-the-art orthopedic cements.[131] Furthermore, magnesium phosphate nanoparticles can be efficiently used *in vitro* and *in vivo* for targeted drug delivery.[132] In the following chapter 3, the previously developed synthesis approach for Ca^{2+}-based phosphate nanoparticles was modified to obtain mesoporous biodegradable magnesium phosphate-citrate (MPC) nanocarriers.[133] Interestingly, MPCs are non-toxic, both to healthy and to cancerous cells, and were successfully used as drug delivery vehicles.

1.1.3. **Cyclodextrin-based Nanoparticles**

Cyclodextrins (CDs) are a family of cyclic oligosaccharides that are composed of glucose monomers. The most common types of cyclodextrins are alpha (α)-, beta (β)-, and gamma (γ)-cyclodextrin, which consist of 6, 7, and 8 glucose units, respectively, linked by α-1,4 glycosidic bonds. A CD's shape is that of a hollow truncated cone, with a hydrophobic cavity and a hydrophilic external surface (Figure 1.9).

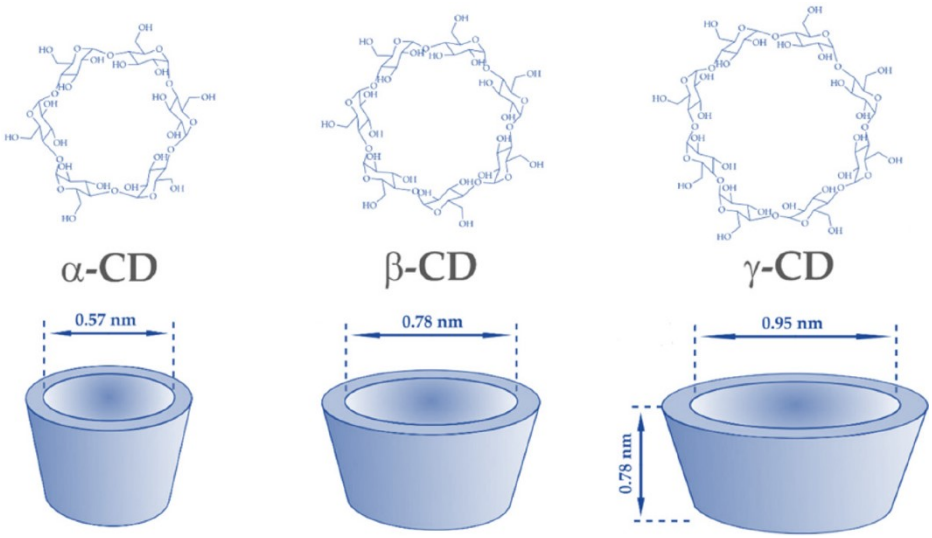

Figure 1.9: Dimensions and structure of α-CD, β-CD and γ-CD, respectively.[134]

Cyclodextrins have several properties that make them advantageous for drug delivery applications. They are generally non-toxic, biodegradable and biocompatible, which allowed them to be approved by the Food and Drug Administration (FDA) and the European Medicines Agency (EMA) for use in pharmaceutical formulations.

With their structural arrangement, they are able to form inclusion complexes. The encapsulation is based on hydrogen bonding, van-der-Waals forces and/or hydrophobic interactions and is used in various application fields such as biomedicine, catalysis, environmental protection, the food industry, and separation processes.[135-136] Numerous guest moieties, including, for

example, adamantane, azobenzene, ferrocene, cholesterol, etc., can be encapsulated. Although CDs are hydrophilic, they, along with the CD-guest complexes, can self-assemble to form either non-inclusion or CD/guest complexes, respectively, to form micro- and nanostructures that precipitate from aqueous CD solutions.[137-138] The encapsulation occurs if a dimensional fit between the host cavity and the guest molecule is achieved.[139] The adamantyl group is one of the most suitable guest moieties that can be accommodated by β-CD, due to its size. Exploiting the strong interactions of CD-adamantane complexes and the associated self-assembly behavior, multiple examples of supramolecular nanoparticle carriers were created that self-assembled from cyclodextrin- and adamantane-functionalized polymers for targeted drug delivery.[140-142] However, the non-covalent interactions could limit the use of supramolecular self-assemblies for drug delivery applications, since they might degrade easily before they reach their target. Furthermore, they have to be optimized for each new guest molecule that is incorporated or loaded due to different interactions with the particle structure.

Thus, covalently-crosslinked cyclodextrin materials open the possibility of building a platform for safe and efficient drug delivery. Recently, different approaches were used to prepare covalently-crosslinked CD molecule-containing materials. Groundbreaking work in this field was conducted by Dichtel *et al*.. β-CD was polymerized in a nucleophilic aromatic substitution reaction with tetrafluoro terephthalonitrile (TFTN), and mesoporous bulk material was obtained that was used to rapidly remove organic micropollutants from waste water.[143] Based on this work, our group developed β-CD-based nanoparticles which were crosslinked by TFTN for anti-cancer drug delivery applications.[144-145] The successful synthesis of covalently crosslinked cyclodextrin nanoparticles using carbonyldiimidazole as a linker molecule is discussed in detail in chapter 4. Biocompatible and biodegradable nanocarriers were obtained. Their synthesis as well as their degradation behavior was studied. In the following chapter 5, the potential of these

nanoparticles was demonstrated when they were used for the effective delivery of hydrophobic drugs in order to suppress inflammatory responses in macrophages.

Overall, innovative and biocompatible β-CD-based nanocarriers offer a promising platform for the development of controllable and efficient nanocarrier systems.

1.3. References

1. International Organization for Standardization., Nanotechnologies - Vocabulary - Part 1: Core terms. **2015,** Edition ISO/TS 80004-1.

2. Boverhof, D. R.; Bramante, C. M.; Butala, J. H.; Clancy, S. F.; Lafranconi, M.; West, J.; Gordon, S. C., Comparative assessment of nanomaterial definitions and safety evaluation considerations. Regulatory toxicology and pharmacology : RTP **2015,** 73 (1), 137-50.

3. U.S. Food and Drug Adminsitration., Considering whether an FDA-regulated product involves the application of nanotechnology. **2014,** FDA-2010-D-0530.

4. Faraday, M., X. The Bakerian Lecture. —Experimental relations of gold (and other metals) to light. Philosophical Transactions of the Royal Society of London **1857,** 147, 145-181.

5. Zsigmondy, R., Über kolloidale Lösungen. Zeitschrift für Elektrochemie **1902,** 8 (36), 684-687.

6. Feynman, R. P., There's Plenty of Room at the Bottom. Engineering and Science **1960,** 23 (5), 22-36.

7. Binnig, G.; Rohrer, H.; Gerber, C.; Weibel, E., Tunneling through a controllable vacuum gap. Applied Physics Letters **1982,** 40 (2), 178-180.

8. Binnig, G.; Rohrer, H.; Gerber, C.; Weibel, E., Surface Studies by Scanning Tunneling Microscopy. Physical Review Letters **1982,** 49 (1), 57-61.

9. Binnig, G.; Quate, C. F.; Gerber, C., Atomic Force Microscope. Physical Review Letters **1986,** 56 (9), 930-933.

10. Binnig, G. K. Atomic force microscope and method for imaging surfaces with atomic resolution. 1988.

11. Kroto, H. W.; Heath, J. R.; O'Brien, S. C.; Curl, R. F.; Smalley, R. E., C60: Buckminsterfullerene. Nature **1985,** 318 (6042), 162-163.

12. Iijima, S., Helical microtubules of graphitic carbon. Nature **1991,** 354 (6348), 56-58.

13. Novoselov, K. S.; Geim, A. K.; Morozov, S. V.; Jiang, D.; Zhang, Y.; Dubonos, S. V.; Grigorieva, I. V.; Firsov, A. A., Electric Field Effect in Atomically Thin Carbon Films. Science **2004,** 306 (5696), 666-669.

14. Xu, X.; Ray, R.; Gu, Y.; Ploehn, H. J.; Gearheart, L.; Raker, K.; Scrivens, W. A., Electrophoretic Analysis and Purification of Fluorescent Single-Walled Carbon Nanotube Fragments. Journal of the American Chemical Society **2004,** 126 (40), 12736-12737.

15. Li, J. Y.; Yao, M.; Shao, Y. X.; Yao, D. F., The application of bio-nanotechnology in tumor diagnosis and treatment: a view. Nanotechnol. Rev. **2018,** 7 (3), 257-266.

16. Emerich, D. F.; Thanos, C. G., Nanotechnology and medicine. Expert Opin. Biol. Ther. **2003,** 3 (4), 655-663.

17. Gmeiner, W. H.; Ghosh, S., Nanotechnology for cancer treatment. Nanotechnol. Rev. **2014,** 3 (2), 111-122.

18. Lou, J.; Zhang, L.; Zheng, G., Advancing Cancer Immunotherapies with Nanotechnology. Adv. Therap. **2019,** 2 (4), 31.

19. Ochekpe, N. A.; Olorunfemi, P. O.; Ngwuluka, N. C., Nanotechnology and Drug Delivery Part 2: Nanostructures for Drug Delivery. Trop. J. Pharm. Res. **2009,** 8 (3), 275-287.

20. Freitas, R. A., What is nanomedicine? Nanomed.-Nanotechnol. Biol. Med. **2005,** 1 (1), 2-9.

21. Krammer, F., SARS-CoV-2 vaccines in development. Nature **2020,** 586 (7830), 516-527.

22. Chung, Y. H.; Beiss, V.; Fiering, S. N.; Steinmetz, N. F., COVID-19 Vaccine Frontrunners and Their Nanotechnology Design. ACS nano **2020,** 14 (10), 12522-12537.

23. Meslé, M. M.; Brown, J.; Mook, P.; Hagan, J.; Pastore, R.; Bundle, N.; Spiteri, G.; Ravasi, G.; Nicolay, N.; Andrews, N.; Dykhanovska, T.; Mossong, J.; Sadkowska-Todys, M.; Nikiforova, R.; Riccardo, F.; Meijerink, H.; Mazagatos, C.; Kyncl, J.; McMenamin, J.; Melillo, T.; Kaoustou, S.; Lévy-Bruhl, D.; Haarhuis, F.; Rich, R.; Kall, M.; Nitzan, D.; Smallwood, C.; Pebody, R. G., Estimated number of deaths directly averted in people 60

years and older as a result of COVID-19 vaccination in the WHO European Region, December 2020 to November 2021. Eurosurveillance **2021,** 26 (47), 2101021.

24. World Health Organization, https://www.who.int/europe/emergencies/situations/covid-19 (accessed April 18th, 2023).

25. Miele, E.; Spinelli, G. P.; Miele, E.; Tomao, F.; Tomao, S., Albumin-bound formulation of paclitaxel (Abraxane (R) ABI-007) in the treatment of breast cancer. Int. J. Nanomed. **2009,** 4 (1), 99-105.

26. Ai, D.; Guan, Y.; Liu, X. J.; Zhang, C. F.; Wang, P.; Liang, H. L.; Guo, Q. S., Clinical comparative investigation of efficacy and toxicity of cisplatin plus gemcitabine or plus Abraxane as first-line chemotherapy for stage III/IV non-small-cell lung cancer. OncoTargets Ther. **2016,** 9, 5693-5698.

27. Koczula, K. M.; Gallotta, A., Lateral flow assays. Essays in biochemistry **2016,** 60 (1), 111-20.

28. Granade, T. C.; Workman, S.; Wells, S. K.; Holder, A. N.; Owen, S. M.; Pau, C.-P., Rapid Detection and Differentiation of Antibodies to HIV-1 and HIV-2 Using Multivalent Antigens and Magnetic Immunochromatography Testing. Clinical and Vaccine Immunology **2010,** 17 (6), 1034-1039.

29. Ardekani, L. S.; Thulstrup, P. W., Gold Nanoparticle-Mediated Lateral Flow Assays for Detection of Host Antibodies and COVID-19 Proteins. Nanomaterials (Basel, Switzerland) **2022,** 12 (9).

30. Wang, J.; Li, Y.; Nie, G., Multifunctional biomolecule nanostructures for cancer therapy. Nat. Rev. Mater. **2021,** 6 (9), 766-783.

31. Park, H.; Otte, A.; Park, K., Evolution of drug delivery systems: From 1950 to 2020 and beyond. Journal of controlled release : official journal of the Controlled Release Society **2022,** 342, 53-65.

32. Song, M.; Liu, C.; Chen, S.; Zhang, W., Nanocarrier-Based Drug Delivery for Melanoma Therapeutics. International Journal of Molecular Sciences **2021,** 22 (4), 1873.

33. Babu, A.; Templeton, A. K.; Munshi, A.; Ramesh, R., Nanodrug Delivery Systems: A Promising Technology for Detection, Diagnosis, and Treatment of Cancer. AAPS PharmSciTech **2014,** 15 (3), 709-721.

34. Peer, D.; Karp, J. M.; Hong, S.; Farokhzad, O. C.; Margalit, R.; Langer, R., Nanocarriers as an emerging platform for cancer therapy. Nature Nanotechnology **2007,** 2 (12), 751-760.

35. Shah, A.; Aftab, S.; Nisar, J.; Ashiq, M. N.; Iftikhar, F. J., Nanocarriers for targeted drug delivery. Journal of Drug Delivery Science and Technology **2021,** 62, 102426.

36. Jha, R.; Singh, A.; Sharma, P. K.; Fuloria, N. K., Smart carbon nanotubes for drug delivery system: A comprehensive study. Journal of Drug Delivery Science and Technology **2020,** 58, 101811.

37. Zhao, M.-X.; Zhu, B.-J., The Research and Applications of Quantum Dots as Nano-Carriers for Targeted Drug Delivery and Cancer Therapy. Nanoscale Research Letters **2016,** 11 (1), 207.

38. Hrkach, J. S.; Peracchia, M. T.; Bomb, A.; Lotan, n.; Langer, R., Nanotechnology for biomaterials engineering: structural characterization of amphiphilic polymeric nanoparticles by 1H NMR spectroscopy. Biomaterials **1997,** 18 (1), 27-30.

39. Calvo, P.; Remuñan-López, C.; Vila-Jato, J. L.; Alonso, M. J., Chitosan and chitosan/ethylene oxide-propylene oxide block copolymer nanoparticles as novel carriers for proteins and vaccines. Pharmaceutical research **1997,** 14 (10), 1431-6.

40. El-Samaligy, M. S.; Rohdewald, P., Reconstituted collagen nanoparticles, a novel drug carrier delivery system. Journal of Pharmacy and Pharmacology **2011,** 35 (8), 537-539.

41. De, R.; Mahata, M. K.; Kim, K.-T., Structure-Based Varieties of Polymeric Nanocarriers and Influences of Their Physicochemical Properties on Drug Delivery Profiles. Advanced Science **2022,** 9 (10), 2105373.

42. Kong, F. Y.; Zhang, J. W.; Li, R. F.; Wang, Z. X.; Wang, W. J.; Wang, W., Unique Roles of Gold Nanoparticles in Drug Delivery, Targeting and Imaging Applications. Molecules (Basel, Switzerland) **2017,** 22 (9).

43. Ghiuță, I.; Cristea, D., Silver nanoparticles for delivery purposes. Nanoengineered Biomaterials for Advanced Drug Delivery. 2020:347-71. doi: 10.1016/B978-0-08-102985-5.00015-2. Epub 2020 Jun 26.

44. Chauhan, A. S., Dendrimers for Drug Delivery. Molecules (Basel, Switzerland) **2018,** 23 (4).

45. Wang, J.; Li, B.; Qiu, L.; Qiao, X.; Yang, H., Dendrimer-based drug delivery systems: history, challenges, and latest developments. Journal of Biological Engineering **2022,** 16 (1), 18.

46. Ahmad, Z.; Shah, A.; Siddiq, M.; Kraatz, H.-B., Polymeric micelles as drug delivery vehicles. RSC Advances **2014,** 4 (33), 17028-17038.

47. Ghezzi, M.; Pescina, S.; Padula, C.; Santi, P.; Del Favero, E.; Cantù, L.; Nicoli, S., Polymeric micelles in drug delivery: An insight of the techniques for their characterization and assessment in biorelevant conditions. Journal of Controlled Release **2021,** 332, 312-336.

48. Son, I.; Lee, Y.; Baek, J.; Park, M.; Han, D.; Min, S. K.; Lee, D.; Kim, B.-S., pH-Responsive Amphiphilic Polyether Micelles with Superior Stability for Smart Drug Delivery. Biomacromolecules **2021,** 22 (5), 2043-2056.

49. Gao, Y.; Gao, D.; Shen, J.; Wang, Q., A Review of Mesoporous Silica Nanoparticle Delivery Systems in Chemo-Based Combination Cancer Therapies. Frontiers in Chemistry **2020,** 8.

50. Bharti, C.; Nagaich, U.; Pal, A. K.; Gulati, N., Mesoporous silica nanoparticles in target drug delivery system: A review. International journal of pharmaceutical investigation **2015,** 5 (3), 124-33.

51. Utzeri, G.; Matias, P. M. C.; Murtinho, D.; Valente, A. J. M., Cyclodextrin-Based Nanosponges: Overview and Opportunities. Frontiers in Chemistry **2022,** 10.

52. Horcajada, P.; Chalati, T.; Serre, C.; Gillet, B.; Sebrie, C.; Baati, T.; Eubank, J. F.; Heurtaux, D.; Clayette, P.; Kreuz, C.; Chang, J.-S.; Hwang, Y. K.; Marsaud, V.; Bories, P.-N.; Cynober, L.; Gil, S.; Férey, G.; Couvreur, P.; Gref, R., Porous metal–organic-framework nanoscale carriers as a potential platform for drug delivery and imaging. Nature Materials **2010,** 9 (2), 172-178.

53. Lawson, H. D.; Walton, S. P.; Chan, C., Metal–Organic Frameworks for Drug Delivery: A Design Perspective. ACS Applied Materials & Interfaces **2021,** 13 (6), 7004-7020.

54. Ding, M.; Zhang, Y.; Li, J.; Pu, K., Bioenzyme-based nanomedicines for enhanced cancer therapy. Nano Convergence **2022,** 9 (1), 7.

55. Zhang, P.; Zhang, Y.; Ding, X.; Shen, W.; Li, M.; Wagner, E.; Xiao, C.; Chen, X., A Multistage Cooperative Nanoplatform Enables Intracellular Co-Delivery of Proteins and Chemotherapeutics for Cancer Therapy. Advanced Materials **2020,** 32 (46), 2000013.

56. Gößl, D.; Singer, H.; Chiu, H.-Y.; Schmidt, A.; Lichtnecker, M.; Engelke, H.; Bein, T., Highly active enzymes immobilized in large pore colloidal mesoporous silica nanoparticles. New Journal of Chemistry **2019,** 43 (4), 1671-1680.

57. Yan, G.; Li, A.; Zhang, A.; Sun, Y.; Liu, J., Polymer-Based Nanocarriers for Co-Delivery and Combination of Diverse Therapies against Cancers. Nanomaterials (Basel, Switzerland) **2018,** 8 (2).

58. Huang, P. W.; Chang, J. W., Immune checkpoint inhibitors win the 2018 Nobel Prize. Biomedical journal **2019,** 42 (5), 299-306.

59. Chen, Z.; Kankala, R. K.; Yang, Z.; Li, W.; Xie, S.; Li, H.; Chen, A. Z.; Zou, L., Antibody-based drug delivery systems for cancer therapy: Mechanisms, challenges, and prospects. Theranostics **2022,** 12 (8), 3719-3746.

60. Abedin, M. R.; Powers, K.; Aiardo, R.; Barua, D.; Barua, S., Antibody–drug nanoparticle induces synergistic treatment efficacies in HER2 positive breast cancer cells. Scientific Reports **2021,** 11 (1), 7347.

61. Chen, F.; Ehlerding, E. B.; Cai, W. B., Theranostic Nanoparticles. J. Nucl. Med. **2014,** 55 (12), 1919-1922.

62. Sousa, F.; Castro, P.; Fonte, P.; Kennedy, P. J.; Neves-Petersen, M. T.; Sarmento, B., Nanoparticles for the delivery of therapeutic antibodies: Dogma or promising strategy? Expert Opinion on Drug Delivery **2017,** 14 (10), 1163-1176.

63. Cross, D.; Burmester, J. K., Gene therapy for cancer treatment: past, present and future. Clinical medicine & research **2006,** 4 (3), 218-27.

64. Mansoori, B.; Sandoghchian Shotorbani, S.; Baradaran, B., RNA interference and its role in cancer therapy. Advanced pharmaceutical bulletin **2014,** 4 (4), 313-21.

65. Ghidini, M.; Silva, S. G.; Evangelista, J.; do Vale, M. L. C.; Farooqi, A. A.; Pinheiro, M., Nanomedicine for the Delivery of RNA in Cancer. Cancers **2022,** 14 (11).

66. Tian, Z.; Liang, G.; Cui, K.; Liang, Y.; Wang, Q.; Lv, S.; Cheng, X.; Zhang, L., Insight Into the Prospects for RNAi Therapy of Cancer. Frontiers in Pharmacology **2021,** 12.

67. Yu, B.; Zhao, X.; Lee, L. J.; Lee, R. J., Targeted Delivery Systems for Oligonucleotide Therapeutics. The AAPS Journal **2009,** 11 (1), 195-203.

68. Chen, Y.; Gao, D.-Y.; Huang, L., In vivo delivery of miRNAs for cancer therapy: Challenges and strategies. Advanced drug delivery reviews **2015,** 81, 128-141.

69. Houseley, J.; Tollervey, D., The Many Pathways of RNA Degradation. Cell **2009,** 136 (4), 763-776.

70. Paunovska, K.; Loughrey, D.; Dahlman, J. E., Drug delivery systems for RNA therapeutics. Nature Reviews Genetics **2022,** 23 (5), 265-280.

71. Graham-Gurysh, E. G.; Carpenter, B. W.; Beck, W. A.; Varma, D. M.; Vincent, B. G.; Bachelder, E. M.; Ainslie, K. M., Chapter Fourteen - Delivery strategies for cancer vaccines and immunoadjuvants. In Systemic Drug Delivery Strategies, Amiji, M. M.; Milane, L. S., Eds. Academic Press: 2022; pp 359-408.

72. Sabado, R. L.; Pavlick, A.; Gnjatic, S.; Cruz, C. M.; Vengco, I.; Hasan, F.; Spadaccia, M.; Darvishian, F.; Chiriboga, L.; Holman, R. M.; Escalon, J.; Muren, C.; Escano, C.; Yepes, E.; Sharpe, D.; Vasilakos, J. P.; Rolnitzsky, L.; Goldberg, J.; Mandeli, J.; Adams, S.; Jungbluth, A.; Pan, L.; Venhaus, R.; Ott, P. A.; Bhardwaj, N., Resiquimod as an immunologic adjuvant for NY-ESO-1 protein vaccination in patients with high-risk melanoma. Cancer immunology research **2015,** 3 (3), 278-287.

73. Wagner, J.; Gößl, D.; Ustyanovska, N.; Xiong, M.; Hauser, D.; Zhuzhgova, O.; Hočevar, S.; Taskoparan, B.; Poller, L.; Datz, S.; Engelke, H.; Daali, Y.; Bein, T.; Bourquin, C., Mesoporous Silica Nanoparticles as pH-Responsive Carrier for the Immune-Activating Drug Resiquimod Enhance the Local Immune Response in Mice. ACS nano **2021,** 15 (3), 4450-4466.

74. Maeda, H.; Wu, J.; Sawa, T.; Matsumura, Y.; Hori, K., Tumor vascular permeability and the EPR effect in macromolecular therapeutics: a review. Journal of controlled release : official journal of the Controlled Release Society **2000,** 65 (1-2), 271-84.

75. Nakamura, Y.; Mochida, A.; Choyke, P. L.; Kobayashi, H., Nanodrug Delivery: Is the Enhanced Permeability and Retention Effect Sufficient for Curing Cancer? Bioconjugate chemistry **2016,** 27 (10), 2225-2238.

76. Wu, J., The Enhanced Permeability and Retention (EPR) Effect: The Significance of the Concept and Methods to Enhance Its Application. Journal of personalized medicine **2021,** 11 (8).

77. Longmire, M.; Choyke, P. L.; Kobayashi, H., Clearance properties of nano-sized particles and molecules as imaging agents: considerations and caveats. Nanomedicine **2008,** 3 (5), 703-717.

78. Veronese, F. M.; Mero, A., The impact of PEGylation on biological therapies. BioDrugs : clinical immunotherapeutics, biopharmaceuticals and gene therapy **2008,** 22 (5), 315-29.

79. Matsumura, Y.; Maeda, H., A New Concept for Macromolecular Therapeutics in Cancer Chemotherapy: Mechanism of Tumoritropic Accumulation of Proteins and the Antitumor Agent Smancs1. Cancer Research **1986,** 46 (12_Part_1), 6387-6392.

80. Pearce, A. K.; O'Reilly, R. K., Insights into Active Targeting of Nanoparticles in Drug Delivery: Advances in Clinical Studies and Design Considerations for Cancer Nanomedicine. Bioconjugate chemistry **2019,** 30 (9), 2300-2311.

81. Strebhardt, K.; Ullrich, A., Paul Ehrlich's magic bullet concept: 100 years of progress. Nature Reviews Cancer **2008,** 8 (6), 473-480.

82. Marcucci, F.; Lefoulon, F., Active targeting with particulate drug carriers in tumor therapy: fundamentals and recent progress. Drug discovery today **2004,** 9 (5), 219-228.

83. Toporkiewicz, M.; Meissner, J.; Matusewicz, L.; Czogalla, A.; Sikorski, A. F., Toward a magic or imaginary bullet? Ligands for drug targeting to cancer cells: principles, hopes, and challenges. Int J Nanomedicine **2015,** 10, 1399-414.

84. van Zandwijk, N.; Pavlakis, N.; Kao, S.; Clarke, S.; Lee, A.; Brahmbhatt, H.; Macdiarmid, J.; Pattison, S.; Leslie, F.; Huynh, Y.; Linton, A.; Reid, G., P1.02 - MesomiR 1: A Phase I study of TargomiRs in patients with refractory malignant pleural mesothelioma (MPM) and lung cancer (NSCLC). Annals of Oncology **2015,** 26, ii16.

85. Santos, E. d. S.; Nogueira, K. A. B.; Fernandes, L. C. C.; Martins, J. R. P.; Reis, A. V. F.; Neto, J. d. B. V.; Júnior, I. J. d. S.; Pessoa, C.; Petrilli, R.; Eloy, J. O., EGFR targeting for cancer therapy: Pharmacology and immunoconjugates with drugs and nanoparticles. International Journal of Pharmaceutics **2021,** 592, 120082.

86. Caldorera-Moore, M.; Guimard, N.; Shi, L.; Roy, K., Designer nanoparticles: incorporating size, shape and triggered release into nanoscale drug carriers. Expert Opin Drug Deliv **2010,** 7 (4), 479-95.

87. Karimi, M.; Sahandi Zangabad, P.; Ghasemi, A.; Amiri, M.; Bahrami, M.; Malekzad, H.; Ghahramanzadeh Asl, H.; Mahdieh, Z.; Bozorgomid, M.; Ghasemi, A.; Rahmani Taji Boyuk, M. R.; Hamblin, M. R., Temperature-Responsive Smart Nanocarriers for Delivery Of Therapeutic Agents: Applications and Recent Advances. ACS Appl Mater Interfaces **2016,** 8 (33), 21107-33.

88. Liang, J.; Liu, B., ROS-responsive drug delivery systems. Bioengineering & translational medicine **2016,** 1 (3), 239-251.

89. Linsley, C. S.; Wu, B. M., Recent advances in light-responsive on-demand drug-delivery systems. Therapeutic delivery **2017,** 8 (2), 89-107.

90. Rühle, B.; Datz, S.; Argyo, C.; Bein, T.; Zink, J. I., A molecular nanocap activated by superparamagnetic heating for externally stimulated cargo release. Chemical Communications **2016,** 52 (9), 1843-1846.

91. Li, M.; Zhao, G.; Su, W.-K.; Shuai, Q., Enzyme-Responsive Nanoparticles for Anti-tumor Drug Delivery. Frontiers in Chemistry **2020,** 8.

92. Zhu, Y. J.; Chen, F., pH-responsive drug-delivery systems. Chemistry, an Asian journal **2015,** 10 (2), 284-305.

93. Yang, Q.; Wang, S. H.; Fan, P. W.; Wang, L. F.; Di, Y.; Lin, K. F.; Xiao, F. S., pH-responsive carrier system based on carboxylic acid modified mesoporous silica and polyelectrolyte for drug delivery. Chemistry of Materials **2005,** 17 (24), 5999-6003.

94. Zhao, Y.-L.; Li, Z.; Kabehie, S.; Botros, Y. Y.; Stoddart, J. F.; Zink, J. I., pH-Operated Nanopistons on the Surfaces of Mesoporous Silica Nanoparticles. Journal of the American Chemical Society **2010,** 132 (37), 13016-13025.

95. Li, Z.; Barnes, J. C.; Bosoy, A.; Stoddart, J. F.; Zink, J. I., Mesoporous silica nanoparticles in biomedical applications. Chemical Society Reviews **2012,** 41 (7), 2590-2605.

96. Cho, E. J.; Holback, H.; Liu, K. C.; Abouelmagd, S. A.; Park, J.; Yeo, Y., Nanoparticle Characterization: State of the Art, Challenges, and Emerging Technologies. Molecular Pharmaceutics **2013,** 10 (6), 2093-2110.

97. Alshawwa, S. Z.; Kassem, A. A.; Farid, R. M.; Mostafa, S. K.; Labib, G. S., Nanocarrier Drug Delivery Systems: Characterization, Limitations, Future Perspectives and Implementation of Artificial Intelligence. Pharmaceutics **2022,** 14 (4).

98. Möller, K.; Bein, T., Degradable Drug Carriers: Vanishing Mesoporous Silica Nanoparticles. Chemistry of Materials **2019,** 31 (12), 4364-4378.

99. von Schirnding, C.; Giopanou, I.; Hermawan, A.; Wehl, L.; Ntaliarda, G.; Illes, B.; Datz, S.; Geisslinger, F.; Bartel, K.; Sommer, A.-K.; Lianou, M.; Weiß, V.; Feckl, J.; Vollmar, A. M.; Bräuchle, C.; Stathopoulos, G. T.; Wagner, E.; Roidl, A.; Bein, T.; Engelke, H., Synergistic Combination of Calcium and Citrate in Mesoporous Nanoparticles Targets Pleural Tumors. Chem **2021,** 7 (2), 480-494.

100. Bai, X.; Wang, J.; Mu, Q.; Su, G., In vivo Protein Corona Formation: Characterizations, Effects on Engineered Nanoparticles' Biobehaviors, and Applications. Frontiers in Bioengineering and Biotechnology **2021,** 9.

101. van Rijt, S. H.; Bölükbas, D. A.; Argyo, C.; Wipplinger, K.; Naureen, M.; Datz, S.; Eickelberg, O.; Meiners, S.; Bein, T.; Schmid, O.; Stoeger, T., Applicability of avidin protein coated mesoporous silica nanoparticles as drug carriers in the lung. Nanoscale **2016,** 8 (15), 8058-8069.

102. Zheng, H.; Tai, C.-W.; Su, J.; Zou, X.; Gao, F., Ultra-small mesoporous silica nanoparticles as efficient carriers for pH responsive releases of anti-cancer drugs. Dalton Transactions **2015,** 44 (46), 20186-20192.

103. Manzano, M.; Vallet-Regi, M., Mesoporous Silica Nanoparticles for Drug Delivery. Advanced Functional Materials **2020,** 30 (2).

104. Intermolecular and Surface Forces. In Intermolecular and Surface Forces (Third Edition), Israelachvili, J. N., Ed. Academic Press: Boston, 2011; p iii.

105. Beck, J. S.; Vartuli, J. C.; Roth, W. J.; Leonowicz, M. E.; Kresge, C. T.; Schmitt, K. D.; Chu, C. T. W.; Olson, D. H.; Sheppard, E. W.; McCullen, S. B.; Higgins, J. B.; Schlenker, J. L., A new family of mesoporous molecular sieves prepared with liquid crystal templates. Journal of the American Chemical Society **1992,** 114 (27), 10834-10843.

106. Kresge, C. T.; Leonowicz, M. E.; Roth, W. J.; Vartuli, J. C.; Beck, J. S., Ordered mesoporous molecular sieves synthesized by a liquid-crystal template mechanism. Nature **1992,** 359 (6397), 710-712.

107. Sadasivan, S.; Khushalani, D.; Mann, S., Synthesis and shape modification of organo-functionalised silica nanoparticles with ordered mesostructured interiors. Journal of Materials Chemistry **2003,** 13 (5), 1023-1029.

108. Stöber, W.; Fink, A.; Bohn, E., Controlled growth of monodisperse silica spheres in the micron size range. Journal of Colloid and Interface Science **1968,** 26 (1), 62-69.

109. Huh, S.; Wiench, J.; Yoo, J.-C.; Pruski, M.; Lin, V., Organic Functionalization and Morphology Control of Mesoporous Silicas via a Co-Condensation Synthesis Method. Chemistry of Materials - CHEM MATER **2003,** 15.

110. Cai, Q.; Luo, Z.-S.; Pang, W.-Q.; Fan, Y.-W.; Chen, X.-H.; Cui, F.-Z., Dilute Solution Routes to Various Controllable Morphologies of MCM-41 Silica with a Basic Medium. Chemistry of Materials **2001,** 13 (2), 258-263.

111. Nooney, R. I.; Thirunavukkarasu, D.; Chen, Y.; Josephs, R.; Ostafin, A. E., Synthesis of Nanoscale Mesoporous Silica Spheres with Controlled Particle Size. Chemistry of Materials **2002,** 14 (11), 4721-4728.

112. Lin, H.-P.; Tsai, C.-P., Synthesis of Mesoporous Silica Nanoparticles from a Low-concentration CnTMAX–Sodium Silicate Components. Chemistry Letters **2003,** 32, 1092-1093.

113. Möller, K.; Kobler, J.; Bein, T., Colloidal Suspensions of Nanometer-Sized Mesoporous Silica. Advanced Functional Materials **2007,** 17 (4), 605-612.

114. Lv, X.; Zhang, L.; Xing, F.; Lin, H., Controlled synthesis of monodispersed mesoporous silica nanoparticles: Particle size tuning and formation mechanism investigation. Microporous and Mesoporous Materials **2016,** 225, 238-244.

115. Narayan, R.; Nayak, U. Y.; Raichur, A. M.; Garg, S., Mesoporous Silica Nanoparticles: A Comprehensive Review on Synthesis and Recent Advances. Pharmaceutics **2018,** 10 (3).

116. Lim, M. H.; Stein, A., Comparative Studies of Grafting and Direct Syntheses of Inorganic−Organic Hybrid Mesoporous Materials. Chemistry of Materials **1999,** 11 (11), 3285-3295.

117. Kecht, J.; Schlossbauer, A.; Bein, T., Selective Functionalization of the Outer and Inner Surfaces in Mesoporous Silica Nanoparticles. Chemistry of Materials **2008,** 20 (23), 7207-7214.

118. Argyo, C.; Weiss, V.; Bräuchle, C.; Bein, T., Multifunctional Mesoporous Silica Nanoparticles as a Universal Platform for Drug Delivery. Chemistry of Materials **2014,** 26 (1), 435-451.

119. Qiu, C.; Wu, Y.; Guo, Q.; Shi, Q.; Zhang, J.; Meng, Y.; Xia, F.; Wang, J., Preparation and application of calcium phosphate nanocarriers in drug delivery. Materials Today Bio **2022,** 17, 100501.

120. Dorozhkin, S. V.; Epple, M., Biological and medical significance of calcium phosphates. Angewandte Chemie (International ed. in English) **2002,** 41 (17), 3130-46.

121. Albee, F. H., STUDIES IN BONE GROWTH: TRIPLE CALCIUM PHOSPHATE AS A STIMULUS TO OSTEOGENESIS. Annals of surgery **1920,** 71 (1), 32-9.

122. Palmer, L. C.; Newcomb, C. J.; Kaltz, S. R.; Spoerke, E. D.; Stupp, S. I., Biomimetic Systems for Hydroxyapatite Mineralization Inspired By Bone and Enamel. Chemical Reviews **2008,** 108 (11), 4754-4783.

123. Pittella, F.; Cabral, H.; Maeda, Y.; Mi, P.; Watanabe, S.; Takemoto, H.; Kim, H. J.; Nishiyama, N.; Miyata, K.; Kataoka, K., Systemic siRNA delivery to a spontaneous pancreatic tumor model in transgenic mice by PEGylated calcium phosphate hybrid micelles. Journal of Controlled Release **2014,** 178, 18-24.

124. Jung, H.; Kim, S. A.; Yang, Y. G.; Yoo, H.; Lim, S.-J.; Mok, H., Long chain microRNA conjugates in calcium phosphate nanoparticles for efficient formulation and delivery. Archives of Pharmacal Research **2015,** 38 (5), 705-715.

125. Chow, L. C., Next generation calcium phosphate-based biomaterials. Dental materials journal **2009,** 28 (1), 1-10.

126. Li, J.; Chen, Y. C.; Tseng, Y. C.; Mozumdar, S.; Huang, L., Biodegradable calcium phosphate nanoparticle with lipid coating for systemic siRNA delivery. Journal of controlled release : official journal of the Controlled Release Society **2010,** 142 (3), 416-21.

127. Kuśnieruk, S.; Wojnarowicz, J.; Chodara, A.; Chudoba, T.; Gierlotka, S.; Lojkowski, W., Influence of hydrothermal synthesis parameters on the properties of hydroxyapatite nanoparticles. Beilstein Journal of Nanotechnology **2016,** 7, 1586-1601.

128. Westin, K. J.; Rasmuson, Å. C., Crystal growth of aragonite and calcite in presence of citric acid, DTPA, EDTA and pyromellitic acid. Journal of Colloid and Interface Science **2005,** 282 (2), 359-369.

129. Davies, E.; Müller, K. H.; Wong, W. C.; Pickard, C. J.; Reid, D. G.; Skepper, J. N.; Duer, M. J., Citrate bridges between mineral platelets in bone. Proceedings of the National Academy of Sciences **2014,** 111 (14), E1354-E1363.

130. Pechini, M. P. Method of preparing lead and alkaline earth titanates and niobates and coating method using the same to form a capacitor 1963.

131. Babaie, E.; Lin, B.; Goel, V. K.; Bhaduri, S. B., Evaluation of amorphous magnesium phosphate (AMP) based non-exothermic orthopedic cements. Biomedical Materials **2016,** 11 (5), 055010.

132. Bhakta, G.; Shrivastava, A.; Maitra, A., Magnesium phosphate nanoparticles can be efficiently used in vitro and in vivo as non-viral vectors for targeted gene delivery. Journal of biomedical nanotechnology **2009,** 5 (1), 106-14.

133. Wehl, L.; von Schirnding, C.; Bayer, M. C.; Zhuzhgova, O.; Engelke, H.; Bein, T., Mesoporous Biodegradable Magnesium Phosphate-Citrate Nanocarriers Amplify Methotrexate Anticancer Activity in HeLa Cells. Bioconjugate chemistry **2022,** 33 (4), 566-575.

134. Păduraru, D. N.; Niculescu, A.-G.; Bolocan, A.; Andronic, O.; Grumezescu, A. M.; Bîrlă, R., An Updated Overview of Cyclodextrin-Based Drug Delivery Systems for Cancer Therapy. Pharmaceutics **2022,** 14 (8), 1748.

135. Cid-Samamed, A.; Rakmai, J.; Mejuto, J. C.; Simal-Gandara, J.; Astray, G., Cyclodextrins inclusion complex: Preparation methods, analytical techniques and food industry applications. Food Chemistry **2022,** 384, 132467.

136. Crini, G.; Fourmentin, S.; Fenyvesi, É.; Torri, G.; Fourmentin, M.; Morin-Crini, N., Cyclodextrins, from molecules to applications. Environmental Chemistry Letters **2018,** 16 (4), 1361-1375.

137. Loftsson, T.; Jarho, P.; Másson, M.; Järvinen, T., Cyclodextrins in drug delivery. Expert Opinion on Drug Delivery **2005,** 2 (2), 335-351.

138. Loftsson, T.; Saokham, P.; Sá Couto, A. R., Self-association of cyclodextrins and cyclodextrin complexes in aqueous solutions. International Journal of Pharmaceutics **2019,** 560, 228-234.

139. Palepu, R.; Reinsborough, V., beta-Cyclodextrin Inclusion of Adamantane Derivatives in Solution. Australian Journal of Chemistry **1990,** 43 (12), 2119-2123.

140. Ang, C. Y.; Tan, S. Y.; Wang, X.; Zhang, Q.; Khan, M.; Bai, L.; Tamil Selvan, S.; Ma, X.; Zhu, L.; Nguyen, K. T.; Tan, N. S.; Zhao, Y., Supramolecular nanoparticle carriers self-assembled from cyclodextrin- and adamantane-functionalized polyacrylates for tumor-targeted drug delivery. Journal of Materials Chemistry B **2014,** 2 (13), 1879-1890.

141. Kojima, R.; Aubel, D.; Fussenegger, M., Novel theranostic agents for next-generation personalized medicine: small molecules, nanoparticles, and engineered mammalian cells. Current Opinion in Chemical Biology **2015,** 28, 29-38.

142. Ghitman, J.; Voicu, S. I., Controlled drug delivery mediated by cyclodextrin-based supramolecular self-assembled carriers: From design to clinical performances. Carbohydrate Polymer Technologies and Applications **2023,** 5, 100266.

143. Alsbaiee, A.; Smith, B. J.; Xiao, L.; Ling, Y.; Helbling, D. E.; Dichtel, W. R., Rapid removal of organic micropollutants from water by a porous β-cyclodextrin polymer. Nature **2016,** 529 (7585), 190-4.

144. Datz, S.; Illes, B.; Gößl, D.; Schirnding, C. v.; Engelke, H.; Bein, T., Biocompatible crosslinked β-cyclodextrin nanoparticles as multifunctional carriers for cellular delivery. Nanoscale **2018,** 10 (34), 16284-16292.

145. Möller, K.; Macaulay, B.; Bein, T., Curcumin Encapsulated in Crosslinked Cyclodextrin Nanoparticles Enables Immediate Inhibition of Cell Growth and Efficient Killing of Cancer Cells. Nanomaterials (Basel, Switzerland) **2021,** 11 (2).

CHAPTER 2

Characterization

2. Characterization

For the characterization of nanomaterials, several different analytical techniques can be applied. First, dynamic light scattering (DLS) can be used to determine the size (distribution) of nanoparticles. Scanning electron microscopy (SEM) and transmission electron microscopy (TEM) allow the imaging of a specimen and can be used to gain information about the particle size, morphology and pore structure. Further information about the surface area, pore size distribution and pore volume of porous material can be obtained with nitrogen sorption measurements. Furthermore, various functional groups of different functionalization steps can be identified using Fourier-transform-infrared (FTIR) microscopy and Raman spectroscopy. Additionally, zeta potential measurements were performed to examine the surface charge of samples and to evaluate changes in surface charge through incorporated organic moieties. The relative amounts of organic functionalization were determined using thermogravimetric analysis (TGA). Loading and release properties of loaded fluorescent dyes or other cargos into the pores of the sample can be investigated using fluorescence spectroscopy, confocal fluorescence microscopy and UV-Vis measurements.

2.1. Dynamic Light Scattering

Dynamic light scattering (DLS) enables the fast and easy measurement of the hydrodynamic diameter of NPs and their size distribution. The general method is based on the principle that particles in solution will exhibit Brownian motion, which results in fluctuations in the scattered light intensity that can be measured and analysed.[1]

Particles in suspension undergo Brownian motion due to random collisions of solvent molecules and particles. Here, larger particles show slower Brownian motion in comparison to smaller ones. The movement of the particles leads to a fluctuation in interference and scattered light intensity. The fluctuations of scattered light intensity due to the movement of the individual scattering centers can be analyzed using second-order autocorrelation functions. The autocorrelation function describes the time-dependent fluctuations in the scattered light intensity to measure how similar the intensity function is to itself over different delay times.[2]

$$g_2(\tau) = \frac{\langle I(t)I(t+\tau)\rangle}{\langle I(t)\rangle^2} \tag{2.1}$$

τ: delay time, I: Intensity

To clarify, when the movement of particles over time is monitored, information on the size can be obtained since large particles diffuse slowly, resulting in more similar positions at different time points and a slower decay time in the correlation functions. Small particles move faster and therefore leave their positions more quickly. Consequently, they have a faster rate of decay in the correlation function. Thus, it is possible to obtain the translational diffusion coefficient D that is related to the size of the particles in solution, the hydrodynamic radius *d(H) via* the Stokes-Einstein equation (equation 2.2).

$$\boldsymbol{d(H) = \frac{kT}{3\pi\eta D}} \tag{2.2}$$

Stokes-Einstein equation: k: Boltzmann's constant, T: temperature, η: viscosity of the suspending medium, D: diffusion coefficient.

The hydrodynamic radius is defined as the size of a sphere that diffuses at the same rate as the particle being measured. This sphere comprises the particle as well as everything that is bound to the surface of the particle, e.g., ions or adsorbed polymers. Consequently, the hydrodynamic radius can be influenced by factors like the ionic strength of the medium and the nature of the particle's surface. Furthermore, it should be noted that bigger particles scatter light significantly more than smaller ones so that even small amounts of agglomerated particles can cause high scattering intensity. As a result, the method is only suitable for relatively monodisperse and uncontaminated (e.g. by dust), non-agglomerated samples. If all those considerations are taken into account, DLS is a very powerful and commonly used method to investigate the sizes of particles between about 1 and 1000 nm.

2.2. Zeta Potential Measurements

Zeta potential measurements can be conducted to obtain information about the surface charge of nanoparticles, which can be employed to assess the stability of a colloidal system. In aqueous solution, nanoparticles are usually (slightly) charged due to the dissociation of surface groups or adsorption of solvent molecules. Hereby, oppositely charged ions of the dispersion medium attach to the surface of the nanoparticle, forming an electric double-layer (Figure 2.1). The inner layer consists of tightly bound counter ions, called Stern layer, while weakly bound counter ions can be found in the outer layer (up to the slipping plane). The double layer (up to the slipping plane) remains attached to the particle and follows its Brownian motion. The

electric potential difference between this double layer and the surrounding dispersion medium is defined as the zeta potential ζ.[3]

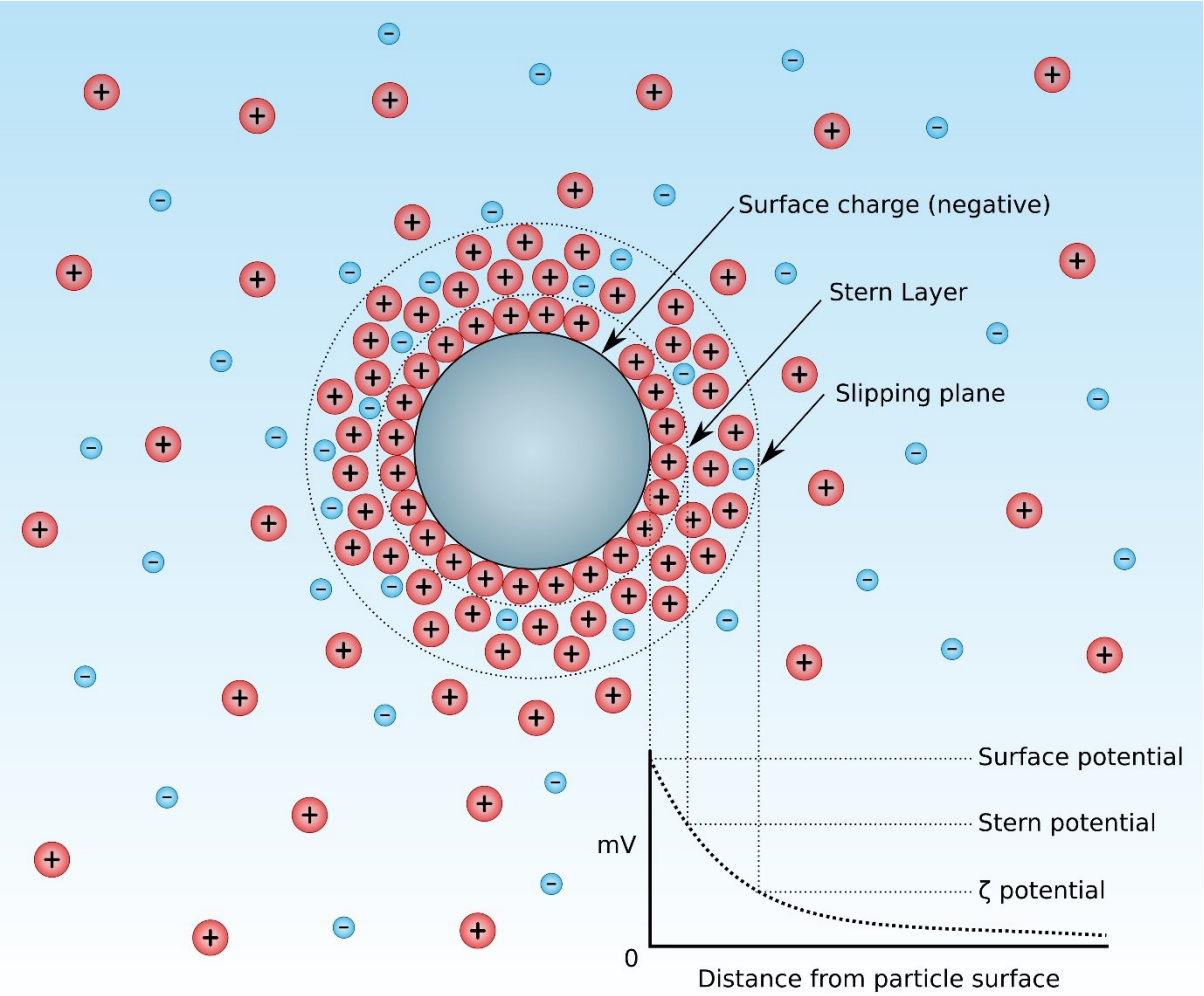

Figure 2.1: Schematic drawing showing a nanoparticle with negative surface charge surrounded by attached counter ions in a dispersion medium and the potential difference as a function of distance.[4]

The measurement of the zeta potential can take place in a cuvette with two gold electrodes where a laser measures how fast the particles move when an external electric field is applied. Charged particles will move towards the electrode with the opposite charge. The velocity of the movement, referred to as the electrophoretic mobility of particles, is related to the zeta potential by the Henry equation (equation 2.3) and depends on the strength of the electric field, the dielectric constant of the medium, the viscosity of the medium and the zeta potential.

$$U_E = \frac{2\,\varepsilon\,\zeta\,f(\kappa a)}{3\,\eta} \tag{2.3}$$

Henry equation. U_E: electrophoretic mobility; ε: dielectric constant of the medium; η: viscosity of the medium; ζ: zeta potential; $f(\kappa a)$: Henry function with κ Debye length and a particle radius.

The magnitude of the zeta potential gives an indication of the stability of the colloidal system due to the degree of repulsion between the charged particles in the dispersion. Large values (positive or negative) indicate good colloidal stability because of the strong electrostatic repulsion of individual particles. Small zeta potential values and a poor resulting colloidal stability can affect particle agglomeration and flocculation because there is no force to prevent the particles from coming together.

2.3. Nitrogen Sorption measurements

The properties of porous materials, e.g. surface area, pore size distribution and pore volume can be determined with sorption measurements.[5] The term adsorption refers to the attachment of gaseous particles (adsorptive) on a solid surface (adsorbent). Nitrogen at 77 K is the most common adsorptive and can undergo attractive interactions when it is brought into contact with the solid surface of the adsorbent. This general phenomenon is classified as physisorption and is a result of weak *van-der-Waals* interactions.

Static volumetric determination of the sorption isotherm is a widely used procedure for surface analysis. The method involves measuring the amount of nitrogen gas adsorbed onto the material at various pressures, and then using these data to calculate the surface area and pore size distribution.

The measurement involves introducing a known quantity of nitrogen gas to the sample material at a low temperature, typically around -196°C (77 K). As the gas is introduced, it begins to adsorb onto the surface of the sample, filling up the available pores and probing the surface area of the sample. The amount of gas adsorbed at each pressure after equilibration is then measured using a volumetric method, and the data are plotted on a graph called an adsorption isotherm. The reverse process, decreasing the amount of adsorptive in the sample chamber, leads to the desorption isotherm.

According to IUPAC the isotherms are classified into six different isotherm types (Figure 2.2). The sorption isotherms are plotted as the amount of adsorptive as a function of relative pressure p/p_0, with p_0 being the equilibrium vapor pressure and p the actual pressure.

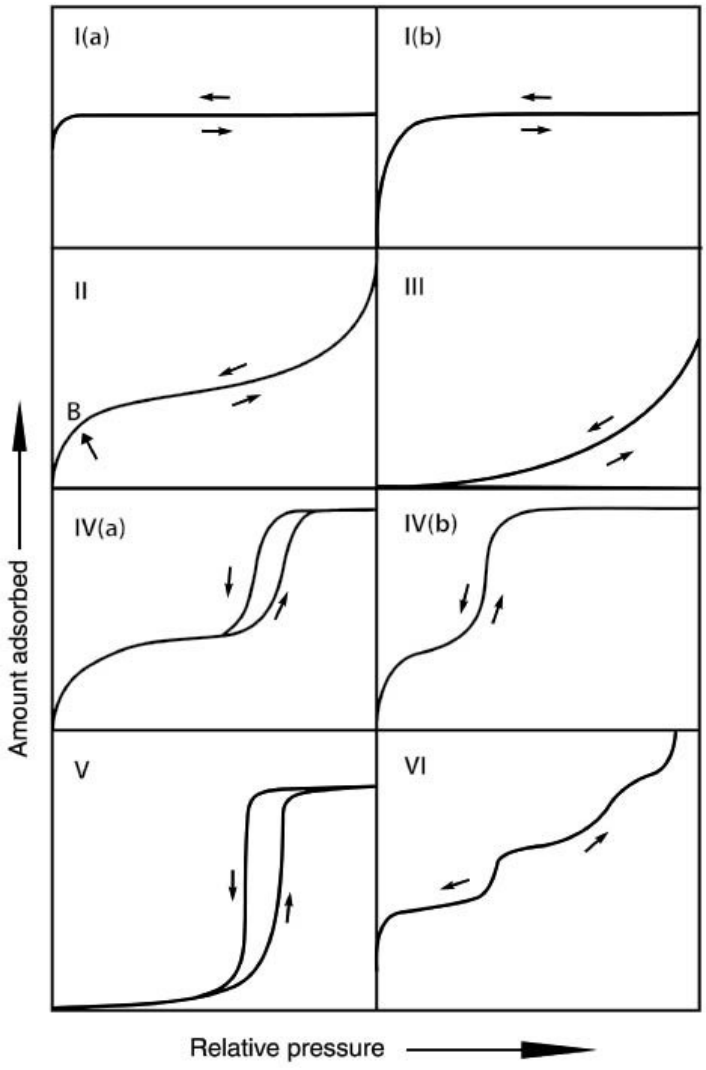

Figure 2.2: IUPAC classification of physisorption isotherms. Adapted from reference [6], IUPAC Technical Report, 2015, © IUPAC.

The isotherms are grouped into six main types according to the materials' pore size and structure and its interaction with the adsorptive. Type I isotherms include microporous solids with narrow pores < ~ 1nm (Type Ia) or wider pores with a pore width of < ~ 2.5 nm (Type Ib). Nonporous material falls into the category of type II isotherms. A substrate with only weak adsorbent-adsorptive interactions is represented by a type III isotherm. Type IV isotherms comprise mesoporous samples. For material with a pore width greater than ~ 4 nm, additional phenomena such as capillary condensation can lead to a hysteresis loop (type IVa). This is the case when the relative pressure p/p_0 is reduced and more energy is needed to remove the

condensed adsorbate molecules from the pore than for the adsorption of the adsorptive molecules. In materials with pores smaller than 4 nm no capillary condensation and no hysteresis is typically observed (type IVb). The type V isotherm is similar to type III and representative of weak adsorbent-adsorptive interactions. Here, at higher p/p_0 values the adsorption of additional adsorptive molecules is favored due to previously adsorbed molecules followed by pore filling. The type VI isotherm shows stepwise multilayer adsorption on well-defined surfaces.

The most widely used principle for the evaluation of the surface area is the Brunauer-Emmett-Teller (BET) method expressed in the BET equation [6-7]:

$$\frac{p/p^0}{\boldsymbol{n}(1-p/p^0)} = \frac{1}{\boldsymbol{n}_m C} + \frac{C-1}{\boldsymbol{n}_m C}(p/p_0) \tag{2.4}$$

BET equation. n: specific amount adsorbed at relative pressure p/p_0; n_m: specific monolayer capacity; C: BET constant.

The BET method involves plotting the quantity $\frac{p/p_0}{\boldsymbol{n}(1-p/p_0)}$ against the relative pressure (p/p_0) for a given adsorbate gas. The resulting linear plot is called a BET plot. The range of linearity is limited to a part of the isotherm, normally within the (p/p_0) range of ~ 0.05-0.30. In the application of the BET method, the monolayer capacity n_m has to be derived from a "BET plot". Then, the BET specific area A can be calculated with the obtained value n_m using equation 2.5. For this a knowledge of the average area, a_m, occupied by the adsorbate molecules in the complete monolayer is required. For each nitrogen molecule in a close-packed monolayer at 77 K, a value of $a_m(N_2) = 0.162$ nm^2 is usually assumed.

$$A(BET) = n_m^a \cdot L \cdot a_m \tag{2.5}$$

Calculation of BET area with n_m^a monolayer capacity, L Avogadro constant and a_m average area occupied by adsorptive molecule.[8]

2.4. Thermogravimetric Analysis

Thermogravimetric analysis (TGA) is a technique to characterize materials by measuring the change of mass of a substance as a function of temperature or time. The mass changes may be caused by thermal decomposition or combustion of the material as well as chemical reactions, e.g., oxidation of components.

The TGA instrument consists of a sample holder within a furnace which is coupled to a microbalance mechanism. During analysis the sample is heated stepwise and the microbalance mechanism detects mass changes in the sample. TGA is often used together with differential scanning calorimetry (DSC) for a simultaneous measurement of both mass change and heat flow during thermal analysis. This coupling provides complementary information about the thermal behavior of materials.[9]

During DSC, a sample is heated or cooled at a constant rate while its heat flow is monitored. This allows for the detection of thermal events such as phase transitions, chemical reactions, and crystallization processes, which are accompanied by a change in heat flow. By measuring the heat flow as a function of temperature, DSC can provide information about the enthalpy (heat) changes associated with these events, as well as their onset temperature and rate of occurrence.[10]

By combining TGA and DSC in a single instrument, TGA-DSC can help to identify the causes of mass changes observed in TGA, by providing information about the thermal events that are occurring.

2.5. Molecular Spectroscopy

Molecular spectroscopy is a powerful tool to study the interaction of matter with electromagnetic radiation.[11] This technique is applied when determining the composition and

structure of a sample, which is essential for the characterization of chemical compounds. There are several different types of molecular spectroscopy relevant to this thesis, including ultraviolet-visible- (UV-Vis-) infrared- (IR) and Raman, as well as fluorescence spectroscopy, each of which will be introduced in the following.

Electromagnetic radiation is characterized by its wavelength λ or its frequency ν. The electromagnetic spectrum is typically divided into different segments as shown in Figure 2.3. The energy E of the light quantum, namely a photon, is related to the frequency ν through the Planck constant h:

$$E = h\nu \tag{2.6}$$

Depending on the type of spectroscopy, the sample is irradiated with light of different wavelengths and energies.

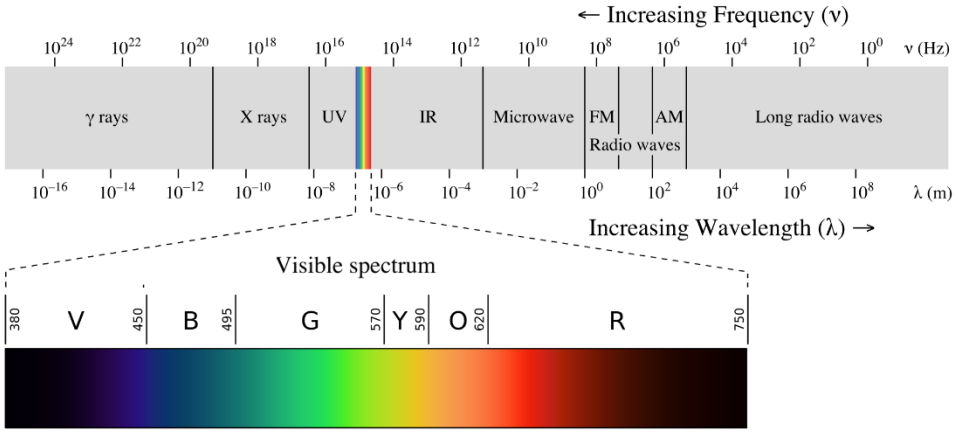

Figure 2.3: Overview of the electromagnetic spectrum with respect to frequency and wavelength, highlighting the visible spectrum.[12]

The principle of molecular spectroscopy is based on different absorption and emission processes caused by the interaction of molecules with electromagnetic radiation (Figure 2.4).

Molecules can absorb light with appropriate frequency and are thus excited to higher energy levels. With the emission of energy, the molecule regresses back to its former lower energy level, usually the ground energy level (or distribution) at the given temperature.[13]

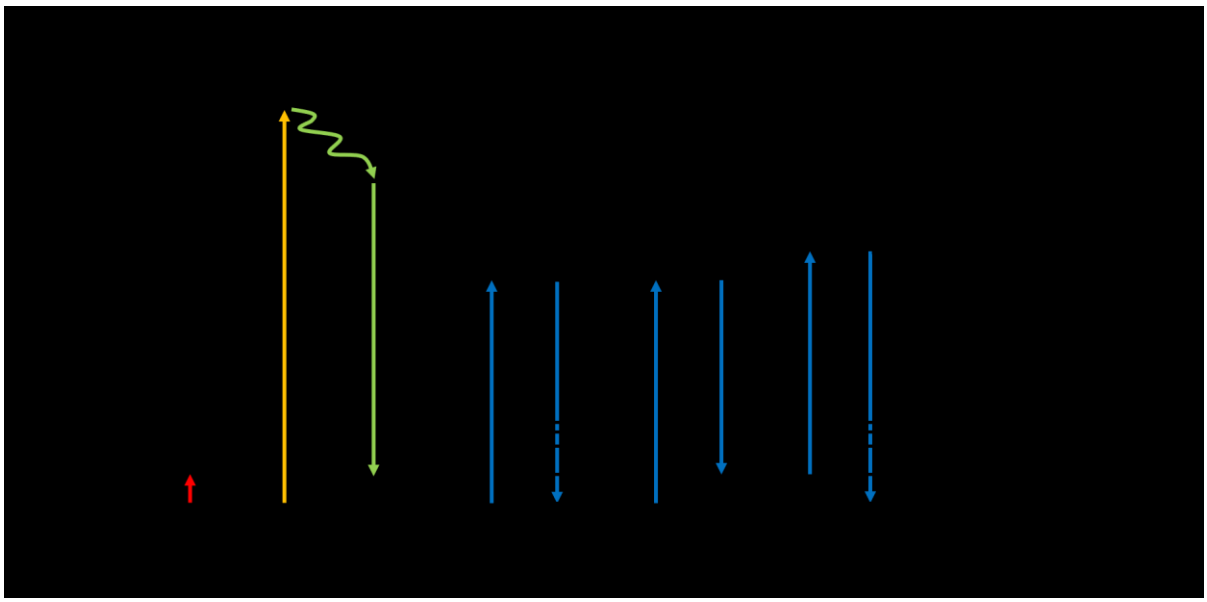

Figure 2.4: Schematic representation of electronic energy levels (S_0 and S_1), of vibrational energy levels (v=1, v=2, etc.), and virtual energy states showing the different absorption and emission processes involved in IR- (red arrow), UV Vis- (orange absorption arrow), fluorescence (green arrow) and Raman spectroscopy (blue arrows).

2.5.1. UV-Vis Spectroscopy

UV-Vis spectroscopy is a common analytical technique used in qualitative and quantitative analysis.[13-14] In this technique, a sample – often in solution or suspension – is irradiated with light in the ultraviolet and visible region of the electromagnetic spectrum, typically using wavelengths between 200 and 800 nm. When a molecule absorbs electromagnetic radiation in this wavelength range, the process involves excitation of electrons, typically outer shell valence electrons, to an excited state at higher energy levels. The energy absorbed by the sample is determined by the ratio between the intensity of the incident beam and the transmitted one. This process is repeated for each distinctive wavelength, and the resulting absorption bands show a distinct position, intensity, and fine structure that correspond to defined transitions in

the sample. However, these transitions are often accompanied by rotational and vibrational transitions, leading to complex fine structures that result in broad absorption bands.

The absorption observed in UV-Vis spectroscopy can be quantitatively described using the Beer-Lambert-Bouger Law, which states that absorbance (A) is equal to the product of the molar absorptivity (ε), concentration (c), and path length (d) of the sample. This law allows the amount of light absorbed by a sample to be quantified and the concentration of an absorbing species in a solution to be determined. For example, this is often used for the quantification of nucleic acids.

$$A = log\frac{I_0}{I} = \varepsilon\ c\ d \tag{2.7}$$

2.5.2. Infrared Spectroscopy

Infrared spectroscopy is a technique that relies on the interaction of infrared radiation with matter. Molecular vibrations and rotations are excited and can be measured directly as absorption in an IR spectrum.[13] In contrast to the UV (~190-400 nm) and visible (~400-800 nm) regions of the electromagnetic spectrum, the energy of radiation in the IR region is not sufficient to excite electrons to higher energy levels. Instead, IR energy excites vibrational motions of the nuclei and covalent bonds in molecules. Molecular vibrations refer to the motion of atoms within a molecule, where atoms oscillate about their equilibrium positions. These vibrations can be excited by the absorption of light, which can cause the molecule to move from its ground state to an excited vibrational level. The energy of the absorbed light corresponds to the difference in energy between the ground and excited states of the molecule.

A molecular vibration is IR-active if the dipole moment of the molecule changes during the excitation.

The specific frequencies at which the vibrations in molecules absorb depend on the composition and structure of the compound. In a common IR spectrum the wavenumber – defined as the reciprocal of wavelength – is used instead of frequencies to show the absorbed radiation. The common range of an IR spectrum lays in the mid-IR region between 4000 and 400 cm^{-1} (which approximately corresponds to the wavelength range of 2.5 µm to 25 µm, see Figure 2.3). In the mid-infrared region, the absorption of vibrations by covalently bound molecules as well as by functional, organic groups can be detected, which makes IR spectroscopy a powerful tool to determine its chemical composition and structure and identify functional groups in a molecule.

2.5.3. Raman Spectroscopy

Raman spectroscopy is based on the inelastic scattering of light by a sample, which causes a shift in the frequency of the scattered light, providing information about the vibrational modes of the sample. For vibrations to be Raman active, the polarizability of bonds has to change due to scattering of (monochromatic) light.[15]

In Raman spectroscopy, a laser is used to irradiate the sample, the absorbed light excites an electron from a vibrational state into a virtual energy state, and the scattered light is collected and analyzed. The main part is scattered elastically at the same frequency as the incident light (Rayleigh scattering) and a small fraction is scattered inelastically. The inelastically scattered light can be either at a higher frequency (anti-Stokes scattering) or at a lower frequency (Stokes scattering) than the incident laser light, depending on the vibrational modes of the sample. The

respective shifts in frequency observed as anti-Stokes or Stokes shifts are characteristic for each molecule and can give information about the molecular structure.

The Raman spectrum of a sample shows peaks at specific frequencies, which correspond to the vibrational modes of the chemical bonds in the sample. The Raman spectrum can be used to identify the functional groups in a molecule, and to determine its chemical composition and structure.

2.5.4. Fluorescence Spectroscopy

Fluorescence spectroscopy is a method that involves the emission of light from a fluorescent molecule after it has been excited by absorbing light.[16] Fluorescence is a phenomenon where a molecule absorbs light energy and then releases it as light at a longer wavelength (Figure 2.3). This process is called fluorescence emission and is the basis for fluorescence spectroscopy.

The excitation process in fluorescence spectroscopy involves irradiating a fluorophore with light with a specific wavelength, called the excitation wavelength. When a molecule in the sample absorbs the excitation light, it becomes excited to a higher (typically electronic) energy level. The energy difference between the ground state and excited state of the molecule corresponds to the energy of the excitation light.

After electronic excitation to a higher vibrational energy level, commonly of the multiplicity S_1 or S_2, the molecule typically decays to the lowest vibrational level of the first excited singlet state, S_1. This loss is mostly due to non-radiative processes, e.g., vibrational decay and/or internal conversion.

This excited molecule is unstable and may decay to its ground state via emission of radiation (fluorescence). Due to the energy loss during vibrational relaxation, the emitted photon has a longer wavelength than the excitation light. This is known as the Stokes shift. Emitted light is

detected by a fluorescence spectrometer. The resulting spectrum shows the wavelengths of light emitted by the molecule which can be used to identify and /or quantify the chemical species present in the sample.

2.6. Microscopy

Microscopy is an essential tool for imaging samples at a microscopic or nanoscale, such as cells, nanoparticles, and other small objects. It allows for the observation of the intricate details of biological, chemical, and physical systems, providing insight into their structure, behavior, and interactions.

The diffraction limit, as described by Ernst Abbe, is a fundamental limit to the resolution of any optical system. It states that the smallest resolvable detail, meaning the minimal distance between two resolvable objects, in an image is proportional to the wavelength of the light used to illuminate the sample. This limit is often expressed in terms of the numerical aperture of the lens, which determines the amount of light that can be collected from the sample.

$$d = \frac{\lambda}{2n \sin\theta} \tag{2.8}$$

Abbe diffraction limit: d: minimal distance between two resolvable objects, λ: wavelength, n: index of refraction, θ: maximal half-angle of the cone of the light.

However, recent advancements in microscopy have enabled super-resolution imaging beyond the diffraction limit. Super-resolution imaging techniques have overcome the diffraction limit by harnessing various principles and methodologies. One notable example is stimulated emission depletion (STED) microscopy, which utilizes a depletion beam to confine the excitation spot below the diffraction limit. Additionally, single-molecule localization microscopy techniques, such as stochastic optical reconstruction microscopy (STORM) and photoactivated localization microscopy (PALM), enable super-resolution imaging by precisely localizing individual fluorophores. These techniques, collectively known as high resolution microscopy, have revolutionized the field of microscopy by allowing researchers to visualize biological and physical systems in unprecedented detail.[17] While optical imaging beyond the diffraction limit was not used in this thesis, the potential for high resolution imaging of different

samples and structures using confocal fluorescence microscopy, scanning electron microscopy and transmission electron microscopy is described in the following.

2.6.1. Confocal Fluorescence Microscopy

Confocal fluorescence microscopy is a powerful imaging technique that uses laser light to excite fluorescent molecules within a sample. By selectively illuminating specific regions of the sample and detecting the resulting fluorescence while eliminating out-of-focus light, high resolution images of cells, tissues, and other structures can be generated.[18-19]

Confocal fluorescence microscopy is a technique intended to increase the optical resolution in all three spatial dimensions compared to a standard light microscope. A typical confocal microscope consists of a light source (usually a laser), a scanning system, a pinhole, a dichroic mirror, an objective lens, and a detector. When the laser light is directed at the sample, it causes fluorescent molecules within the sample to emit light of a longer wavelength (compare Figure 2.4). This emitted light is then collected by the objective lens, which focuses it, before it is detected by a detector such as a photomultiplier tube.

The pinhole acts as a spatial filter, blocking out-of-focus light from other planes within the sample. In contrast to standard light microscopy, this increases the contrast of the image and reduces background noise. By scanning the laser beam across the sample in a controlled manner, a three-dimensional image can be constructed from the collected data. Figure 2.5 illustrates confocal fluorescence microscopy.

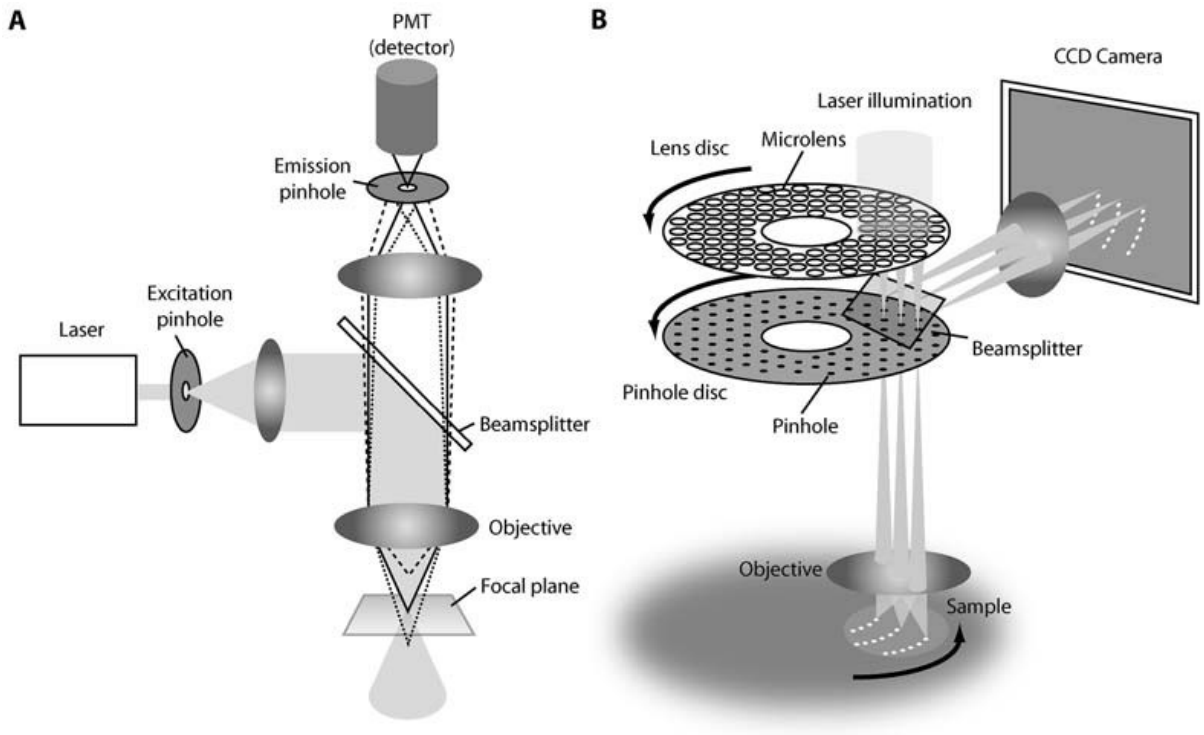

Figure 2.5: Excitation and emission light pathways a) in a basic confocal fluorescence microscope and b) when a spinning disc is used for image acquisition.[20]

In confocal fluorescence microscopy, a spinning disc can be used to speed up image acquisition. The spinning disc consists of multiple concentrically arranged pinholes. As the disc spins, each pinhole passes through the image plane, allowing light from multiple points in the sample to be collected simultaneously. This drastically speeds up the image generation process as compared to a single pinhole system where the entire image range has to be scanned to acquire the image. The spinning disc technique also reduces photobleaching and phototoxicity by reducing the amount of time the sample is exposed to the excitation light.

2.6.2. Scanning Electron Microscopy

Scanning electron microscopy (SEM) is an examination method used for surface and morphology characterization and enables resolution on the nanoscale.

As stated in equation 2.8, the resolution that can be achieved in classical optical microscopy is limited by the Abbe diffraction limit and is determined by the wavelength and the numerical aperture of the lens used to focus the beam. Unlike optical microscopes, which use visible light, SEM can achieve higher resolution because electrons have a shorter wavelength than visible light. In 1924, De Broglie proposed that moving particles with distinct mass possess wave-like characteristics. He built upon the earlier works of Albert Einstein and Max Planck to develop his theory. De Broglie's equation (2.13) established a correlation between the wavelength (λ) and the momentum (p) of moving particles, which helped him win the Nobel Prize in Physics in 1929.[21]

$$\lambda = \frac{h}{p} = \frac{h}{mv} \tag{2.13}$$

λ: Wavelength, h: Planck´s constant, p: Momentum, m: Mass, v: Velocity.

When electrons are accelerated by a high voltage of 300 kV, they generate a wavelength of approximately λ = 1.97 pm. These electrons can be utilized for electron-optical imaging techniques.[22]

To obtain topographic information of a sample surface, SEM uses a different approach towards manipulating the beam. Instead of using a lens and a static beam, SEM uses a series of electromagnetic lenses to scan the beam across the surface of the sample.

Specifically, an electron beam scans the surface of sample in a raster scan pattern and the position of the beam is combined with the intensity of the detected signal to produce an image.

To obtain a beam of primary electrons, the electron source emits free electrons that are accelerated downwards with an anode. The obtained beam of primary electrons features energies between about 0.1 keV and 30 keV. The beam is focused on the sample with electron lenses using electromagnetic forces to control the beam's direction. The raster scan generator enables the systematic scanning of the surface of the sample point for point. A possible electron-sample interaction, when the beam hits the sample, is ionization of a weakly bound electron of the sample through inelastic scattering of the primary electron. These ejected electrons are called secondary electrons (SE) and have a low kinetic energy (E_{kin}<50 eV). Other products of the electron-sample interactions are backscattered electrons, X-rays, Bremsstrahlung and so called Auger-electrons, while in most common SEM modes SE are detected using a secondary detector. Because of their low kinetic energy, their mean free path in solid matter is limited and only SE that were generated close to the surface can escape and be detected. This enables/produces a very high spatial resolution because the spatial resolution is mainly determined by the size of the interaction volume of the primary electron beam in the sample. The number of the detected SE from every point in the sample defines the image contrast. When the sample surface is scanned point for point and the SE intensity is recorded for each point, a microscopic image of the sample is generated (Figure 2.6).

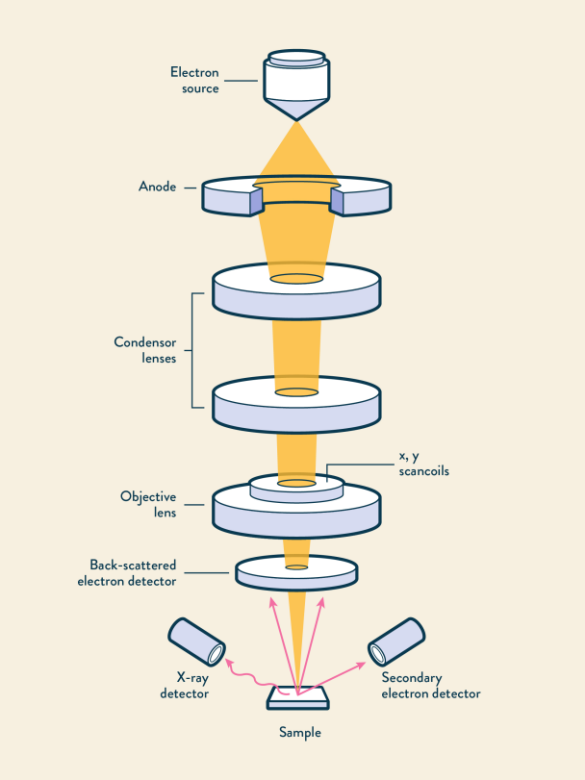

Figure 2.6: Schematic setup of an SEM.[23]

For this type of analysis, the microscope has to work under high vacuum to avoid interactions of electrons with gas molecules. Therefore, the samples need to be suitable for being exposed to high vacuum. Also, non-conductive materials should be coated with electrically conductive compounds such as carbon to ensure good image resolution.

2.6.3. Transmission Electron Microscopy

Another powerful tool for materials characterization is transmission electron microscopy (TEM), which provides high-resolution images and detailed information about the crystal structure, morphology, and chemical composition of materials. Similar to SEM, TEM also uses an accelerated electron beam for the investigation of samples but it can achieve an even higher resolution, which can be as low as 0.05 nm.[24]

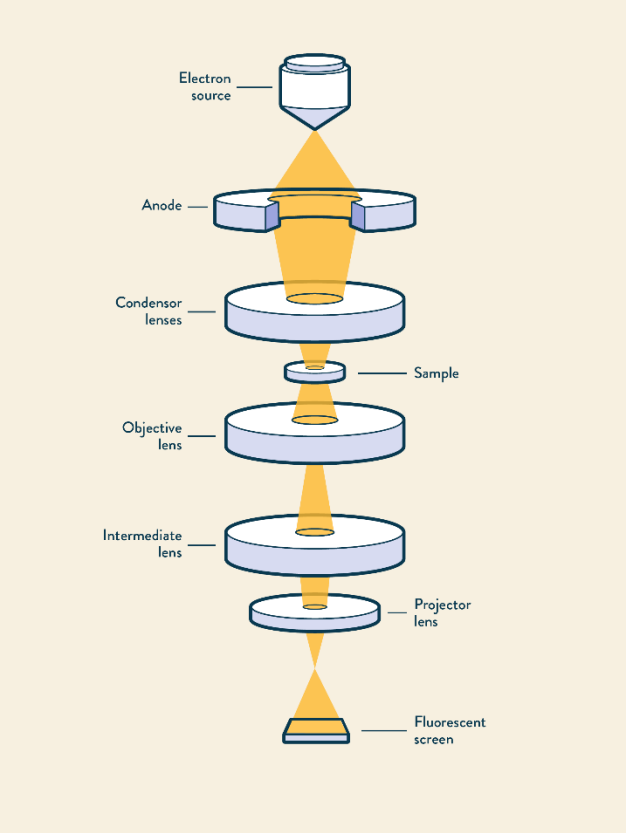

Figure 2.7: Schematic setup of a TEM.[23]

In TEM measurements electrons are accelerated with energies of about 100-400 kV. A thin specimen is placed in the path of the beam. The principle of TEM measurements is based on an electron beam which is transmitted through the sample. A wide area of the sample is illuminated and the primary electron beam passes through the sample (Figure 2.7). During

transmission, the electrons of the beam gain phase and diffraction information of the sample due to elastic scattering. Electrons can experience elastic incoherent scattering depending on the atomic number as well as the thickness and the density of the sample. They can also experience elastic coherent scattering on periodic structures. Both events determine the image contrast of the microscopy image. Similar to SEM, additional information can be obtained through other types of particles and energy losses generated as a result of the electron-sample interactions.

2.7. References

Stetefeld, J.; McKenna, S. A.; Patel, T. R., Dynamic light scattering: a practical guide and applications in biomedical sciences. Biophysical reviews **2016**, 8 (4), 409-427.

2. Goldburg, W. I., Dynamic light scattering. American Journal of Physics 1999, 67 (12), 1152-1160.

3. Lyklema, J., Fundamentals of interface and colloid science. Volume 2: Solid-liquid interfaces. With special contributions by A. de Keizer, B.H. Bijsterbosch, G.J. Fleer and M.A. Cohen Stuart. Academic Press: London, **1995**; Vol. Volume 2.

4. Larryisgood; Mjones1984 Diagram of zeta potential and slipping plane. https://commons.wikimedia.org/wiki/File:Diagram_of_zeta_potential_and_slipping_planeV2.svg (accessed accessed April 4th 2023).

5. Lee, C. K.; Chiang, A. S. T.; Tsay, C. S., The characterization of porous solids from gas adsorption measurements. Porous Ceramic Materials **1996**, 115, 21-43.

6. Thommes, M.; Kaneko, K.; Neimark, A. V.; Olivier, J. P.; Rodriguez-Reinoso, F.; Rouquerol, J.; Sing, K. S. W., Physisorption of gases, with special reference to the evaluation of surface area and pore size distribution (IUPAC Technical Report). Pure and Applied Chemistry **2015**, 87 (9-10).

7. Brunauer, S.; Emmett, P. H.; Teller, E., Adsorption of Gases in Multimolecular Layers. Journal of the American Chemical Society **1938**, 60 (2), 309-319.

8. Rouquerol, J.; Avnir, D.; Fairbridge, C. W.; Everett, D. H.; Haynes, J. M.; Pernicone, N.; Ramsay, J. D. F.; Sing, K. S. W.; Unger, K. K., Recommendations for the characterization of porous solids (Technical Report). Pure and Applied Chemistry **1994**, 66 (8), 1739-1758.

9. Heal, G. R., Thermogravimetry and Derivative Thermogravimetry in Principles of Thermal Analysis and Calorimetry, Chapter 2. The Royal Society of Chemistry**: 2002**.

10. Laye, P. G., Principles of Thermal Analysis and Calorimetry, Chapter 3. The Royal Society of Chemistry: **2002**.

11. Molekülspektroskopie. In Instrumentelle Analytik und Bioanalytik: Biosubstanzen, Trennmethoden, Strukturanalytik, Applikationen, Gey, M. H., Ed. Springer Berlin Heidelberg: Berlin, Heidelberg, **2008**; pp 211-290.

12. Ronan, P.; Gringer Revised diagram with re-aligned spectrum. https://commons.wikimedia.org/wiki/File:EM_spectrumrevised.png (accessed April 4th 2023).

13. Dunmur, R.; Murray, M., Spectroscopic Methods in Organic Chemistry. 2th Edition ed.; Hesse, M.; Meier, H.; Zeeh, B., Eds. Georg Thieme Verlag KG: Stuttgart, **2008**. http://www.thieme-connect.de/products/ebooks/book/10.1055/b-003-108602.

14. Gorog, S., Ultraviolet-Visible Spectrophotometry in Pharmaceutical Analysis (1st ed.). CRC Press. . CRC Press: **1995**.

15. Larkin, P., Chapter 1 - Introduction: Infrared and Raman Spectroscopy. In Infrared and Raman Spectroscopy, Larkin, P., Ed. Elsevier: Oxford, **2011**; pp 1-5.

16. Basic Principles of Fluorescence Spectroscopy. In Handbook of Fluorescence Spectroscopy and Imaging, **2011**; pp 1-30.

17. Beyond the diffraction limit. Nature Photonics **2009**, 3 (7), 361-361.

18. Super-Resolution Fluorescence Imaging. In Handbook of Fluorescence Spectroscopy and Imaging, **2011**; pp 219-240.

19. Minsky, M., Memoir on inventing the confocal scanning microscope. Scanning **1988**, 10 (4), 128-138.

20. Gräf, R., Rietdorf, J., Zimmermann, T. Live cell spinning disk microscopy. Advances in Biochemical Engineering/Biotechnology **2005**, 95 , pp 57-75.

21. Broglie, L. D., Recherches sur la théorie des Quanta, Migration - Université en Cours d'affectation. **1924**.

22. Krumeich, F. In Properties of Electrons, their Interactions with Matter and Applications in Electron Microscopy, **2015**.

23. Gleichmann, N. SEM vs TEM. https://www.technologynetworks.com/analysis/articles/sem-vs-tem-331262 (accessed April 5th, **2023**).

24. Akashi, T.; Takahashi, Y.; Tanigaki, T.; Shimakura, T.; Kawasaki, T.; Furutsu, T.; Shinada, H.; Müller, H.; Haider, M.; Osakabe, N.; Tonomura, A., Aberration corrected 1.2-MV cold field-emission transmission electron microscope with a sub-50-pm resolution. Applied Physics Letters **2015**, 106 (7), 074101.

CHAPTER 3

Mesoporous Biodegradable Magnesium Phosphate-Citrate Nanocarriers Amplify Methotrexate Anticancer Activity

Parts of this chapter originate from the PhD thesis “Mesoporous metal phosphate-citrate nanoparticles as anti-cancer agents” by Constantin von Schirnding 2017, LMU München: Faculty of Chemistry and Pharmacy.

3. Mesoporous Biodegradable Magnesium Phosphate-Citrate Nanocarriers Amplify Methotrexate Anticancer Activity

This chapter was published as:

Lisa Wehl[§], Constantin von Schirnding[§], Marie C. Bayer, Olga Zhuzhgova, Hanna Engelke, Thomas Bein *Bioconjugate Chemistry* **2022**, 33, 566-575.

[§] These authors contributed equally.

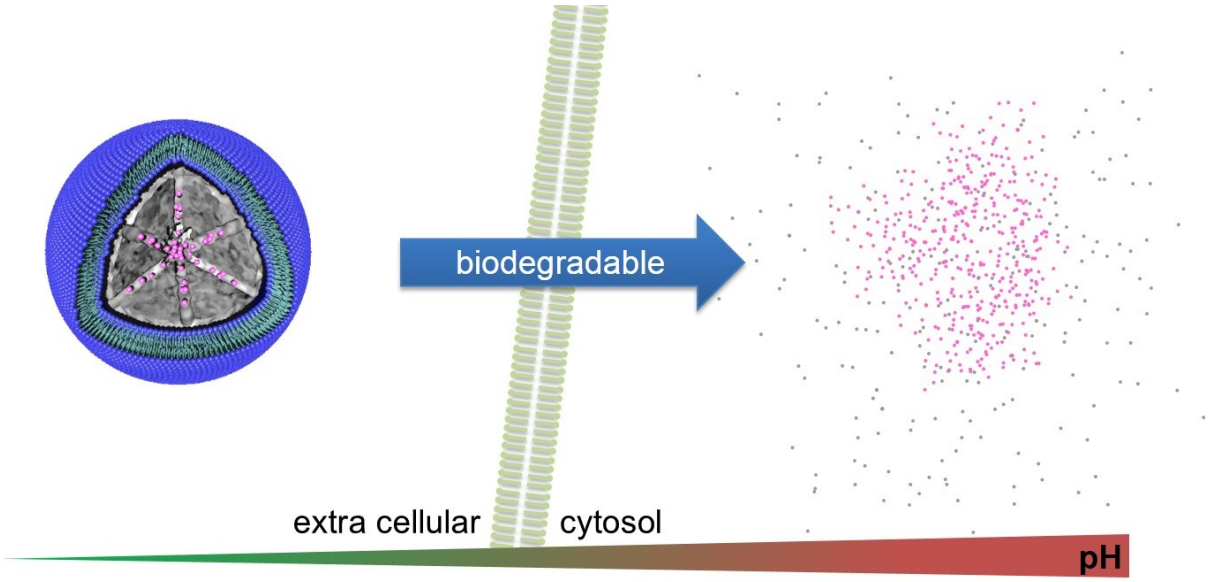

Abstract

We present the synthesis of amorphous, mesoporous, colloidal magnesium phosphate-citrate nanoparticles (MPCs) from biogenic precursors, resulting in a biocompatible and biodegradable nanocarrier that amplifies the action of the anticancer drug methotrexate (MTX). Synthesis conditions were gradually tuned to investigate the influence of the chelating agent citric acid on the colloidal stability and the mesoporosity of the obtained nanoparticles. With optimised synthesis conditions a large BET surface area of 560 m^2/g was achieved. We demonstrate the potential of these biocompatible and biodegradable mesoporous MPCs as a drug delivery system. Lipid-coated MPCs were used to load the fluorescent dye calcein and the chemotherapeutic agent MTX into the mesopores. *In vitro* experiments show very low premature release of the cargo but efficient stimuli-responsive release in an environment of pH 5.5, in which MPCs degrade. Lipid-coated MPCs are taken up by cancer cells and are nontoxic up to concentrations of 100 µg/mL. When loaded with MTX serving as a representative model drug for *in vitro* studies, MPCs induced efficient cell death with an IC_{50} value of 1.1 µg/mL. Compared to free MTX, its delivery with MPCs enhances its efficiency by an order of magnitude. In summary, we have developed a biodegradable nanomaterial synthesized from biocompatible precursors that are neither toxic by themselves nor in the form of nanoparticles. With these features MPCs may be applied as drug delivery system and have the potential to reduce the side effects of current chemotherapies.

3.1. Introduction

Since the consideration of nanoparticles for drug delivery applications, many materials including inorganic silica[1-5], carbon materials[6, 7], layered double hydroxides[8, 9], liposomes[10, 11] and polymers[12-15], and DNA-origami[16] have been investigated.[17, 18] However, existing nanomaterials are still limited with respect to their efficient loading and release, their targeted uptake by specific cells, their ability to escape the endosome, their increased efficacy, and their biodistribution, biodegradability and biocompatibility[19-24]. Drug delivery systems based on biomaterials and synthetic analogues such as magnesium carbonates[25], phosphates[26] and calcium phosphates[27], may help to overcome these shortcomings due to their excellent biocompatibility and biodegradability resulting in reduced side effects.[28-30] We recently obtained promising results with calcium phosphate-citrate nanoparticles, which induce apoptosis selectively in cancer cells and successfully reduce pleural tumors in mice with minimal adverse effects.[31] These nanoparticles release calcium and citrate ions in toxic amounts when introduced into the cytosol of cancer cells. However, the ions are not toxic when added to a nontumorigenic environment. Calcium is an essential biomineral in the tumorigenic pathway but simultaneously represents the most abundant messenger for cell survival mechanisms including apoptosis.[32] As an alternative, magnesium phosphate (MgP) based materials provide attractive features for biomedical applications, because the human body possesses mechanisms to degrade MgP materials and therefore the risks of side effects are decreased. [33, 34] Additionally, magnesium and phosphate ions are inherent components of the human body. So far, different MgP based materials have been synthesized under various conditions such as Mg/P ratio, temperature, and pH value.[35] MgP based materials are mainly investigated as material for bone repair and substitution, for example as bone cement or also as a reservoir for anti-inflammatory drugs.[36] Dense and lipid coated magnesium phosphate nanoparticles were used by Fang *et al.* to deliver proteins into the cytosol of cells.[26] Bhakta *et*

al. presented a co-precipitation synthesis to yield magnesium phosphate nanoparticles with encapsulated pDNA.[37, 38] Their nanoparticles were dense precipitates and did not contain any mesoporosity. Mesoporosity is an attractive feature as it may enable the design of flexible, biodegradable drug delivery platforms with efficient release of drug molecules loaded into the pores of such nanocarriers.[2, 39, 40] So far, mesoporous magnesium-based materials exist only in combination with calcium phosphates[31, 41], silicates[42] or oxides[43] and with fairly low mesoporosity. For example, a BET surface area of 306 m^2/g was reported for a porous magnesium oxide structure.[43] A much smaller BET surface area of 132 m^2/g was reported for a magnesium-calcium phosphate structure.[41] The development of colloidal mesoporous magnesium phosphate-based materials at the nanometer scale with high mesoporosity will therefore extend the portfolio of magnesium phosphate materials to biomaterials that are readily biodegradable, biocompatible, and allow for efficient loading and release of bioactive guest-molecules. This would leverage the use of magnesium phosphate materials in biomedical applications.

Here, we present the synthesis of colloidal, mesoporous magnesium-phosphate citrate nanoparticles (MPCs) as nanomaterial that offers a large BET surface area – up to 650 m^2/g - and degrades at lysosomal pH 5.5. A lipid coating allows for very low premature release of incorporated drugs. Furthermore, MPCs are efficiently taken up by cells and exhibit high biocompatibility. We investigate the influence of the complexing agent citrate on the nanoarchitecture of MPCs. We use MPCs with the best colloidal stability and a large BET surface area of 560 m^2/g for *in vitro* drug delivery experiments. MPCs efficiently load and release methotrexate and increase its cytotoxic efficacy on HeLa cells by a factor of 9 compared to the free drug. With these features, the novel mesoporous colloidal MPCs are a promising nanomaterial for biomedical applications.

3.2. Results and Discussion

Biocompatible, porous MPCs were synthesized via a modified Pechini sol-gel process[44], based on our previously published synthesis of calcium phosphate-citrate nanoparticles.[31] Magnesium ions are dissolved in a citric acid (CA) containing aqueous solution, resulting in complexation of magnesium by citrate ions and an acidic pH. This prevents the rapid precipitation of magnesium phosphate after the addition of phosphate ions and leads to a stabilized solution of magnesium, phosphate, and citrate ions. To obtain a mesoporous structure, the surfactant template cetyltrimethylammonium chloride (CTAC) is added, presumably forming micelles in an ordered mesophase to yield a Mg-P-CA-complex. The interaction of CA with the magnesium ions facilitates the gelation ability of the mixed solution and influences the precipitation behavior.[45] Nanoparticles are formed after a rapid increase of the pH to strongly alkaline conditions. This is achieved with a mixture of triethanolamine and ethanolamine, which not only act as base but additionally as complexing agents, facilitating formation of nanoparticles.[46] The extraction of the surfactant template with an ethanolic ammonium nitrate solution yielded the mesoporous MPCs.

Initially, we investigated the influence of citric acid during the reaction while keeping the concentrations of the other reactants constant. To this end, we prepared three different samples with a molar ratio of Mg/CA = 1:0, 1:0.5, and 1:1.12. The molar ratio of Mg/P was 1:1 for all three samples. Sample Mg/CA = 1:0 served as a control without CA. After extraction of the resulting MPCs, we determined the hydrodynamic radius with dynamic light scattering (DLS) and the morphology with scanning electron microscopy (SEM). The hydrodynamic particle size of MPCs in ethanolic solution and corresponding SEM images are depicted in Figure 3.1. All samples show a narrow size distribution. Samples Mg/CA = 1:0 and 1:0.5 have a similar hydrodynamic particle size distribution with maxima at 530 nm and 615 nm, respectively. For the sample Mg/CA = 1:1.12 smaller particle sizes with a maximum at 255 nm are observed.

SEM images show that all particles exhibit spherical morphology. They also show agglomeration due to the drying process during sample preparation (Figure 3.1). The DLS results suggest that the content of citric acid during synthesis may influence the colloidal stability in solution. This is of importance for applications in drug delivery, since it influences cell uptake. Sample Mg/CA = 1:1.12 with the smallest hydrodynamic size is therefore preferable for such applications.

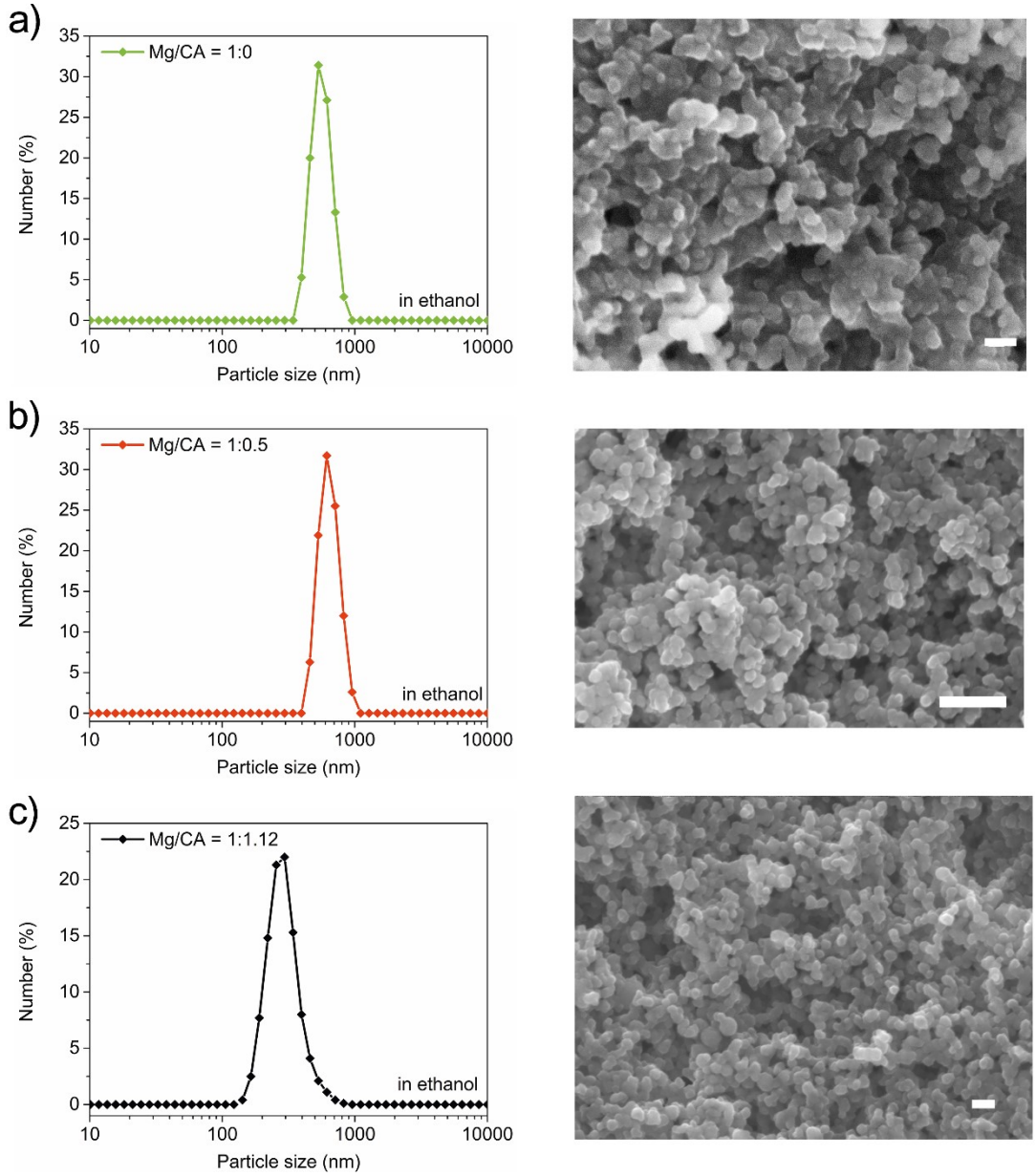

Figure 3.1 Particle size of MPC samples. Left column depicts the dynamic light scattering data, right column depicts the corresponding scanning electron microscopy images. Scale bars: 200 nm **a,** MPCs with a molar ratio of Mg/CA = 1:0 (green line). **b,** MPCs with a molar ratio of Mg/CA = 1:0.5 (red line). **c,** MPCs with a molar ratio of Mg/CA = 1:1.12 (black line).

Additionally, energy dispersive X-ray (EDX) measurements were performed with the samples having molar ratios of Mg/CA = 1:0, 1:0.5, and 1:1.12. The averaged results for each ratio are presented in Table 3.1. They increase from 1.19 to 1.25 with increasing CA content.

Table 3.1: Energy dispersive X-ray analysis for MPCs with a molar ratio of Mg/CA = 1:0, 1:0.5, and 1:1.12.

Mg/CA molar ratio	**Magnesium (atom%)**	**Phosphorus (atom%)**	**Mg:P**
1:1.12	4.20	3.36	1.25
1:0.5	5.12	4.23	1.21
1:0	6.25	5.23	1.19

The IR-spectra of the MPC samples obtained with a molar ratio of Mg/CA = 1:0, 1:0.5, and 1:1.12 are depicted in Figure 3.2a. They are normalized to the *v3*(PO_4) stretching vibration at 1081 cm^{-1}. The two strong vibrations at 1423 cm^{-1} and 1616 cm^{-1} (marked with asterisks) are attributed to the symmetric and the anti-symmetric stretching modes of COO- groups of citric acid incorporated into the MPCs structure.[47, 48] The vibrations at 1428 cm^{-1} and 1635 cm^{-1} of the sample with no citric acid result from the incorporation of carbonate ions into the structure.[49] The incorporation of carbonate ions is attributed to their presence in the aqueous reaction solution. The intensity increase of the COO^- vibrations with the relative citric acid content Mg/CA = 1:0, 1:0.5, and 1:1.12 in the sample reflects the increasing amount of citrate and carbonate ions incorporated into the MPC structure. The vibrations at 1269 cm^{-1} and 879 cm^{-1} are assigned to H-OPO_3^{2-} and HO-PO_3^{2-}, respectively (marked with pound signs).[50] Their appearance suggests that MPCs exhibit undissociated POH groups with respect to the trimagnesium phosphate stoichiometry $Mg_3(PO_4)_2$, which is in accordance with the EDX results. The broad band between 3600 cm^{-1} and 2200 cm^{-1} is attributed to the O–H vibration of water remaining in the pores of the samples.

To quantify the amount of citrate in the MPC structure, thermogravimetric analysis (TGA) was performed on all samples up to 850 °C (see Figure 3.2b). The moderate mass loss of all samples

up to 120 °C is assigned mainly to water (~ 8 wt%). Up to 180 °C, we attribute the mass loss in all samples to weakly bound organics (~ 6 wt%). Between 180 °C and 700 °C a significant mass loss is observed for all samples, attributed to the decomposition of strongly bound organics incorporated in the MPCs. Above 700 °C the mass stays almost constant up to 850 °C. In the sample Mg/CA = 1:0, the mass loss of organics adds up to 13 wt%. This drop is caused by residues of surfactant template, carbonates, ammonia, and crystal water within the nanoparticles.[51] The sample Mg/CA = 1:0.5 loses mass of 23 wt%, the sample Mg/CA = 1:1.12 loses 28 wt%. Therefore, in the samples containing citric acid an additional mass loss of 10 wt% and 15 wt%, respectively is recorded in comparison to the sample without citric acid. We attribute these additional mass losses to the decomposition of citrate ions incorporated in the structure of MPCs. Confirming the conclusions from IR data, the results show that the incorporation of citrate ions into the structure of MPCs increases with increasing initial CA content.

For the application as drug delivery system a large surface area is desired.[2, 39] The porosity of MPCs was investigated with nitrogen sorption analysis. The measurements revealed the typical type IV isotherm for all samples. The isotherms with the molar ratios of Mg/CA = 1:0, 1:0.5, and 1:1.12 are shown in Figure 3.2c and the pore size distributions of all samples are represented in Figure 3.2d. The presence of mesoporosity is visible in a strong increase of adsorbed nitrogen volume at relative pressures between 0.4 and 0.8, which is very pronounced for sample Mg/CA = 1:1.12, and the narrow pore size distribution, which is apparent for all samples. With increasing amounts of citric acid in the reaction solution, the degree of porosity of MPCs increases. While the samples Mg/CA = 1:0 and 1:0.5 show rather low mesoporosity, sample Mg/CA = 1:1.12 exhibits the largest BET surface area with 560 m^2/g, a maximum of the pore size distribution at 6.3 nm and a corresponding pore volume of 0.8 cm^3/g (see also Table S3.1).

We conclude that the amount of citric acid strongly influences the formation and resulting nanoarchitecture of mesoporous MPCs. The coordination complex Mg-citrate apparently slows down the kinetics of the precipitation reaction, allowing the solid structure to form around the micelles of the surfactant template. This results in a large BET surface area and high pore volume of the MPCs with molar ratio Mg/CA = 1:1.12, featuring an additional promising characteristic as drug delivery system.

X-ray analysis reveals an amorphous structure for all samples (Figure 3.2e). This is in accordance with the observed *v3*(PO_4) stretching vibration at 1081 cm^{-1} in the IR-spectra, which is shifted to higher wavenumbers compared to crystalline magnesium phosphate structures.[52] With transmission electron microscopy the mesoporous structure of MPCs can be visualized. The nanoparticles are strongly agglomerated due to the drying process during sample preparation (Figure 3.2f). To better visualize the spherical morphology of MPCs with initial molar ratio of Mg/CA = 1:1.12 additional SEM images are depicted in the supporting information Figure S3.1.

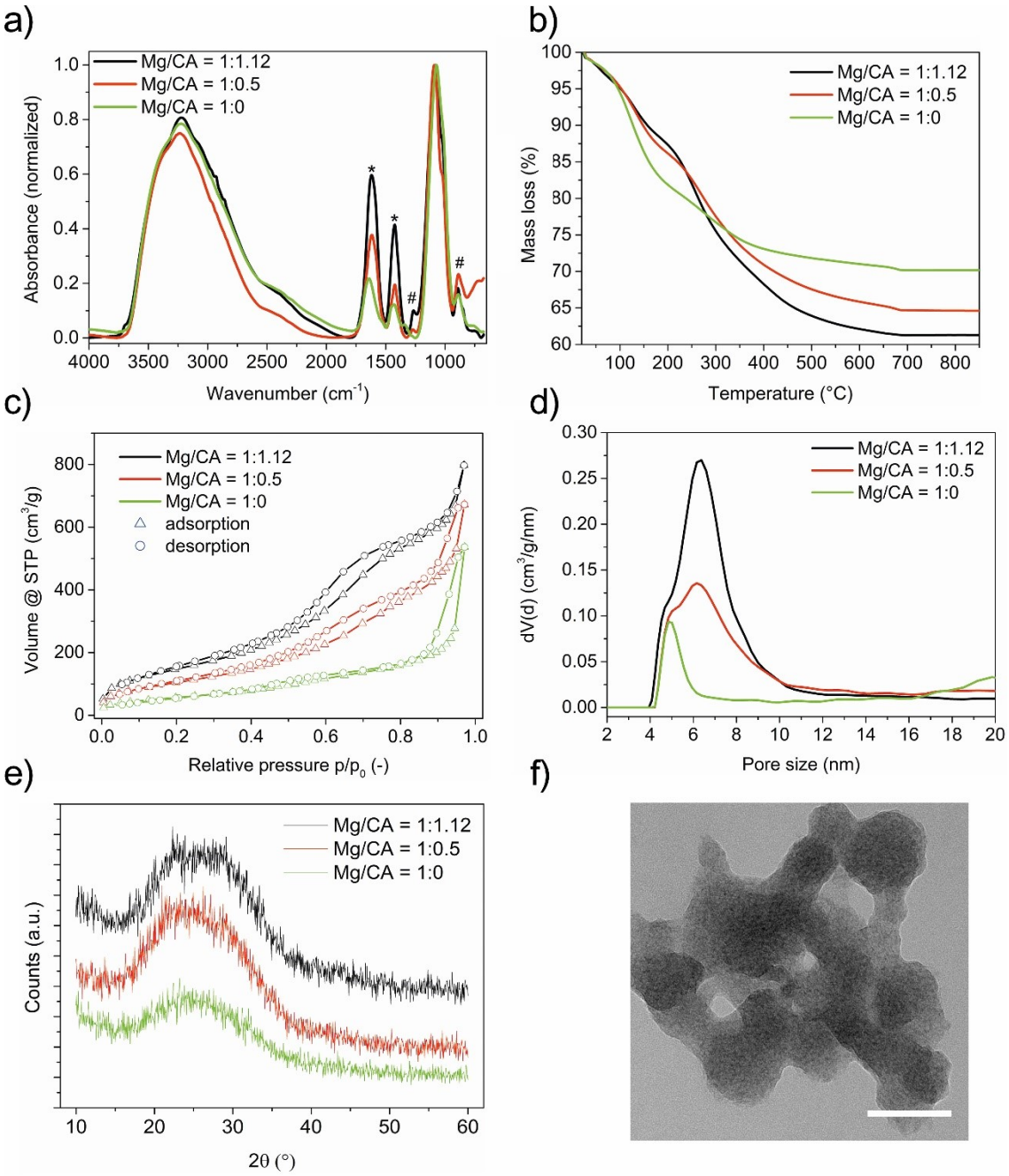

Figure 3.2: **a,** Infrared spectra of MPCs with a molar ratio of Mg/CA = 1:1.12 (black line), 1:0.5 (red line), and 1:0 (green line). **b,** Thermogravimetric analysis of the samples with a molar ratio of Mg/CA = 1:1.12 (black line), 1:1.05 (red line), and 1:0 (green line). **c,** Adsorption and desorption isotherms. **d,** Calculated pore size distributions. **e,** X-ray diffraction of the amorphous MPCs with a molar ratio of Mg/CA = 1:1.12 (black line), 1:0.5 (red line), and 1:0 (green line). **f,** Transmission electron microscopy image of MPCs with a molar ratio of Mg/CA = 1:1.12. Scale bar: 100 nm.

As demonstrated, the initial concentration of citric acid in the range of molar ratios of Mg/CA = 1:0, 1:0.5, and 1:1.12 has a significant effect on the resulting material. To also investigate

the influence of initial phosphate content on nanoparticle formation, we used the MPCs with a molar ratio of Mg/CA =1:1.12 as they were shown to offer the most promising characteristics for application as drug delivery system including a high surface area, small particle diameter, and high colloidal stability in solution. We kept the Mg/CA molar ratio constant at 1:1.12, while decreasing the phosphate content from a molar ratio of Mg/P of 1:1 to 1:0.6.

The hydrodynamic diameter of the resulting particles was characterized using DLS. Figure S3.2a shows a size distribution around a maximum of 370 nm, which is increased compared to MPCs with Mg/P ratio of 1:1. Again, particles showed a spherical morphology in the SEM (Figure S3.2b). As expected from the decreased initial phosphate content, EDX measurements of the MPCs with a molar ratio of Mg/P = 1:0.6 confirm a slightly decreased incorporation of phosphate in the nanoparticle structure (Table S3.2) with an atom percentage of Mg:P of 1.17 (in comparison to 1.25 for MPCs synthesized with an initial molar ratio of Mg/P = 1:1). The IR spectra exhibit the same features as for the molar ratio of Mg/P = 1:1 described above. The only difference is an increase in the intensity of the carboxylic groups suggesting an increase in incorporated citric acid (Figure S3.2c). The amount of citrate in the MPC structure was again quantified using TGA. Between 180°C and 700°C a mass loss of 33 wt% was observed, corresponding to a mass loss of 20 wt% that can be attributed to decomposition of citrate ions (Figure S3.2d). The mass loss due to incorporated citrate ions is thus increased for MPCs with Mg/P = 1:0.6 compared to Mg/P = 1:1. This result shows that the incorporation of citrate into the structure of MPCs is not only dependent on the initial molar ratio of Mg/CA, but also dependent on the initial molar ratio of Mg/P. Nitrogen sorption measurements resulted in a typical type IV isotherm. The surface analysis for Mg/P = 1:0,6 indicates a higher BET surface area of 650 m^2/g in comparison to MPCs with a molar ratio Mg/P = 1:1 and a slightly smaller pore size of 5.6 nm corresponding to a pore volume of 0.9 cm^3/g (Figure S3.2e and f). These findings support the mesoporosity of MPCs to follow the observed trend of an increasing

surface area with increasing amounts of citrate incorporated into the MPC structure. For the MPCs with a molar ratio of Mg/P = 1:0.6 we achieved the highest citrate concentration of 20 wt% resulting in the highest BET surface area of 650 m^2/g. The amorphous structure of the MPCs with a molar ratio of Mg/P = 1:0.6 was confirmed via X-ray analysis (Figure S3.2g). Hence, we now have introduced a synthesis route that leads to small, biodegradable magnesium phosphate-citrate nanoparticles. Additionally, by tuning the synthesis parameters we were able to vary the amount of citrate incorporated into the structure of magnesium phosphate-citrate, changing the properties of the nanoarchitecture. Because the colloidal stability of nanoparticles is an important factor for their application as drug delivery systems, the sample Mg/CA = 1:1.12 with an initial Mg/P molar ratio of 1:1 was chosen in the following for testing the promise of MPCs as drug delivery system. Among all synthesized and characterized MPCs, they offer the most promising characteristics, including the highest colloidal stability of all samples, a large BET surface area, and a highly mesoporous structure.

Next, we established a method for the stable and impermeable coating of the MPCs with a supported lipid bilayer. For this purpose, we loaded the particles in a solution of calcein serving as fluorescent model drug and a small amount of cetyltrimethylammonium chloride (CTAC) as endosomal escape agent[31] for subsequent cell experiments. For the coating we used the solvent exchange method[53] with a mixture of 1,2-dioleoyl-3-trimethylammonium-propane (DOTAP) and 1,2-dioleoyl-sn-glycero-3-phosphocholine (DOPC). This procedure leads to calcein and CTAC-loaded magnesium phosphate-citrate nanoparticles with lipid coating (lipid@MPCs).

While the lipid@MPCs are colloidally stable at pH 7.4 (see supporting information Figure S3.3 for DLS in buffer solution) and can be recovered from solution via centrifugation, acidification leads to degradation of the MPCs and destabilization of the lipid coating, and therefore release of its cargo (see Figure 3.3a). For fluorescence release measurements the lipid@MPCs were

transferred into a special measuring cell for fluorescence detection of the release. The lipid@MPCs were separated from the measuring compartment with a dialysis membrane with a molecular-weight cutoff at 14 kDa. This setup only allows for the penetration of released fluorescent dye through the membrane into the measuring compartment. The release of calcein from the lipid@MPCs was measured for the as-prepared sample at pH 7.4 (Figure 3.3b, red line) and for a sample with acidified, degraded lipid@MPCs (Figure 3.3b, green line). As expected, the increase in fluorescence counts is much stronger for the acidified, degraded sample compared to the non-degraded lipid@MPCs. The latter shows some initial release until saturation is reached. Since MPCs fully degrade upon acidification, we assume 100% of the loaded cargo to be released into the cuvette over time for the acidified sample. With respect to this, the premature release of the as-prepared, sealed sample can be estimated to be no more than 15% of the loaded calcein. Thus, lipid@MPCs degrade at slightly acidic conditions as experienced in the endosome and show only small premature release – two promising properties for applications in drug delivery.

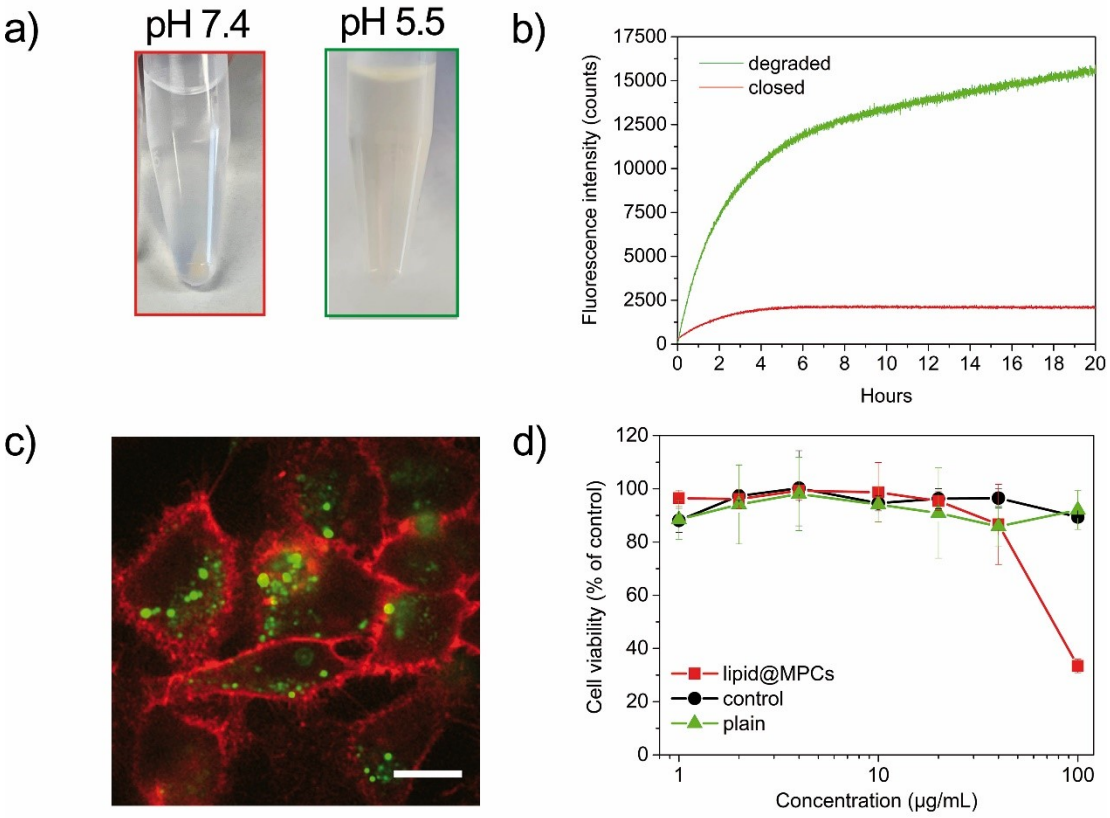

Figure 3.3: **a,** Photograph of centrifuged lipid@MPCs at pH 7.4 (red frame) and degraded lipid@MPCs after acidification at pH 5.5 (green frame) **b,** Fluorescence release measurement of calcein over 20 hours showing the premature release behavior (red line) and a strong increase upon triggered release by acidification (green line). **c,** Confocal microscopy image of HeLa cells with lipid@MPCs (in green) internalized in the WGA-stained cell membrane in red (concentration: 15 µg/mL. incubation for 24 h. Scale bar: 50 µm). **d,** Cell viability assessed by MTT assay for different concentrations of uncoated MPCs (plain, green triangle), MPCs with lipid coating (control, black circles), and MPCs with lipid coating and CTAC (lipid@MPCs, red squares) incubated for 72 h on HeLa cells. Concentrations ranging from 1 to 100 µg/mL.

In vitro cell experiments were carried out to investigate the uptake behavior of lipid@MPCs with HeLa cells. After an incubation of 24 hours with lipid@MPCs, the cells were investigated with a confocal fluorescence microscope, showing efficient particle uptake (Figure 3.3c, supporting information Video S1). The green fluorescent particles are localized inside the cell (marked in red on its membrane) suggesting successful intracellular uptake.

Further, *in vitro* experiments were performed to study the toxicity of magnesium phosphate-citrate particles on cells. Three different kinds of particles were incubated for 72 hours on HeLa cells and analyzed with MTT-assays (Figure 3.3d). The sample plain (green line) represents the bare magnesium phosphate-citrate particles without any further modification. The sample

control (black line) was prepared in the same way as the sample lipid@MPCs (red line) but without the addition of the endosomal escape agent CTAC. The samples plain and control show no cytotoxicity up to particle concentrations of 100 µg/mL. For the sample lipid@MPCs a drop in cell viability at a particle concentration of 100 µg/mL was obtained. We calculated an IC_{50} value of 77 µg/mL. In the supporting information, we depict brightfield images of the control and lipid@MPCs at different times (Figure S3.4). Thus, MPCs are not toxic up to fairly large concentrations and therefore appear to be promising candidates for advanced drug delivery applications.

Finally, we investigated the loading capacity of the newly developed MPCs for methotrexate (MTX), a hydrophobic anti-cancer drug[54], its release behavior, and its efficiency in cell experiments. MPCs (0.5 mg) were loaded for 30 min in an excess MTX-containing solution (0.5 mg) with small amounts of the endosomal escape agent CTAC. After centrifugation of MPCs containing MTX, the particles were sealed with a lipid coating as described above to yield MPCs-MTX. After further washing steps, the maximum loading capacity and the release of MPCs-MTX were investigated with UV-Vis measurements at a wavelength of 303 nm[55]. The same cuvette as that employed for calcein release measurements was used and release from MPCs-MTX and dissolved MPCs-MTX was each measured via UV-Vis spectroscopy and quantified according to the calibration curve shown in Figure S3.5. MPCs-MTX (Figure 3.4a, closed, red line) showed very low release compared to dissolved MPCs-MTX (Figure 3.4a, degraded, green line), which exhibited efficient release. The total amount of MTX released over the course of 12 h from 0.5 mg MPCs-MTX after their dissolution was 0.02 mg corresponding to 4 wt% loading and release. The premature release of MTX from lipid-coated, non-degraded MPCs-MTX is as low as 13 % with respect to the dissolved sample after 12 h.

All in all, the experiments show that MTX is readily loaded into MPCs, retained at pH 7 and released at acidic pH.

To test their effect on cells, the MPCs-MTX were then incubated for 72 hours on HeLa cells and a viability assay was performed (Figure 3.4b, black line). The delivery of MTX into HeLa cells results in an efficient cytotoxicity with an IC_{50} = 1.1 µg/mL for MPCs-MTX. Furthermore, the supernatant of MPCs-MTX was analyzed to verify the safe MTX delivery without premature release. Here, we did observe minor changes in cell viability above 20 µg/mL (Figure 3.4b, green line) reflecting the small amount of prematurely released MTX as detected by UV-Vis.

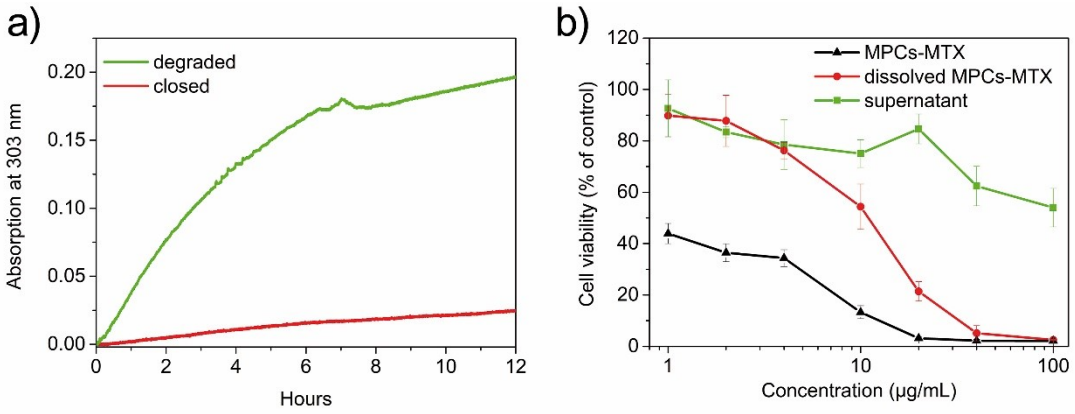

Figure 3.4: **a,** UV-Vis release measurement of MTX over 12 hours showing only premature release (red line) and a strong increase upon triggered release by acidification (green line). **b,** HeLa cell viability measured with MTT-assay. MPCs-MTX (black line) with an IC_{50} = 1.1 µg/mL, dissolved MPCs-MTX (red line) with an IC_{50} = 9.3 µg/mL, and the supernatant of MPCs-MTX (green line) with no IC_{50} obtained. Concentrations ranging from 1 to 100 µg/mL. The control of particles with the same composition but not delivering MTX can be seen in Figure 3.3d (red data).

As in the release experiments, dissolved MPCs-MTX served as control providing approximately the same amount of free MTX in solution as loaded in the respective amount of non-dissolved MPCs-MTX. Free MTX of dissolved MPCs-MTX (Figure 3.4b, red line) shows an IC_{50} of 9.3 µg/mL. Compared to intact MPCs-MTX the IC_{50} is increased by a factor of ~ 9. The experiment with the dissolved MPCs is also a good control yielding the amount of MTX

that is remaining in adjacent tissue after dissolution of the MPCs in the target cells. Comparing the the above results, MPCs enhance the efficiency of MTX by a factor of ~ 9.

3.3. Conclusion

Here, we have presented the synthesis of colloidal mesoporous magnesium phosphate-citrate nanoparticles using a modified Pechini process and investigated the influence of the chelating agent citric acid on the properties of the resulting nanoparticles. The level of citric acid incorporated into the structure of magnesium phosphate-citrate influences the colloidal stability of MPCs in solution. Additionally, incorporated citric acid impacts the mesoporosity of the MPCs. A maximum BET surface area of 650 m^2/g with a pore size of about 5.6 nm and a corresponding pore volume of 0.9 cm^3/g was reached. Particles degrade at slightly acidic pH as present in the lysosome. With the fluorescent model drug calcein, the release of MPCs sealed with a lipid coating was studied. The release measurements show that we established a synthesis method for a tight closure and entrapment of drugs with only 15 % premature release within 12 h. In subsequent cell experiments we observed very good biocompatibility for MPCs. This renders them a promising, biodegradable platform for drug delivery applications. To explore this potential, we loaded the anti-cancer drug methotrexate into MPCs as delivery vehicle and applied the resulting MTX-loaded MPCs to HeLa cells, reaching high cell toxicity with an IC_{50} value of 1.1 µg/mL – an increase in efficiency of a factor of 9 compared to free MTX. In conclusion, we have developed an efficient drug delivery vehicle synthesized from biocompatible precursors that are neither toxic by themselves nor in the form of nanoparticles. With these features – specifically the 100% release and their biodegradability - MPCs overcome the limitations of inefficient release and toxicity due to remaining nanoparticles that many of the current drug delivery systems face. They may thus represent a promising alternative material for drug delivery, and potentially also for other applications, such as bone cement.

3.4. Experimental Part

Chemicals for Nanoparticle Synthesis. Magnesium nitrate hexahydrate (Sigma, 99 %), ammonium dihydrogenphosphate (Alfa Aesar, 99 %), citric acid (Aldrich, 99.5 %), cetyltrimethylammonium chloride (CTAC, Fluka, 25 wt% in H2O), ethylene glycol (Aldrich, 99.8 %), ethanolamine (Fluka, >99 %), triethanolamine (TEA, Aldrich, 98%), ethanol (EtOH, Aldrich, >99.5 %), ammonium nitrate (Sigma, 99 %), calcein (Sigma), simulated body fluid (SBF, prepared as written elsewhere[48], containing: Na^+, K^+, Mg^{2+}, Ca^{2+}, Cl^-, CO_3^{2-}, SO_4^{2-}, PO_4^{3-}, and tris(hydroxymethyl) aminomethane, Sigma, >99 %), methotrexate (Sigma, >99 %), hydrochloric acid (Sigma, 2 M), 1,2-dioleoyl-3-trimethylammonium-propane (DOTAP, Avanti Polar Lipids), 1,2-dioleoyl-sn-glycero-3-phosphocholine (DOPC, Avanti Polar Lipids), sodium hydroxide (Aldrich, 0.1 M).

All chemicals were used as received without further purification. Doubly distilled water from a Millipore system (Milli-Q Academic A10) was used for all synthesis steps.

Synthesis of Magnesium Phosphate-Citrate Nanoparticles (MPCs). The synthesis of MPCs was carried out following a modified Pechini sol-gel process.[44, 56] In a 50 mL polypropylene reactor magnesium nitrate hexahydrate (320 mg, 1.25 mmol) and different amounts of citric acid (0 mg/ 120 mg/ 270 mg; 0 mmol/ 0.625 mmol/ 1.41 mmol) were dissolved in water (17 mL, 0.94 mmol). This leads to solutions with a molar ratio of Mg/CA = 1:0, 1:0.5, and 1:1.12. Then, ammonium dihydrogenphosphate (for samples Mg/P = 1:1: 142 mg, 1.25 mmol; for sample Mg/P = 0.6: 86 mg, 0.76 mmol) was added to the solution and stirred until complete dissolution. Then, cetyltrimethylammonium chloride (622 mg, 1.94 mmol) and ethylene glycol (7.15 g, 115 mmol) were added and the synthesis mixture was stirred at 500 rpm at room temperature. Thereafter, the clear solution was combined with triethanolamine (7.15 g,

48 mmol) and ethanolamine (3.00 g, 49.1 mmol) under vigorous stirring for three minutes. The suspension was diluted approximately 1:1 with ethanol. The particles were separated by centrifugation at 7,830 rpm (7,197 rcf) for 5 minutes and redispersed in NH_4NO_3/EtOH (2 wt%, 80 mL). To extract the template, the suspension was heated under reflux conditions at 90 °C for 30 minutes. Then the particles were again separated by centrifugation at 7,830 rpm (7,197 rcf) for 5 minutes and redispersed in 80 mL ethanol. The mixture was again heated under reflux conditions at 90 °C for 30 minutes, and the particles were separated by centrifugation at 7,830 rpm (7,197 rcf) for 5 minutes and redispersed in 20 mL ethanol.

Preparation of Magnesium Phosphate-Citrate Nanoparticles for Release and Cell Experiments with the Model Drug Calcein. The amount of 0.5 mg of magnesium phosphate-citrate nanoparticles was loaded in 1 mL aqueous calcein solution (0.62 mg, 1 mmol, pH 9.4) and, if needed, cetyltrimethylammonium chloride (6.25 µg, 19.5 nmol) for 30 minutes. The particles were separated by centrifugation at 14,000 rpm (16,873 rcf) for 3 minutes. The loaded particles were redispersed in a lipid solution of 1,2-dioleoyl-3-trimethylammonium-propane (DOTAP, 75 µL of a solution with 12.5 mg/mL 60/40 vol% H_2O/EtOH) and 1,2-dioleoyl-sn-glycero-3-phosphocholine (DOPC, 25 µL of a solution with 12.5 mg/mL 60/40 vol% H_2O/EtOH) under sonication conditions, and bi-distilled water (900 µL, pH adjusted to 9.4 with NaOH) was added. Then, the particles were separated by centrifugation at 14,000 rpm (16,873 rcf) for 5 minutes. The lipid-coated magnesium phosphate-citrate nanoparticles were washed twice by centrifugation at 12,000 rpm (12,396 rcf, 13 °C) for 5 minutes with SBF (500 µL, pH 7.4).

Preparation of Magnesium Phosphate-Citrate Particles for Release and Cell Experiments with the Anti-Cancer Drug Methotrexate. The amount of 0.5 mg of methotrexate was dissolved in 50 µL of sodium hydroxide solution (0.1 M) and cetyltrimethylammonium chloride (6.25 µg, 19.5 nmol) was added. Then 500 µL of bi-distilled water and 0.5 mg of magnesium phosphate-citrate particles were added. The particles were loaded for 30 minutes and then separated by centrifugation at 14,000 rpm (16,873 rcf) for 3 minutes. The loaded particles were redispersed in a lipid solution of 1,2-dioleoyl-3-trimethylammonium-propane (DOTAP, 75 µL of a solution with 12.5 mg/mL 60/40 vol% H_2O/EtOH) and 1,2-dioleoyl-sn-glycero-3-phosphocholine (DOPC, 25 µL of a solution with 12.5 mg/mL 60/40 vol% H_2O/EtOH) under sonication conditions and 900 µL bi-distilled water was added. Then, the particles were separated by centrifugation at 14,000 rpm (16,873 rcf) for 5 minutes. The lipid-coated magnesium phosphate-citrate nanoparticles were washed twice by centrifugation at 12,000 rpm (12,396 rcf, 13 °C) for 5 minutes with SBF (500 µL, pH 7.4).

In vitro **Release Fluorescence and UV-Vis Measurements.** Lipid-coated magnesium phosphate-citrate particles were transferred into the cap of a homebuilt fluorescence and UV-Vis setup (0.5 mg particles in 200 µL SBF) and separated by a cellulose membrane from the measuring cell, which is filled with SBF. Dye or drug that is released from the particles diffuses through the membrane and can be detected in the measuring cell. While detecting the fluorescence of calcein with a fluorescence spectrometer at 512 nm (excitation at 495 nm) as a function of time, the calcein release can be observed. While detecting the absorbance of methotrexate with a UV-Vis spectrometer at 303 nm as a function of time, the MTX release can be observed. All experiments were carried out at least twice on different days to evaluate the reproducibility of the tight supported lipid bilayer.

Cell Line and Culture. HeLa human cervical cancer cells were purchased from and cultured according to American Type Culture Collection (ATCC). HeLa cells were grown in DMEM medium low glucose (Sigma Aldrich) supplemented with 10 % FCS (Gibco) and 2 mM L-glutamine (Gibco) at 37 °C and 5 % CO_2. Cells were routinely tested and confirmed as mycoplasma free.

Cell Viability. Cell viability assays (MTT) were carried out on HeLa cells for particles MPCs-MTX, their supernatant, dissolved MPCs-MTX, control, plain, and lipid@MPCs. Dissolved MPCs-MTX served a reference experiment and were prepared as follows: We dissolved 1 mg of MPCs-MTX that was loaded with MTX and CTAC with 0.1 mL of 0.1 M HCl and added 0.9 mL of SBF to yield a final concentration of 1 mg/mL with a pH value of 7.4. Thus, the dissolved MPCs-MTX have the same composition and concentration as MPCs-MTX and differ only in their morphology (free components in solution vs. nanoparticles). The supernatant of MPCs-MTX was taken 12 h after preparation of the particles and was applied to HeLa cells at the same concentration as the particle solution.

Characterization.

Nitrogen sorption analysis was performed on a Quantachrome Instruments Nova 4000e at 77 K. Samples (25 mg) were outgassed at 120 °C for 12 h *in vacuo* (10 mTorr). Pore size and pore volume were calculated by a QSDFT equilibrium model of N_2 on carbon, based on the desorption branch of the isotherms. The QSDFT method takes the effects of surface roughness and heterogeneity into account. Cumulative pore volumes were evaluated up to a pore size of 12 nm, in order to remove the contribution of inter-particle textural porosity. Surface areas were calculated with the BET model in the range p/p_0 = 0.05–0.2. Thermogravimetric analysis

of the samples was performed on a Netzsch STA 440 C TG/DSC in a stream of synthetic air with a flow rate of 25 mL/min and a heating rate of 10 K/min. Dynamic light scattering measurements were performed on a Malvern Zetasizer-Nano instrument with a 4 mW He-Ne laser (633 nm) in ethanolic suspension with a concentration of 0.5 mg/mL. Scanning electron microscopy (SEM) images were obtained on a JEOL JSM-6400F (Figure 1) and on an FEI Helios G3 (Figure S1 and Figure S2). For sample preparation a droplet of the ethanolic colloidal suspension was placed on a 60 °C preheated carbon pad. Samples were sputtered with carbon before measurement. Transmission electron microscopy (TEM) was performed on an FEI TECNAI G2 instrument at an acceleration voltage of 200 kV. For sample preparation, a droplet of a diluted ethanolic colloidal suspension was deposited on a carbon-coated copper grid and the solvent was allowed to evaporate. Infrared spectra were measured with a Thermo Scientific Nicolet iN 10 infrared microscope. XRD patterns were obtained with a Bruker D8 Discover X-ray diffractometer using Cu-Kα radiation (1.5406 Å). UV/Vis measurements were performed on a Perkin Elmer Lambda 1050 UV-Vis/NIR spectrophotometer with a deuterium arc lamp and a tungsten filament equipped with a 150 mm integrating sphere and an InGaAs detector.

MTT-Assay. For MTT-assays in a 96 well plate we treated 5000 cells per well containing 100 µL of the respective medium with MPCs-MTX, its supernatant, dissolved MPCs-MTX, control, plain, or lipid@MPCs at the indicated concentrations. After 72 h incubation, 10 µL 3-(4,5-dimethylthiazol-2-yl)-2,5-diphenyltetrazolium bromide (MTT) was added to the magnesium phosphate-citrate treated cells and incubated for further 2 h. Unreacted MTT and medium were removed and the 96-well plates were stored at -80 °C for at least 1 h. Then, 100 µL DMSO was added to each well. The absorbance was read out by a Tecan plate reader. All

studies were performed in biological triplicates (three independent experiments on different days, each in triplicates). IC_{50} values were calculated with OriginPro 9.

Live-Cell Fluorescence Microscopy. To visualize nanoparticle internalization by cells, live-cell imaging was performed on a spinning disc microscope based on the Zeiss Cell Observer SD utilizing a Yokogawa spinning disk unit CSU-X1. The system was equipped with a 1.40 NA 63x Plan apochromat oil immersion objective from Zeiss. For all experiments the exposure time was 0.1 s and z-stacks were recorded. Calcein-loaded MPCs were imaged with approximately 0.4 W/mm^2 of 488 nm excitation light. Atto647 was excited with approximately 11 mW/mm^2 of 639 nm. In the excitation path a quad-edge dichroic beamsplitter (FF410/504/582/669-Di01-25x36, Semrock) was used. For two-color detection of calcein and Atto647, a dichroic mirror (560 nm, Semrock) and band-pass filters 525/50 and 690/60 (both Semrock) were used in the detection path. Separate images for each fluorescence channel were acquired using two separate electron multiplier charge coupled device (EMCCD) cameras (PhotometricsEvolveTM). Immediately before imaging, cell membranes were stained using wheat germ agglutinin Alexa Fluor 647 conjugate at a final concentration of 5 µg/mL. After application of the dye, cells were washed twice.

3.5. References

1. Argyo, C.; Weiss, V.; Bräuchle, C.; Bein, T., Multifunctional Mesoporous Silica Nanoparticles as a Universal Platform for Drug Delivery. *Chemistry of Materials* **2014,** *26* (1), 435-451.

2. Slowing, I. I.; Vivero-Escoto, J. L.; Wu, C.-W.; Lin, V. S. Y., Mesoporous silica nanoparticles as controlled release drug delivery and gene transfection carriers. *Advanced Drug Delivery Reviews* **2008,** *60* (11), 1278-1288.

3. Liu, J.; Stace-Naughton, A.; Jiang, X.; Brinker, C. J., Porous Nanoparticle Supported Lipid Bilayers (Protocells) as Delivery Vehicles. *Journal of the American Chemical Society* **2009,** *131* (4), 1354-1355.

4. Rosenholm, J. M.; Meinander, A.; Peuhu, E.; Niemi, R.; Eriksson, J. E.; Sahlgren, C.; Lindén, M., Targeting of Porous Hybrid Silica Nanoparticles to Cancer Cells. *ACS Nano* **2009,** *3* (1), 197-206.

5. Benezra, M.; Penate-Medina, O.; Zanzonico, P. B.; Schaer, D.; Ow, H.; Burns, A.; DeStanchina, E.; Longo, V.; Herz, E.; Iyer, S.; *et al.*, Multimodal silica nanoparticles are effective cancer-targeted probes in a model of human melanoma. *The Journal of Clinical Investigation* **2011,** *121* (7), 2768-2780.

6. Bianco, A.; Kostarelos, K.; Prato, M., Applications of carbon nanotubes in drug delivery. *Current Opinion in Chemical Biology* **2005,** *9* (6), 674-679.

7. Liu, Z.; Chen, K.; Davis, C.; Sherlock, S.; Cao, Q.; Chen, X.; Dai, H., Drug delivery with carbon nanotubes for in vivo cancer treatment. *Cancer Res* **2008,** *68* (16), 6652-6660.

8. Choy, J.-H.; Kwak, S.-Y.; Jeong, Y.-J.; Park, J.-S., Inorganic Layered Double Hydroxides as Nonviral Vectors. *Angewandte Chemie International Edition* **2000,** *39* (22), 4041-4045.

9. Ladewig, K.; Xu, Z. P.; Lu, G. Q., Layered double hydroxide nanoparticles in gene and drug delivery. *Expert Opinion on Drug Delivery* **2009,** *6* (9), 907-922.

10. Sharma, A.; Sharma, U. S., Liposomes in drug delivery: Progress and limitations. *International Journal of Pharmaceutics* **1997,** *154* (2), 123-140.

11. Gregoriadis, G.; Florence, A. T., Liposomes in Drug Delivery. *Drugs* **1993,** *45* (1), 15-28.

12. Wagner, E., Programmed drug delivery: nanosystems for tumor targeting. *Expert Opinion on Biological Therapy* **2007,** *7* (5), 587-593.

13. Duncan, R., The dawning era of polymer therapeutics. *Nature Reviews Drug Discovery* **2003,** *2* (5), 347-360.

14. Duncan, R., Drug-polymer conjugates: potential for improved chemotherapy. *Anti-Cancer Drugs* **1992,** *3* (3).

15. Cabral, H.; Matsumoto, Y.; Mizuno, K.; Chen, Q.; Murakami, M.; Kimura, M.; Terada, Y.; Kano, M. R.; Miyazono, K.; Uesaka, M.; *et al.*, Accumulation of sub-100 nm polymeric micelles in poorly permeable tumours depends on size. *Nature Nanotechnology* **2011,** *6* (12), 815-823.

16. Zhang, Q.; Jiang, Q.; Li, N.; Dai, L.; Liu, Q.; Song, L.; Wang, J.; Li, Y.; Tian, J.; Ding, B.; *et al.*, DNA Origami as an In Vivo Drug Delivery Vehicle for Cancer Therapy. *ACS Nano* **2014,** *8* (7), 6633-6643.

17. Wang, S., Ordered mesoporous materials for drug delivery. *Microporous and Mesoporous Materials* **2009,** *117* (1), 1-9.

18. Peer, D.; Karp, J. M.; Hong, S.; Farokhzad, O. C.; Margalit, R.; Langer, R., Nanocarriers as an emerging platform for cancer therapy. *Nature Nanotechnology* **2007,** *2* (12), 751-760.

19. Hoffman, A. S., The origins and evolution of "controlled" drug delivery systems. *Journal of Controlled Release* **2008,** *132* (3), 153-163.

20. Caruthers, S. D.; Wickline, S. A.; Lanza, G. M., Nanotechnological applications in medicine. *Current Opinion in Biotechnology* **2007,** *18* (1), 26-30.

21. Allen, T. M., Ligand-targeted therapeutics in anticancer therapy. *Nature Reviews Cancer* **2002,** *2* (10), 750-763.

22. Ferrari, M., Cancer nanotechnology: opportunities and challenges. *Nature Reviews Cancer* **2005,** *5* (3), 161-171.

23. Bondarenko, O.; Mortimer, M.; Kahru, A.; Feliu, N.; Javed, I.; Kakinen, A.; Lin, S.; Xia, T.; Song, Y.; Davis, T. P.; *et al.*, Nanotoxicology and nanomedicine: The Yin and Yang of nano-bio interactions for the new decade. *Nano Today* **2021,** *39*, 101184.

24. Croissant, J. G.; Fatieiev, Y.; Khashab, N. M., Degradability and Clearance of Silicon, Organosilica, Silsesquioxane, Silica Mixed Oxide, and Mesoporous Silica Nanoparticles. *Advanced Materials* **2017,** *29* (9), 1604634.

25. Zhang, P.; Forsgren, J.; Strømme, M., Stabilisation of amorphous ibuprofen in Upsalite, a mesoporous magnesium carbonate, as an approach to increasing the aqueous solubility of poorly soluble drugs. *International Journal of Pharmaceutics* **2014,** *472* (1), 185-191.

26. Fang, Y.; Vadlamudi, M.; Huang, Y.; Guo, X., Lipid-Coated, pH-Sensitive Magnesium Phosphate Particles for Intracellular Protein Delivery. *Pharmaceutical Research* **2019,** *36* (6), 81.

27. Huang, D.; He, B.; Mi, P., Calcium phosphate nanocarriers for drug delivery to tumors: imaging, therapy and theranostics. *Biomaterials Science* **2019,** *7* (10), 3942-3960.

28. Cai, A.-Y.; Zhu, Y.-J.; Qi, C., Biodegradable Inorganic Nanostructured Biomaterials for Drug Delivery. *Advanced Materials Interfaces* **2020,** *7* (20), 2000819.

29. Chen, F.; Huang, P.; Qi, C.; Lu, B.-Q.; Zhao, X.-Y.; Li, C.; Wu, J.; Cui, D.-X.; Zhu, Y.-J., Multifunctional biodegradable mesoporous microspheres of Eu3+-doped amorphous calcium phosphate: microwave-assisted preparation, pH-sensitive drug release, and bioimaging application. *Journal of Materials Chemistry B* **2014,** *2* (41), 7132-7140.

30. Epple, M.; Ganesan, K.; Heumann, R.; Klesing, J.; Kovtun, A.; Neumann, S.; Sokolova, V., Application of calcium phosphate nanoparticles in biomedicine. *Journal of Materials Chemistry* **2010,** *20* (1), 18-23.

31. von Schirnding, C.; Giopanou, I.; Hermawan, A.; Wehl, L.; Ntaliarda, G.; Illes, B.; Datz, S.; Geisslinger, F.; Bartel, K.; Sommer, A.-K.; *et al.*, Synergistic Combination of Calcium and Citrate in Mesoporous Nanoparticles Targets Pleural Tumors. *Chem* **2021,** *7* (2), 480-494.

32. Klann, R. C.; Marchok, A. C., Effects of reduced calcium on proliferation and cell viability in tumorigenic and nontumorigenic rat tracheal epithelial cell lines. *Cell Biol Int Rep* **1984,** *8* (2), 137-46.

33. Zhou, H.; Luchini, T. J. F.; Bhaduri, S. B., Microwave assisted synthesis of amorphous magnesium phosphate nanospheres. *Journal of Materials Science: Materials in Medicine* **2012,** *23* (12), 2831-2837.

34. Staiger, M. P.; Pietak, A. M.; Huadmai, J.; Dias, G., Magnesium and its alloys as orthopedic biomaterials: A review. *Biomaterials* **2006,** *27* (9), 1728-1734.

35. Tamimi, F.; Nihouannen, D. L.; Bassett, D. C.; Ibasco, S.; Gbureck, U.; Knowles, J.; Wright, A.; Flynn, A.; Komarova, S. V.; Barralet, J. E., Biocompatibility of magnesium phosphate minerals and their stability under physiological conditions. *Acta Biomaterialia* **2011,** *7* (6), 2678-2685.

36. Xue, W.; Dahlquist, K.; Banerjee, A.; Bandyopadhyay, A.; Bose, S., Synthesis and characterization of tricalcium phosphate with Zn and Mg based dopants. *Journal of Materials Science: Materials in Medicine* **2008,** *19* (7), 2669-2677.

37. Bhakta, G.; Shrivastava, A.; Maitra, A., Magnesium Phosphate Nanoparticles can be Efficiently Used In Vitro and In Vivo as Non-Viral Vectors for Targeted Gene Delivery. *Journal of Biomedical Nanotechnology* **2009,** *5* (1), 106-114.

38. Bhakta, G.; Mitra, S.; Maitra, A., DNA encapsulated magnesium and manganous phosphate nanoparticles: potential non-viral vectors for gene delivery. *Biomaterials* **2005,** *26* (14), 2157-2163.

39. Bae, Y. H.; Park, K., Targeted drug delivery to tumors: Myths, reality and possibility. *Journal of Controlled Release* **2011,** *153* (3), 198-205.

40. Allen, T. M.; Cullis, P. R., Drug Delivery Systems: Entering the Mainstream. *Science* **2004,** *303* (5665), 1818-1822.

41. Wang, S.; Liu, R.; Yao, J.; Wang, Y.; Li, H.; Dao, R.; Guan, J.; Tang, G., Fabrication of mesoporous magnesium substituted β-tricalcium phosphate nanospheres by self-transformation and assembly involving EDTA ions. *Microporous and Mesoporous Materials* **2013,** *179*, 172-181.

42. Wu, Z.; Tang, T.; Guo, H.; Tang, S.; Niu, Y.; Zhang, J.; Zhang, W.; Ma, R.; Su, J.; Liu, C.; *et al.*, In vitro degradability, bioactivity and cell responses to mesoporous magnesium silicate for the induction of bone regeneration. *Colloids and Surfaces B: Biointerfaces* **2014,** *120*, 38-46.

43. Roggenbuck, J.; Tiemann, M., Ordered Mesoporous Magnesium Oxide with High Thermal Stability Synthesized by Exotemplating Using CMK-3 Carbon. *Journal of the American Chemical Society* **2005,** *127* (4), 1096-1097.

44. Pechini, M. P. Method of preparing lead and alkaline earth titanates and niobates and coating method using the same to form a capacitor. 1967.

45. Weng, W.; Ding, Z.; Mao, Y.; Zhang, F., The gelation behaviour of copper ethoxide. *Journal of Non-Crystalline Solids* **1992,** *147-148*, 102-105.

46. Möller, K.; Kobler, J.; Bein, T., Colloidal Suspensions of Nanometer-Sized Mesoporous Silica. *Advanced Functional Materials* **2007,** *17* (4), 605-612.

47. Nakamoto, K., Infrared and Raman Spectra of Inorganic and Coordination Compounds, Applications in Coordination, Organometallic, and Bioinorganic Chemistry. Wiley: 2008.

48. Cifuentes, I.; González-Díaz, P. F.; Cifuentes-Delatte, L., Is there a "citrate-apatite" in biological calcified systems? *Calcified Tissue International* **1980,** *31* (1), 147-151.

49. Aramendia, M. A.; Borau, V.; Jimenez, C.; Marinas, J. M.; Romero, F. J., The Selectivity of Sodium Carbonate-Doped Zinc Phosphate in the Gas-Phase Dehydrogenation-Dehydration of Cyclohexanol. *Journal of Catalysis* **1995,** *151* (1), 44-49.

50. Koleva, V.; Stefov, V., Phosphate ion vibrations in dihydrogen phosphate salts of the type M(H2PO4)2·2H2O (M = Mg, Mn, Co, Ni, Zn, Cd): Spectra structure correlations. *Vibrational Spectroscopy* **2013,** *64*, 89-100.

51. Mousa, S., Study on synthesis of magnesium phosphate materials. *Phosphorus Research Bulletin* **2010,** *24*, 16-21.

52. Assaaoudi, H.; Fang, Z.; Butler, I.; Ryan, D.; Kozinski, J., Characterization of a New Magnesium Hydrogen Orthophosphate Salt, Mg3.5H2(PO4)3, Synthesized in Supercritical Water. *Solid State Sciences* **2007,** *9*, 385-393.

53. Cauda, V.; Engelke, H.; Sauer, A.; Arcizet, D.; Bräuchle, C.; Rädler, J.; Bein, T., Colchicine-Loaded Lipid Bilayer-Coated 50 nm Mesoporous Nanoparticles Efficiently Induce Microtubule Depolymerization upon Cell Uptake. *Nano Letters* **2010,** *10* (7), 2484-2492.

54. Jingou, J.; Shilei, H.; Weiqi, L.; Danjun, W.; Tengfei, W.; Yi, X., Preparation, characterization of hydrophilic and hydrophobic drug in combine loaded chitosan/cyclodextrin nanoparticles and in vitro release study. *Colloids and Surfaces B: Biointerfaces* **2011,** *83* (1), 103-107.

55. Zhang, Y., Jin, T.; Zhuo, R.-X., Methotrexate-loaded biodegradable polymeric micelles: Preparation, physicochemical properties and in vitro drug release. *Colloids and Surfaces B: Biointerfaces* **2005,** *44* (2), 104-109.

56. Yang, P.; Yang, P.; Teng, X.; Lin, J.; Huang, L., A novel luminescent mesoporous silica/apatite composite for controlled drug release. *Journal of Materials Chemistry* **2011,** *21*, 5505-5510.

3.6. Appendix

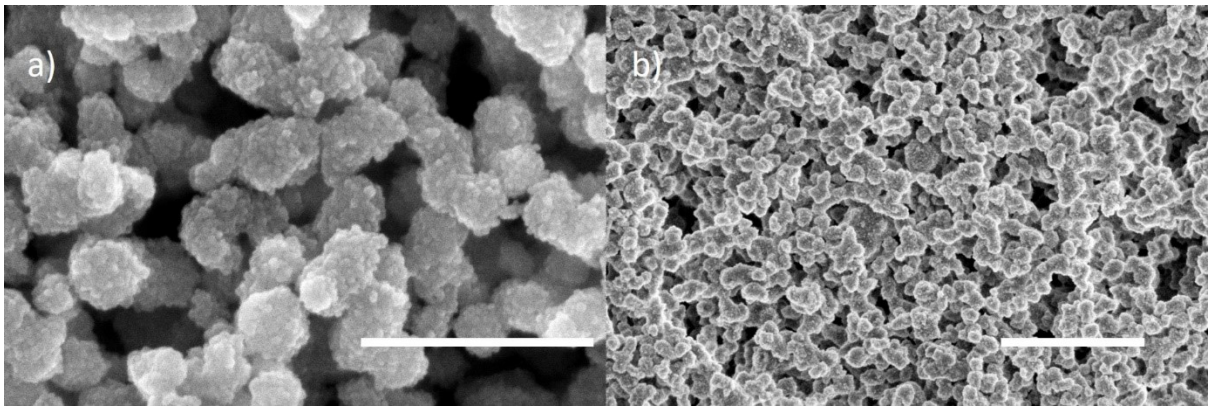

Figure S 3.1: Scanning electron microscopy images of MPCs with an initial molar ratio of Mg/CA = 1:1.12 and Mg/P = 1:1. **a**, Scale bar: 400 nm. **b**, Scale bar: 1 µm.

Table S 3.1: Sorption data analysis for MPCs with a molar ratio of Mg/CA = 1:0, 1:0.5, and 1:1.12 and a molar ratio of Mg/P = 1:1 for all samples.

Mg/CA molar ratio	Pore size distribution		BET surface area
	Size (nm)	Volume (cm^3/g)	(m^2/g)
1:1.12	6.3	0.8	560
1:0.5	6.2	0.52	390
1:0	4.8	0.13	215

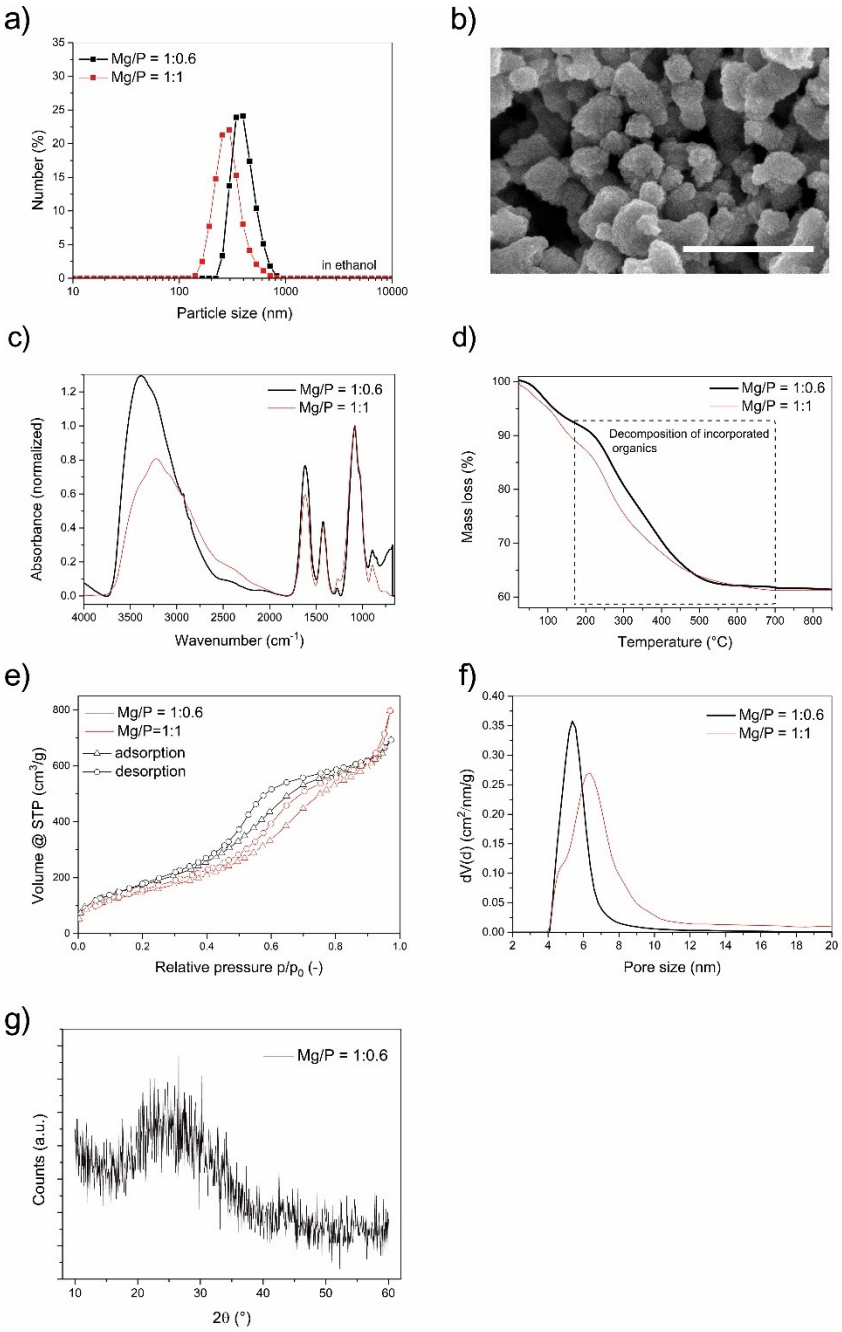

Figure S 3.2: The impact of a decreased phosphate content during synthesis on the MPCs with an initial molar ratio Mg/P = 1:0.6. (black curves) in comparison to Mg/P = 1:1 samples (red curves). For both samples the initial molar ratios of Mg/CA were kept constant at 1:1.12. **a,** Dynamic light scattering measurements, **b,** SEM image. Scale bar: 400 nm. **c,** IR spectra, **d,** TGA curves measured up to 850 °C. The temperature range between 170°C and 700 °C was used to calculate the amount of organics incorporated into the MPC structure. **e,** nitrogen sorption isotherms, **f,** corresponding pore size distribution, and **g,** X-ray diffraction of the amorphous MPCs.

Table S 3.2 Energy dispersive X-ray analysis for MPCs with a molar ratio of Mg/P = 1:0.6 and Mg/CA = 1:1.12 in comparison to the results of MPCs with a molar ratio of Mg/P = 1:1 and varying molar ratios of Mg/CA.

Mg/CA molar ratio	**Mg/P molar ratio**	**Atom % ratio (Mg:P)**
1:1.12	1:0.6	1.17
1:0	1:1	1.19
1:0.5	1:1	1.21
1:1.12	1:1	1.25

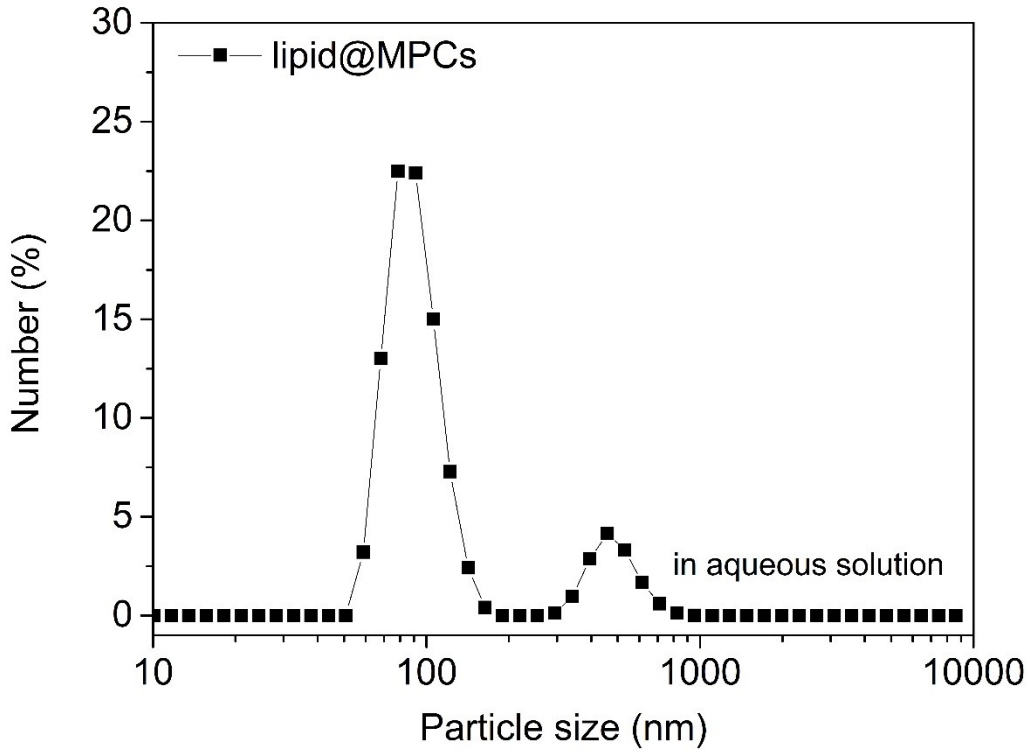

Figure S 3.3: DLS of lipid@MPCs in buffer solution demonstrates colloidal stability in aqueous solution with hydrodynamic particle size distribution with a maximum at 80 nm. The second peak of the size distribution at 460

nm results from some agglomeration of particles. Nevertheless the majority of depicted particle sizes are well suitable for cellular uptake.

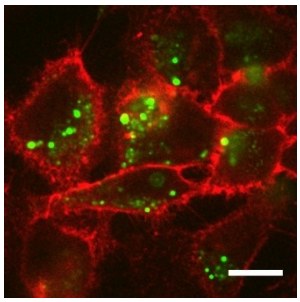

Video S1: Video of z-stack from the bottom of the cell to the top. Lipid@MPCs (green) are internalized within the cell membrane (red). Particle concentration was 15 µg/mL. The video was recoreded after 24 h of pafticle treatment on HeLa cells.

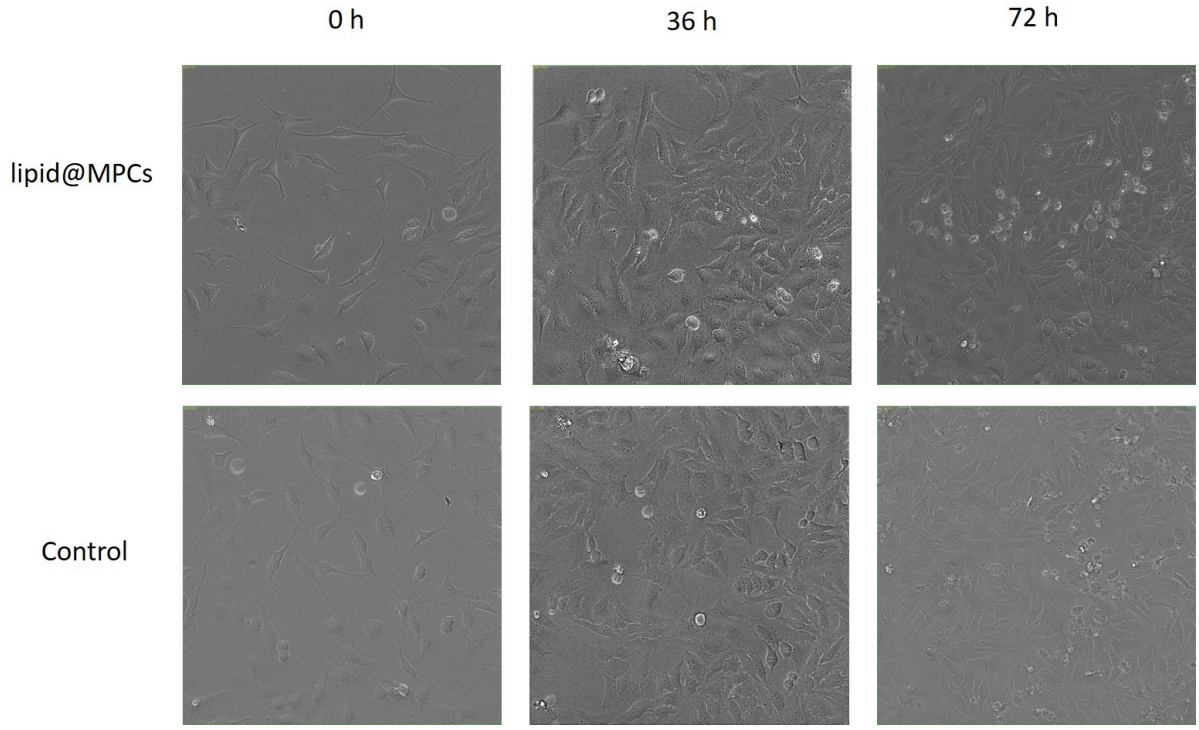

Figure S 3.4: Brightfield images of the control and lipid@MPCs at different time spots were recorded. The used particles treatment concentration was 100 µg/mL @ 5000 seeded cells per 100 µL well. The observation of growing and vital cells supplements observations of MTT assay. At even high concentrations particles are non-toxic.

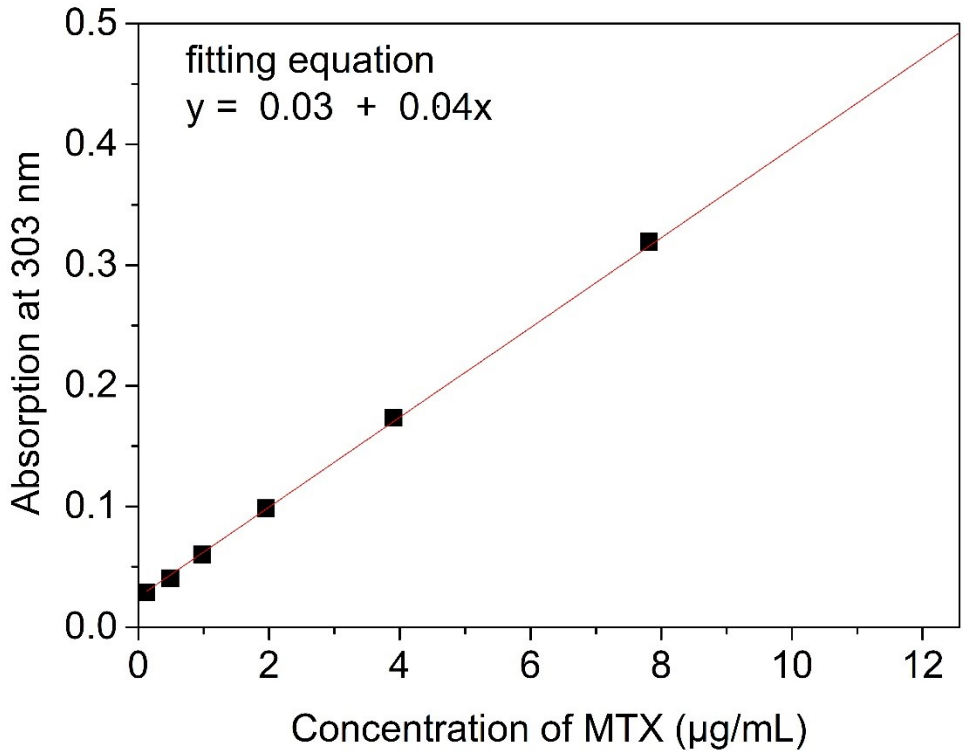

Figure S 3.5: Absorption fitting curve of methotrexate with different concentrations measured at 303 nm.

CHAPTER 4

Crosslinked Cyclodextrin-based Nanoparticles as Drug Delivery Vehicles: Synthesis Strategy and Degradation Studies

The study was guided by Thomas Bein and the described nanoparticles are the basis for a part of the experiments described in Chapter 5.

4. Crosslinked Cyclodextrin-based Nanoparticles as Drug Delivery Vehicles: Synthesis Strategy and Degradation Studies

This chapter is based on the manuscript:

Lisa Wehl, Katharina Muggli, Hanna Engelke, Thomas Bein, ACS Omega 2023, submitted

Abstract

In this work, we report on the synthesis and characterization of cyclodextrin-based nanocarriers, intended as new biogenic and biodegradable drug-delivery agents. Specifically, β-cyclodextrins were covalently crosslinked by carbonyl linkages using carbonyldiimidazol (CDI) and were colloidally stabilized via PEGylation (β-CD-CDI-PEG). The optimized synthesis results in size-controlled nanoparticles with a narrow particle size distribution and a hydrodynamic diameter of around 200 nm in water and 100 nm in dried powder as observed by scanning electron microscopy. β-CD-CDI-PEG nanoparticles are promising drug delivery carriers as they offer an intrinsic pore system originating from the β-cyclodextrin building units and an additional intra-particle pore space gained by crosslinking these β-cyclodextrin units. We demonstrate the biodegradability of these materials and show exemplarily their drug delivery potential using two different model cargos. Time-based fluorescence release measurements *in cuvette* established a stable cargo-retention of the fluorescent dye Hoechst at neutral pH, and in contrast, an efficient stimuli-responsive release at pH 5, accompanied by efficient nanoparticle degradation. These findings were supported by infrared spectroscopy measurements, where upon the degradation of nanoparticles at acidic pH, the efficient release of the second model cargo, the hydrophobic small drug necrosulfonamide, was shown. Finally, the cell uptake of these covalently labeled β-CD-CDI-PEG nanoparticles into HeLa cells was

followed with *in vitro* fluorescence microscopy where the membrane-permeable Hoechst dye was delivered time-delayed in comparison to the free Hoechst dye, establishing the drug-delivery potential of these new nanoparticles.

In summary, our work aims to contribute to the design and understanding of cyclodextrin-based nanocarriers as a promising drug delivery platform.

4.1. Introduction

In recent years, many different materials have been explored as nanocarriers for drug delivery.[1-3] These include liposomes, polymer nanoparticles, micelles, dendrimers, and inorganic nanoparticles. The use of nanocarriers is anticipated to overcome many challenges experienced upon direct therapeutic use of drugs in classical treatments, such as limited stability and solubility, unfavorable pharmacokinetics and the potential off-target toxicity of small (hydrophobic) drugs. Using nanocarrier systems can enhance the bioavailability, reduce side effects of toxic drugs, may allow for a controlled release or function as slow release reservoir, and improve the stability of drugs by preventing premature degradation, thus overall enhancing the final efficacy. However, nanocarriers must also meet several requirements, including sufficient drug loading capacity, good biocompatiblity and timely biodegradability.

In this context cyclodextrins (CDs) have emerged as interesting materials due to their favorable properties. CD are cyclic oligosaccharides composed of 6, 7 or 8 D-glucopyranose units forming alpha-, beta- (β-) or gamma-CD, respectively, with 0.5 to 0.8 nm cone-shaped cavities.[4] They are natural products obtained from enzymatic conversion of starch. They have an inner hydrophobic cavity, while free hydroxyl groups point outward and form a hydrophilic surface. Cyclodextrins can form host-guest inclusion complexes, making them interesting candidates for numerous drug delivery applications. The cone-shaped cavity can form inclusion complexes with small organic or inorganic lipophilic molecules. Thus, a low solubility of hydrophobic molecules can be overcome by incorporating these guests in the cavity. Labile drugs can simultaneously be stabilized and protected against premature degradation.

Together these aforementioned properties have resulted in an extensive use of CDs for drug delivery applications, following various strategies.[5-8] The simplest CD drug delivery vehicles consist of formulations of free CDs or their water-soluble derivatives by forming inclusion complexes with various poorly soluble drug guest molecules.[9] In addition, CDs can

spontaneously self-assemble to form visible microparticles in aqueous media[10], therefore, self-assembled aggregates of either non-inclusion or CD/drug complexes can lead to drug delivery systems, like micro- or nanoparticles.[11-12] Self-assembly can be guided by polymers or polymer-functionalized CDs.[13] In groundbreaking work, Davis et al. designed a targeted CD-based nano-assembly for siRNA delivery by the conjugation of a neutral stabilizing polymer, polyethylene glycol (PEG) to the targeting ligand and adamantane, the latter forming strong inclusion complexes with β-CD. This targeted siRNA nanoparticle-delivery system reached clinical trial.[14-15] Another strategy assembles CD units onto the surface of nanoparticles, e.g. gold or silica NP, assisted by host-guest interactions between CDs and surface functional groups decorating the metal NPs.[16-18] Nanosized and well-defined polymeric drug delivery materials can also be obtained with CD-based dendrimers. Dendrimers are highly branched nanoscale polymers. For example, cyclodextrins can be conjugated to the surface of the dendrimer to enhance the drug encapsulation (loading) ratio and simultaneously provide targeting moieties for specific cells or tissues.[19]

Conceptually different routes use direct chemical crosslinking or van der Waals association of CDs with different linker molecules. The large number of available linker molecules and strategies for crosslinking leads to a wide variety of resulting materials with tunable properties. This family of cyclodextrin-based cross-linked porous structures involves metal organic frameworks (MOFs)[20], crosslinked CD-nanoparticles[21], hydrogels[8] and nanosponges.[22-24] In CD-based metal organic frameworks, cyclodextrin molecules act as linkers, connecting metal ions or clusters to form a three-dimensional porous structure. However, the coordinative bonds between metal ions and hydroxyl groups in metal-organic frameworks are not stable in aqueous solution at neutral pH, leading to rapid dissolution of the frameworks in water. On the other hand, covalently crosslinked three-dimensional networks, as present in crosslinked CD-based nanoparticles, hydrogels and nanosponges, can enhance the stability of the nanocarriers. In

contrast to the small size of nanoparticles, nanosponges, however, result in larger, often even macroscopic powders requiring mechanical degradation or size-exclusion chromatography methods to reach the nanoscale.[25]

Interestingly, crosslinking creates additional adsorption space beyond the CD-inherent cavities in the polymeric network, resulting in a higher loading capacity for guest molecules.[26] For example, unusually high payloads of curcumin were recently achieved in tetrafluoroterephthalonitrile crosslinked CD-nanoparticles, resulting in a molar ratio of 2.3:1 of curcumin molecules : CD units.[27] Moreover, Pivato *et al.* observed prolonged multistep drug release kinetics with pyromellitic dianhydride crosslinked β-cyclodextrin nanosponges due to the beneficial adsorption properties of the cyclodextrin-drug polymer network.[28]

Crosslinking CDs with the above two linker molecules leads directly to nanoparticles respectively nanosponges with favorable properties for successful drug delivery. However, in terms of biocompatibility as well as biodegradability, the choice of crosslinker needs to be carefully considered. In this respect, short linkers, forming only a carbonate diester bond as crosslinking unit, such as carbonyldiimidazol (CDI), are well suited because they are expected to be degradable on the one side and promise to form, in combination with β-CD, only harmless fragments after degradation.[29] CD nanosponges crosslinked with CDI have been used successfully as potent drug carriers.[30-35] One of the most relevant applications in this field is the use in cancer therapy, for example, *in vitro* anti-cancer drug delivery was shown with the hydrophobic anticancer drugs paclitaxel[36] or flutamide.[37] However, to the best of our knowledge, the CDI crosslinked nanosponges were produced by mechanochemical size reduction of the respective bulk materials, often resulting in particle sizes > 400 nm, without intrinsic size control during the synthesis.

It should be noted that the application of cyclodextrin nanosponges in the biomedical context is still at an early stage. Aiming at enhanced control and understanding of the direct synthesis of crosslinked cyclodextrin nanoparticles sized about 200 nm for drug delivery, here we present a synthesis strategy resulting in colloidally stable, size-controlled CD-based nanoparticles. Moreover, we show that these 'true' nanoparticles are degradable under physiological conditions and are well tolerated by cells. Drug-delivery capabilities are demonstrated with two different probe molecules. In our approach discussed here, we crosslinked β-cyclodextrins with CDI, forming covalent carbamate bonds as linker units, and stabilized the nanoparticles using amino-PEG. The resulting nanoparticles show a particle size of 100 nm (obtained with scanning electron microscopy, SEM) and a hydrodynamic diameter of around 200 nm, which is stable over weeks in aqueous solution at neutral pH. We show the encapsulation as well as the stimuli-responsive release of guest molecules, achieved through acidification, which is typical for late endosomes. Overall, the nanoparticles show a high potential for drug delivery applications regarding their suitable size, porosity, degradability and low toxicity. They have already demonstrated their potential for the effective delivery of hydrophobic drugs in a recent comparative study being one of three examined porous nanoparticles in order to suppress inflammatory responses in macrophages.[38] Now, we present a detailed report of the synthesis conditions as well as the impact of stabilization to obtain suitable nanoparticles for drug delivery applications.

4.2. Results and Discussion

In this study, β-cyclodextrin (β-CD) based nanoparticles crosslinked with N,N-carbonyldiimidazole (CDI) and stabilized via PEGylation were synthesized. We first focused on the synthesis of unPEGylated nanoparticles by crosslinking β-CD with CDI serving as crosslinker. First, we examined in more detail the β-CD : crosslinker ratio with respect to resulting particle size. This synthesis was performed in DMF at room temperature. The complete polymerization of β-CD with CDI at elevated temperatures resulted in a gel-like bulk material, and resembles the nanosponge material established by Trotta *et al.*.[39-40] They dried these bulk materials and subsequentially crushed them mechanically into smaller fragments to obtain nanosized powders. To avoid these secondary treatments and directly obtain colloidally stable nanoparticles, we modified the synthesis conditions, finally resulting in size-controlled, reproducible β-CD-CDI nanoparticles termed unPEGylated β-CD-CDI NP in the following.

The synthesis conditions for unPEGylated β-CD-CDI nanoparticles are summarized in the following: β-CD and CDI were dissolved in anhydrous N,N-dimethylformamide (DMF) and the mixture was stirred at room temperature for 3 hours. Afterwards, the solution was aged at 4 °C for 2-3 days without stirring (details are discussed in the appendix). This procedure is based on the known crosslinking reaction of CDI with two molecules having free hydroxyl groups (e.g., free OH-groups from β-CD) which occurs in two steps. With the first hydroxyl group an imidazole carbamate intermediate is formed. The intermediate can react with a second hydroxyl group to form a crosslinked ester bond.[41] An illustrative reaction scheme with CDI and free hydroxyl groups of β-cyclodextrin is shown in Figure 4.1a.

The resulting unPEGylated β-CD-CDI nanoparticles can be precipitated with water, however, they are unstable and flocculate within minutes when kept in aqueous solution. We assume that this is caused by the formation of CDI-activated hydroxyl units - the imidazole carbamate intermediate or diesters which are reactive towards water and amines (Figure 4.1b). To prevent

flocculation, unPEGylated β-CD-CDI nanoparticles were freeze-dried directly after precipitation and used mainly as powder samples for further characterization.

In order to optimize the formation of uniform nanoparticles with small size distribution, we varied the β-CD : cross-linker ratio in three steps between 1:6 and 1:18. Dynamic light scattering (DLS) measurements of aqueous suspensions, immediately after precipitation, and SEM images of the dried powder show that mostly uniform β-CD-CDI nanoparticles were obtained when a molar ratio of 1:12 was used (Figure S4.1, supplemental material). For the following experiments, the molar ratio of CD : CDI was kept at 1:12.

The amount of β-CD in β-CD-CDI NP was quantified using FTIR spectroscopy. First, increasing concentrations of the β-CD precursor were measured using KBr pellets (Figure S4.2a). To obtain a calibration curve, peaks at 2975 cm^{-1} (C-H stretching vibration) were used for the calculation (Figure S4.2b). The β-CD amount in nanoparticles was determined by comparing spectra of a defined mass of β-CD-CDI powder samples to the calibration curve (Figure S4.2c). The amount of β-CD in β-CD-CDI NP was determined to be 60 wt%.

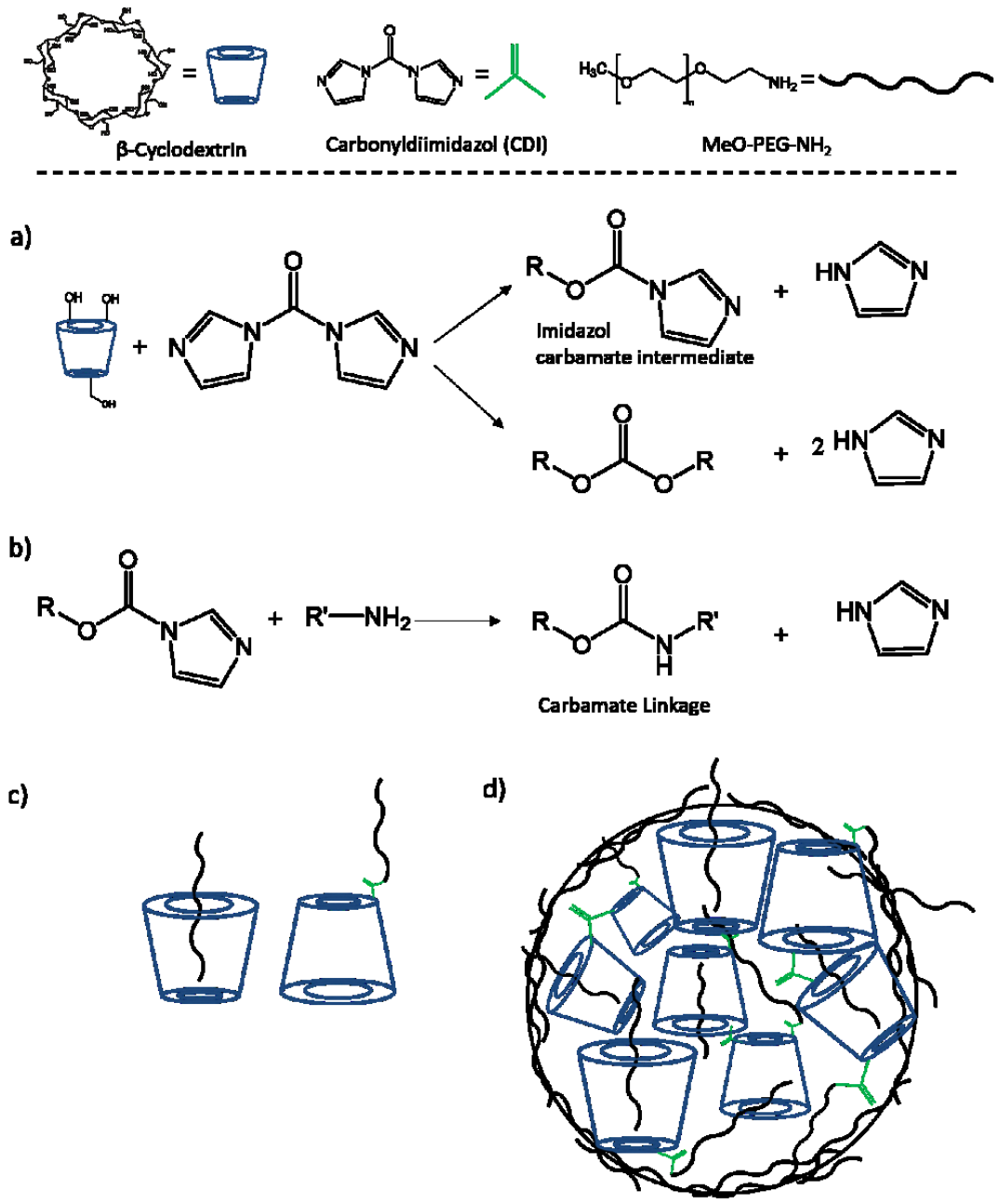

Figure 4.1: Reaction scheme of a) CDI with free hydroxyl groups of β-CD and b) imidazole carbamate intermediates with amines. Schematic representation c) of the possible reaction of β-CD-CDI with the used amine-PEG and d) synthesized β-CD-CDI-PEG NP.

To obtain colloidally stable nanoparticles meeting key requirements for drug delivery, the nanoparticles were stabilized with polyethylene glycol. It was anticipated that residual exterior carbamate linkers can be coupled to amine-functionalized PEG, thus establishing a stable solvatization of the nanoparticles. Therefore, methoxy-polyethylene glycol amine (MeO-

PEG_{750}-NH_2) was added to the DMF reaction solution after aging at 4 °C, followed by stirring overnight at room temperature. Cyclodextrins are known to form inclusion complexes with linear polymers such as polyethylene glycol (PEG).[42] Thus, the amine-functionalized PEG molecules can potentially also form these inclusion complexes but are also likely to bind to β-CD-CDI units forming stable N-alkyl carbamate linkages (Figure 4.1b).[43] By applying this procedure, we obtained colloidally stable, water-dispersible spherical nanoparticles (NP) which we call β-CD-CDI-PEG NP in the following.

Characterization of β-CD-CDI-PEG NP

Transmission electron microscopy (TEM) and scanning electron microscopy (SEM) images of β-CD-CDI-PEG NP show spherical nanoparticles with a size distribution of 100-160 nm (Figure 4.2a and b). Dynamic light scattering measurements in aqueous solution are in good agreement with the microscopically measured size distribution, showing a hydrodynamic diameter of 200 nm (Figure 4.2c, black line). Furthermore, the DLS measurements reveal long-term colloidal stability of these nanoparticles. We could not detect major changes in the hydrodynamic diameter when nanoparticles were stored for 1 month in H_2O (Figure 4.2c, red line). The formation of β-CD-CDI-PEG NP was also established using Fourier transform infrared (FTIR) spectroscopy (Figure 2d). The spectra of the final nanoparticles exhibit a strong signal at 1035 cm^{-1}, which corresponds to characteristic stretching vibrations of the oligosaccharide ring of incorporated β-CD (marked with hash) and a strong signal at 1761 cm^{-1} (marked with asterisk), which can be assigned to the C=O stretching vibration of carbonate ester units formed by CDI. Carbamate linkages resulting from covalent binding of amine-PEG show characteristic peaks at 1650 cm^{-1} (due to amide-I like carbonyl stretching) and 1530 cm^{-1} (assignable to amide-II like N−H bending).[44]

The surface area of dried β-CD-CDI-PEG NP was examined using nitrogen sorption experiments. The overall surface of crosslinked cyclodextrin nanoparticles is generated from a combination of the inner cavities of the oligosaccharides, the additional interstitial (intraparticle) polymer surface resulting from crosslinking, as well as interparticle textural porosity depending on particle size. When rigid linker molecules like tetrafluoroterephthalonitrile were used for crosslinking, BET surface areas of up to 140 m^2/g were reported for small cyclodextrin nanoparticles.[21] However, here the CD units are coupled via a short and more flexible carbonyl residue formed when using CDI as linker precursor. Consequently, the framework of the β-CD-CDI-PEG NP is expected to (partially) collapse under the high vacuum conditions employed during the nitrogen sorption measurements, resulting in a moderate BET surface area of β-CD-CDI-PEG NP of around 20-40 m^2/g (Figure 4.2e). Here, microporosity does not contribute to the overall porosity, indicating that the cyclodextrin cavities are blocked in vacuum, for example by the PEG chains or by collapsing particles. The thermogravimetric analysis (TGA) of β-CD-CDI-PEG NP, using a heating rate of 10 °C/min up to 900 °C with a stream of synthetic air of about 25 $mL \cdot min^{-1}$, indicates a complete decomposition of the material within a temperature range between 170 °C and 620 °C. Zeta potential measurements show a negative surface charge of -14 mV at pH 7.3 due to the free hydroxyl groups of the oligosaccharide.

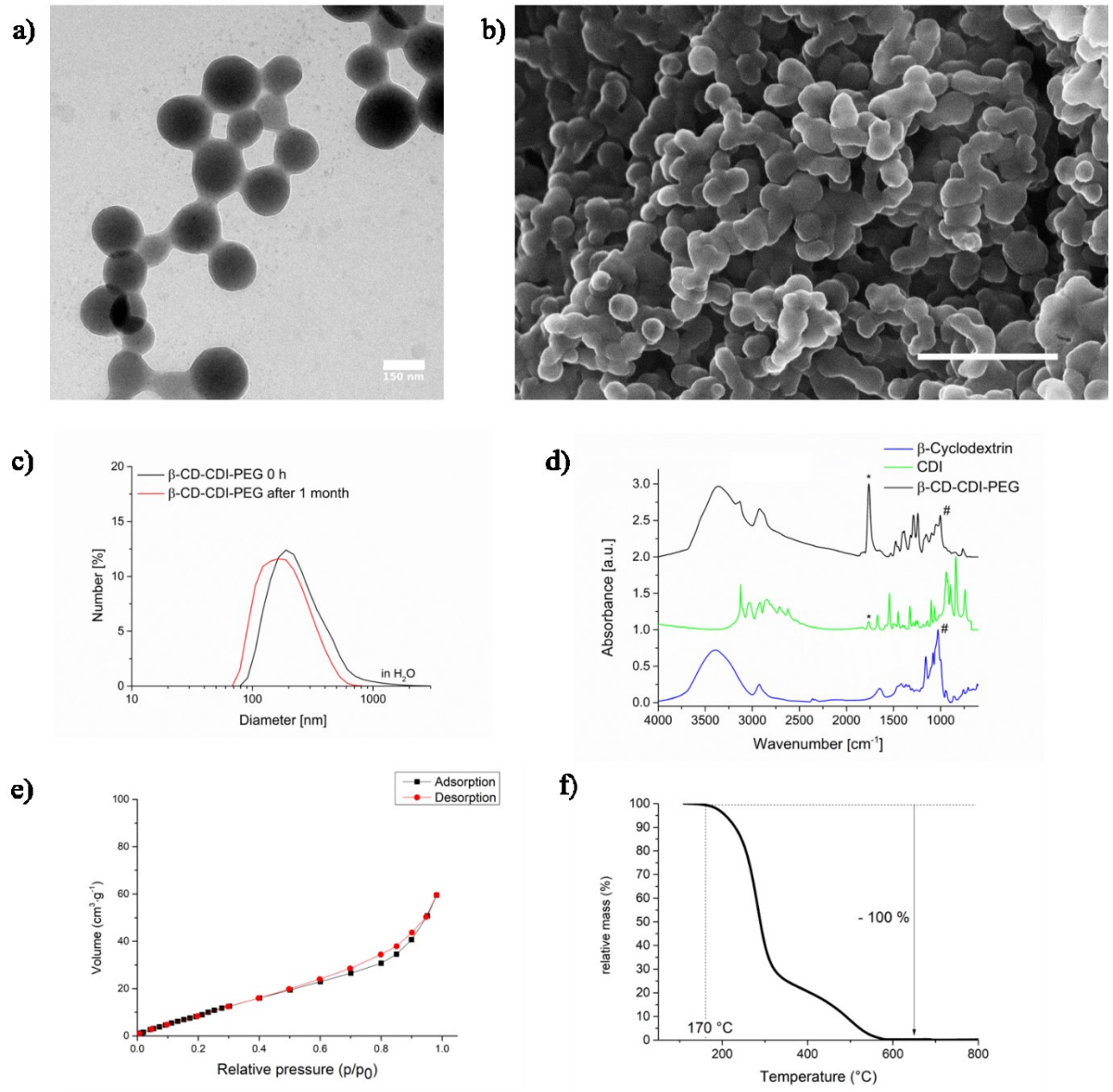

Figure *4.2*: Characterization of β-CD-CDI-PEG NP. a) TEM (scale bar: 150 nm) and b) SEM (scale bar: 500 nm) images show a spherical morphology of the nanoparticles with a particle size ranging between 100-160 nm). c) DLS measurements of β-CD-CDI-PEG NP show (hydrodynamic) particle sizes of around 200 nm and a colloidal stability over months in water. d) FTIR spectra of the final NP in comparison to the reagents β-CD and CDI reveal the formation of crosslinked and PEG-stabilized cyclodextrin-based nanoparticles. The signals at 1760 cm^{-1} and 1035 cm^{-1} (indicated by * and #, respectively) indicate the presence of carbonyl groups (from CDI crosslinking) and of an oligosaccharide ring (from β-CD). e) Nitrogen sorption isotherm and f) TGA curve of β-CD-CDI-PEG NP.

In-vitro experiments

The synthesized β-CD-CDI-PEG NP were subsequently used for *in vitro* experiments. Biocompatibility of the nanoparticles was studied via a cell viability assay. A concentration

series of plain nanoparticles was added to HeLa cells for 48 h, when the cellular metabolic activity (MTT assay) was measured as indicator for cell survival. Notably, after this prolonged incubation time, the metabolic activity of Hela cells was not strongly affected, even for high particle concentrations of 100 µg/mL, indicating a good biocompatibility (Figure 4.3a). To follow the uptake of β-CD-CDI-PEG NP into HeLa cells, nanoparticles were covalently labelled with the fluorescent dye Atto633-NH_2. The amine group of the dye was used to form a stable N-alkyl carbamate linkage with the imidazole carbamate intermediate of the β-CD-CDI units, thereby covalently attaching the dye to the nanoparticles. After several washing steps, the particles were used for fluorescence microscopy imaging. The uptake of the labeled nanoparticles was followed by time-based fluorescence microscopy (Figure 4.3b, transmission light image of HeLa cells overlaid with the red fluorescence channel for labelled β-CD-CDI-PEG NP). After 5 h of particle incubation, an association of the nanoparticles with HeLa cells can be observed.

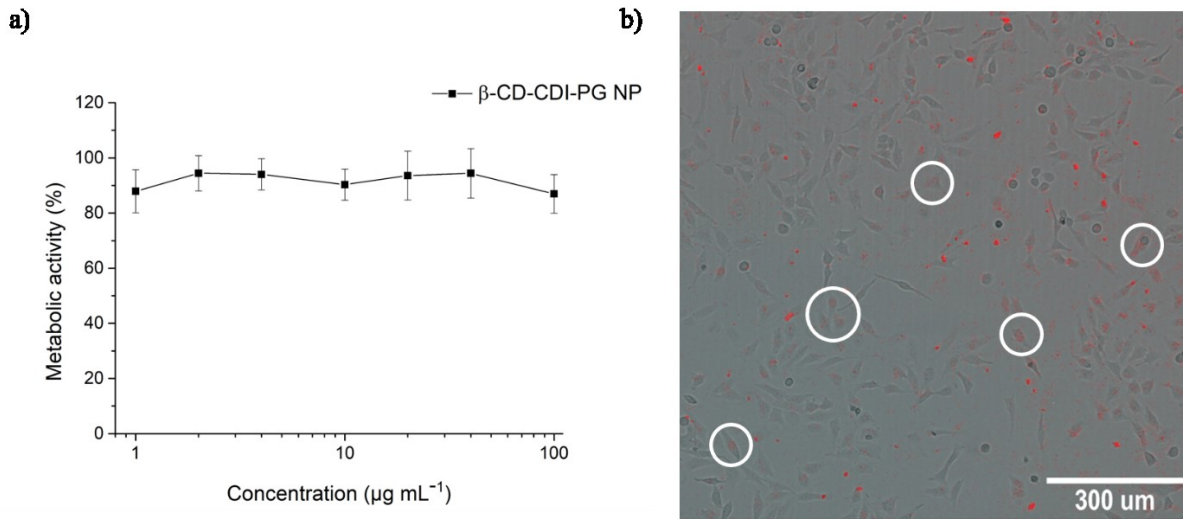

Figure 4.3: *In vitro* studies of β-CD-CDI-PEG NP on HeLa cells. a) MTT cell viability assay of different concentrations of β-CD-CDI-PEG NP samples on HeLa cells after 48 h incubation. b) Uptake of labelled β-CD-CDI-PEG NP (red) after 5 h of particle incubation followed by fluorescence microscopy.

Degradation of β-CD-CDI-PEG-NP

The degradability of drug carriers is a prerequisite for safe applications in living systems. Therefore, the degradation of β-CD-CDI-PEG NP was studied in detail. As shown above (Figure 4.2c), β-CD-CDI-PEG NP can be stored in water for weeks without change of particle size. In contrast, in acidic environments (around pH 5), prevalent in late endosomes, the nanoparticles are hydrolyzed and will degrade, as demonstrated below. This is a favorable situation for drug delivery applications, preventing unwanted accumulation of nanoparticles and simultaneously triggering the release of guest molecules. With crosslinked cyclodextrin nanoparticles it is therefore expected to be possible to efficiently release the cargo upon cellular uptake in the late endosomes without premature release. The degradation mechanism of β-CD-CDI-PEG NP originates presumably from breaking the cross-linking sites, the carbamate- and ester bonds. We suggest that after hydrolysis free PEG molecules support the formation of inclusion complexes with free β-CD leading to weakly aggregated fragments. Thus, nanoparticles hydrolyze into fragments followed by re-assembly as seen by particle size

measurements. The DLS studies were conducted at different time points after particles were kept in suspension either at pH 7 or at pH 5. At pH 7 we observed unchanged particle sizes of around 300 nm over 48 h when particles were stored as aqueous suspensions as well as in buffered solution or cell culture medium (at pH 7.4 in phosphate buffered saline (PBS) or DMEM cell culture medium, see Figure S4.3). In striking contrast, when particles were stored at pH 5, we observed an immediate increase in hydrodynamic size directly after acidification, which increased until sedimentation of hydrolyzed and self-assembled aggregates occurred after 48 h, indicating particle disintegration and re-aggregation (see Figure 4.4a,b). Particle disintegration is studied in more detail in the following using loaded β-CD-CDI-PEG NP with encapsulated guest molecules.

Guest absorption and release in β-CD-CDI-PEG NP upon degradation

Crosslinked beta-cyclodextrin-based nanoparticles offer a versatile and effective approach for the encapsulation and controlled release of guest molecules. β-CD-CDI-PEG NP can absorb guest molecules within their cavities and a pH-sensitive release is achieved through the use of CDI as crosslinking agent, when crosslinking is degraded at acidic pH.

For further investigations of guest absorption and release under drug-delivery conditions, we loaded cargo molecules into the β-CD-CDI-PEG NP. We used a hydrophobic small molecule as first model compound for adsorption into our β-CD-CDI-PEG NP. Specifically, we used the immune-suppressant necrosulfonamide (NSA), which we have recently successfully delivered to macrophages by means of these particles.[38] The loading was performed using a yellow stock solution of NSA in DMSO, of which aliquots were added to an aqueous particle suspension, resulting in highly loaded NP suspensions with over 20 wt% cargo as determined by UV-Vis measurements (Figure S4.4).

The encapsulation of NSA into our cyclodextrin nanoparticles was confirmed by XRD measurements. The comparison of crystalline free NSA (black line) and amorphous β-CD-CDI-PEG NP (red line) is shown in Figure 4.4c). A physical mixture of the two individual powdered samples (green line) still contained distinct peaks of the free NSA at 12 °, 14 ° and 26 °2θ. In contrast, when NSA was adsorbed into the CD particles, a diffractogram without any indication of crystalline material was obtained.

Evidence of the NSA uptake and release was further obtained with IR spectroscopy (Figure 4.4d). The characteristic vibration at 1685 cm^{-1} (indicated by hash) of the amide groups of NSA is clearly present in the spectra of β-CD-CDI-PEG-NSA nanoparticles (red line). In addition, a significant shift in the position of this peak to 1689 cm^{-1} with respect to the free NSA was observed, pointing to an interaction with the cyclodextrin surface. These samples were then remeasured after treatment in acidic solutions at pH 5 for 48 h. For this, the suspension was centrifuged, the pellet washed with water to remove soluble fragments of degraded particles, dried and subsequently analyzed. The spectrum of this sample after degradation (green line) completely misses the absorption peak at 1761 cm^{-1}, assigned to the C=O stretching vibrations from crosslinking as seen in the undegraded nanoparticles (red line, indicated by asterisk). Only small residues of NSA remained after washing, indicated by a signal at 1685 cm^{-1}. Thus, major amounts of NSA were released from the nanoparticles upon degradation.

As a second model cargo in form of the fluorescent dye Hoechst was loaded into β-CD-CDI-PEG NP (β-CD-CDI-PEG-Hoechst). Here, a stimuli-responsive release upon degradation at pH 5 was studied by UV-Vis measurements (Figure 4.4e) and fluorescence spectroscopy (Figure 4.4f). For time-based UV-Vis release measurements, particles were collected by centrifugation after shaking in an aqueous solution either at pH 7 or pH 5 at different time points. The supernatant was then used to follow the release of the dye. As seen before, also the Hoechst loaded β-CD-CDI-PEG NP were stable at pH 7 and could be recovered from solution

via centrifugation without detectable release of Hoechst dye into the supernatant. Acidification, as expected at this point, led to particle degradation and release of the Hoechst dye into the supernatant, demonstrated by an intense absorption peak at around 340 nm.

These findings were supported by in-situ fluorescence spectroscopy. To this end, we used a home-made cell for fluorescence detection of the released cargo, consisting of a separate sample compartment on top of a cuvette. Cap and measuring compartment were separated by a dialysis membrane, with a molecular cut-off at 14 kDa. This ensures that only small molecules, like the released dye, can pass freely through the membrane into the measuring compartment. The β-CD-CDI-PEG-Hoechst samples were transferred into the cap of the measuring compartment, while the cuvette contained an aqueous solution either at pH 7 or at pH 5. The time-based release of Hoechst dye from β-CD-CDI-PEG NP was first measured for the as-prepared samples at pH 7 (black line) and then for β-CD-CDI-PEG in an acidified solution (red line). Here, an increase in fluorescent counts over time can only be detected for the acidified, degraded sample while the non-degraded sample shows just a very weak signal. When free Hoechst dye was measured accordingly, we observed an increase in fluorescence after approximately four hours. This is a similar time-delay as observed with our β-CD-CDI-PEG-Hoechst samples and indicates an immediate start of nanoparticle disintegration at pH 5.

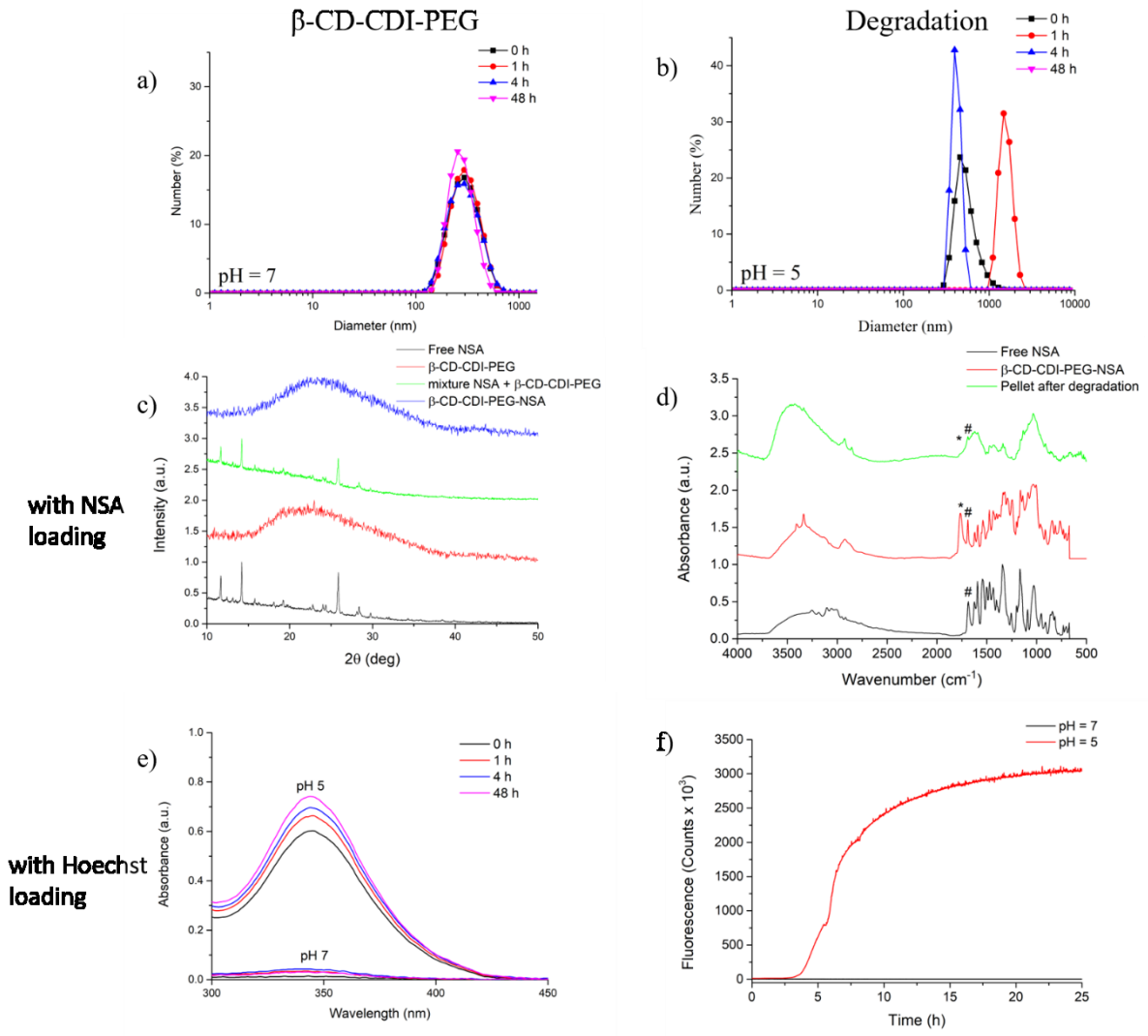

Figure 4.4. Degradation and release studies of β-CD-CDI-PEG NP. a, b) DLS measurements of β-CD-CDI-PEG NP in aqueous solution at a) pH 7 and b) pH 5 at diferent time points. c) XRD measurements of the model compound NSA as free compound, mixed with and loaded in β-CD-CDI-PEG. d) FT-IR spectroscopy of NSA in β-CD-CDI-PEG before and after degradation. The asterisk marks the absorption peak at 1761 cm^{-1}, assigned to the C=O stretching vibrations from crosslinking, which is completely missing for degraded particles. The hash marks the characteristic NSA absorption peak at 1685 cm^{-1}. For degraded samples, only a weak signal can be detected, indicating that major amounts of NSA were released upon degradation. Release measurements of model compound Hoechst dye in β-CD-CDI-PEG studied by e) UV-Vis and f) time-based fluorescence spectroscopy at pH 7 or at pH 5. Please note, due to the strong measured fluorescence of the released Hoechst dye (red line), the noise of control sample at pH 7 (black line) is not visible because of the required large scale.

pH triggered release of Hoechst in HeLa cells

The *in vitro* application of Hoechst-loaded nanoparticles to HeLa cells was studied to learn more about the pH-sensitive degradation and simultaneous release of the Hoechst model drug. The delivery of Hoechst dye into HeLa cells was followed by life-cell fluorescence

microscopy. Hoechst-loaded NP were added to HeLa cells seeded in a 96 well plate, and studied by time-lapse fluorescence measurements every 5 minutes. Images of the blue channel at selected time intervals after particle addition are shown in Figure 4.5. The corresponding transmission light images of cells are inserted as insets. The blue fluorescence of the Hoechst dye develops only after intercalation of Hoechst into the DNA located in the nucleus. Image acquisition was started directly after nanoparticle addition. When Hoechst-loaded particles were added to HeLa cells (column a in Figure 4.5) a slight blue staining of cell nuclei can be observed after 20 minutes, increasing steadily in intensity and reaching a maximum after around 90 minutes. In contrast, when free Hoechst dye was added to HeLa cells (column b in Figure 4.5) the staining was immediately visible. Free Hoechst dye is membrane-permeable and able to efficiently stain the nuclei of HeLa cells within a very short time period of less than 3 minutes (time interval of addition until image acquisition). This difference in nuclei staining kinetics shows that Hoechst is indeed initially enclosed in the β-CD-CDI-PEG particles and can efficiently be released upon cell contact because it is cell-permeable and/or upon cell uptake into the acidic environment of endosomes causing degradation of the NP.

For a reference experiment, we kept an identical particle suspension as the one used for the in vitro cell experiments for 2 h at 37 °C, then centrifuged the solutions and used the supernatants on HeLa cells (column c in Figure 4.5). Now, no nuclei staining was observed, clearly demonstrating that no Hoechst dye molecules were released prematurely from the NP.

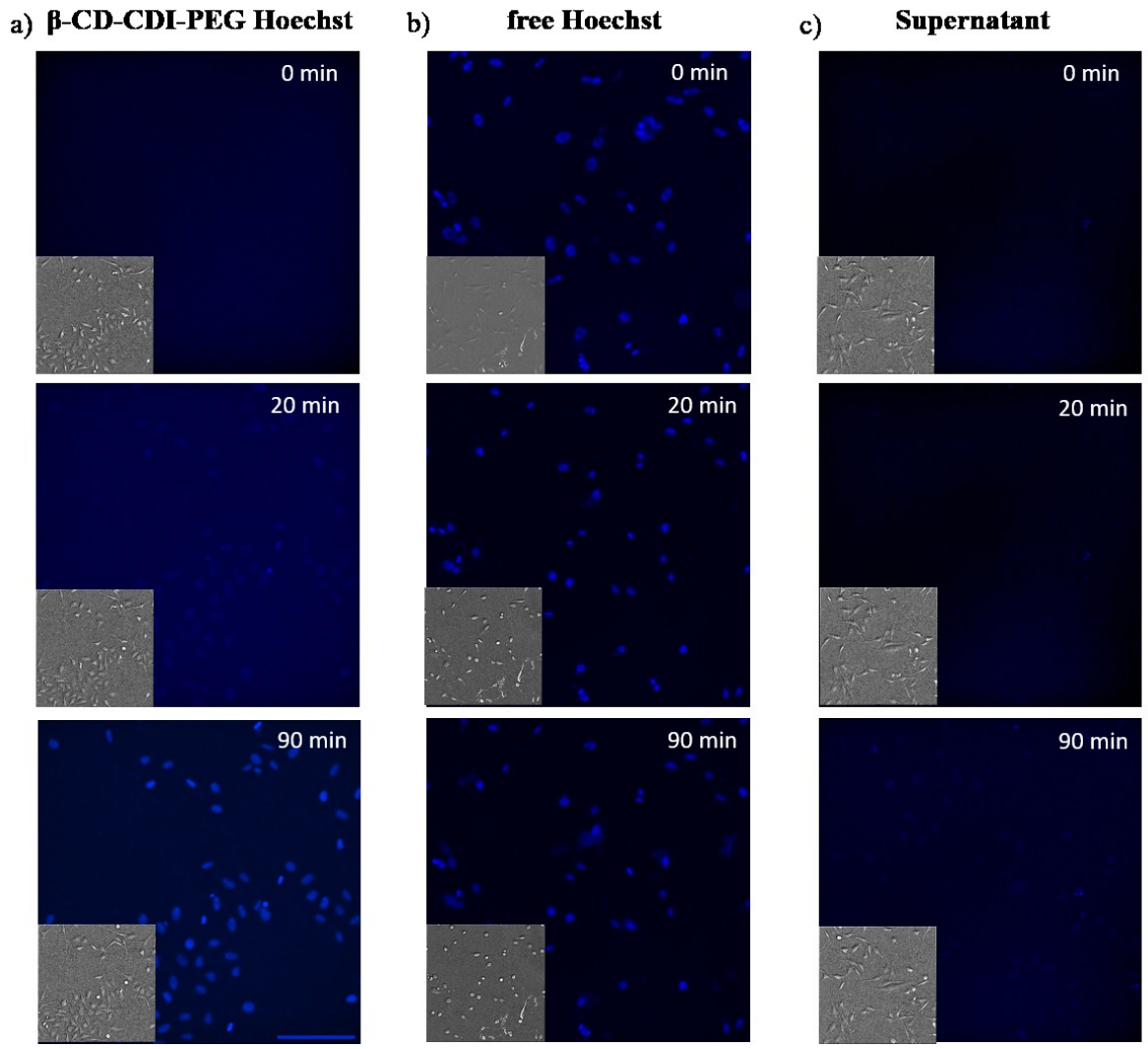

Figure 4.5: Time-based fluorescence microscopy to follow Hoechst nuclei staining by a) cargo release from β-CD-CDI-PEG-Hoechst nanoparticles, b) free Hoechst dye and c) supernatant of the β-CD-CDI-PEG Hoechst suspension pretreated in DMEM cell culture media for 2 h.

4.3. Conclusion

In summary, we have developed biocompatible and colloidally stable, yet also degradable crosslinked β-cyclodextrin-based nanoparticles that are able to carry guest molecules at high loadings. The obtained nanoparticles are small (100 nm when imaged in the scanning electron microscope, 200 nm hydrodynamic diameter in the DLS), highly dispersible and stable in aqueous solution over long periods. The nanoparticles were generated by crosslinking β-CD via carbonic acid diesters and were stabilized by means of short PEG molecules. As expected, *in vitro* metabolic activity studies showed that β-CD-CDI-PEG NP were extremely well tolerated by HeLa cells, indicating excellent biocompatibility. Moreover, biodegradability is an important feature for a safe use as drug nanocarrier and a feature that can enable favorable drug release behavior. We established that β-CD-CDI-PEG NP are stable at pH 7 but could be degraded at pH 5 and are able to efficiently release cargo molecules into cells. This is exemplarily shown by delivering the model cargo Hoechst dye into HeLa cells and efficiently staining the nuclei without experiencing a premature release. As a result, these nanoparticles show great potential for future applications as a biocompatible drug carrier system.

4.4. Experimental Part

Methods

Chemicals:

β-Cyclodextrin (Sigma, 97 %), 1,1'-carbonyldiimidazole (CDI, Sigma, ≥ 90 %), Hoechst 33342 (Sigma, 97 %), methoxy-polyethylene glycol amine (750) (OMe-PEG-NH_2, Sigma), N,N-dimethylformamide (anhydrous) (Sigma, 99.8 %), necrosulfonamide (NSA, Cayman chemical, %), DMSO, hydrochloric acid (Sigma, 2 M), MTT reagent (3-(4,5-dimethylthiazol-2-yl)-2,5-diphenyl tetrazolium bromide, Sigma), Atto633-Amine (Atto-Tec).

All chemicals were used as received without further purification. Doubly distilled water from a Millipore system (Milli-Q Academic A10) was used for all synthesis steps.

Cell Line and culture

HeLa human cervical cancer cells were purchased from and cultured according to American Type Culture Collection (ATCC). HeLa cells were grown in DMEM medium (Sigma Aldrich) supplemented with 10 % FCS (Gibco) and 2 mM L-glutamine (Gibco) at 37 °C and 5 % CO_2. Cells were routinely tested and confirmed as mycoplasma free.

Synthesis of β-CD-CDI-PEG

β-Cyclodextrin (200 mg, 0.176 mmol) and CDI (342 mg, 2.11 mmol) were dissolved in anhydrous DMF (8 mL) and stirred at room temperature for three hours. Then the reaction mixture was aged at 4 °C without further stirring for 1-3 days. Afterwards, in a small glass vial 1 mL of the reaction solution was mixed with 7 mg of methoxy-polyethylene glycol amine

(OMe-PEG-NH_2) and stirred overnight. This leads to nanoparticles named β-CD-CDI-PEG. 30 µL of β-CD-CDI-PEG reaction solution (corresponds to 0.5 mg of unPEGylated β-CD-CDI nanoparticles) was added in 1.5 mL H_2O for precipitation. To remove unreacted reagents, the particles were separated by centrifugation (5 min, 14 000 rpm), the supernatant was discarded and particles redispersed in 1 mL doubly distilled water.

Preparation of labeled β-CD-CDI-PEG nanoparticles: β-CD-CDI-PEG-Atto633

The preparation of covalently labelled nanoparticles with the dye Atto633-Amine was performed as described in the section above "Synthesis of β-CD-CDI-PEG". When OMe-PEG-NH_2 was added to the reaction solution, additionally 2 µL of Atto633-Amine was added directly into the solution and stirred overnight in the dark. To remove excess dye, the labeled nanoparticles were washed in three centrifugation steps with 1 mL bi-distilled water.

Cargo loading of β-CD-CDI-PEG NP

For NSA loading a stock solution of NSA (10 mg/mL in DMSO) was used. For Hoechst dye loading a Hoechst solution was prepared by dissolving Hoechst 33342 (5 mg) in 1 mL water. 20 µL of either the NSA or the Hoechst stock solution was added to 0.5 mg β-CD-CDI-PEG in 1 mL H_2O and shaken (700 rpm) for 2 h at room temperature. The loaded particles were washed three times with 1 mL water by centrifugation (5 min, 14 000 rpm).

Characterization

TEM: For transmission electron microscopy, samples were prepared on a carbon-coated copper grid. A droplet of a diluted aqueous solution of β -CD-CDI-PEG NP was dried at room temperature on the sample holder overnight. The measurements were performed on a Tecnai G2 20 S-Twin operated at 200 kV using a TemCam-F216 camera (TVIPS).

SEM: For scanning electron microscopy, a droplet of an aqueous solution of NP was dried overnight on a silicon wafer. Measurements were performed on an FEI Helios Nanolab G3 UC. The microscope was equipped with a field emission gun and was operated at acceleration voltages of 2-3 kV using working distances of about 3 mm.

DLS and Zeta-potential: Dynamic light scattering and zeta-potential measurements were performed with diluted colloidal suspensions of NP on a Malvern Zetasizer-Nano instrument with a 4 mW He-Ne laser (633 nm) using PMMA cuvettes.

FTIR: Infrared spectra were measured with a Thermo Scientific Nicolet iN 10 infrared 6700 Microscope (Figure 4.2 and 4.4), and with a Smart OMNI Transmission attachment when using KBr-pelleted samples (Figure S4.2).

Nitrogen sorption: Nitrogen sorption analysis was performed on a Quantachrome Instruments Nova 4000e at 77 K. Samples (25 mg) were outgassed at 120 °C for 12 h *in vacuo* (10 mTorr). Surface areas were calculated with the BET model in the range p/p_0 = 0.05–0.2.

TGA: Thermogravimetric analysis of the samples was performed on a Netzsch STA 440 C TG/DSC in a stream of synthetic air with a flow rate of 25 mL/min and a heating rate of 10 K/min.

XRD: XRD patterns were obtained with a Bruker D8 Discover X-ray diffractometer using Cu-Kα radiation (1.5406 Å).

UV-VIS: UV-Vis measurements using 2 µl of the liquid samples were performed on a NanoDrop 2000c spectrometer from Thermo Scientific Fisher.

Fluorescence spectroscopy: Time-based fluorescence release experiments were performed at 37 °C on a PTI spectrofluorometer equipped with a xenon short arc lamp (UXL-75XE USHIO) and a photomultiplier detection system (Model 810/814) with λ_{ex} = 340 nm and λ_{em} = 510 nm.

Degradation studies with FTIR spectroscopy. Aliquots of β-CD-CDI-PEG-NSA suspension, containing 0.5 mg β-CD-CDI-PEG NP, were centrifuged (5 min, 14 000 rpm) and the supernatant was discarded. The pellet was resuspended in 1 mL phosphate buffered saline (PBS), adjusted with HCl to pH 5. The suspension was shaken for 48 h and again centrifuged. The resulting pellet was washed with 1 mL water and again re-suspended in 1 mL water. The dried powder of the sample was further used for IR spectroscopy.

Fluorescence release measurements with fluorescence spectroscopy. The NP were transferred into the cap of a homebuilt setup (0.5 mg particles per 200 µL water) and separated by a cellulose dialysis membrane from the measuring cuvette, which was filled with water. For control experiments the water was adjusted to pH 7.3 with NaOH, while the water was acidified using HCl to pH 5 for degradation and release studies. Dye that was released from the particles diffused through the membrane and could be detected in the measuring cuvette.

Live cell Fluorescence Microscopy. Live cell fluorescence microscopy was performed using an ImageXpress Micro XLS (Molecular Devices) wide-field high content imaging system using an environmental cell. Bright field images were recorded in addition to fluorescence

images using Cy 5 (wavelength: 631/28 nm) and DAPI channels (wavelength: 377 / 50 nm). A 20x objective from Nikon was used (Ph1 S Plan Fluor 0.45 NA).

24 Hours prior to particle incubation, HeLa cells were seeded in 96 well plates. β-CD-CDI-PEG NP were added in 10 µL aliquots (final particle concentration in well: 500 µg mL^{-1}) to each well. Plates were carefully shaken and transferred into the environmental control chamber at 37 ° under the flow of a 5 % CO_2 humidified atmosphere. Samples were measured in triplicates, with four images per well.

Metabolic activity determined by MTT Assay. MTT assays were performed in triplicates in 96-well plates. One day prior to transfection, HeLa cells were seeded at 5000 cells/well. Before particle addition, medium was replaced by 80 µL fresh medium. β-CD-CDI-PEG samples (20 µL suspension) were added at different concentrations in PBS and the cells were incubated for 48 h at 37 °C. Afterwards, a viability assay was performed. For this, an MTT solution (100 µL/well; 0.5 mg mL^{-1} in DMEM) was added for 2 h. Then, the supernatant was removed and cells were lysed by freezing at –80 °C for at least 1 h. Then, cells were allowed to return to room temperature and DMSO (100 µL) was added. Absorption at 590 nm against a reference wavelength of 630 nm was measured using a SpectraFluorTM Plus microplate reader S4 (Tecan, Groeding, Austria). Metabolic activity was calculated as percentage of absorption compared to wells treated only with PBS.

Loading control and release studies with UV-Vis spectroscopy (Nanodrop). To follow the loading of NSA into the CD nanoparticles, the supernatant resulting after the loading process was analyzed with the Nanodrop spectrometer (2 µL sample, blank: corresponding

water/DMSO solution). Furthermore, the successful washing procedure was monitored by measuring the decreasing UV-Vis absorption of the washing supernatants. For time-based release studies, the supernatants obtained after distinct time points were analyzed with the Nanodrop spectrometer.

4.5. References

1. Mura, S.; Nicolas, J.; Couvreur, P., Stimuli-responsive nanocarriers for drug delivery. *Nature Materials* **2013,** *12* (11), 991-1003.

2. Hossen, S.; Hossain, M. K.; Basher, M. K.; Mia, M. N. H.; Rahman, M. T.; Uddin, M. J., Smart nanocarrier-based drug delivery systems for cancer therapy and toxicity studies: A review. *Journal of Advanced Research* **2019,** *15*, 1-18.

3. Chamundeeswari, M.; Jeslin, J.; Verma, M. L., Nanocarriers for drug delivery applications. *Environmental Chemistry Letters* **2019,** *17* (2), 849-865.

4. Szejtli, J., Introduction and General Overview of Cyclodextrin Chemistry. *Chemical Reviews* **1998,** *98* (5), 1743-1754.

5. Shelley, H.; Babu, R. J., Role of Cyclodextrins in Nanoparticle-Based Drug Delivery Systems. *Journal of Pharmaceutical Sciences* **2018,** *107* (7), 1741-1753.

6. Tian, B.; Liu, Y.; Liu, J., Smart stimuli-responsive drug delivery systems based on cyclodextrin: A review. *Carbohydrate Polymers* **2021,** *251*, 116871.

7. Liu, G.; Yuan, Q.; Hollett, G.; Zhao, W.; Kang, Y.; Wu, J., Cyclodextrin-based host–guest supramolecular hydrogel and its application in biomedical fields. *Polymer Chemistry* **2018,** *9* (25), 3436-3449.

8. Liu, J.; Tian, B.; Liu, Y.; Wan, J. B., Cyclodextrin-Containing Hydrogels: A Review of Preparation Method, Drug Delivery, and Degradation Behavior. *International journal of molecular sciences* **2021,** *22* (24).

9. Muankaew, C.; Loftsson, T., Cyclodextrin-Based Formulations: A Non-Invasive Platform for Targeted Drug Delivery. *Basic & Clinical Pharmacology & Toxicology* **2018,** *122* (1), 46-55.

10. Ryzhakov, A.; Do Thi, T.; Stappaerts, J.; Bertoletti, L.; Kimpe, K.; Sá Couto, A. R.; Saokham, P.; Van den Mooter, G.; Augustijns, P.; Somsen, G. W.; Kurkov, S.; Inghelbrecht, S.; Arien, A.; Jimidar, M. I.; Schrijnemakers, K.; Loftsson, T., Self-Assembly of Cyclodextrins and Their Complexes in Aqueous Solutions. *Journal of Pharmaceutical Sciences* **2016,** *105* (9), 2556-2569.

11. Loftsson, T., Self-assembled cyclodextrin nanoparticles and drug delivery. *Journal of Inclusion Phenomena and Macrocyclic Chemistry* **2014,** *80* (1), 1-7.

12. Jansook, P.; Ogawa, N.; Loftsson, T., Cyclodextrins: structure, physicochemical properties and pharmaceutical applications. *Int J Pharm* **2018,** *535* (1-2), 272-284.

13. Zhang, Y.-M.; Liu, Y.-H.; Liu, Y., Cyclodextrin-Based Multistimuli-Responsive Supramolecular Assemblies and Their Biological Functions. *Advanced Materials* **2020,** *32* (3), 1806158.

14. Davis, M. E., The First Targeted Delivery of siRNA in Humans via a Self-Assembling, Cyclodextrin Polymer-Based Nanoparticle: From Concept to Clinic. *Molecular Pharmaceutics* **2009,** *6* (3), 659-668.

15. Davis, M. E.; Zuckerman, J. E.; Choi, C. H. J.; Seligson, D.; Tolcher, A.; Alabi, C. A.; Yen, Y.; Heidel, J. D.; Ribas, A., Evidence of RNAi in humans from systemically administered siRNA via targeted nanoparticles. *Nature* **2010,** *464* (7291), 1067-1070.

16. Chen, Y.; Li, N.; Yang, Y.; Liu, Y., A dual targeting cyclodextrin/gold nanoparticle conjugate as a scaffold for solubilization and delivery of paclitaxel. *RSC Advances* **2015,** *5* (12), 8938-8941.

17. Badruddoza, A. Z. M.; Rahman, M. T.; Ghosh, S.; Hossain, M. Z.; Shi, J.; Hidajat, K.; Uddin, M. S., β-Cyclodextrin conjugated magnetic, fluorescent silica core–shell nanoparticles for biomedical applications. *Carbohydrate Polymers* **2013,** *95* (1), 449-457.

18. Lv, S.; Zhao, M.; Cheng, C.; Zhao, Z., β-Cyclodextrin polymer brushes decorated magnetic colloidal nanocrystal clusters for the release of hydrophobic drugs. *Journal of Nanoparticle Research* **2014,** *16* (5), 2393.

19. Arima, H., Twenty Years of Research on Cyclodextrin Conjugates with PAMAM Dendrimers. *Pharmaceutics* **2021,** *13* (5), 697.

20. Roy, I.; Stoddart, J. F., Cyclodextrin Metal–Organic Frameworks and Their Applications. *Accounts of Chemical Research* **2021,** *54* (6), 1440-1453.

21. Datz, S.; Illes, B.; Gößl, D.; Schirnding, C. v.; Engelke, H.; Bein, T., Biocompatible crosslinked β-cyclodextrin nanoparticles as multifunctional carriers for cellular delivery. *Nanoscale* **2018,** *10* (34), 16284-16292.

22. Utzeri, G.; Matias, P. M. C.; Murtinho, D.; Valente, A. J. M., Cyclodextrin-Based Nanosponges: Overview and Opportunities. *Frontiers in Chemistry* **2022,** *10*.

23. Cavalli, R.; Trotta, F.; Tumiatti, W., Cyclodextrin-based Nanosponges for Drug Delivery. *Journal of inclusion phenomena and macrocyclic chemistry* **2006,** *56* (1), 209-213.

24. Trotta, F.; Zanetti, M.; Cavalli, R., Cyclodextrin-based nanosponges as drug carriers. *Beilstein journal of organic chemistry* **2012,** *8*, 2091-9.

25. Krabicová, I.; Appleton, S. L.; Tannous, M.; Hoti, G.; Caldera, F.; Rubin Pedrazzo, A.; Cecone, C.; Cavalli, R.; Trotta, F., History of Cyclodextrin Nanosponges. *Polymers* **2020,** *12* (5).

26. Vyas, A.; Saraf, S.; Saraf, S., Cyclodextrin based novel drug delivery systems. *Journal of Inclusion Phenomena and Macrocyclic Chemistry* **2008,** *62* (1), 23-42.

27. Möller, K.; Macaulay, B.; Bein, T., Curcumin Encapsulated in Crosslinked Cyclodextrin Nanoparticles Enables Immediate Inhibition of Cell Growth and Efficient Killing of Cancer Cells. *Nanomaterials* **2021,** *11* (2), 489.

28. Pivato, R. V.; Rossi, F.; Ferro, M.; Castiglione, F.; Trotta, F.; Mele, A., β-Cyclodextrin Nanosponge Hydrogels as Drug Delivery Nanoarchitectonics for Multistep Drug Release Kinetics. *ACS Applied Polymer Materials* **2021,** *3* (12), 6562-6571.

29. Shende, P.; Kulkarni, Y. A.; Gaud, R. S.; Deshmukh, K.; Cavalli, R.; Trotta, F.; Caldera, F., Acute and Repeated Dose Toxicity Studies of Different β-Cyclodextrin-Based Nanosponge Formulations. *Journal of Pharmaceutical Sciences* **2015,** *104* (5), 1856-1863.

30. Rao, M. R. P.; Chaudhari, J.; Trotta, F.; Caldera, F., Investigation of Cyclodextrin-Based Nanosponges for Solubility and Bioavailability Enhancement of Rilpivirine. *AAPS PharmSciTech* **2018,** *19* (5), 2358-2369.

31. Allahyari, S.; Valizadeh, H.; Roshangar, L.; Mahmoudian, M.; Trotta, F.; Caldera, F.; Jelvehgari, M.; Zakeri-Milani, P., Preparation and characterization of cyclodextrin nanosponges for bortezomib delivery. *Expert Opinion on Drug Delivery* **2020,** *17* (12), 1807-1816.

32. Allahyari, S.; Zahednezhad, F.; Khatami, M.; Hashemzadeh, N.; Zakeri-Milani, P.; Trotta, F., Cyclodextrin nanosponges as potential anticancer drug delivery systems to be introduced into the market, compared with liposomes. *Journal of Drug Delivery Science and Technology* **2022,** *67*, 102931.

33. Yaşayan, G.; Şatıroğlu Sert, B.; Tatar, E.; Küçükgüzel, İ., Fabrication and characterisation studies of cyclodextrin-based nanosponges for sulfamethoxazole delivery. *Journal of Inclusion Phenomena and Macrocyclic Chemistry* **2020,** *97* (3), 175-186.

34. Srivastava, S.; Mahor, A.; Singh, G.; Bansal, K.; Singh, P. P.; Gupta, R.; Dutt, R.; Alanazi, A. M.; Khan, A. A.; Kesharwani, P., Formulation Development, In Vitro and In Vivo Evaluation of Topical Hydrogel Formulation of Econazole Nitrate-Loaded β-Cyclodextrin Nanosponges. *Journal of Pharmaceutical Sciences* **2021,** *110* (11), 3702-3714.

35. Khazaei Monfared, Y.; Mahmoudian, M.; Cecone, C.; Caldera, F.; Zakeri-Milani, P.; Matencio, A.; Trotta, F., Stabilization and Anticancer Enhancing Activity of the Peptide Nisin by Cyclodextrin-Based Nanosponges against Colon and Breast Cancer Cells. *Polymers* **2022,** *14* (3), 594.

36. Mognetti, B.; Barberis, A.; Marino, S.; Berta, G.; De Francia, S.; Trotta, F.; Cavalli, R., In vitro enhancement of anticancer activity of paclitaxel by a Cremophor free cyclodextrin-based nanosponge formulation. *Journal of Inclusion Phenomena and Macrocyclic Chemistry* **2012,** *74* (1), 201-210.

37. Allahyari, S.; Esmailnezhad, N.; Valizadeh, H.; Ghorbani, M.; Jelvehgari, M.; Ghazi, F.; Zakeri-Milani, P., In-vitro characterization and cytotoxicity study of flutamide loaded cyclodextrin nanosponges. *Journal of Drug Delivery Science and Technology* **2021,** *61*, 102275.

38. Boersma, B.; Möller, K.; Wehl, L.; Puddinu, V.; Huard, A.; Fauteux-Daniel, S.; Bourquin, C.; Palmer, G.; Bein, T., Inhibition of IL-1β release from macrophages targeted with necrosulfonamide-loaded porous nanoparticles. *Journal of Controlled Release* **2022,** *351*, 989-1002.

39. Trotta, F.; Cavalli, R., Characterization and Applications of New Hyper-Cross-Linked Cyclodextrins. *Composite Interfaces* **2009,** *16* (1), 39-48.

40. Trotta, F.; Tumiatti, W. Cross-linked polymers based on cyclodextrin for removing polluting agents. 2005.

41. Hermanson, G. T., *Bioconjugate Techniques*. 2nd Edition ed.; Elsevier: 2008.

42. Wenz, G.; Han, B.-H.; Müller, A., Cyclodextrin Rotaxanes and Polyrotaxanes. *Chemical Reviews* **2006,** *106* (3), 782-817.

43. Beauchamp, C. O.; Gonias, S. L.; Menapace, D. P.; Pizzo, S. V., A new procedure for the synthesis of polyethylene glycol-protein adducts; Effects on function, receptor recognition, and clearance of superoxide dismutase, lactoferrin, and α2-macroglobulin. *Analytical Biochemistry* **1983,** *131* (1), 25-33.

44. Lo Meo, P.; Mundo, F.; Terranova, S.; Conte, P.; Chillura Martino, D., Water Dynamics at the Solid–Liquid Interface to Unveil the Textural Features of Synthetic Nanosponges. *The Journal of Physical Chemistry B* **2020,** *124* (9), 1847-1857.

4.6. Appendix

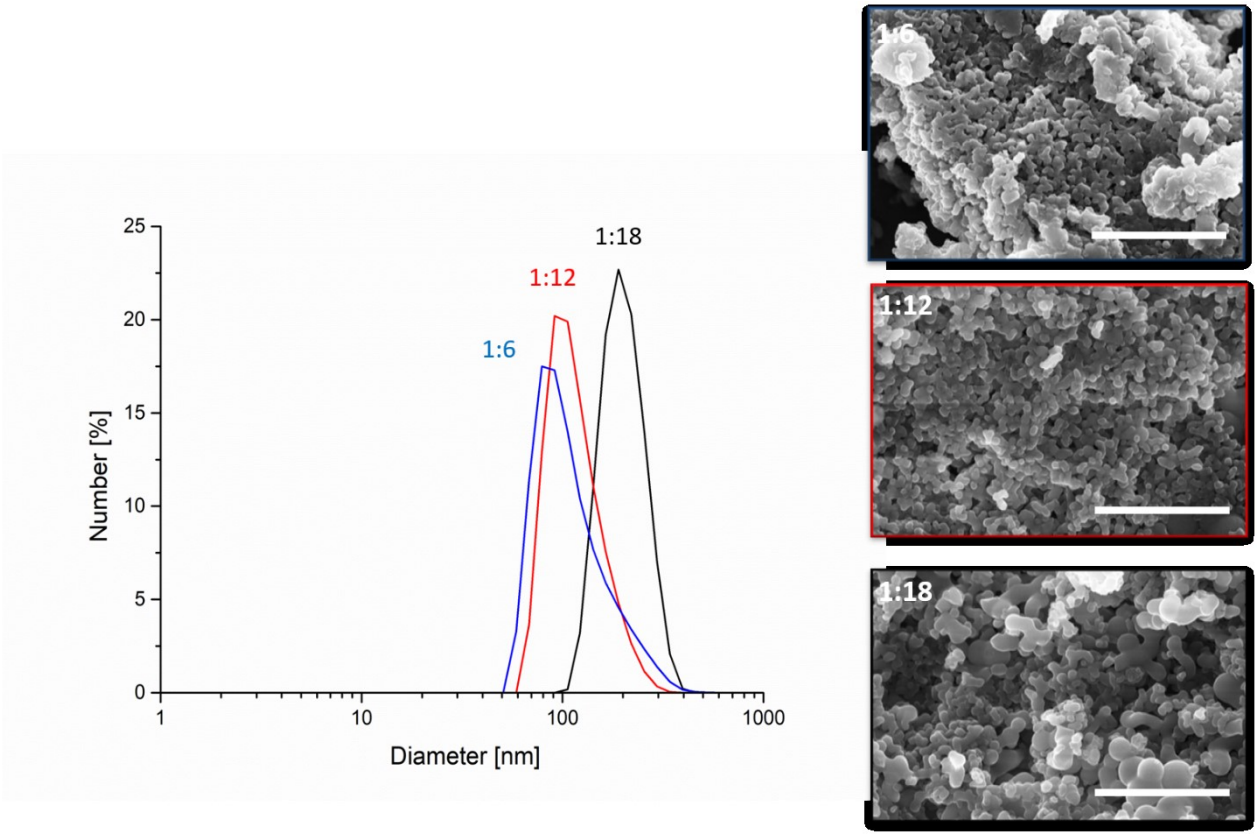

Figure S4.1. DLS in water (left side) and SEM measurements (right side) of unPEGylated β-CD-CDI nanoparticles prepared with CD:CDI molar ratios of 1:6 (blue), 1:12 (red) and 1:18 (black). Scale bars on SEM images: 3 µm

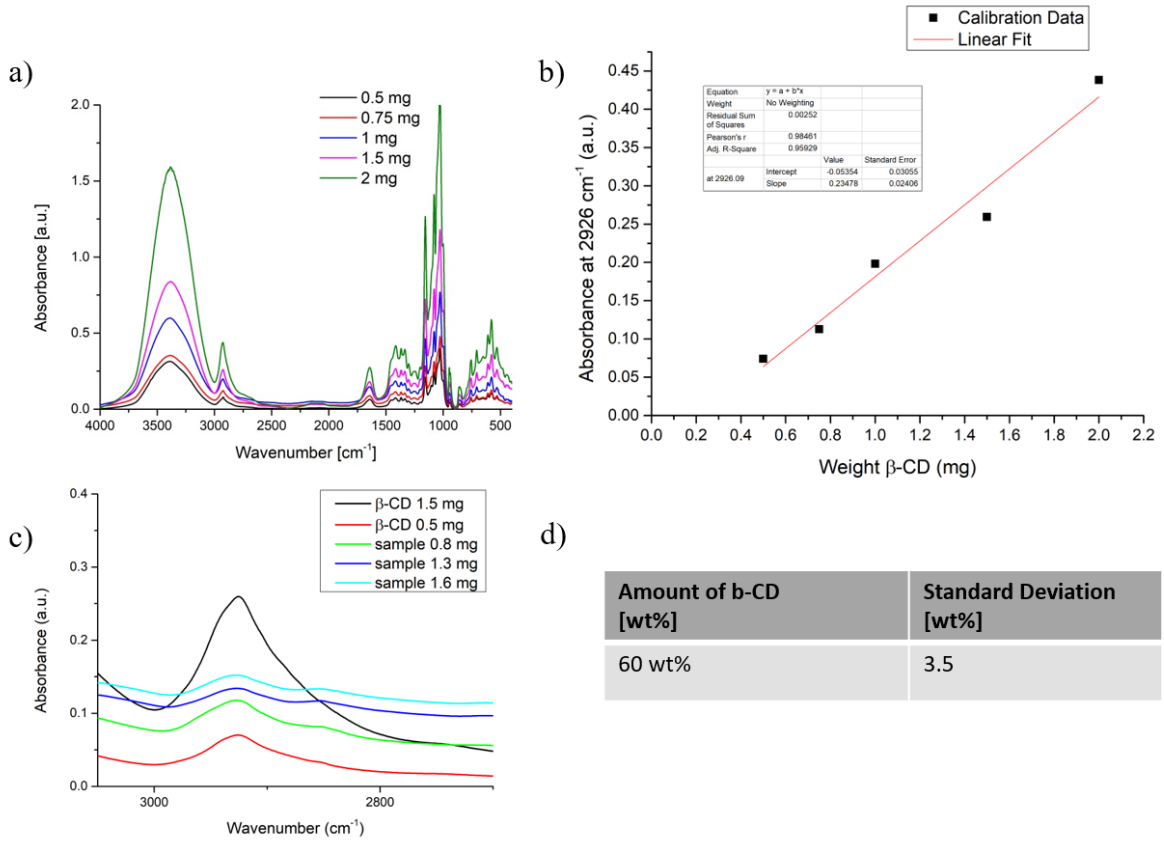

Amount of b-CD [wt%]	Standard Deviation [wt%]
60 wt%	3.5

Figure S4.2.FTIR calibration to determine the amount of β-CD in unPEGylated β-CD-CDI NP. a) IR spectra of increasing amounts of pelleted β-CD precursor. Respecting amounts of β-CD (0.5-2 mg) were mixed with KBr, until a final mass of 200 mg was reached to further press KBr pellets. b) Resulting calibration curve using the C-H vibration at 2926 cm^{-1} c) IR spectra of β-CD-CDI samples prepared with CD:CDI molar ratio of 1:12. FTIR measurements were conducted using three different KBr pellets from the same β-CD-CDI stock samples. Different amounts of the sample (0.8 mg, 1.3 mg and 1.6 mg (green, blue and turquoise line, respectively) were mixed with KBr, until a final mass of 200 mg was reached to further press KBr pellets. For visualization in Figure S4.2 c) the FTIR spectra of the samples are depicted in comparison to the spectra of β-CD with known mass (black and red line) in the wavenumber range around 2926 cm^{-1}. d) Results of the calculations based on the calibration curve.

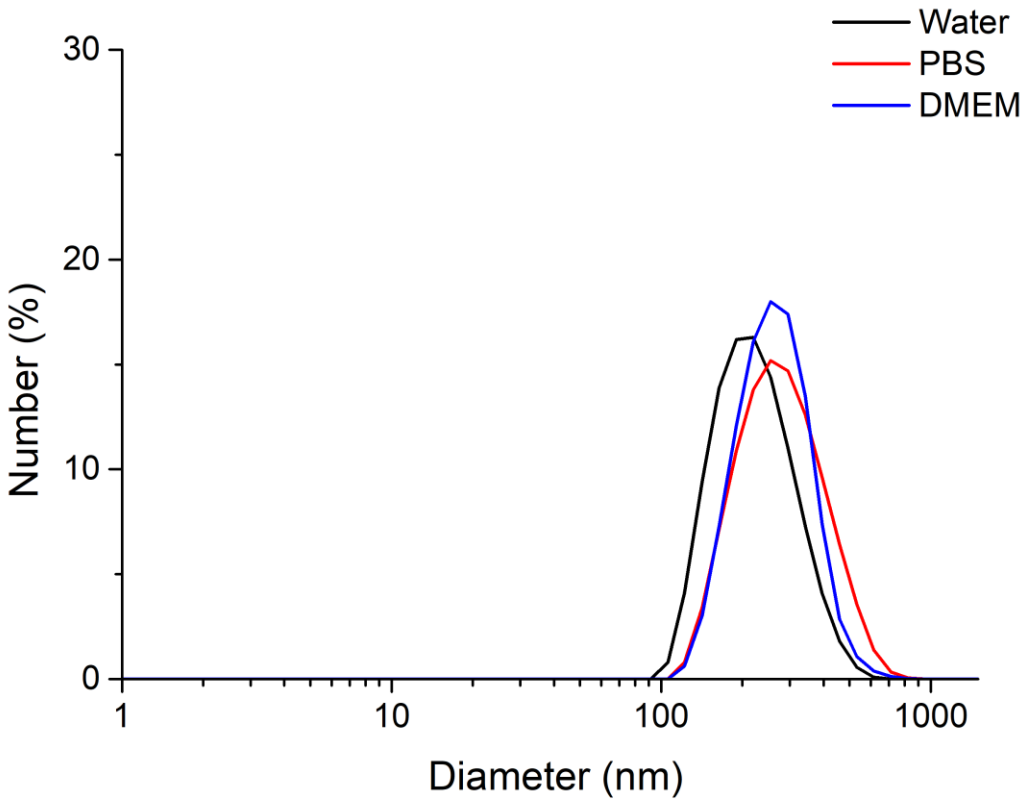

Figure S4.3. DLS measurements of sample β-CD-CDI-PEG in aquoues solution at pH 7 (black line), in PBS buffer at pH 7.4 (red line), and in FluoroBrite DMEM cell culture medium at pH 7.4 (blue line).

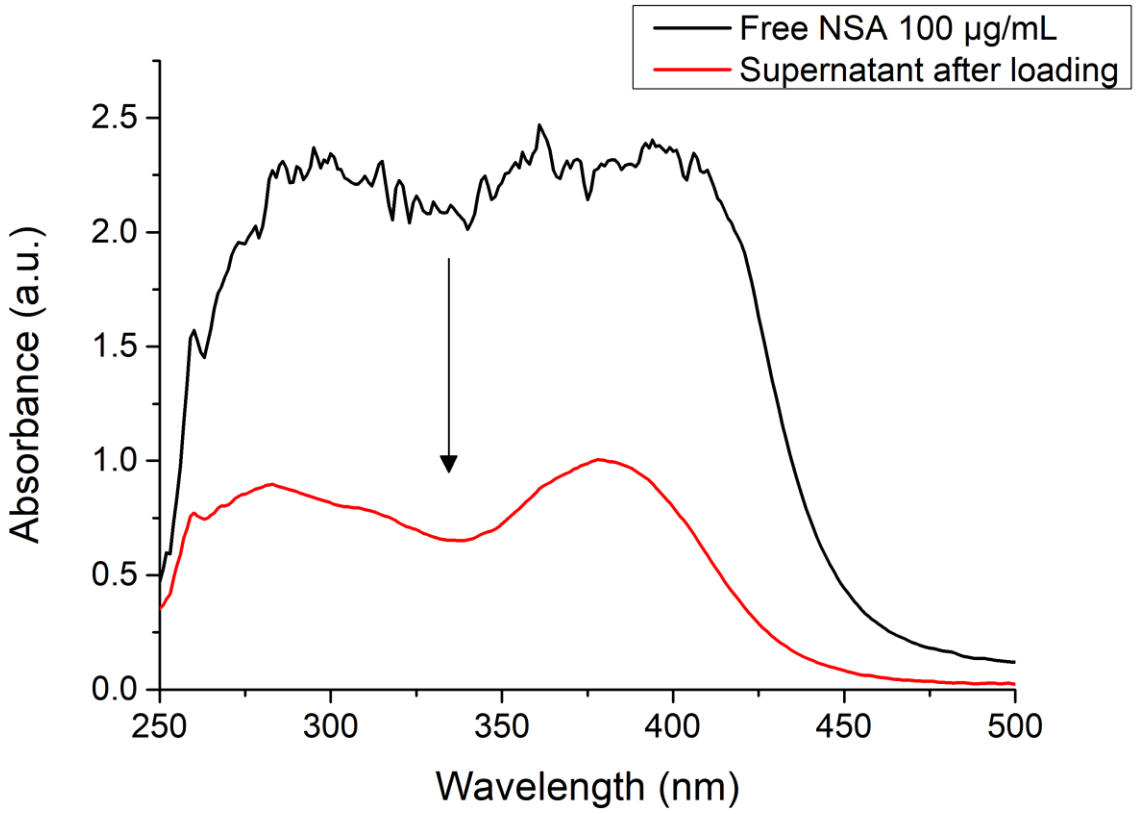

Figure S4.4. UV-Vis spectra used to follow uptake of NSA into β-CD-CDI-PEG NP. Black curve: UV-Vis spectrum of free NSA at a concentration of 100 µg/mL. For loading the NP, an even higher concentration of 200 µg/mL was used. The lower concentration of 100 µg/mL is depicted here for visualization because it is already at the upper detection limit. Red curve: The supernatant after loading the nanoparticles. NSA-loaded NP were centrifuged down and the supernatant with residual NSA was analyzed to determine the nanoparticle loading by difference.

CHAPTER 5

Inhibition of IL-1β Release from Macrophages Targeted with Necrosulfonamide-loaded Porous Nanoparticles

5. Inhibition of IL-1β Release from Macrophages Targeted with Necrosulfonamide-loaded Porous Nanoparticles

This chapter was published as:

Bart Boersma[§], Karin Möller[§], Lisa Wehl[§], Viola Puddinu, Arnaud Huard, Sébastien Fauteux-Daniel, Carole Bourquin, Gaby Palmer, Thomas Bein *Journal of Controlled Release* **2022**, *351*, 989-1002.

[§] These authors contributed equally.

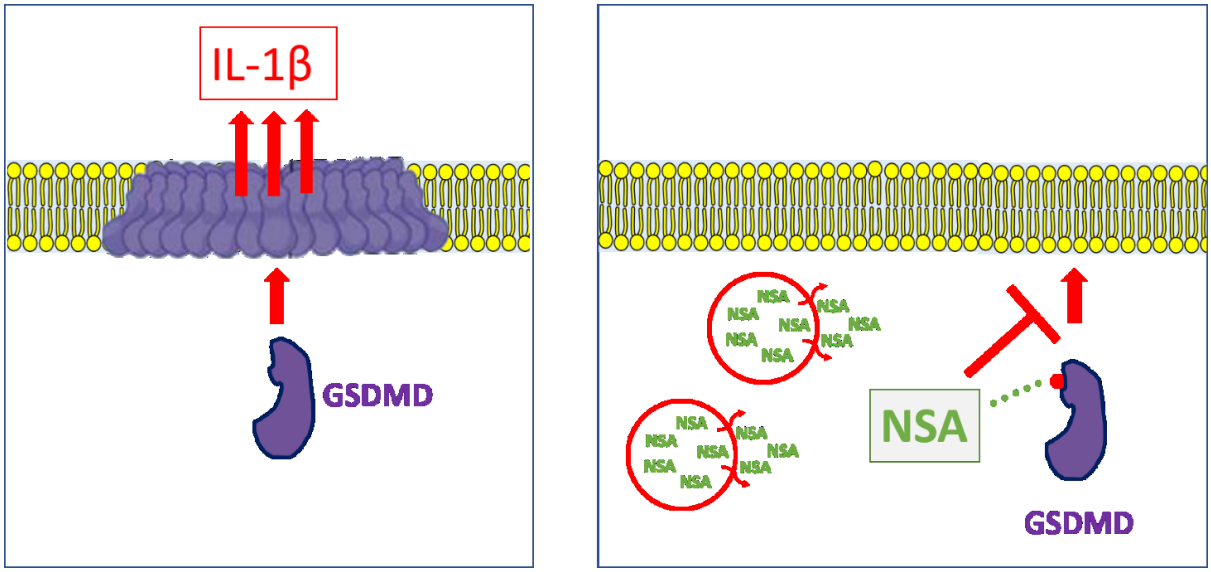

Abstract

Inflammation is required for protective responses against pathogens and is thus essential for survival, but sustained inflammation can lead to diseases, such as atherosclerosis and cancer. Two important mediators of inflammation are the cytokines IL-1β and IL-18, which are produced by myeloid cells of the immune system, including macrophages. These cytokines are released into the extracellular space through pores formed in the plasma membrane by the oligomerized protein gasdermin D (GSDMD). Necrosulfonamide (NSA) was recently identified as an effective GSDMD inhibitor and represents a promising therapeutic agent in GSDMD-dependent inflammatory diseases. Here, we targeted NSA to both mouse and human macrophages by using three different types of porous nanoparticles (NP), i.e. mesoporous silica (MSN), porous crosslinked cyclodextrin carriers (CD-NP), and a mesoporous magnesium-phosphate carrier (MPC-NP), all displaying high loading capacities for this hydrophobic drug. Cellular uptake and intracellular NSA delivery were tracked in time-lapse experiments by live-cell, high-throughput fluorescence microscopy, demonstrating rapid nanoparticle uptake and effective targeted delivery of NSA to phagocytic cells. Notably, a strong cytostatic effect was observed when a macrophage cell line was exposed to free NSA. In contrast, cell growth was much less affected when NSA was delivered via the nanoparticle carriers. Utilizing NSA-loaded nanoparticles, a successful concentration-dependent suppression of IL-1β secretion from freshly differentiated primary murine and human macrophages was observed. Functional assays showed the strongest suppressive effect on human macrophages when using CD-NP for NSA delivery, followed by MSN-NP. In contrast, MPC-NP completely blocked the metabolic activity in macrophages when loaded with NSA. This study demonstrates the potential of porous nanoparticles for the effective delivery of hydrophobic drugs to macrophages in order to suppress inflammatory responses.

5.1. Introduction

Inflammation is a physiological response of the organism that is essential for the defense against pathogens. However, chronic inflammation can be detrimental for many diseases, including cardiovascular and autoimmune disorders, as well as different types of cancer.[1, 2] Two major mediators of inflammation are the cytokines interleukin (IL)-1β and IL-18, which are released from immune cells, such as macrophages, upon activation by danger signals from pathogens or by endogenous stress signals. The release of these cytokines can trigger and sustain inflammatory processes throughout the body.[1, 3]

The release of IL-1β and IL-18 from immune cells is the result of a sequential process illustrated in Scheme 5.1a. First, the detection by sensor proteins of bacterial or viral components, which function as danger signals, triggers a cascade of intracellular events leading to the activation of caspase-1 by proteolytic cleavage. Activated caspase-1 is in turn able to cleave several other proteins, including the proforms of IL-1β and IL-18 and the pore-forming protein gasdermin D (GSDMD).[4, 5] GSDMD cleavage liberates its N-terminal domain, which oligomerizes to form a 10–14 nm pore that inserts into the plasma membrane.[6, 7] Ultimately, GSDMD-mediated pore formation allows the release of pro-inflammatory mediators, such as IL-1β, IL-18, high mobility group box 1 (HMGB1) and adenosine triphosphate (ATP) and results in a form of inflammatory cell death termed pyroptosis.[8]

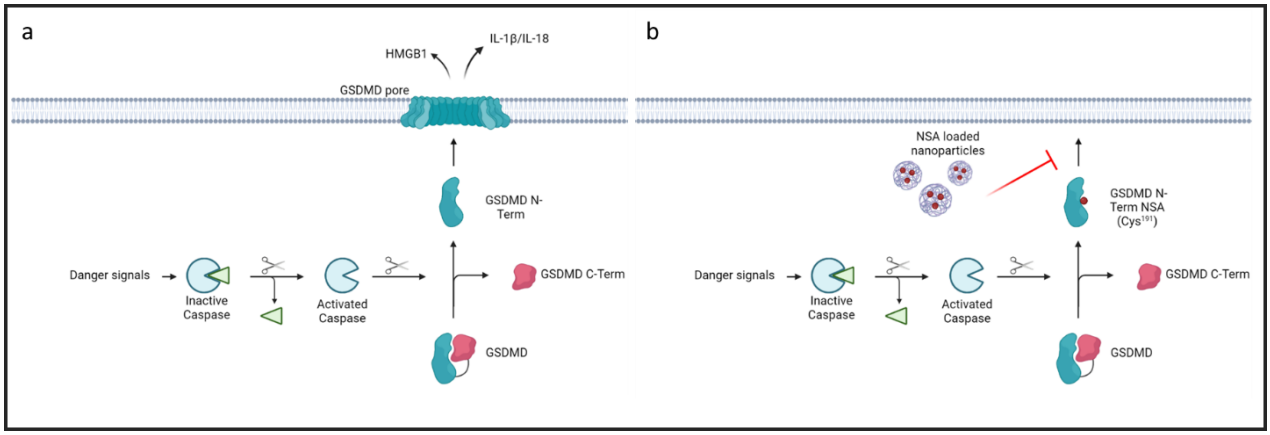

Scheme 5.1 Schematic overview of the GSDMD activation mechanism resulting in transmembrane pore formation and cytokine release (a) and its blocking through particle-delivered NSA (b).

Recently, high-throughput screening efforts have identified two GSDMD pore formation antagonist molecules, disulfiram and necrosulfonamide (NSA); see Figure 5.2 for the structure of NSA.[9-11] NSA inhibits GSDMD pore formation by binding directly to Cys191 of human GSDMD or to Cys192 of mouse GSDMD.[10] By preventing pore formation, NSA inhibits the release of pro-inflammatory mediators such as IL-1β (Scheme 1b). NSA thus represents a promising new effector molecule against GSDMD-dependent inflammation. However, the extremely hydrophobic nature of this molecule complicates drug administration *in vivo* since it requires the use of potentially toxic organic solvents. Furthermore, NSA has demonstrated toxicity towards immune cells and, as a small molecule, may present less than ideal pharmacokinetic behavior within the organism.[12]

To overcome limitations with respect to limited stability, unfavorable pharmacokinetics and the potential toxicity of small (hydrophobic) molecular delivery, different nano-carrier systems have been developed over the years.[13] These are made of organic materials such as polymers, micelles and liposomes or consist of solid/porous inorganic materials. Especially porous nanocarriers have evolved as promising drug-carrier systems because they allow for an internal encapsulation of small molecular drugs within the host as opposed to an attachment onto the

surface of solid nanoparticles (NP). In this way, toxicity issues or a premature degradation of attached molecules can be avoided. Mesoporous silica NP are a prominent class of porous carrier systems, which have proven to be effective delivery agents for a broad range of applications, including cancer (immuno)-therapy, combination drug delivery or gene delivery.[14-20] Similarly, cyclodextrins[21] and crosslinked cyclodextrin-based NP[22, 23] show a high capacity to encapsulate both hydrophobic and hydrophilic drugs and were found to improve the solubility of poorly water-soluble molecules.[24]

In this work, we explore for the first time the feasibility of targeting NSA to macrophages with porous NP. In addition to their ability to initiate inflammation, an essential function of macrophages is their capacity to engulf particulate material such as bacteria or dying cells by phagocytosis.[25] We have taken advantage of this specialized function by using NP as vehicle to deliver NSA specifically to macrophages and other phagocytic cells. We show that the exposure of murine and human macrophages to these NSA-loaded carriers enables a solvent-free NSA delivery that inhibits release of proinflammatory IL-1β. Three in-house developed nanocarriers featuring different composition and structure were evaluated in this study. The nanocarriers comprise mesoporous silica nanoparticles (MSN), our newly developed covalently crosslinked cyclodextrin NP (CD-NP) and recently established mesoporous magnesium phosphate NP (MPC).[26] The efficacy of NP cellular uptake, NSA delivery and toxicity were studied using a macrophage cell line and primary mouse splenocytes. Murine bone marrow-derived macrophages (BMDM), as well as human monocyte-derived macrophages (MDM) were then used to evaluate the efficacy of cytokine suppression upon NSA delivery. Overall, we demonstrate that a high NSA loading capacity is reached with our nanocarrier systems and that NSA delivery is successful and efficient with several of the carriers, as established by a concentration-dependent suppression of the GSDMD-mediated

release of IL-1β. Importantly, the toxicity of NSA towards immune cells is strongly reduced by NP delivery.

5.2. Results and Discussion

Synthesis and characterization of nanoparticles

Three different materials were evaluated for their ability to efficiently deliver NSA to immune cells. All porous nanocarriers used in this project are biocompatible and were chosen for their beneficial properties regarding a sustained, solvent-free drug delivery. The robust NP stability often allows for a storage in ethanolic solutions for years and thus potential "off-the-shelf" applications. Nevertheless, such NP are completely degradable under drug-delivery conditions, as established, for example, for mesoporous silica NP (MSN).[27, 28] Their large surface areas and the presence of mesopores are suitable for the uptake of large amounts of NSA into their internal cavities. All NP used here were synthesized with or without a lipid bilayer consisting of a cationic dioleoyl-containing lipid mixture (DOTAP/DOPC, DD). This was done for two reasons: a) to study its impact on cell uptake, and b) to provide a shield against premature drug release.

The first class of materials used in this study, MSN, has been continuously developed in our group over the years and was used in diverse biomedical applications based on their exceptional flexibility with respect to particle and pore size, as well as NP composition and molecular functionalization.[29, 30] For the adsorption of the hydrophobic molecule NSA, we synthesized core-shell MSN consisting of a silica core functionalized with 5 wt% of a phenylsilane precursor in order to create a hydrophobic interior. The outer MSN surface was then co-condensed with 2 wt% mercaptopropyl-triethoxysilane to create a negatively charged particle surface decorated with mercapto-groups for future fluorophore attachment or bilayer adhesion. These particles have an average size of about 80 nm based on transmission electron microscopy (TEM) (see Figure 5.1a, b) and a hydrodynamic particle size of around 245 nm in water as measured by dynamic light scattering (DLS; see SI Table S5.1). A large surface area of 1098 m^2/g was determined with nitrogen sorption. A relatively small pore size of 3.4 nm with a pore

volume of 0.75 cm^3/g was implemented here to best fit the dimensions and diffusive transport of the small NSA guest molecules (Figure 5. 1c, d).

The second class of materials consists of new cyclodextrin-based nanoparticles (CD-NP). Cyclodextrin-based materials have been used as carriers for anti-inflammatory drugs before.[31] Pioneering work creating crosslinked cyclodextrin 'nanosponge' materials was performed by the group of Trotta, who used carbonyl- or dicarboxylate-based linker molecules.[32, 33] Here, we synthesized nanoparticles of cyclodextrin by covalently cross-linking □-cyclodextrin with carbonyldiimidazole (CDI) in dimethylformamide (DMF). These particles were subsequently stabilized by addition of polyethylene glycol (PEG). The NP were finally precipitated with water, resulting in NP with a controlled particle size distribution and a hydrodynamic diameter of around 195 nm in water (DLS). The dried powder shows a particle size of 90 nm in the scanning electron microscope (SEM; Figure 5. 1e, f). Cyclodextrin NP are promising materials because they offer small integrated cavities of 0.7 nm with hydrophobic character originating from the β-CD molecular subunits. By crosslinking these units with spacer molecules such as tetrafluoroterephthalonitrile (TFTN) or CDI, nanoparticles with added interstitial adsorption sites are generated.[34] This creates space for additional guest adsorption, thus expanding the molecular capacity of the CD entities as recently demonstrated with related β-CD-TFTN NP for the adsorption of hydrophobic curcumin.[35] The high adsorption capacity of CD-CDI NP becomes apparent upon NSA loading (please consult the Supplemental Information (SI) for further details of materials synthesis and characterisation). We have also evaluated NSA delivery with the mentioned TFTN crosslinked CD-NP (CD-TFTN-NP). Although NSA delivery was successful with this carrier system, cellular toxicity was observed already in the unloaded state (data not shown). We therefore concentrated our efforts on the alternative cyclodextrin NP crosslinked via CDI -linker (CD-NP).

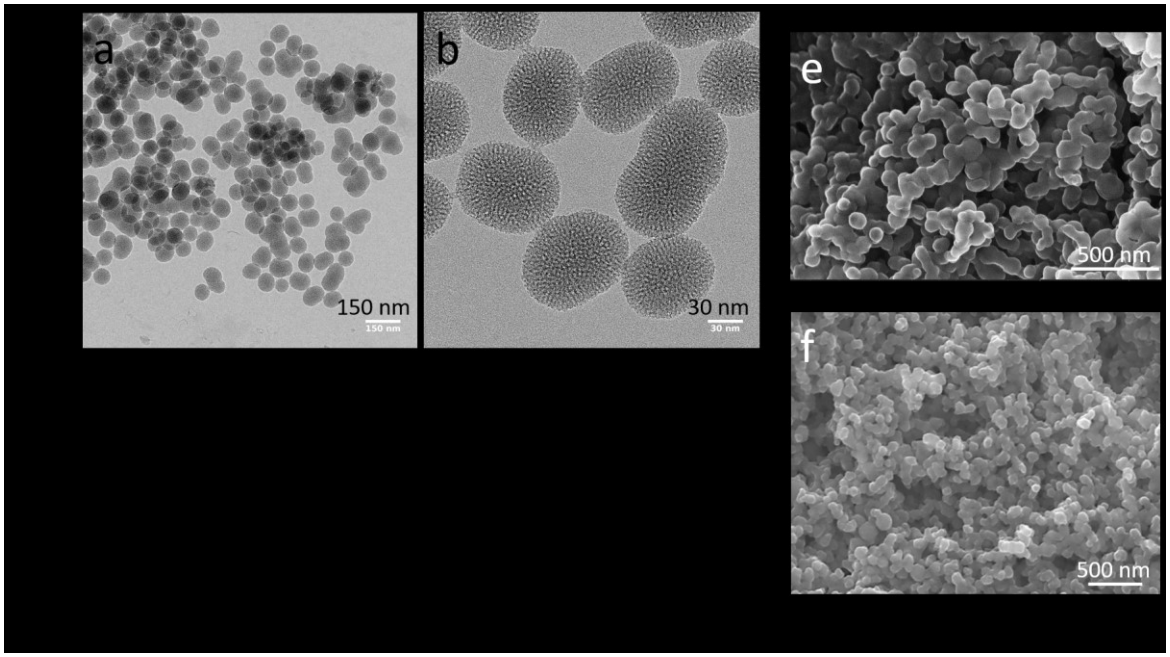

Figure 5.1 MSN, CD- and MPC-NP materials characterization. a,b) TEM images of MSN, c,d) MSN nitrogen sorption isotherm and pore size distribution. e) SEM images of CD-CDI-NP, f) SEM images of MPC-NP.

The third material is composed of completely biogenic magnesium phosphate citrate NP (MPC-NP). We recently showed that a cetyltrimethylammonium (CTAC)-templated precipitation method resulted in evenly sized MPC NP of around 80 nm diameter (SEM).[36] Nitrogen sorption established a high surface area of 560 m^2/g of template-extracted particles and most importantly, a high pore volume of 0.8 cm^3/g originating from pores of 6.3 nm. These particles are stable at neutral to basic conditions when coated with a DOTAP/DOPC lipid bilayer, however, are completely biodegradable under acidic conditions at pH 5.5.

In the following, we will describe cellular interactions with MSN carriers in more detail and refer to the other carrier systems where applicable.

Porous NP show high loading capacities for NSA

The uptake of NSA into the pores of the different carriers is conveniently followed by UV-VIS spectroscopy. NSA displays a prominent absorption band at 377 nm (see SI, Figure S5.1) that

allows one to determine the uptake by difference calculation regarding the NSA amounts offered in solution. Loading efficiencies (amount taken up vs. amount offered) calculated after extensive washings were usually high for all materials, ranging from 80 to 95%. When a standard amount of 200 µg NSA was offered to 1 mg of carrier, an uptake between 16-19 wt% was reached. Samples with this loading level were used for all cell experiments for comparability. In principle, however, it is possible to increase the loading capacity up to 49 wt% in MSN, up to 29% in CD-NP or up to 32 wt% in MPC-NP.

The rapid and nearly complete absorption of NSA into the MSN carrier was indicated when the light-yellow suspension of MSN and added NSA was centrifuged. A yellow cake and a nearly clear supernatant were obtained (see SI, Figure S5.2). UV-Vis analysis confirmed that most of the NSA had been adsorbed, even after a short exposure time of 30 minutes. Spectroscopic evidence of the NSA uptake was further obtained with FT-Raman spectroscopy (Figure 5.2). In contrast to FTIR spectroscopy that showed only very weak additional signals of NSA in the MSN NP, prominent Raman signals were obtained due to the phenyl, thiophene, pyrazine as well as the sulfoxide groups present in NSA (purple trace in Figure 5.2). While MSN particles (blue) show weak Raman scattering, strong peaks were observed from NSA in MSN. In addition, NSA-MSN show significant shifts in position as well as relative intensity with respect to the solid NSA precursor, pointing to strong interactions with the internal MSN surface.

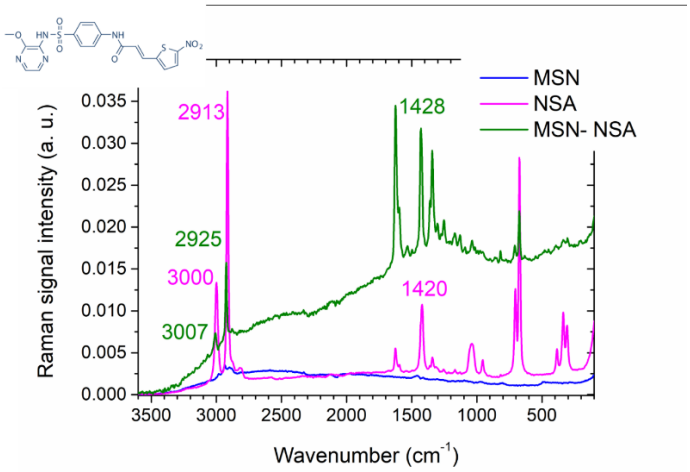

Figure 5.2 FT-Raman spectroscopy of the carrier MSN (blue), NSA powder (purple) and NSA absorbed in MSN (green).

The apparent dimensions (hydrodynamic diameter) of the NP when measured in solution are dependent on the dispersing agent and are least influenced in an ethanolic solution. For instance, for unloaded MSN, we observe a particle size of 140 nm in ethanolic solution that increases to 245 nm in aqueous solution. CD-NP have a particle size of 195 nm in water, yet the measured particle size of dry CD-NP is 90 nm as obtained by SEM. However, even after loading with NSA, the application of a lipid bilayer (coded DD = DOTAP/DOPC), or after addition of a fluorophore for imaging, hydrodynamic diameters were all around 200 nm or below (see Figure 5.3 as well as SI Figure S5.3 and Table 5.1). These dimensions are suitable for cell experiments, where NP samples with and without a lipid bilayer were used to study their cellular uptake.

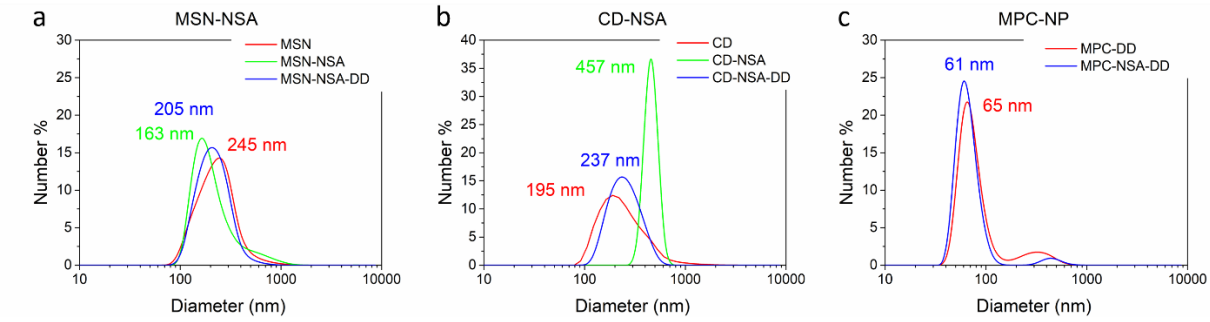

Figure 5.3 Dynamic light scattering (DLS) curves of NSA-loaded samples in water with and without a lipid bilayer (DD), a) MSN, b) CD and c) MPC NP.

Following the absorption of NSA, MSN samples with or without a lipid bilayer were examined regarding spontaneous NSA release in different media. No release was measurable by UV-Vis spectroscopy when samples were dispersed in aqueous solution and stirred for 1 h at pH 7 or pH 5. Even in cell medium (fluobrite DMEM) or medium containing 10% of fetal bovine serum (FBS) the release was minimal with or without a lipid bilayer, ranging between 2-5% of the absorbed NSA (see SI, Figure S5.4). We can therefore assume that no significant premature release would occur in cell experiments with these NP even without a lipid bilayer.

Rapid phagocytosis of NSA-loaded nanoparticles and fast release of NSA in a murine macrophage cell line

First, we examined the rate of uptake of unloaded MSN-NP in the murine macrophage cell line RAW 264.7. In order to follow the uptake by fluorescence microscopy, we labeled the particles with a red fluorophore resulting in MSN-633 NP. RAW 264.7 cells seeded in a 96-well plate were placed into an environmental chamber located directly within the microscope. Cells were kept at 37 °C and 5% CO_2 atmosphere to perform time-lapse measurements every 3 minutes

over 3 h. Images were obtained at a 40x magnification. Selected time intervals are shown in Figure 5.4 (transmitted light and red fluorescence channel). The first image was collected as soon as possible after NP addition, after about 3 minutes. Strikingly, MSN particles were almost immediately associated with cells. NP were clearly seen around the cells, close to the cell wall, directly after sample addition. Accumulation of additional particles within the cells was observed continuously with time, with particles moving deeper into the cellular interior. No particles were observed in the nucleus at any time. No additional particle uptake was observed by visual inspection after about 60 minutes. Following cell division, particles were still detected in daughter cells, albeit at apparently lower amounts per cell, as expected (see SI, Figure S5.5).

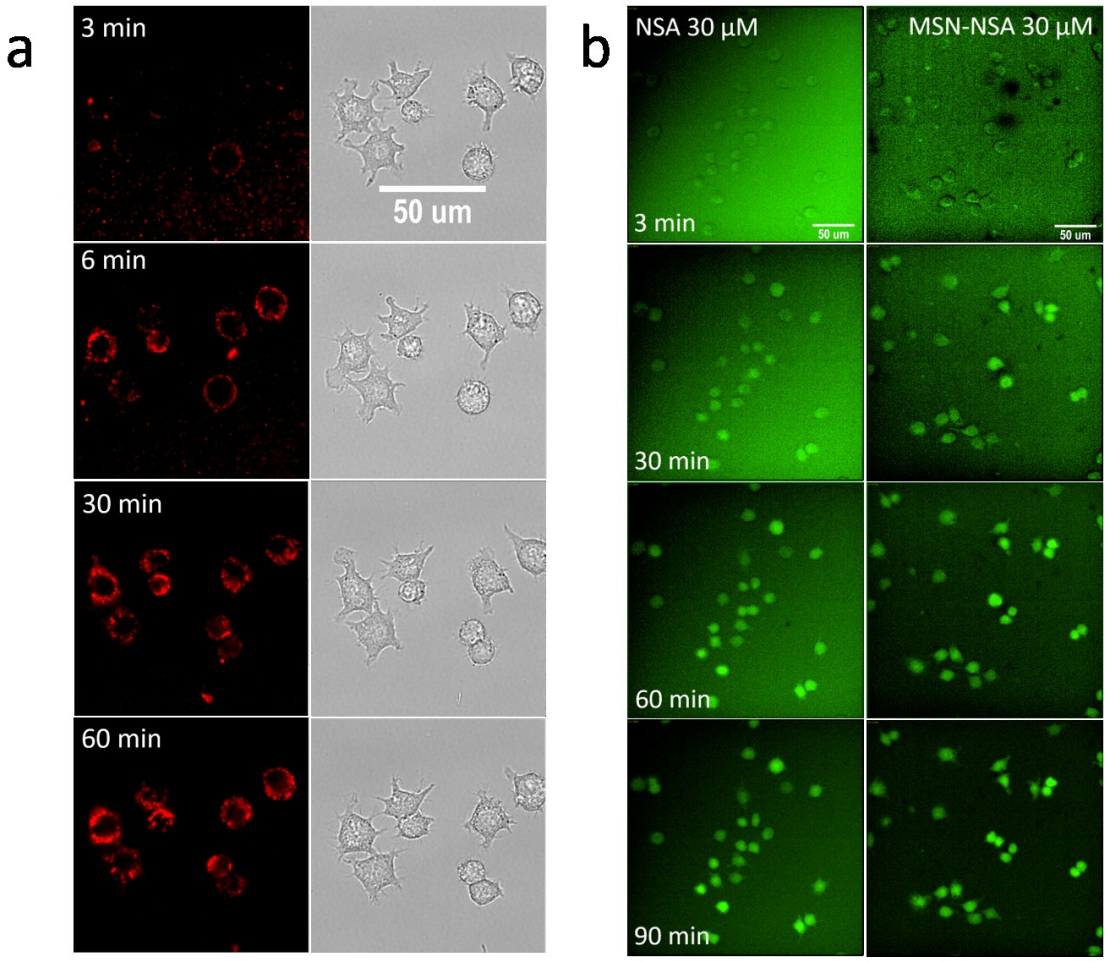

Figure 5.4 a) Time-lapse images of RAW 264.7 cells directly after exposure to ATTO-633-labeled MSN (red) NP (40x, transmitted light and CY5 channel). b) Time-lapse images of RAW 264.7 cells directly after exposure to

free NSA (left column) or to NSA-loaded MSN-particles of corresponding NSA concentration (right column). NSA was detected in the GFP channel (20x).

Having established a very rapid uptake of the unloaded MSN NP in this macrophage cell line, we examined the rate of NSA delivery by means of MSN carriers. Comparable imaging experiments were thus performed with either NSA-loaded MSN NP or with free NSA at the same nominal concentrations. As shown in Figure 5.4b, we observed an increase in green fluorescence originating from the accumulation of NSA in RAW 264.7 cells. Visible evidence of NSA appeared after about 30 minutes and increased in intensity up to about 90 minutes. No major difference in time of uptake was noticed between free NSA and NSA originating from MSN particles. We noticed that NSA started to fluoresce only after accumulating intracellularly. Further, we observed that the NSA was distributed in the cytosol as well as in the nucleus (for higher magnification see SI, Figure S5.6).

When the NSA-loaded CD-NP were studied in RAW 264.7 cells, we encountered a comparable time scale of NSA delivery as with MSN particles. While first indications for NSA uptake appeared already after 10 minutes, an evenly distributed green fluorescence in the cytosol was again encountered after 30 minutes. This fluorescence increased in intensity for up to 2 h as seen before. We noticed a difference between MSN and CD NP accumulation in the cells: while MSN NP were readily and strongly taken up by the RAW 264.7 as discussed above, apparently fewer CD NP were encountered within the cells after 2 h incubation. Evidence for NSA delivery with ATTO-633 labeled CD NP, as well as for the cellular uptake as observed with confocal microscopy can be found in the Supplemental information (see SI, Figure S5.7). In summary, NSA delivery into cells occurs on a similar time scale with free NSA as well as through NP delivery. Since a premature release of NSA from MSN-NP into aqueous phases was not observed as described above, and having established a very rapid phagocytosis/membrane attachment of the nanoparticles, we propose that the intracellular NSA

release from the nanoparticles occurs via diffusion along concentration gradients, driven by the lipophilic character of NSA upon contact with lipophilic intracellular components.

Assessment of the toxicity/compatibility of nanoparticles and NSA in a macrophage cell line: unloaded and NSA-loaded nanoparticles are better tolerated than free NSA

The compatibility of NSA-loaded NP carriers with macrophages was tested on the murine RAW 264.7 macrophage cell line with MSN NP in long-term exposure experiments. Cell growth of the macrophages was monitored using a lensless “Cellwatcher” imaging device. Growth curves of untreated and particle-loaded RAW 264.7 cells were obtained by following the confluency in single wells of a 24-well plate continuously up to about 30 h after NP exposure without medium change. Figure 5.5a shows a steady increase in confluency of untreated RAW 264.7 cells over time, represented by the black curve. This graph is mirrored by growth curves of cells treated with either unloaded MSN (purple trace) or NSA-loaded MSN, reflecting a 20 μM or 30 μM NSA concentration (blue and green traces). These results establish that the cells are not compromised in their growth kinetics by the presence of these nanocarriers. Corresponding measurements on RAW 264.7 cells were made with comparable concentrations of free NSA. Here, NSA was added in form of aqueous suspensions derived from a DMSO stock solution. A steady increase of cell proliferation was also observed for these samples, however, displaying slower growth kinetics (Figure 5.5b). Thus, free NSA inhibits cell proliferation compared to untreated control cells.

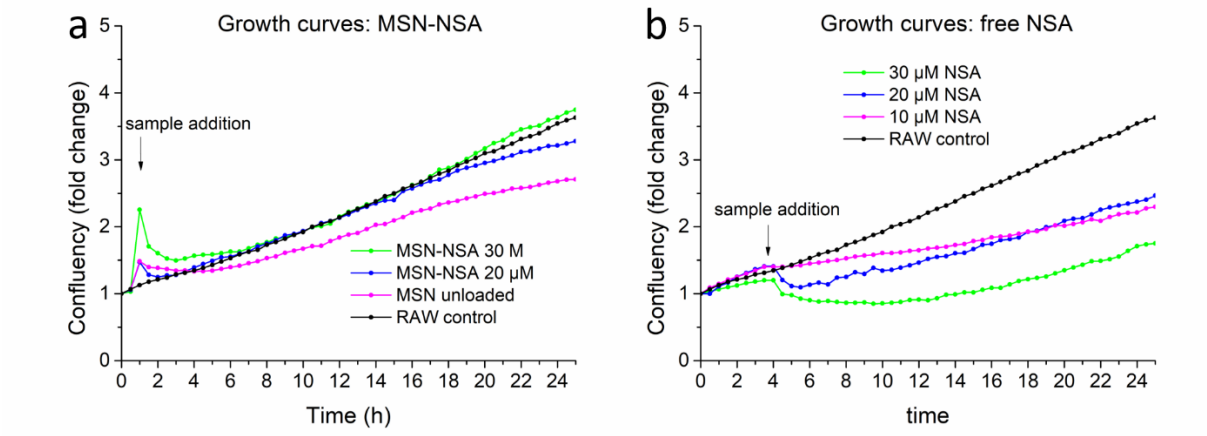

Figure 5.5 Compatibility test of RAW 264.7 cells for free NSA and NSA loaded into MSN. Normalized confluency of RAW 264.7 cells in time as measured with a Cellwatcher, a) MSN-exposed cells, growth curves of untreated cells (black trace), cells exposed to unloaded MSN (purple) and MSN-NSA samples (20 µM NSA, blue; 30 µM NSA green. b) free NSA exposed cells, growth curves of untreated cells (black) and cells exposed to increasing concentration of DMSO-derived NSA: 10 µM (purple), 20 µM (blue) and 30 µM (green). Growth curves were normalized to the initial confluency (observed to be around 20%).

Corresponding endpoint images taken after 45 h confirm the greater negative impact of free NSA on cell growth kinetics (see SI, Figure S5.8) Notably, all cells were alive at this point and the successful delivery of NSA into the cells was evidenced by the green fluorescence of NSA in all cells (see SI, Figure S5.9).

Having established a successful NSA delivery with the NP carrier systems and preserved cell growth following NP exposure, we quantified the metabolic activity of RAW cell response to the unloaded and NSA-loaded carriers. For this we used incubation times of 45 h without performing a medium change.

RAW 264.7 cells were exposed to the different NP, that is, MSN, CD and MPC-NP with increasing concentrations and metabolic activity was measured by an MTT assay. None of the three unloaded carriers showed a substantial impact on metabolic activity up to 100 µg carrier/mL. The particles were also applied with or without a lipid bilayer of DOTAP/DOPC (DD, see Figure 5.6 a,b).

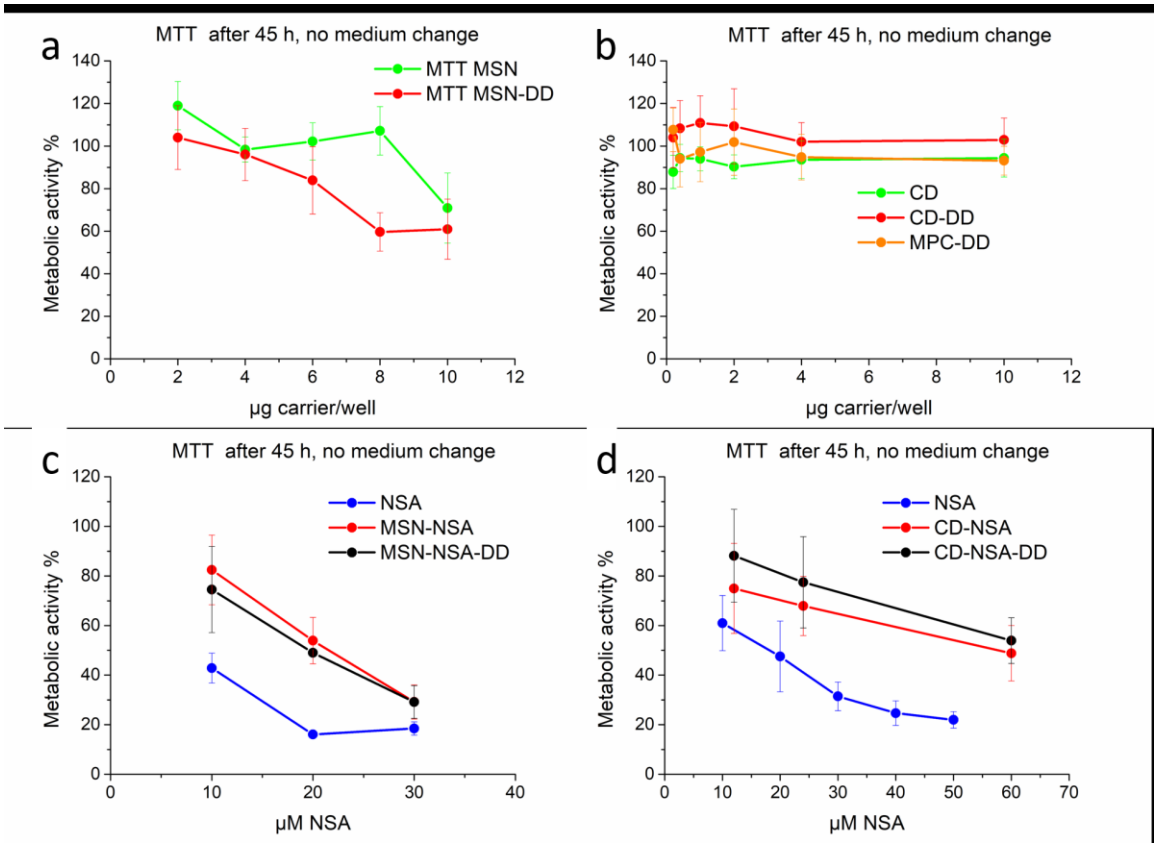

Figure 5.6 Assessment of RAW 264.7 cell survival after long incubation times of 45 h without medium change with unloaded and NSA-loaded NP in comparison to exposure to free NSA. a,b) MTT assay of unloaded MSN, CD and MPC particles with and without a lipid bilayer (DD), c,d) MTT assay of MSN and CD NP loaded with NSA. Results are expressed in % as compared to untreated cells.

We also tested the RAW 264.7 metabolic cell activity under comparable conditions with NSA-loaded carriers. In Figure 5.6 c,d we compared the impact of NSA-loaded MSN and CD carriers with and without a lipid bilayer to that of the free NSA compound at increasing concentrations. A decrease in cell activity was observed with increasing NSA concentrations for both particles. However, cell metabolism was less inhibited by particle-delivered NSA than by the same amount of free NSA. This decreased cell activity was not associated with increased cell death, as observed by live microscopy (See SI, Figure S5.11).

In contrast, NSA-loaded MPC-NP completely blocked metabolic activity in RAW 264.7 macrophages already at low NSA concentrations under these conditions. Loading of these MPC particles with NSA required the addition of small concentrations of the surfactant

cetyltrimethylammonium chloride (CTAC), which may be detrimental for RAW 264.7 cell survival (see SI, Figure S5.10).

We also examined NSA delivery under the more realistic condition of a shorter exposure time as likely encountered in in vivo situations and performed a medium exchange after 3 h, while the final assay was again performed after 45 h. Under these less severe exposure conditions, we did not observe any influence on metabolic cell activity with either MSN-NSA NP or free NSA (see SI, Figure S5.12).

Porous nanoparticles are taken up by primary macrophages and are not toxic

Having established that NP delivery of NSA to a macrophage cell line is successful and better tolerated by the cells than the free compound, we examined whether particles were taken up in primary macrophages. To this end, macrophages were differentiated either from freshly isolated murine bone marrow (bone marrow-derived macrophages, BMDM) or from human monocytes isolated from peripheral blood mononuclear cells (PBMC) of healthy volunteers (human monocyte-derived macrophages, hMDM).

To visualize the uptake of NP in primary macrophages, mouse BMDM were incubated with fluorescently labeled MSN (Figure 5.7a) and CD (Figure 5.7b) particles (green) and examined by confocal microscopy. Cellular and endosomal membranes were stained with a lipophilic dye (red). Pictures were taken approximately one minute after particles were added to the cell cultures. Co-localization of the membrane marker and NP signals demonstrated that the NP were rapidly internalized by the macrophages.

To determine whether the porous nanoparticles are toxic in primary macrophages, mouse BMDM and human hMDM were exposed to the NP for 2 hours. The 2-hour time point was chosen because NP release their cargo within 2 hours (see Figure 5.4 and Fig. S5.7, SI). The

amount of NP was equal to the maximum concentration used for the functional studies described below. Metabolic activity was assessed by a cell counting kit-8 (CCK-8) assay. This assay, similar to MTT assays, is based on the reduction of a tetrazolium salt in the presence of an electron carrier. A lactate dehydrogenase (LDH) release assay was performed to determine membrane integrity. The assays showed that neither the unloaded particles nor the free NSA at 100 µM had an effect on metabolic activity (Figure 5.7 c,e) or membrane integrity (Figure 5.7 d,f) in mouse BMDM or hMDM after this exposure time.

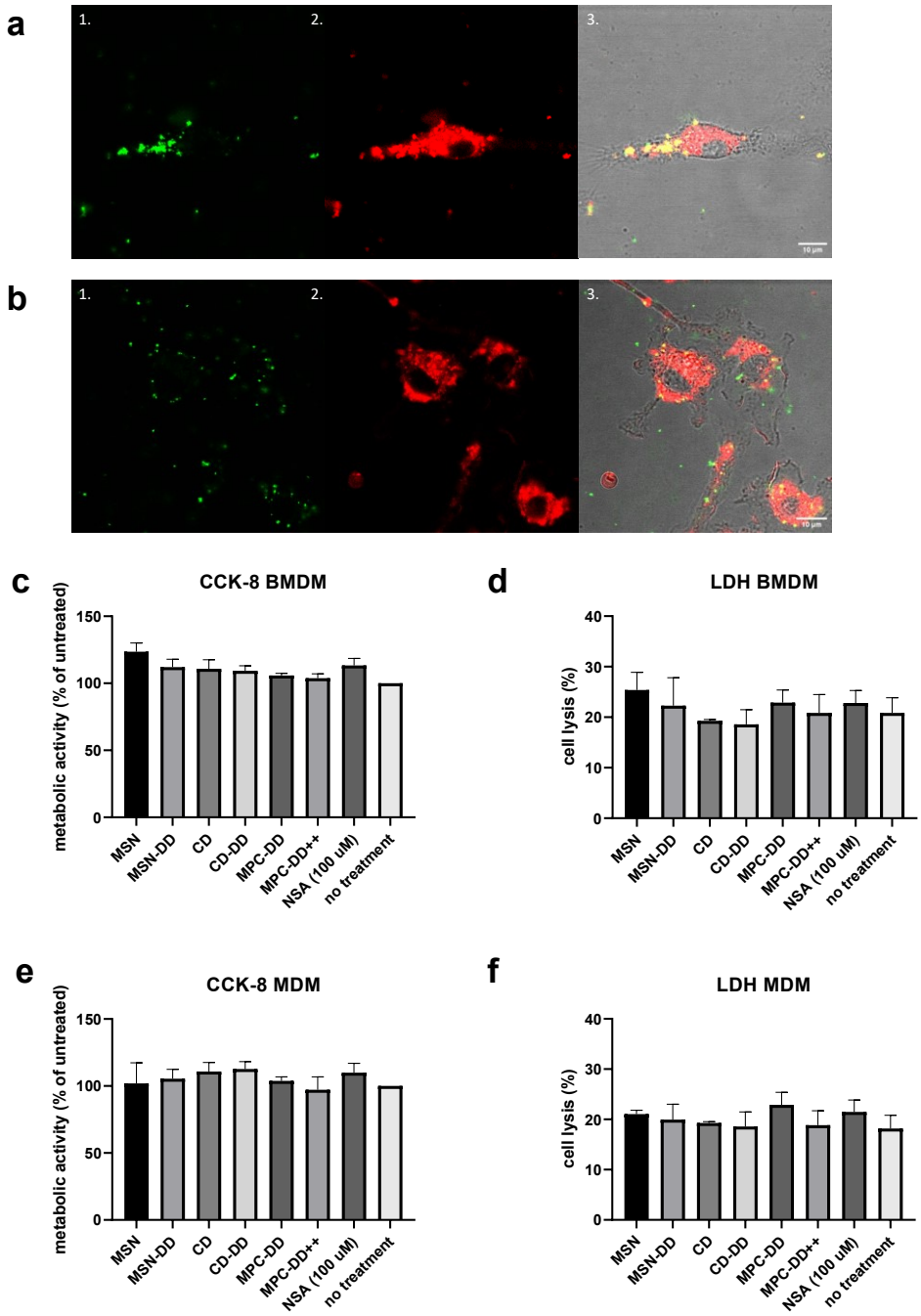

Figure 5.7 BMDM were exposed to fluorescently labeled MSN (a) or CD particles (b) for approximately 1 minute. Left) endosomal staining (red), middle) Atto-488 labeled particles (green) and right) merge (red and green), overlay with phase contrast image.

Murine BMDM and human MDM were treated with unloaded NP with and without lipid bilayer (DD) or with free NSA (100 µM). After 2 hours CCK-8 (c,e) and LDH assays (d,f) were performed. (c,e) Metabolic activity of untreated cells was set at 100%. (d,f): LDH release by detergent-lysed control cells was set at 100%.

NSA prevents IL-1β and IL-18 release from primary macrophages upon GSDMD activation

In a next step, we examined whether we could successfully inhibit GSDMD-mediated cytokine release using NSA. Traditionally, a two-signal model is proposed for the stimulation of GSDMD mediated IL-1β release by immune cells. A first priming signal, such as lipopolysaccharide (LPS), which activates Toll like receptor 4 (TLR4), triggers the intracellular accumulation of pro-IL-1β. Then, a second signal, such as high concentrations of extracellular ATP, leads to activation of caspase 1 and allows for maturation and release of IL-1β through GSDMD pores.[37] Mouse BMDM were primed for 4 hours with LPS, of which the last 30 min included exposure to NSA. After priming, GSDMD was activated by treating the BMDM for 1 hour with ATP (see also scheme in Figure 5.9 a). Inhibition of GSDMD pore formation was evaluated by measuring secretion of IL-1β and IL-18 into the cell medium by ELISA. LPS combined with ATP induced IL-1β and IL-18 secretion, while LPS or ATP alone did not have an effect on the release of IL-1β or IL-18. NSA dose-dependently inhibited the release of IL-1β and IL-18 induced by the combination of LPS and ATP. At 40 μM, NSA was able to completely prevent both IL-1β and IL-18 release from LPS and ATP-treated BMDM (Figure 5.8 a,b). Because IL-1β and IL-18 release both appear to reflect GSDMD pore formation equally well, we decided to continue using IL-1β release as a readout for GSDMD activation.

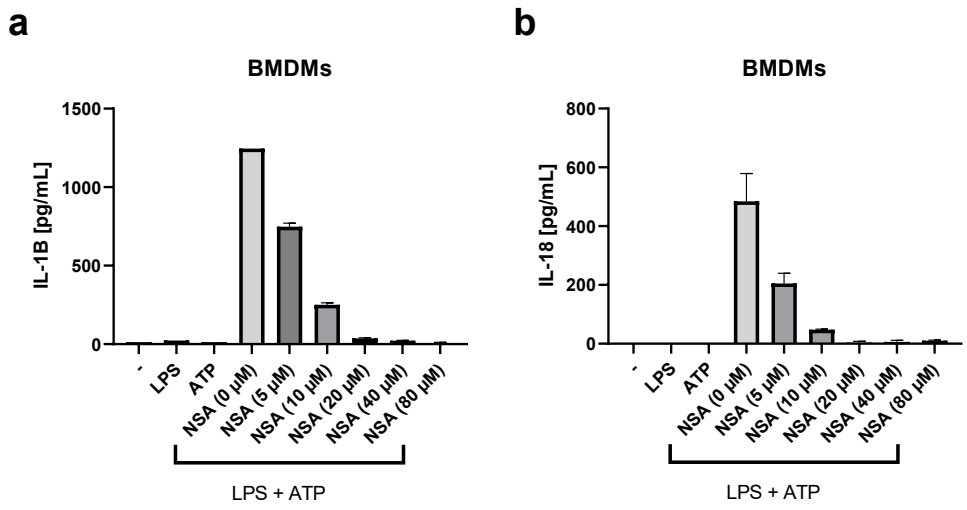

Figure 5.8 Concentration of a) IL-1β and b) IL-18 in cell culture supernatant after mouse BMDM were treated with LPS (100 ng/ml), ATP (5 mM) and NSA at increasing concentrations.

NSA-loaded nanoparticles inhibit IL-1β release from murine BMDM and human MDM in a dose-dependent manner

Next, we investigated whether porous NP could successfully deliver NSA to BMDM and inhibit the release of IL-1β. As in Figure 5.8, the LPS and ATP combination was used to activate GSDMD in BMDM. NSA-loaded NPs were added to BMDM during the last 2 hours of priming with LPS (see priming/activation scheme in Figure 5.9a). After priming, the cell culture medium was exchanged to remove LPS and cells were activated with ATP for 1 hour. Cells were exposed to NP containing NSA concentrations of up to 60 µM, considering that particle-delivered NSA concentrations of up to 80 µM were well tolerated in RAW 264.7 cells (see SI, Figure S5.13), and that IL-1β release was completely inhibited in BMDM at 40 µM of free NSA (see Figure 8a). ELISA assays were performed to measure IL-1β release and values were expressed as % of response to unloaded particles, to allow for comparison with other cells types described below. All NSA-loaded particles inhibited GSDMD-mediated IL-1β release in a dose-dependent manner (Figure 5.9b-g). However, only CD particles were able to fully prevent the release of IL-1β, similar to the effect of free NSA (Figure 5.9d).

Empty MSN, MSN-DD and CD particles did not induce release of IL-1β from unstimulated mouse BMDM, nor by human MDM (See SI, S14a and b). Only the empty MPC-DD++ and CD-DD particles induced small amounts of IL-1β release, suggesting that these particles may cause low levels of inflammation. Empty MSN, CD and MPC particles with and without lipid bilayers did not inhibit LPS+ATP-induced IL-1β release (See SI, S14c and d).

To determine if the IL-1β suppression with NSA-loaded nanoparticles seen in primary murine macrophages could also be observed in human macrophages, hMDM were activated with the LPS+ATP combination and exposed to NP according to the activation scheme in Figure 5.9a. In human macrophages, all NSA-loaded particles showed a dose-dependent inhibitory effect on IL-1β release. As seen with BMDM, the strongest inhibition was observed with NSA-loaded CD particles (Figure 5.10 a-f). Thus, porous NP can successfully deliver NSA to both mouse and human macrophages, allowing a strong inhibition of IL-1β release in the absence of particle toxicity.

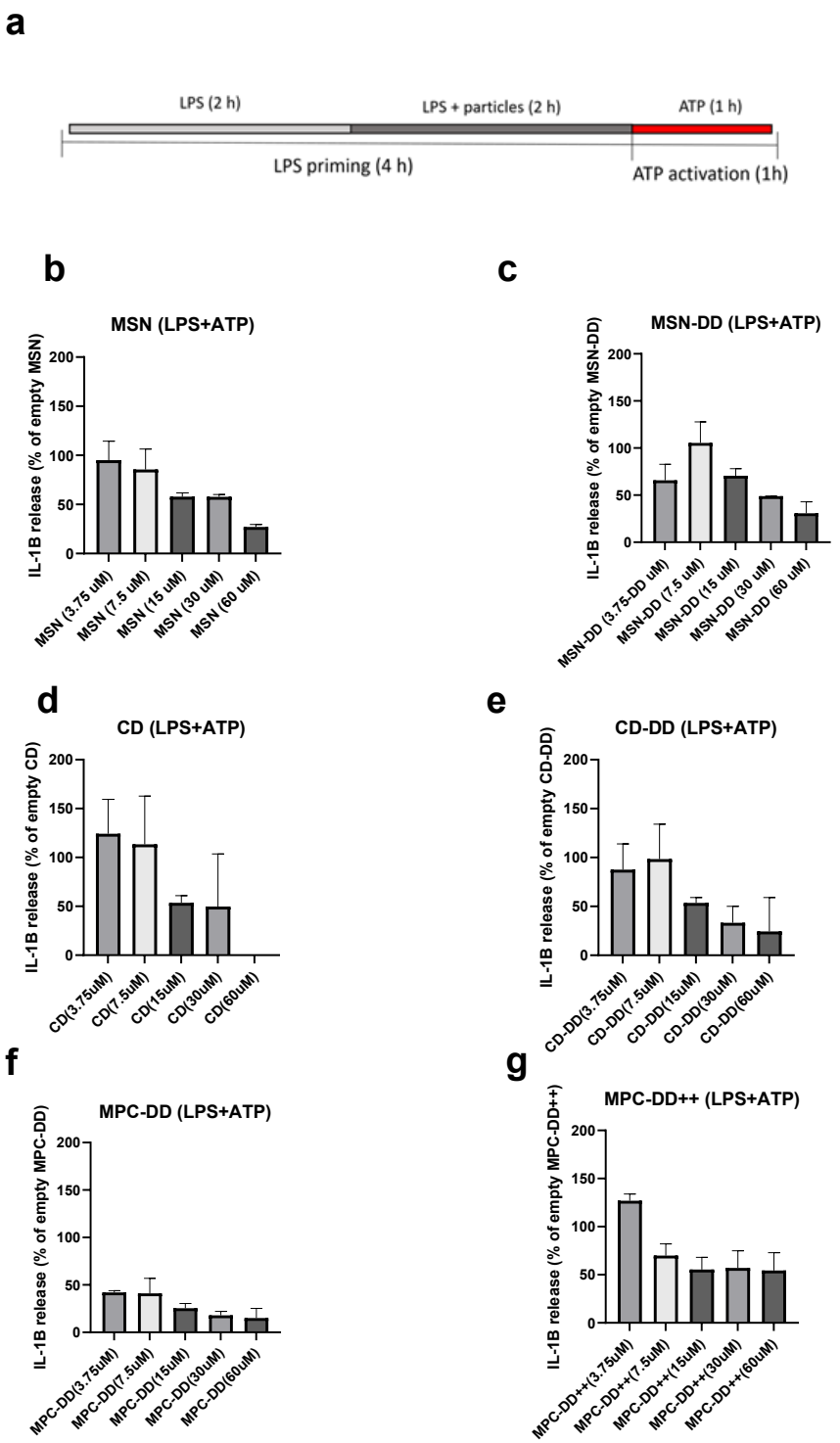

.

Figure 5.9 IL-1β release by mouse BMDM exposed to NSA-loaded nanoparticles: a) cells were primed for 2 hours with LPS and 2 hours additionally with particles. After 4 hours of priming, cells were treated with ATP to activate caspase 1 and GSDMD. b) MSN, b) MSN-DD, c) CD, d) CD-DD, e) MPC-DD, f) MPC-DD++. Particles were used empty and NSA-loaded, containing NSA at final well concentrations of 3.75, 7.5, 15, 30, and 60 µM.

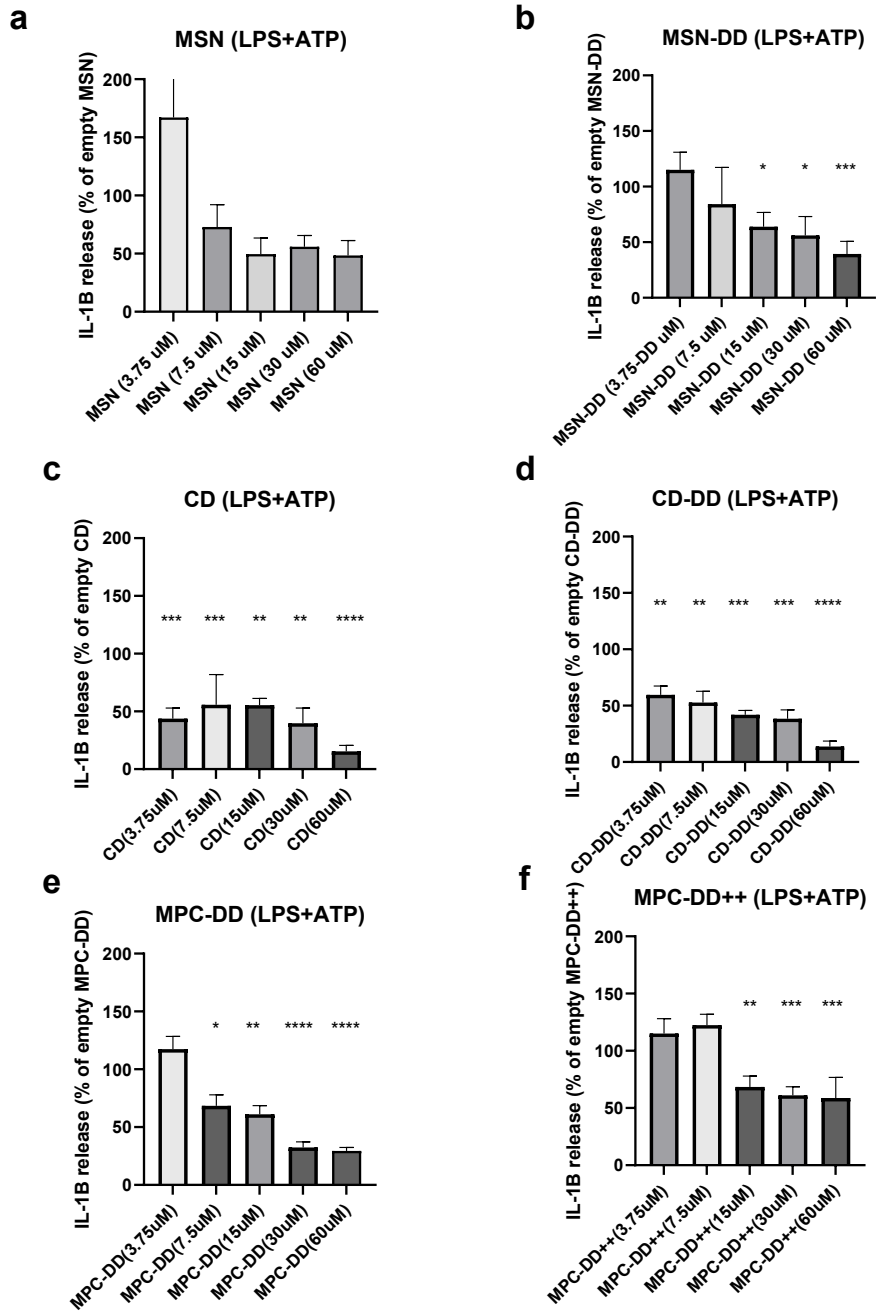

Figure 5.10 IL-1β release by human MDM: cells were activated with LPS and ATP as in Figure 5.9. a) MSN, b) MSN-DD, c) CD, d) CD-DD, e) MPC-DD, f) MPC-DD++. Particles were used empty and containing NSA at final well concentrations of 3.75, 7.5, 15, 30, and 60 µM.

Nanoparticles are preferentially taken up by phagocytes such as macrophages

Since myeloid cells, such as macrophages, are the main producers of the proinflammatory cytokines IL-1β and IL-18 in a GSDMD-dependent manner, it is of great interest to target NSA

specifically to these cell types in order to avoid off-target effects of the drug. NP provide an opportunity to selectively deliver the drug to these cells, as myeloid cells are professional phagocytes and are well-known to take up particulate material.[25]

To determine whether the NP in this work permit effective targeting of myeloid cells, murine splenocytes were exposed to the different types of porous particles. Mouse splenocytes are composed of different immune cell populations, including myeloid cells, such as macrophages and dendritic cells, as well as B and T lymphocytes.[38] Freshly isolated splenocytes were cultured with fluorescently-labeled MSN, MSN-DD, CD and CD-DD particles for 2, 6 and 24 hours. An acidic wash (pH 3) was performed to remove surface-bound particles as previously described.[39] Immune cell types, their viability and their positivity for the fluorescent NP were determined by flow cytometry (see SI, Figure S5.15 for gating strategy used). Viability was assessed for the CD45.2-positive cells, representing all immune cells within the splenocytes. No decrease in viability was observed at any of the timepoints, after exposure to the different porous NP compared to untreated cells (Figure 5.11a).

The percentage of NP-positive cells was measured for dendritic cells, macrophages, B cells and T cells. After 2 hours, the proportion of positive cells within each cell type ranged from 5% to 30% and was similar among the different cell types (Figure 5.11b). Overall, particles with a lipid bilayer tended to be taken up less than their non-coated counterparts. This effect may be traced to a bilayer-induced modulation of the metabolism in the phagocytic cells.[40] After 24 hours, over 70% of dendritic cells and over 40% of macrophages and B cells were positive for uncoated CD particles, whereas less than 20% of T cells were positive for these particles. Less than 10% of all cell types were positive for MSN and MSN-DD. Thus, CD particles were taken up by a high proportion of phagocytic cells including dendritic cells, macrophages and B cells, but much less by T cells, which are non-phagocytic cells.

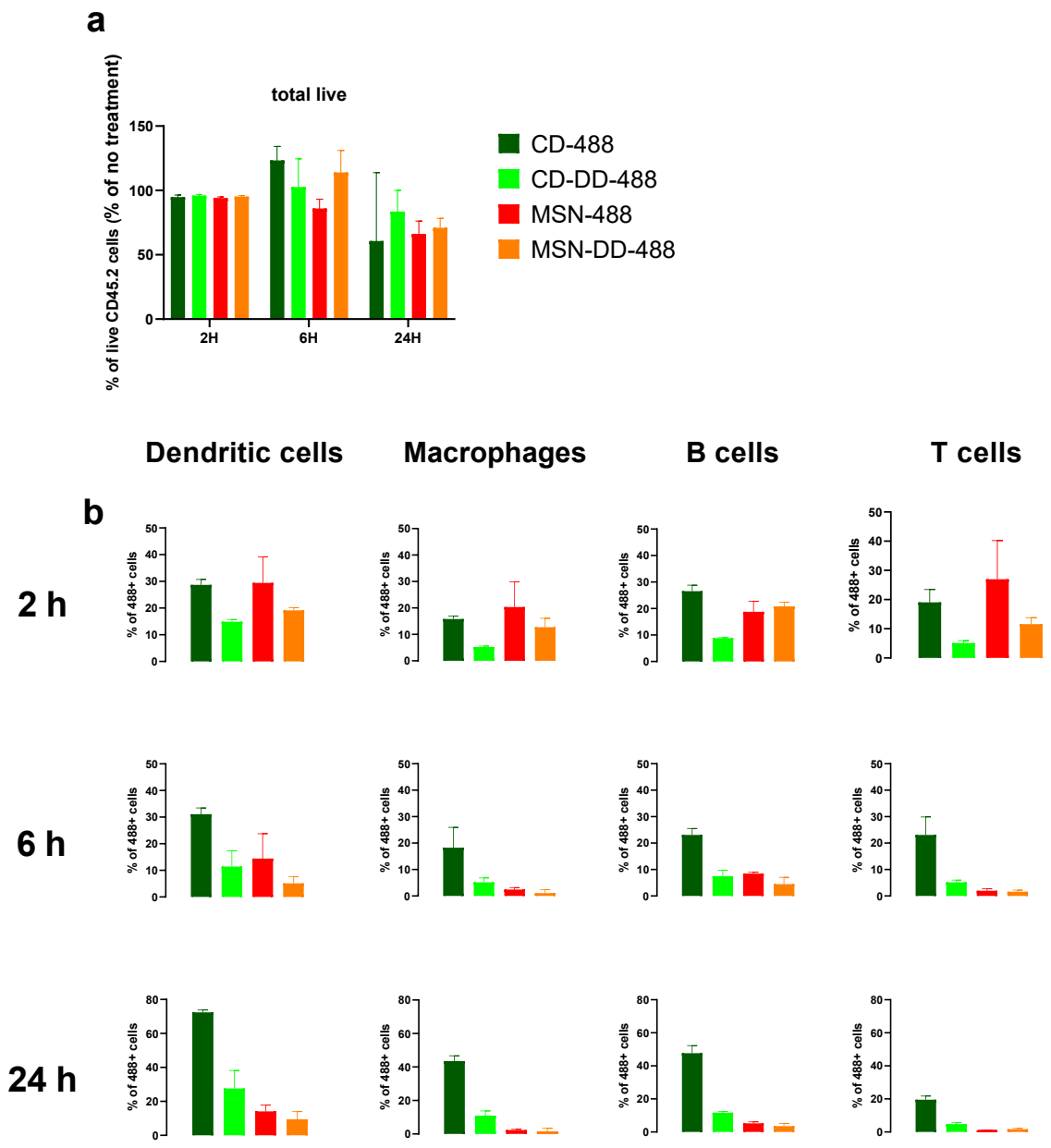

Figure 5.11: a) Percentage of live CD45.2+ splenocytes after treatment with CD (dark green), CD-DD (light green), MSN (red) and MSN-DD (orange) particles compared to untreated cells after 2 h, 6 h and 24 h. b) Percentage of NP-positive dendritic cells (CD11c+), macrophages (CD11b+, CD11c-), B cells (CD19+) and T cells (CD3+) after 2 h, 6 h and 24 h.

5.3. Conclusion

NSA was recently discovered as a specific antagonist against GSDMD-mediated pyroptotic cell death and inflammatory cytokine release. One of the major cell types that express GSDMD are macrophages, which play an important role for the initiation of inflammatory processes. It is therefore relevant to target NSA specifically to these cells in order to limit inflammation, while at the same time preventing unwanted toxicity of the drug to other cell types.[8] The use of NP as delivery system can allow for the selective targeting of macrophages, since these cells are specialized in the uptake of particulate material.[25] We could show that the highly hydrophobic NSA can be absorbed into three different nanocarriers at high loading, allowing for a solvent-free delivery of NSA. Both MSN and CD particles were rapidly taken up by macrophages and delivered their NSA cargo into the cells. After 24h of exposure to a mixed population of immune cells, a high proportion of macrophages and dendritic cells, which are also phagocytic cells with inflammatory properties, were positive for CD particles. Interestingly, a substantial percentage of B lymphocytes was also positive for CD particles after 24h. B lymphocytes are capable of phagocytosis,[41] and we have previously shown that B lymphocytes can take up certain types of particles such as gold nanoparticles.[42] In contrast, few T cells, which are non-phagocytic cells, were positive for CD particles. This suggests that NSA delivery by porous NP may be an effective manner to target macrophages and dendritic cells as the main initiators of inflammation.

Utilizing a macrophage cell line, as well as freshly differentiated primary macrophages from mice and human donors in a variety of in vitro studies, we showed a good compatibility of all unloaded carriers with these cell types, even in long-term incubation experiments of over 45 h. The particles themselves did not induce inflammation in macrophages, with the exception of lipid-coated MPC-DD++ and CD-DD particles. This lipid bilayer coating was applied to evaluate its effect on the speed of cellular uptake as well as a protective coating, preventing

premature release of NSA. Since we did not observe major release of NSA even from uncoated NP and did recognize a reduced effect of DD-covered NP with respect to IL-1β suppression, we conclude that for future applications bilayer-free particles can be used advantageously, thus avoiding potential immune responses.

We have previously shown that different types of NP can be taken up into phagocytic cells without immune activation.[43] In contrast, other particles, including certain types of silica-based NP, can induce inflammation and GSDMD-mediated pyroptosis in macrophages.[44, 45] Early screening for proinflammatory effects in standardized conditions is therefore essential during the development of particles for clinical applications.[25]

When loaded with NSA, MSN and CD NP were better tolerated by macrophages than the free NSA compound, which forms aggregates in aqueous media. In contrast, NSA-loaded MPC particles completely blocked metabolic activity of macrophages even at low NSA concentrations. MPC particles require small amounts of surfactant for loading of NSA, which may have toxic effects on these cells.[46] Thus, with the exception of MPC particles, delivery by porous NP may enhance the compatibility of NSA with macrophages.

In functional assays with freshly differentiated macrophages from mice and human donors, a concentration-dependent suppression of IL-1β release was established with all three types of NP. The strongest suppressive effect on human macrophages was obtained with CD particles and was observed already at the lowest NSA concentrations. None of the unloaded particles impaired IL-1β release after GSDMD activation, demonstrating that the anti-inflammatory effect is due to the drug cargo rather than to the carrier.

In summary, our screening of particles has established two valuable candidates for NSA delivery in the form of MSN and CD-CDI NP. Both particles are easily synthesized, scalable, storable as well as biodegradable and can deliver high contents of this hydrophobic molecule

without further application of a capping layer to phagocytic cells, inducing a successful suppression of the IL-1β cytokine. While MSN NP are rapidly taken up in large numbers by macrophages, we established that CD-NP are apparently even more effective in intracellular NSA release, leading to the highest reduction of the IL-1β cytokine.

Here, we have focused on the characterization of different NSA-NP systems and on their in vitro effects on macrophages and other immune cells. However, we expect additional benefits of these nanoparticle formulations *in vivo*. Indeed, we have previously shown that following subcutaneous injection, MSN nanoparticles accumulate in phagocytic cells in the lymph nodes draining the injection site.[19] Nanoparticle formulation may therefore also allow for site-specific, DMSO-free delivery of NSA in vivo.

This study establishes the potential of porous biocompatible NP for the effective and targeted delivery of potentially toxic, hydrophobic drugs in order to regulate inflammatory responses in both primary murine and human immune cells.

5.4. Experimental Part

Materials: All chemicals were used as received.

Ammonium fluoride (NH_4F, Fluka), Cetyltrimethylammonium chloride 25% solution in water (CTAC, Sigma-Aldrich), Triethanolamine (TEA, 98% Fluka), Tetraethylorthosilicate (TEOS, 99%, Aldrich), Phenyltriethoxysilane (PhTES, 98% Aldrich), 3-Mercaptopropyl-triethoxysilane (MTES, > 80%, Fluka), β-Cyclodextrin (Sigma, 97 %), 1,1'-Carbonyldiimidazole (CDI, Sigma, ≥ 90 %), Methoxy-polyethylene glycol amine (750) (OMe-PEG-NH2, Sigma), N, N-Dimethylformamide (DMF, anhydrous) (Sigma, 99.8 %), Tetrafluoroterephthalonitrile (TFTN, Alfa Aesar, 98%), Potassium carbonate (K_2CO_3, Aldrich 99.99%), Poly(ethylene glycol)200 (PEG200, Sigma-Aldrich), Magnesium nitrate hexahydrate (Sigma, 99 %), ammonium dihydrogenphosphate (Alfa Aesar, 99 %), citric acid (Aldrich, 99.5 %), ethylene glycol (Aldrich, 99.8 %), ethanolamine (Fluka, >99 %), ethanol (EtOH, Aldrich, >99.5 %), ammonium nitrate (Sigma, 99 %),

1,2-dioleoyl-3-trimethylammonium-propane (DOTAP, Avanti Polar Lipids), 1,2-dioleoyl-sn-glycero-3-phosphocholine (DOPC, Avanti Polar Lipids), Dopamine HCl (Fluka) Hoechst 33342 (Sigma, 97 %), ATTO-633 amine, ATTO-633 maleimid and ATTO-488 maleimid (all ATTO-Tech), bidistilled water (Millipore system Milli-Q Academic A10) was used for all synthesis steps. Necrosulfonamide (Cayman chemical, %), dimethylsulfoxide (DMSO, anhydrous, Sigma, > 99.9%),

RAW 264.7 cells: Dulbecco's Modified Eagle Medium (DMEM, high Glucose, GlutaMAX) and FluoBrite DMEM (both ThermoFisher), penicillin, streptomycin, and fetal bovine serum (FBS) were purchased from Life Technologies. Thiazolyl Blue Tetrazolium Bromide (MTT,

97.5% Aldrich), CCK-8 cell counting kits (Dojindo Molecular Technologies).

Methods

Synthesis of MSN-NP: MSN with co-condensation of 5 mol% phenyl-groups in core and 2 mol% mercapto-groups in shell

Solution 1: 100 mg NH_4F (2.7 mmol), 21.7 mL H_2O (1.12 mol) and 2.41 mL of a 25% CTAC solution (1.83 mmol) were mixed in a 50 mL polypropylene reactor and heated to 60 °C under stirring in an oil bath.

Solution 2: was prepared in a 20 mL polypropylene reactor, containing 14.3 g TEA (97 mmol) to which was added a premixed solution of 1.8 mL TEOS (8.1 mmol) combined with 0.124 mL PhTES (0.5 mmol), for forming the core of the MSN particles. This solution was heated to 90 °C under static conditions for 1 h.

Solution 2 was added to solution 1 under strong stirring. The combined solutions were subsequently allowed to cool to room temperature under stirring. After 20 minutes we added, dropwise, the ingredients for the shell layer, consisting of a premixed solution of 44 µL MTES (0.22 mmol) and 44 µL TEOS (0.20 mmol). The condensation reaction was allowed to continue over night at room temperature.

The next day, this suspension was mixed with an additional 50 ml ethanol for 15 minutes, and the nanoparticles were then retrieved via centrifugation at 7830 rpm (7197 rcf) for 15 minutes. The sample cake was redispersed in a 90:10 vol% solution of ethanol: concentrated HCl (37%). Twofold template extraction was performed at 90° under reflux for 45 minutes in a 100 mL round bottom flask. After cooling, the sample was collected by centrifugation and a threefold washing cycle in i) ethanol, ii) water and iii) ethanol again was performed. The final sample was kept concentrated in absolute ethanol until further use. The concentration of this stock solution was determined gravimetrically by drying 1 mL of the ethanolic stock solution.

Preparation of labelled MSN nanoparticles: MSN-633-MAL or MSN-488-MAL: Usually, 1 mg MSN particles co-condensed with 2 mol% mercaptogroups on the particle surface were dispersed in 1 mL ethanol and 1 µL Atto-633-MAL (or Atto-488-MAL, DMF stock solution, 0.5 mg mL^{-1}) was added. Samples were stirred in the dark for 1-2 h and finally washed repeatedly in bidistilled water.

Synthesis of CD-CDI-PEG: β-Cyclodextrin (200 mg, 0.176 mmol) and 1,1'-carbonyldiimidazole (CDI, 342 mg, 2.11 mmol) were dissolved in anhydrous DMF (8 mL) and stirred at room temperature for three hours and were subsequently aged at 4 °C without further stirring for 1-3 days. 1 mL of this precursor solution was then mixed with 7 mg of methoxy-polyethylene glycol amine (OMe-PEG-NH_2) in a small glass vial and was stirred overnight to result in a CD-CDI-PEG stock solution. 30 µL of this stock solution (corresponding to 0.5 mg of un-PEGylated CD-CDI nanoparticles) was then added to 1.5 mL H_2O for nanoparticle precipitation. Sample purification was performed by centrifugation (5 min, 14 000 rpm; 16,873 rcf). Samples were finally redispersed in 1 mL doubly distilled water (pH = 7).

Preparation of labelled CD-CDI-PEG nanoparticles: CD-CDI-PEG-Atto633: Covalently labeled nanoparticles were obtained directly during the nanoparticle synthesis by adding 2 µL Atto-633-amine (1 mg/mL DMSO) mixed together with the OMe-PEG-NH_2 to the reaction solution, as described above. These samples were stirred overnight in the dark and were washed in three centrifugation steps with 1 mL bidistilled water to remove excess dye.

Synthesis of MPC-NP: In a 50 mL polypropylene reactor magnesium nitrate hexahydrate (320 mg, 1.25 mmol) and citric acid (270 mg, 1.41 mmol) was dissolved in water (17 mL, 0.94 mmol). This leads to solutions with a molar ratio of Mg/CA = 1:1.12. Then, ammonium dihydrogenphosphate (for samples Mg/P = 1:1: 142 mg, 1.25 mmol) was added to the solution and stirred until complete dissolution. Subsequently, cetyltrimethylammonium chloride (622

mg, 1.94 mmol) and ethylene glycol (7.15 g, 115 mmol) were added and the synthesis mixture was stirred at 700 rpm at room temperature for 5 minutes. This clear solution was combined with triethanolamine (7.15 g, 48 mmol) and ethanolamine (3.00 g, 49.1 mmol) under vigorous stirring (3 minutes). The obtained suspension was finally diluted 1:1 with ethanol. Particles were separated by centrifugation at 7,830 rpm (7,197 rcf) for 5 minutes and redispersed in NH_4NO_3/EtOH (2 wt%, 80 mL). Template extraction was performed by heating the latter suspension under reflux at 90 °C for 30 minutes. Following centrifugation (7,830 rpm, 7,197 rcf, 5 minutes), samples were redispersed in 80 mL ethanol. This extraction procedure was repeated one more time. The particles were separated by centrifugation at 7,830 rpm (7,197 rcf) for 5 minutes and redispersed in 20 mL ethanol. These particles were always used after applying a lipid bilayer of DOTAP/DOPC (Lipid coating see below).

Loading of NSA into nanoparticles:

a) MSN-NSA, and CD-CDI-PEG-NSA: Aliquots of 1 mg nanoparticles/mL in bidistilled water were exposed to different amounts of an NSA stock solution (10 mg/mL in DMSO, aliquots kept at -20°C) and stirred at room temperature for 3 h. Samples were freed of excessive NSA by multiple centrifugation (three times for 3 min at 14 000 rpm) and redispersion in bidistilled water. Supernatants were kept for UV-VIS analysis. Sample loading was determined by difference calculation of offered NSA concentration to residual NSA in the supernatants. Under these conditions loading efficiencies of over 90-95% were obtained, usually in a range between 15-19 wt% NSA loading. However, higher loadings of up to 49 wt% could also be achieved in MSN or when higher concentrations of NSA were offered to these nanoparticles.

b) Loading of NSA into MPC: A loading of substantial amounts of NSA required the addition of CTAC. 20 µL of the NSA stock solution was mixed in a 1.5 mL reaction tube with CTAC

(CTAC concentration used for MPC: 60.5 µg, 184 nmol; MPC++: 151.25 µg, 460 nmol) and filled up to 1 mL with water, and 0.5 mg of MPCs were added as ethanolic suspension. The reaction tube was shaken (700 rpm) for 4 hours. The loaded particles were separated by centrifugation, the supernatant was collected and kept for quantification of the loaded amount of NSA. Particles were wrapped with a lipid bilayer of DOTAP/DOPC (see below) after NSA loading. Loading of MPC-NP with NSA resulted in an uptake of 16 wt%. For MPC++ higher loadings up to 32% NSA were achieved.

Preparation of lipid-coated NSA loaded nanoparticles:

MSN-NSA-DD, CD-CDI-PEG-NSA-DD and MPC-DD: 1 mg of NSA-loaded particles were usually centrifuged for 5 minutes at 14 000 rpm, freed of the supernatant and subsequently carefully redispersed in 100 µL of a DOTAP solution (2.5 mg DOTAP/mL of a 60/40 vol% H_2O/EtOH solution) by up-down-pipetting. Bi-distilled water (900 µL) was then added and again mixed by pipetting. Samples were again centrifuged and a second layer consisting of DOTAP/DOPC was added by redispersing the sample pellets now in a mixture of 50 µL each of DOTAP and DOPC (1,2-dioleoyl-sn-glycero-3-phosphocholine with 2.5 mg DOPC/mL of a 60/40 vol% H_2O/EtOH) under short sonication. 900 µL bi-distilled water was finally added. The lipid-coated nanoparticles were washed twice by centrifugation at 14,000 rpm (16,873 rcf) for 5 minutes with H_2O (1 mL).

Characterization:

Sorption measurements: Nitrogen sorption measurements were performed on a Quantachrome NOVA 4000e Instrument at 77 K. Template-extracted nanoparticle samples of 10-15 mg were degassed for 12 h at 120 °C under vacuum (10^{-5} Torr) before measurement.

Brunauer Emmett Teller (BET) surface areas were calculated using the linearized form of the BET equation (in the range of 0.08 to 0.2 P/P_0). The pore volume and pore size distribution were calculated based on the NLDFT equilibrium model for N_2 on silica.

UV-VIS: UV-VIS spectra were recorded in transmission with a Nanodrop instrument in disposable UV-VIS micro-cuvettes. A calibration curve of NSA was prepared from a stock solution (10 mg NSA/mL in DMSO) by diluting 80 µg NSA/mL DMSO successively in an aqueous solution.

TEM: Transmission electron microscopy was performed on a Tecnai G2 20 S-Twin operated at 200 kV using a TemCam-F216 camera (TVIPS). A drop of an MSN-ethanol suspension was placed on a carbon-coated copper grid and dried at room temperature for several hours before TEM observation.

SEM: Scanning electron microscopy, using an FEI Helios Nanolab G3 UC. The microscope was equipped with a field emission gun and was operated at acceleration voltages of 2-3 kV using working distances of about 3 mm. Samples were dispersed in ethanol or DMSO solution, shortly treated by ultrasonication and dropped on a Si wafer. Samples were dried over night before analysis.

DLS and Zeta potential: The hydrodynamic size distribution of samples was measured by dynamic light scattering (DLS) analysis in disposable PMMA cuvettes using a Malvern Zetasizer-Nano instrument equipped with a 4 mW He-Ne laser (633 nm). Particle size distribution was measured in aqueous solutions containing a concentration of 0.1 mg/mL. Zeta potentials were measured with an attached multi-purpose titrator. Measurements were performed with 10 mL of an aqueous solution of nanoparticles (0.1 mg/mL) using an automated titrator scanning the pH range from 3 to 8 (with pH steps of 0.5) using diluted NaOH and HCl

solutions. Single-point measurements were performed with a concentration of 0.1 mg/mL at pH = 7.3.

FTIR: Infrared spectra were obtained with a Thermo Scientific Nicolet iN10 IR 6700 Microscope with a Smart OMNI Transmission attachment using KBr-pelleted samples.

Raman: Spectra were recorded on a Bruker Vertex 70 RAM II FT-IR-Raman instrument using an N_2 cooled Ge detector and an Nd:YAG 1064 cm^{-1} laser. Spectra were collected in backscattering mode on powders. 10.000 scans were accumulated for the MSN carrier while only 1000 scans were needed for the pure NSA as well as the NSA-loaded MSN sample.

Cell culture

RAW 264-7 cells: RAW 264.7 macrophage cells were received as a gift from Prof. Wagner, Pharmaceutical Department, LMU Munich. Cells were cultured in Dulbecco's modified Eagle's medium (DMEM), supplemented with 10 % FBS, 100 U/mL penicillin and 100 µg/mL streptomycin at 37 °C and a 5 % CO_2 humidified atmosphere. For cell experiments, cells were seeded in 96-well plates (Ibidi, 15 µ bottom thickness, black, ibiTreat) or in 24-well Corning plates and were allowed to adhere for 24 h before incubation with the respective NP in a Heracell Incubator (Thermo Fisher) at 37 °C and 5% CO_2.

Generation of L929 cell conditioned medium: Conditioned medium collected from L929 cells was used as a source of M-CSF.[1] Briefly, $2.5*10^5$ L929 cells were cultured in a T75 flask in 25 ml of DMEM supplemented with Glutamax (ThermoFisher), 10% FBS (PAN Biotech, P30-3302), 1% L-glutamine (Gibco, 25030081), 1% non-essential amino acids (Gibco, 11140050), 1% sodium pyruvate (Gibco, 11360070), 1% penicillin/streptomycin (Gibco 15140122) at 37°C, 5% CO_2. Conditioned medium was collected when cells reached

confluency, filtered on 0.22 µm Stericup filters (Millipore, 05469) and used for generation of mouse bone marrow-derived macrophages (BMDM).

Generation of murine bone marrow-derived macrophages (BMDM): Bone marrow cells were flushed out of the cavities of fresh tibias and femurs of naïve adult (12 weeks) C57BL/6 mice in bone marrow differentiation medium (DMEM (Gibco, 11966025), 20% FBS, 1% penicillin/streptomycin, and 20% L929 cell conditioned medium). Cells were passed through a 40 µM filter (Greiner, 7542041), seeded in Petri dishes (TPP, 93100, 1 bone per 10 cm^2 dish) and incubated in bone marrow differentiation medium at 37°C, 5% CO_2. Four days after isolation, cells were split to 50% density and incubated for 2 additional days. Animal studies were approved by the Geneva cantonal authority for animal experimentation under the approval number GE182.

Generation of human monocyte-derived macrophages (MDM): MDM were isolated from buffy coats obtained from anonymous healthy donors at the Geneva University Hospital Blood Transfusion Center (Geneva, Switzerland) after informed consent. LeucosepTM 50 ml tubes (Greiner, 7.227 290) tubes were loaded with 15 ml Lymphocyte separation medium (Ficoll) (GE Healthcare, 17-1440-02), 25 ml human blood, and filled to 50 ml with PBS, 2 mM EDTA. The tubes were centrifuged at 440 g for 35 min at room temperature without brake. The PBMC fraction was then transferred into a fresh 50 ml Falcon tube and washed twice with PBS, 2 mM EDTA. Monocytes were enriched by adhesion and differentiated for 7 days into macrophages in RPMI 1640 (Gibco 61870010), 1% penicillin/streptomycin containing 2.5 % human plasma (Geneva University Hospital Blood Transfusion Center) in LeucosepTM 6 well plates (Greiner, 163288).

RAW 264.7 cell treatment with NSA-loaded nanoparticles: Exposure of RAW 264.7 cells to nanoparticles was performed after allowing the cells to adhere for 24 h. Usually, to each 100

µL well volume we added aliquots of 10 µL suspensions containing increasing amounts of (NSA-loaded) nanoparticles, ranging between 2 to 10 µg nanoparticles /100 µL. The respective NSA concentration in µM is included in the figures.

Imaging and flow cytometry

Continuous cell growth measurements: Cellwatcher, PHIO scientific GmbH, Munich, lensless microscope for continuous cell growth monitoring (https://www.phio.de/index.html). RAW 264.7 cells were seeded in 24 well plates to give a starting confluency of about 20% (1 mL cell medium). Plates were inserted into PHIO holders, located in the incubator, and continuously monitored for changes in confluency. 24 h after seeding, cells were incubated with nanoparticle suspension. After reaching close to 90% confluency, cells were imaged with higher resolution in the ImageXpress microscope.

Live-cell imaging: ImageXpress Micro XLS, widefield high-content microscope, equipped with an environmental cell chamber, Molecular Devices.

RAW 264.7 cells were seeded with 3000 cells/well. 24 h after seeding, MSN nanoparticles were added in 10 µl aliquots to each well (in triplicates). Plates were carefully shaken and immediately transferred into the life-cell imaging environmental control chamber of the high-content-screening wide-field microscope. They were kept in the microscope at 37°C under flow of a 5% CO_2 humidified atmosphere over the whole measuring time. Images of all assigned wells in the plate were taken of 4 different areas in each well, and automated sequential scans were performed usually every 5 h over extended times of up to 72 h. Objectives from Nikon were used with magnifications as indicated: 10x (Plan Fluor 0.3 NA),

20x (Ph1 S Plan Fluor 0.45 NA) or 40x (Plan Apo Lambda 0.95 NA). Bright field images were recorded in addition to fluorescence images of the GFP, DAPI, or CY5 channels using a filter cube changer (Semrock filters).

Image analysis: Cell proliferation information was acquired from bright field images (at 20x or 40x magnification) of unlabeled cells at specified time-intervals, usually in 5 h steps. Final cell viability was assessed after Hoechst nucleus staining. Automated cell counts were performed using ImageXpress Custom Modules. Results for each sample and time point reflect the averaged information of three different wells, with four images taken from each well (total n=12).

Confocal Microscopy of RAW 264.7 cells: Fluorescence microscopy was performed with a Zeiss Observer SD spinning disk confocal microscope using a Yokogawa CSU-X1 spinning disc unit and an oil objective (63x magnification) and BP 525/50 (WGA488) and LP 690/50 (Atto633) emission filters. A 488 nm and a 639 nm laser were used for excitation. At 24 h prior to addition of NP, 3500 RAW 264.7 cells per well were seeded in 8-well plates in 280 µL growth medium. A total of 20 µL CD-CDI-PEG covalently labelled with Atto-633-amino (200 µg mL-1 CD-CDI-NP in PBS buffer) were added to each well and incubated for 2 h, at 37 °C followed by addition of WGA-488 to the medium for cell membrane staining. Cells were washed with PBS and after addition of 300 µL fresh medium, cells were directly imaged.

Confocal microscopy of BMDM: BMDM were seeded at 2x104 cells/well in IbiTreat microscopy chambers (Ibidi, 80826) and incubated overnight at 37°C, 5% CO2. Cell membranes were fluorescently labeled using 5 µg/ml FM™ 4-64 Dye (ThermoFisher, T13320) in ice cold HBSS (Gibco, 24020117) for 1 minute. Nanoparticles were then added at 25 ng/µl and the chamber was placed immediately inside a temperature and CO2 controlled Nikon a1r spectral confocal microscope for live cell imaging.

Flow cytometric analysis of nanoparticle uptake by mouse splenocytes: Fresh spleens were harvested from 3 adult C57BL/6 mice (Charles River Laboratories) and passed through a 40 μM filter (Greiner, 7542041) in PBS. Red blood cells were lysed for one minute using BD Pharm Lyse (BD Biosciences, 555899). Cells were seeded at 1x106 cells/well in RPMI (12633012, Gibco), 10% FBS (PAN Biotech, P30-3302), 1% L-glutamine, 1% non-essential amino acids (11140050, Gibco), 1% sodium pyruvate (11360036, Gibco), 0.1% β- mercaptanol in a 96 well plate and incubated at 37°C, 5% CO2. Nanoparticles were added immediately after seeding for 2, 6 and 24 hours. Cells were washed using a light acidic wash (pH=3, 100 mM NaCl, 50 mM glycine). Cells were treated with Fc block (101320, BioLegend) and stained with the following antibodies: PE CD11c (117308, BioLegend), PE-Cy7 CD45 (103114, BioLegend), APC-Cy7 CD3 (100222, BioLegend), BV510 CD19 (115546, BioLegend), BV785 CD11b (101243, BioLegend), all in a 1:200 dilution ratio. Zombie violet (423114, BioLegend) was used to exclude dead cells. Stained cells were analyzed using a NovoCyte Flow Cytometer 3000 (Agilent). Data represent average and standard deviation (SD) from 3 individual mice.

Functional assays

Metabolic and membrane integrity assays: Endpoint assays were performed with MTT or the cell counting Kit-8 assays (CCK-8) according to manufacturer's instructions, using the water-soluble tetrazolium salt, which is reduced by dehydrogenases in living cells to a water-soluble orange formazan dye. 8 μL of the CCK-8 solution was added to each 100 μl well volume and the wells were incubated for 2 hours at 37°C under 5% CO2 atmosphere. The relative concentration of living cells was then evaluated using a microplate reader (TECAN

plate reader spark 10M or CLARIOstar Plus) by referencing against untreated cells in the same plate holder.

LDH release was measured using the LDH-Glotm (Promega, J2380) kit according to manufacturer's instructions. Cells were lysed with 1:200 diluted TritonX-100 (ThermoFisher, 85111) as positive control for 100% lysed cells. Cell medium was incubated for 30 min with assay buffer (1:1 volume) and absorbance was measured using CLARIOstar Plus (BMG Labtech).

CCK8 and LDH assays were performed on BMDM or MDM pooled from 3 mice or 3 healthy donors. Data represent average and SD of 3 technical replicates.

Induction and measurement of IL-1β and IL-18 secretion: Mouse BMDM (1,25x106 cells/mL) or human MDM (1,25x106 cells/mL) were seeded in 96-well plates (Greiner, 655180), respectively in DMEM, 7,5% FBS, 1% penicillin/streptomycin or in RPMI 1640, 1% penicillin/streptomycin, 2.5 % human plasma and incubated overnight at 37°C, 5% CO2. Cells were primed for 4 hours using LPS (Invivogen, Tlrl-pb5lps) at 100 ng/ml in culture medium. After 2 hours of priming, nanoparticles were added to the medium for the remaining 2 hours. Cells were then washed in PBS and incubated with 5 mM ATP (Sigma, A6419) for 2 hours in OptiMEM (ThermoFisher, 31985062). Culture supernatants were collected and stored at -20°C. IL-1β concentrations in culture supernatants were measured using ELISA MAX™ (Biolegend, 437004, 432604). Mouse IL-18 concentrations were measured by ELISA using recombinant IL-18BPa (AB2 bio) and in house biotinylated anti IL-18 antibody (clone74, RnD) as described.[47,48] Concentrations for IL-18 were determined from optical densities by interpolating values within a linear regression generated by optical densities of varying concentration of mature IL-18 (RnD, Cat.B004-5). CLARIOstar Plus (BMG labtech) was used

to measure absorbance. Murine BMDM were pooled from 3 mice and data represent average and SD of 3 technical replicates. Error bars represent standard deviation. Human MDM from 3 healthy donors were assessed individually on 3 separate days. Data represent the average and SD of the separate experiments. A one-way ANOVA, using Graphpad Prism 9, was used to determine P values.

5.5. References

[1] M.G. Netea, F. Balkwill, M. Chonchol, F. Cominelli, M.Y. Donath, E.J. Giamarellos-Bourboulis, D. Golenbock, M.S. Gresnigt, M.T. Heneka, H.M. Hoffman, R. Hotchkiss, L.A.B. Joosten, D.L. Kastner, M. Korte, E. Latz, P. Libby, T. Mandrup-Poulsen, A. Mantovani, K.H.G. Mills, K.L. Nowak, L.A. O'Neill, P. Pickkers, T. van der Poll, P.M. Ridker, J. Schalkwijk, D.A. Schwartz, B. Siegmund, C.J. Steer, H. Tilg, J.W.M. van der Meer, F.L. van de Veerdonk, C.A. Dinarello, A guiding map for inflammation, Nature Immunology, 18 (2017) 826-831.

[2] D. Zamarin, B. Holmgaard Rikke, K. Subudhi Sumit, S. Park Joon, M. Mansour, P. Palese, T. Merghoub, D. Wolchok Jedd, P. Allison James, Localized Oncolytic Virotherapy Overcomes Systemic Tumor Resistance to Immune Checkpoint Blockade Immunotherapy, Science Translational Medicine, 6 (2014) 226ra232-226ra232.

[3] B. Boersma, W. Jiskoot, P. Lowe, C. Bourquin, The interleukin-1 cytokine family members: Role in cancer pathogenesis and potential therapeutic applications in cancer immunotherapy, CYTOKINE & GROWTH FACTOR REVIEWS, 62 (2021) 1-14.

[4] W.-t. He, H. Wan, L. Hu, P. Chen, X. Wang, Z. Huang, Z.-H. Yang, C.-Q. Zhong, J. Han, Gasdermin D is an executor of pyroptosis and required for interleukin-1β secretion, Cell Research, 25 (2015) 1285-1298.

[5] J. Shi, Y. Zhao, K. Wang, X. Shi, Y. Wang, H. Huang, Y. Zhuang, T. Cai, F. Wang, F. Shao, Cleavage of GSDMD by inflammatory caspases determines pyroptotic cell death, Nature, 526 (2015) 660-665.

[6] J. Ding, K. Wang, W. Liu, Y. She, Q. Sun, J. Shi, H. Sun, D.-C. Wang, F. Shao, Pore-forming activity and structural autoinhibition of the gasdermin family, Nature, 535 (2016) 111-116.

[7] J. Ruan, S. Xia, X. Liu, J. Lieberman, H. Wu, Cryo-EM structure of the gasdermin A3 membrane pore, Nature, 557 (2018) 62-67.

[8] X. Chen, W.-t. He, L. Hu, J. Li, Y. Fang, X. Wang, X. Xu, Z. Wang, K. Huang, J. Han, Pyroptosis is driven by non-selective gasdermin-D pore and its morphology is different from MLKL channel-mediated necroptosis, Cell Research, 26 (2016) 1007-1020.

[9] J.J. Hu, X. Liu, S. Xia, Z. Zhang, Y. Zhang, J. Zhao, J. Ruan, X. Luo, X. Lou, Y. Bai, J. Wang, L.R. Hollingsworth, V.G. Magupalli, L. Zhao, H.R. Luo, J. Kim, J. Lieberman, H. Wu, FDA-approved disulfiram inhibits pyroptosis by blocking gasdermin D pore formation, Nature Immunology, 21 (2020) 736-745.

[10] K. Rathkey Joseph, J. Zhao, Z. Liu, Y. Chen, J. Yang, C. Kondolf Hannah, L. Benson Bryan, M. Chirieleison Steven, Y. Huang Alex, R. Dubyak George, S. Xiao Tsan, X. Li, W. Abbott Derek, Chemical disruption of the pyroptotic pore-forming protein gasdermin D inhibits inflammatory cell death and sepsis, Science Immunology, 3 (2018) eaat2738.

[11] Y. Bai, H.C. Lam, X. Lei, Dissecting Programmed Cell Death with Small Molecules, Acc. Chem. Res., 53 (2020) 1034-1045.

[12] S. Chen, W. Lai, X. Li, H. Wang, Necrosulfonamide Selectively Induces DNA Double-Strand Breaks in Acute Myeloid Leukemia Cells, Chemical Research in Toxicology, 35 (2022) 387-391.

[13] M.J. Mitchell, M.M. Billingsley, R.M. Haley, M.E. Wechsler, N.A. Peppas, R. Langer, Engineering precision nanoparticles for drug delivery, Nature Reviews Drug Discovery, 20 (2021) 101-124.

[14] V. Mamaeva, C. Sahlgren, M. Linden, Mesoporous silica nanoparticles in medicine-Recent advances, Adv. Drug Delivery Rev., 65 (2013) 689-702.

[15] Y. Li, X. Zhang, X. Liu, W. Pan, N. Li, B. Tang, Designing and Engineering of Nanocarriers for Bioapplication in Cancer Immunotherapy, ACS Applied Bio Materials, (2020).

[16] Y. Gao, D. Gao, J. Shen, Q. Wang, A Review of Mesoporous Silica Nanoparticle Delivery Systems in Chemo-Based Combination Cancer Therapies, Frontiers in Chemistry, 8 (2020) 1086.

[17] A. Carvalho, R. Cordeiro, H. Faneca, Silica-Based Gene Delivery Systems: From Design to Therapeutic Applications, Pharmaceutics, 12 (2020) 649.

[18] J.J. Aguilera-Correa, J. Esteban, M. Vallet-Regí, Inorganic and Polymeric Nanoparticles for Human Viral and Bacterial Infections Prevention and Treatment, Nanomaterials, 11 (2021).

[19] J. Wagner, D. Gößl, N. Ustyanovska, M. Xiong, D. Hauser, O. Zhuzhgova, S. Hočevar, B. Taskoparan, L. Poller, S. Datz, H. Engelke, Y. Daali, T. Bein, C. Bourquin, Mesoporous Silica Nanoparticles as pH-Responsive Carrier for the Immune-Activating Drug Resiquimod Enhance the Local Immune Response in Mice, ACS Nano, 15 (2021) 4450-4466.

[20] S. Heidegger, D. Gößl, A. Schmidt, S. Niedermayer, C. Argyo, S. Endres, T. Bein, C. Bourquin, Immune response to functionalized mesoporous silica nanoparticles for targeted drug delivery, Nanoscale, 8 (2016) 938-948.

[21] R. Challa, A. Ahuja, J. Ali, R.K. Khar, Cyclodextrins in drug delivery: An updated review, AAPS PharmSciTech, 6 (2005) E329-E357.

[22] G. Tejashri, B. Amrita, J. Darshana, Cyclodextrin based nanosponges for pharmaceutical use: A review, Acta Pharmaceutica, 63 (2013) 335-358.

[23] J.R. Lakkakula, R.W.M. Krause, A vision for cyclodextrin nanoparticles in drug delivery systems and pharmaceutical applications, Nanomedicine, 9 (2014) 877-894.

[24] R. Cavalli, F. Trotta, W. Tumiatti, Cyclodextrin-based Nanosponges for Drug Delivery, Journal of inclusion phenomena and macrocyclic chemistry, 56 (2006) 209-213.

[25] I. Mottas, A. Milosevic, A. Petri-Fink, B. Rothen-Rutishauser, C. Bourquin, A rapid screening method to evaluate the impact of nanoparticles on macrophages, Nanoscale, 9 (2017) 2492-2504.

[26] L. Wehl, C. von Schirnding, M.C. Bayer, O. Zhuzhgova, H. Engelke, T. Bein, Mesoporous Biodegradable Magnesium Phosphate-Citrate Nanocarriers Amplify Methotrexate Anticancer Activity in HeLa Cells, Bioconjugate Chemistry, (2022).

[27] J.G. Croissant, Y. Fatieiev, N.M. Khashab, Degradability and Clearance of Silicon, Organosilica, Silsesquioxane, Silica Mixed Oxide, and Mesoporous Silica Nanoparticles, Adv. Mater., 29 (2017) 1604634.

[28] K. Möller, T. Bein, Degradable Drug Carriers: Vanishing Mesoporous Silica Nanoparticles, Chemistry of Materials, 31 (2019) 4364-4378.

[29] C. Argyo, V. Weiss, C. Bräuchle, T. Bein, Multifunctional Mesoporous Silica Nanoparticles as a Universal Platform for Drug Delivery, Chem. Mater., 26 (2014) 435-451.

[30] K. Möller, T. Bein, Talented Mesoporous Silica Nanoparticles, Chem. Mater., 29 (2017) 371-388.

[31] S. Lucia Appleton, S. Navarro-Orcajada, F.J. Martínez-Navarro, F. Caldera, J.M. López-Nicolás, F. Trotta, A. Matencio, Cyclodextrins as Anti-inflammatory Agents: Basis, Drugs and Perspectives, Biomolecules, 11 (2021).

[32] F. Trotta, R. Cavalli, Characterization and Applications of New Hyper-Cross-Linked Cyclodextrins, Composite Interfaces, 16 (2009) 39-48.

[33] I. Krabicová, S.L. Appleton, M. Tannous, G. Hoti, F. Caldera, A. Rubin Pedrazzo, C. Cecone, R. Cavalli, F. Trotta, History of Cyclodextrin Nanosponges, Polymers, 12 (2020).

[34] S. Datz, B. Illes, D. Gößl, C.v. Schirnding, H. Engelke, T. Bein, Biocompatible crosslinked β-cyclodextrin nanoparticles as multifunctional carriers for cellular delivery, Nanoscale, 10 (2018) 16284-16292.

[35] K. Möller, B. Macaulay, T. Bein, Curcumin Encapsulated in Crosslinked Cyclodextrin Nanoparticles Enables Immediate Inhibition of Cell Growth and Efficient Killing of Cancer Cells, Nanomaterials, 11 (2021).

[36] L. Wehl, C. von Schirnding, M.C. Bayer, O. Zhuzhgova, H. Engelke, T. Bein, Mesoporous Biodegradable Magnesium Phosphate-Citrate Nanocarriers Amplify Methotrexate Anticancer Activity in HeLa Cells, Bioconjugate Chemistry, 33 (2022) 566-575.

[37] Y. Yang, H. Wang, M. Kouadir, H. Song, F. Shi, Recent advances in the mechanisms of NLRP3 inflammasome activation and its inhibitors, Cell Death & Disease, 10 (2019) 128.

[38] V.J. Schüller, S. Heidegger, N. Sandholzer, P.C. Nickels, N.A. Suhartha, S. Endres, C. Bourquin, T. Liedl, Cellular Immunostimulation by CpG-Sequence-Coated DNA Origami Structures, ACS Nano, 5 (2011) 9696-9702.

[39] I. Mellman, H. Plutner, P. Ukkonen, Internalization and rapid recycling of macrophage Fc receptors tagged with monovalent antireceptor antibody: possible role of a prelysosomal compartment, Journal of Cell Biology, 98 (1984) 1163-1169.

[40] A.K. Dey, A. Nougarède, F. Clément, C. Fournier, E. Jouvin-Marche, M. Escudé, D. Jary, F.P. Navarro, P.N. Marche, Tuning the Immunostimulation Properties of Cationic Lipid Nanocarriers for Nucleic Acid Delivery, Frontiers in Immunology, 12 (2021), Article 722411.

[41] A. Martínez-Riaño, E.R. Bovolenta, P. Mendoza, C.L. Oeste, M.J. Martín-Bermejo, P. Bovolenta, M. Turner, N. Martínez-Martín, B. Alarcón, Antigen phagocytosis by B cells is required for a potent humoral response, EMBO reports, 19 (2018) e46016.

[42] S. Hočevar, A. Milošević, L. Rodriguez-Lorenzo, L. Ackermann-Hirschi, I. Mottas, A. Petri-Fink, B. Rothen-Rutishauser, C. Bourquin, M.J.D. Clift, Polymer-Coated Gold Nanospheres Do Not Impair the Innate Immune Function of Human B Lymphocytes in Vitro, ACS Nano, 13 (2019) 6790-6800.

[43] N. Hérault, J. Wagner, S. Abram, J. Widmer, J. Horvath, D. Vanhecke, C. Bourquin, K. Fromm, Silver-Containing Titanium Dioxide Nanocapsules for Combating Multidrug-Resistant Bacteria, Int J Nanomedicine., 15 (2020) 1267-1281.

[44] H. Yin, L. Fang, L. Wang, Y. Xia, J. Tian, L. Ma, J. Zhang, N. Li, W. Li, S. Yao, L. Zhang, Acute Silica Exposure Triggers Pulmonary Inflammation Through Macrophage Pyroptosis: An Experimental Simulation, Frontiers in Immunology, 13 (2022).

[45] M. Tsugita, N. Morimoto, M. Nakayama, SiO2 and TiO2 nanoparticles synergistically trigger macrophage inflammatory responses, Particle and fibre toxicology, 14 (2017) 1-9.

[46] H. Li, X. Tao, E. Song, Y. Song, Iron oxide nanoparticles oxidize transformed RAW 264.7 macrophages into foam cells: Impact of pulmonary surfactant component dipalmitoylphosphatidylcholine, Chemosphere, 300 (2022) 134617.

[47] M. Harel, C. Girard-Guyonvarc'h, E. Rodriguez, G. Palmer, C. Gabay, Production of IL-18 Binding Protein by Radiosensitive and Radioresistant Cells in CpG-Induced Macrophage Activation Syndrome, The Journal of Immunology, 205 (2020) 1167.

[48] C. Girard-Guyonvarc'h, J. Palomo, P. Martin, E. Rodriguez, S. Troccaz, G. Palmer, C. Gabay, Unopposed IL-18 signaling leads to severe TLR9-induced macrophage activation syndrome in mice, Blood, 131 (2018) 1430-1441.

5.6. Appendix

Table S5.1: Particle properties as determined from TEM, nitrogen sorption and zeta potential measurements. (* samples measured with a lipid bilayer).

Sample	Particle size SEM (nm)	Particle size DLS (water) (nm)	Surface area (m^2/g)	Pore vol. (ml/g)	Pore size (nm)	Zeta pot. Pure NP (mV)	Zeta pot. NP-NSA (mV)	Zeta pot. NP-NSA-DD (mV)
MSN	80 (TEM)	245	1098	0.77	3.42	- 36	- 32	- 35
CD-CDI	90	195	40	na	na	- 12	- 12	+ 27
MPC	80	67*	560	0.8	6.3	+ 1/+38*		+ 32

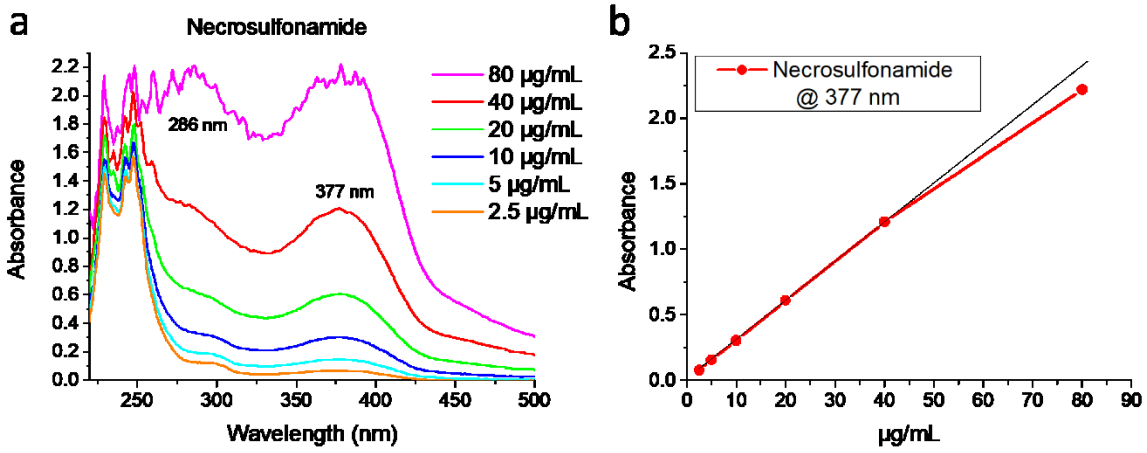

Figure S5.1: UV-VIS absorption spectroscopy of necrosulfonamide (NSA). a) UV-VIS spectra, b) calibration curve derived from absorption intensities at 377 nm.

NSA solutions were derived from a DMSO stock solution (10 mg/mL) and corresponding aliquots were dispersed in water.

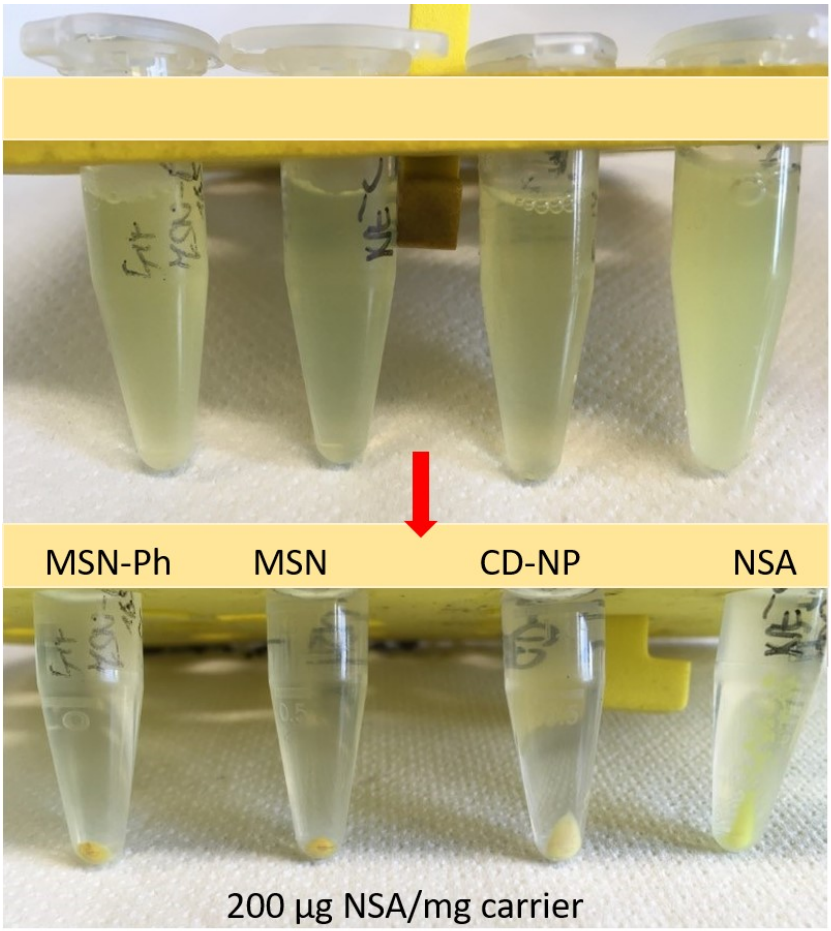

Figure S 5.2: NSA absorption in different carriers before and after centrifugation

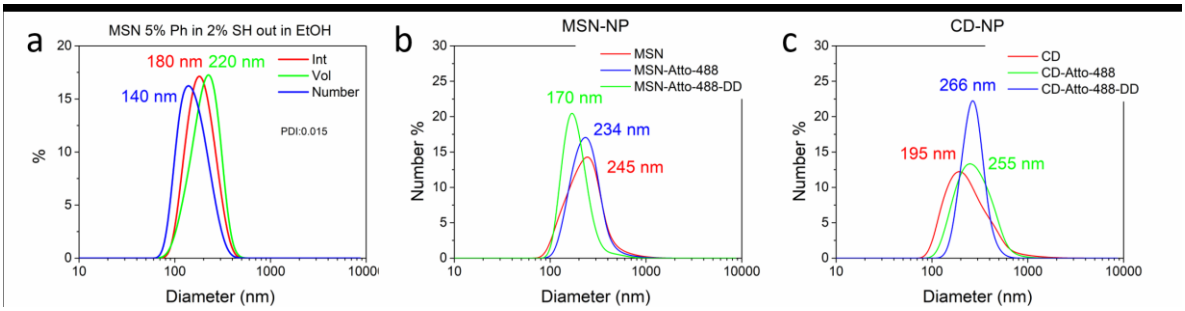

Figure S5.3: DLS measurements of unloaded, ATTO-488 labeled and lipid bilayer covered MSN and CD nanoparticles a) MSN in ethanolic solution, b,c) MSN (b) and CD-NP (c) in aqueous solutions.

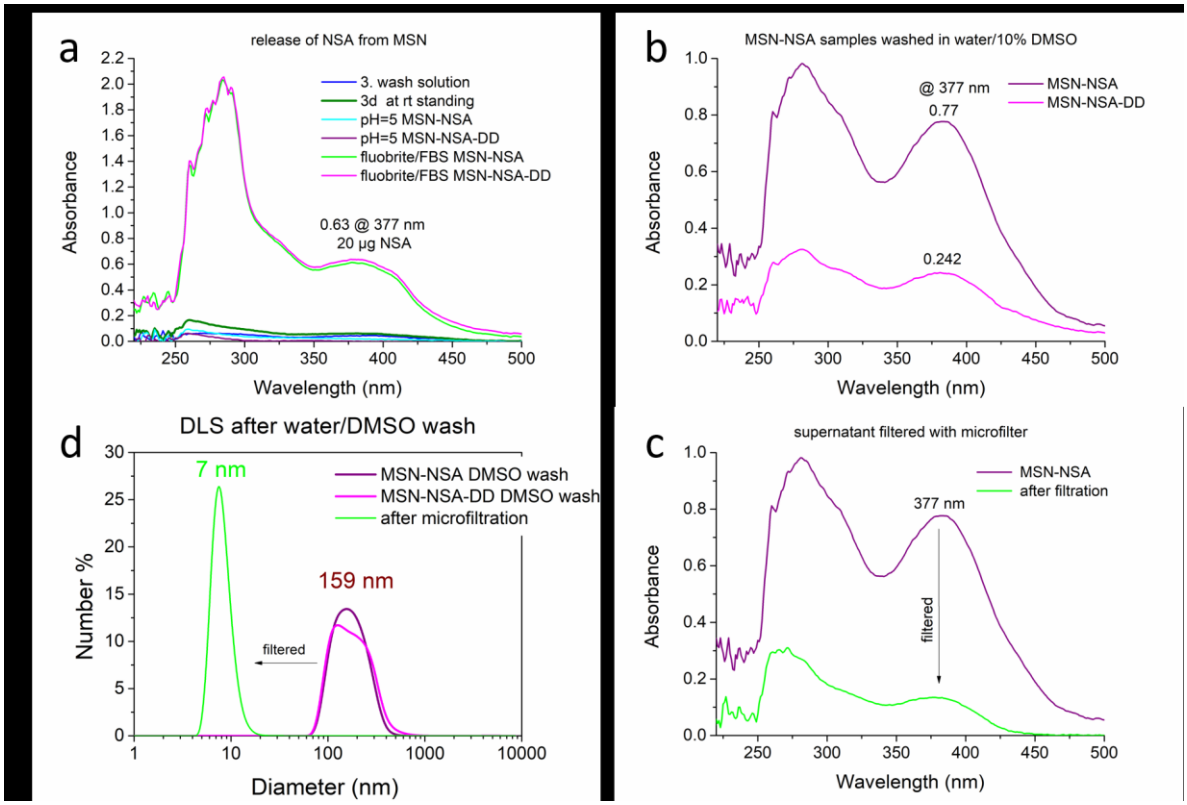

Figure S5.4: NSA release studies in MSN-NSA and MSN-NSA-DD with UV-Vis spectroscopy: 1 mg MSN was loaded with 190 µg NSA (19 wt%) and finally stirred in different solutions. Samples were then centrifuged for 3 minutes and the supernatant was analysed for NSA residues with UV-Vis as shown above. a) Negligible NSA was present in the third washing solution after loading, after 3 days standing in water, or after stirring in aqueous solution at pH=5. When Fluobrite medium containing 10% FBS was used as solution we recovered 20 µg NSA in the supernatant after 1 h stirring with or without a lipid bilayer DD. b) Samples were also stirred in aqueous solution containing 10% DMSO in which NSA is soluble. Under these conditions we recovered 25 µg NSA of the 190 µg from MSN-NSA without lipid bilayer and 7.6 µg NSA from MSN-NSA-DD with lipid bilayer.

We should note that upon measuring the supernatant solutions with dynamic light scattering (DLS) we always encountered a signal typical for MSN particle sizes, indicating incomplete sedimentation of particles. The NSA concentration based on UV-Vis absorption decreased strongly to 4 µg (from 25 µg as measured before) when these solutions were finally filtered with a microfilter (see Fig. S4 c) and the particles vanished, leaving only 7 nm particles in the solution, presumably from very low-concentrated NSA in water (see Fig. S4d). We can therefore conclude that a premature NSA release is unlikely in cell medium even when particles are not covered by a lipid bilayer.

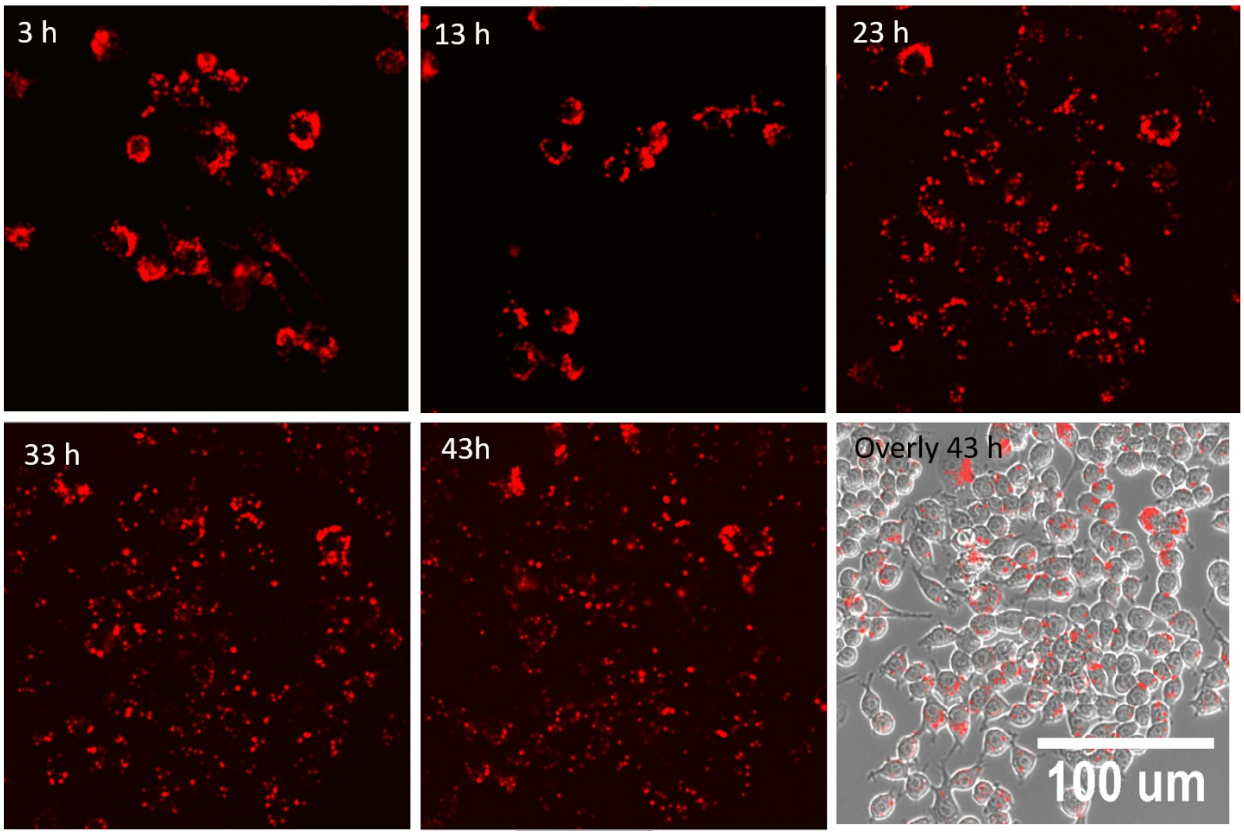

Figure S5.5: Images of RAW 264.7 cells with the CY5 channel (identical spot in time, zoomed-in area, x20 objective) showing the uptake and transfer of unloaded 633-labeled MSN particles upon cell division to new cells in time (a medium change was performed after 3 h).

Even after a period of 43 hours we notice MSN particles in nearly every cell.

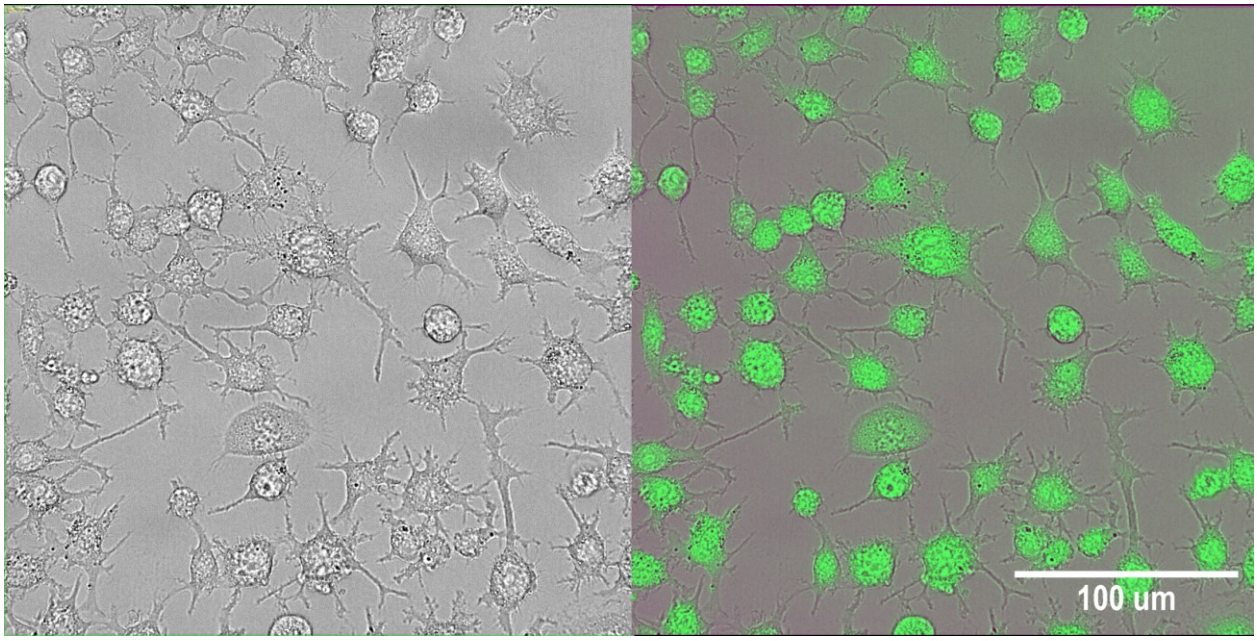

Figure S5.6: RAW264.7 cells after exposure to free NSA as measured in transmitted light and in the GFP fluorescence channel (overlay at right, x40).

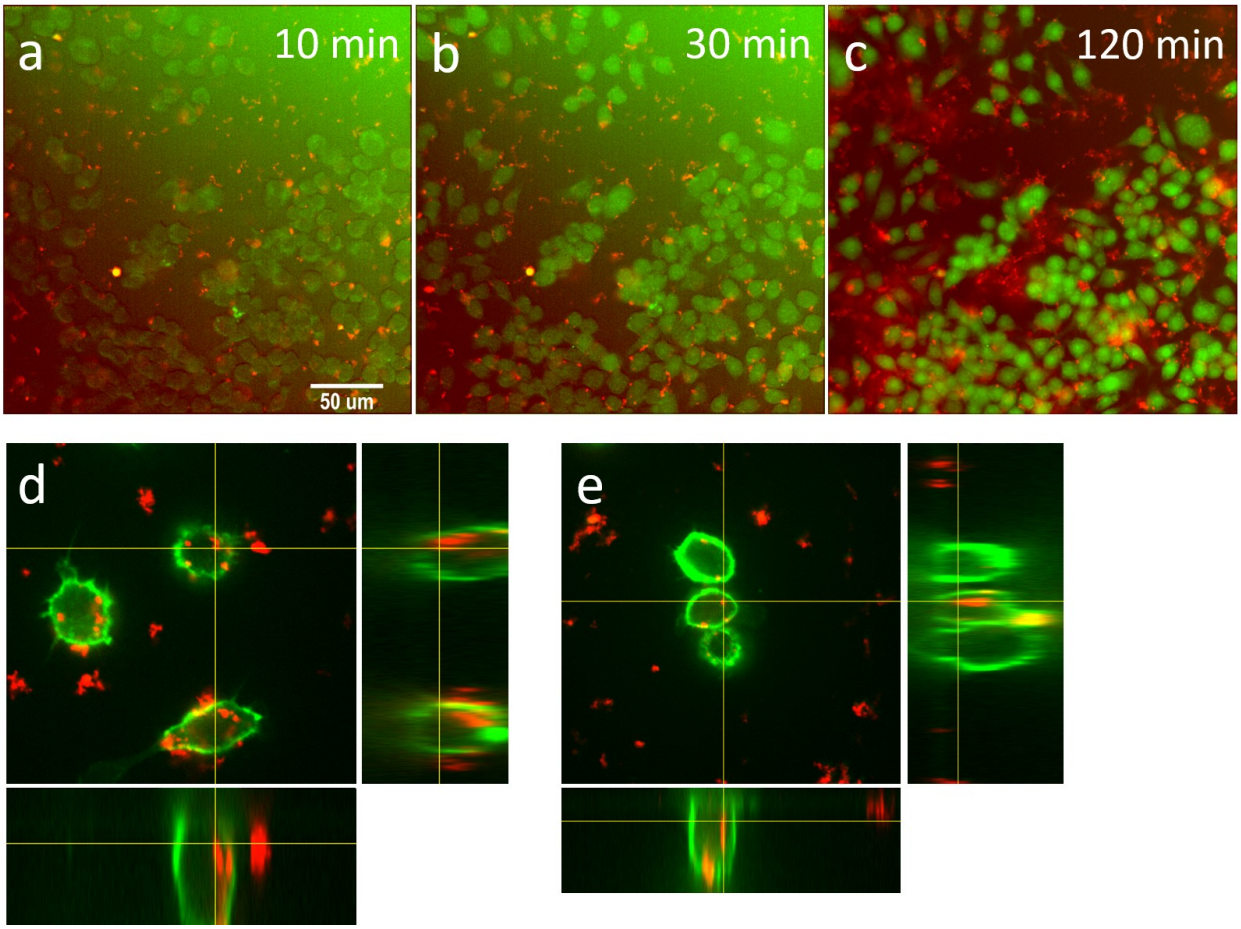

Figure S5.7: a,b,c) Time-lapse images (x20 objective) of NSA delivery (green) to RAW 264.7 cells with NSA-loaded, ATTO-633 labeled CD nanoparticles (red). GFP (NSA) and CY5 channels are overlaid. d,e) Confocal fluorescence microscopy images including cross sections of WGA-stained (green) RAW 264.7 cells incubated with ATTO-633 (red) labeled CD-NP d) without and e) with a lipid bilayer; 2 h after incubation. Cross sections of selected cells show the location of CD-NP within the cellular compartment.

NSA is delivered on a similar time scale as with MSN particles. Confocal microscopy shows the internalization of both CD-NP and lipid-bilayer covered CD-DD nanoparticles.

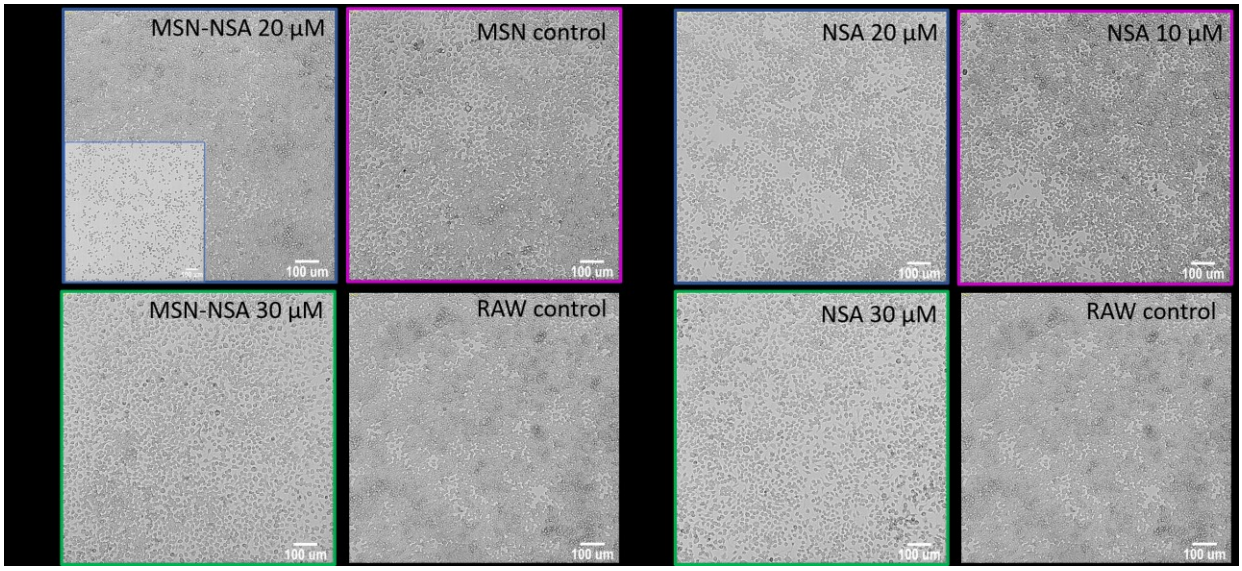

Figure S5.8: Cell density shown in transmitted-light images of RAW 264.7 cells taken 45 h after exposure to a) NSA-loaded MSN (a representative image at the start of the measurements is seen as inset) or b) to free NSA. Images correspond to Fig 5 in the main part of the manuscript. Images were taken with the ImageXpress at x10 magnification.

Cell growth with reduced growth kinetics is observed when pure NSA is added to RAW 264.7 cells. However, cells are still alive even after exposure to 30 µM NSA as seen below in Figure S9.

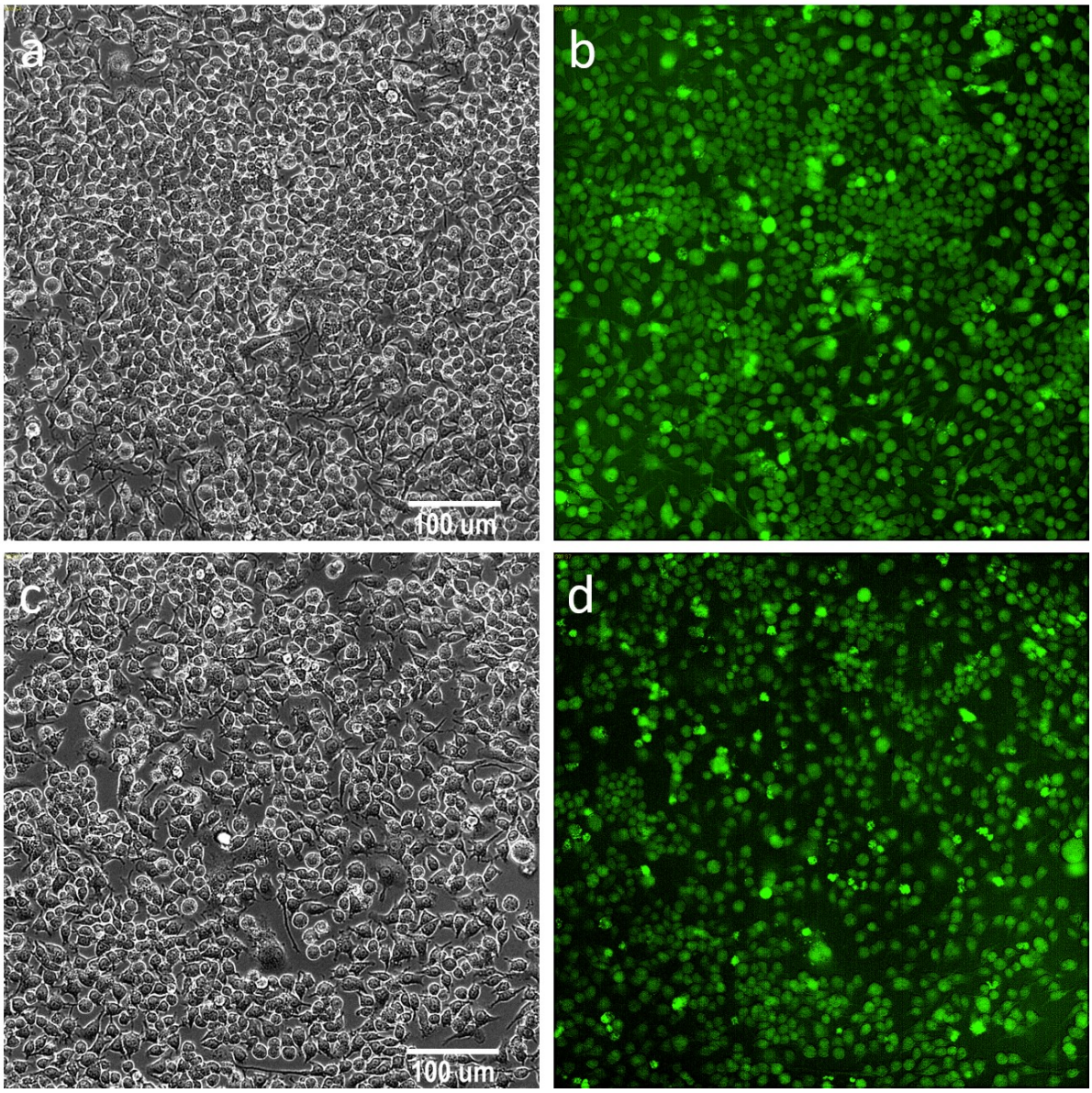

Figure S5.9: ImageXpress micrographs of RAW 264.7 cells after 45 h exposure to NSA-loaded MSN or to free NSA without medium change (transmitted light and GFP filter). a, b) MSN-NSA 30 µM and c, d) free NSA 30 µM. TL and GFP channel (x20 objective).

Images show that cells are alive even after a long incubation time of 45 h. NSA appears auto-fluorescent upon enrichment in cells.

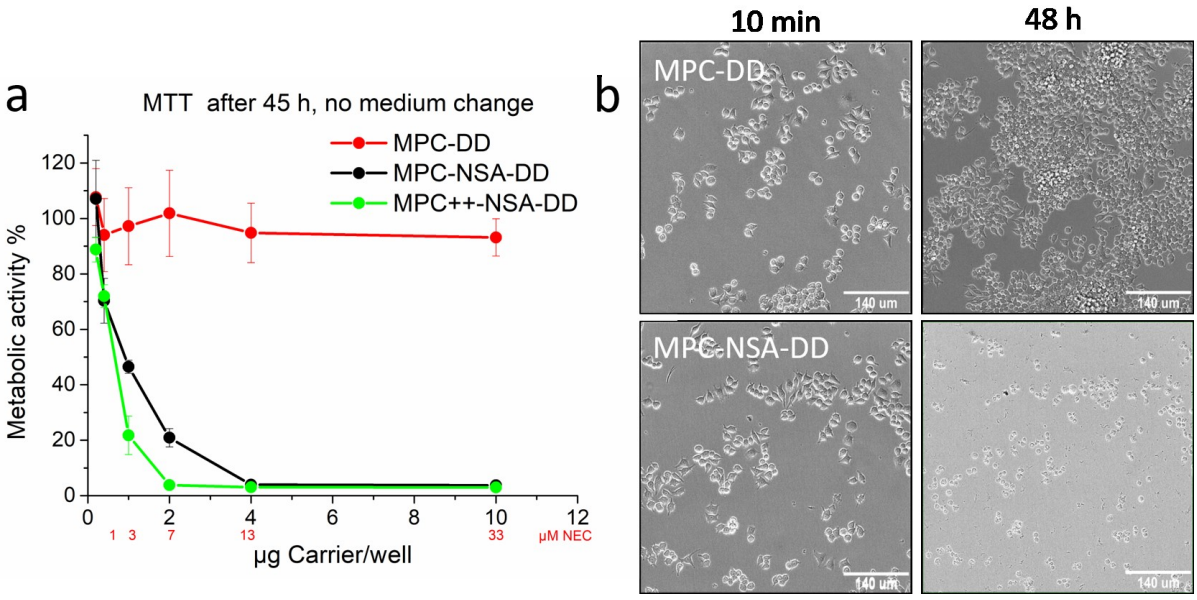

Figure S 5.10: a) MTT assay testing metabolic activity of RAW 264.7 cells after 45 h incubation with unloaded MPC-DD particles and particles loaded with 16 wt% NSA (MPC-NSA-DD) or 32 wt% NSA (MPC++-NSA-DD) without performing a medium change, b) corresponding TL images (20x) of (top row) 4 µg/well pure MPC-NP and (bottom) MPC-NSA-DD-NP after 10 minutes and 48 h incubation.

While empty MPC particles do not affect cell growth kinetics (see Figure 6b main text), a complete block in metabolic activity is observed already after 2 h with MPC-NSA-DD particles, as is also seen in the microscope images showing no cell growth when treated with these particles. We note that loading of these MPC particles with NSA required small concentrations of the surfactant CTAC, which is apparently detrimental for RAW 264.7 cell survival.

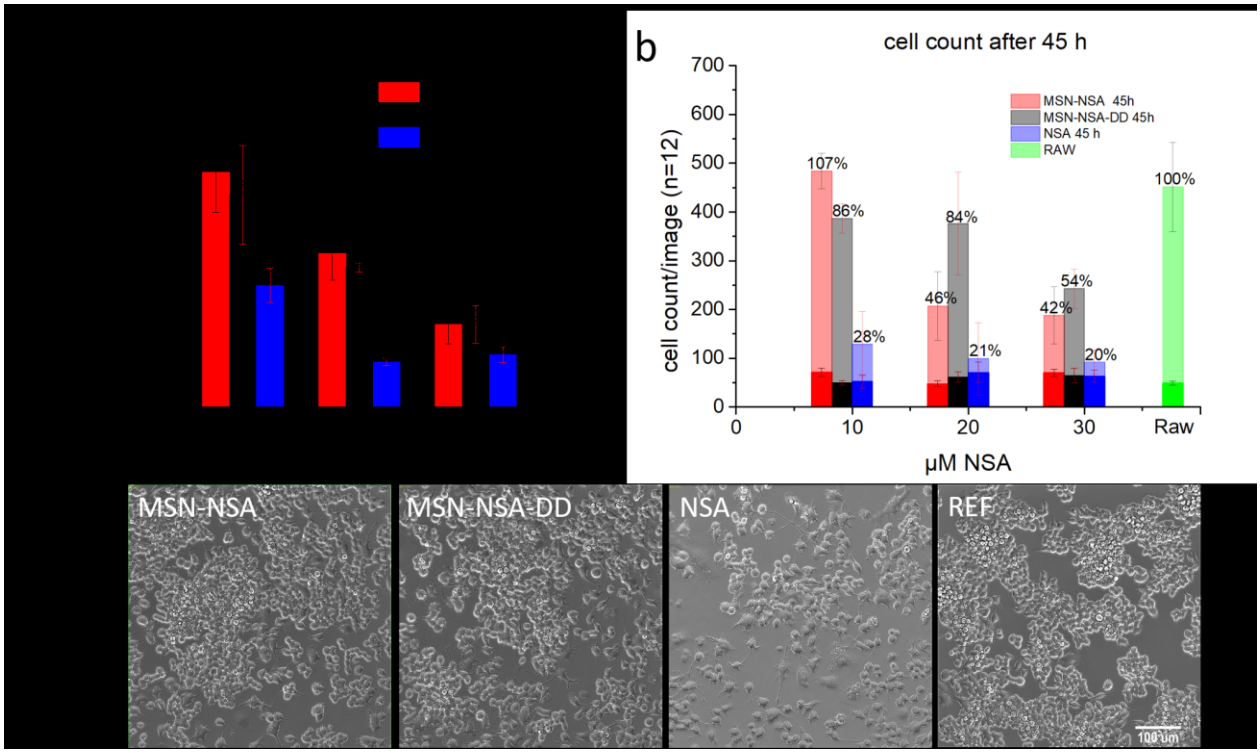

Figure S 5.11: Assessment of RAW 264.7 cell survival after long incubation times of 45 h without medium change with NSA-loaded MSN particles in comparison to exposure to free NSA. a) MTT assay (identical data as shown in Fig. 6a for comparison), b) cell counts obtained from images at start (strong colors) and after 45 h exposure (lighter colors), c) selected images after 45 h exposure to 10 μM NSA (20x).

In addition to the MTT assay shown in S11a, we followed RAW 264.7 cell proliferation by counting the cells in time-lapse images during these measurements in order to show cell growth and thus viability even under exposure of NSA-loaded MSN particles. 12 images were analyzed and averaged for each concentration and time point by an automated cell counting routine. As shown in Fig. S11b, all cells have proliferated during the 45 h when compared to the initial cell count (depicted at the bottom of the bars in bold colors). Untreated cells are represented as green bar and for ease of comparison we have noted the relative cell concentrations on top of the bars. Representative images after 45 h are displayed in Fig. S11c. All images show living cells, only with lower density when compared to the untreated reference cells. Here, the untreated and MSN-NSA treated RAW 264.7 cells have formed typical cell clusters with partial overgrowth after 45 h, while cells exposed to free NSA are evenly spread out with a lower overall confluency.

Overall, MTT assays and cell counts give comparable results concerning the final live cell concentration, showing a greater negative impact of the free NSA on cell proliferation.

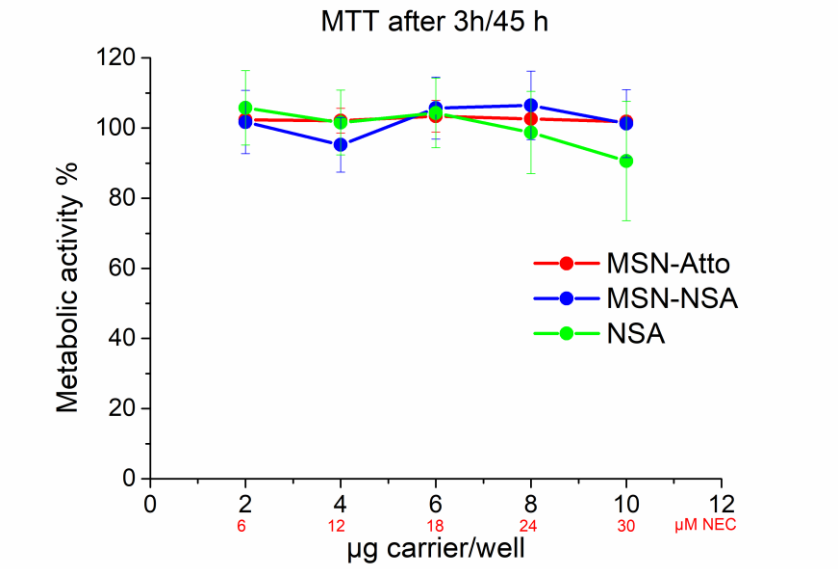

Figure S 5.12: RAW 264.7 cell metabolic activity after MSN exposure, assayed with MTT after 45 h, including a medium change after 3 h. Results are expressed in % as compared to untreated control cells.

When a medium change and thus cell wash is performed 3 h after particle exposure, we do not encounter any effect on cell activity when measured with MTT after 45 h.

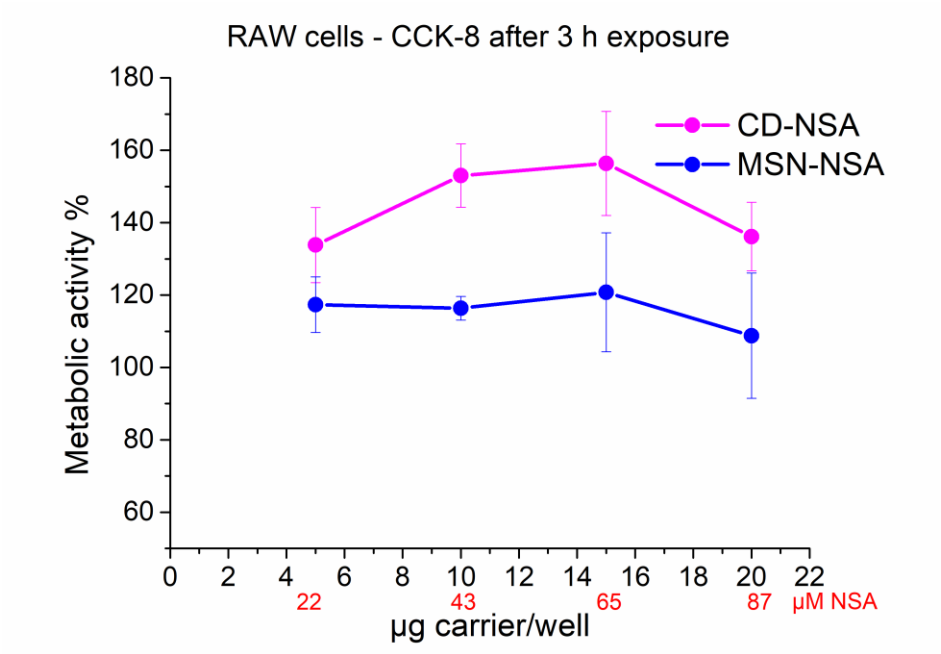

Figure S 5.13: RAW 264.7 cell viability assay performed after 3 h exposure and high NSA concentrations up to 87 µM with NSA-loaded MSN and CD-NP. Results are expressed in % as compared to untreated control cells. NSA concentrations are indicated in red.

Cells are unaffected after 3 h even when exposed to very high NSA concentrations of over 80 µM when the NSA is delivered via nanoparticles.

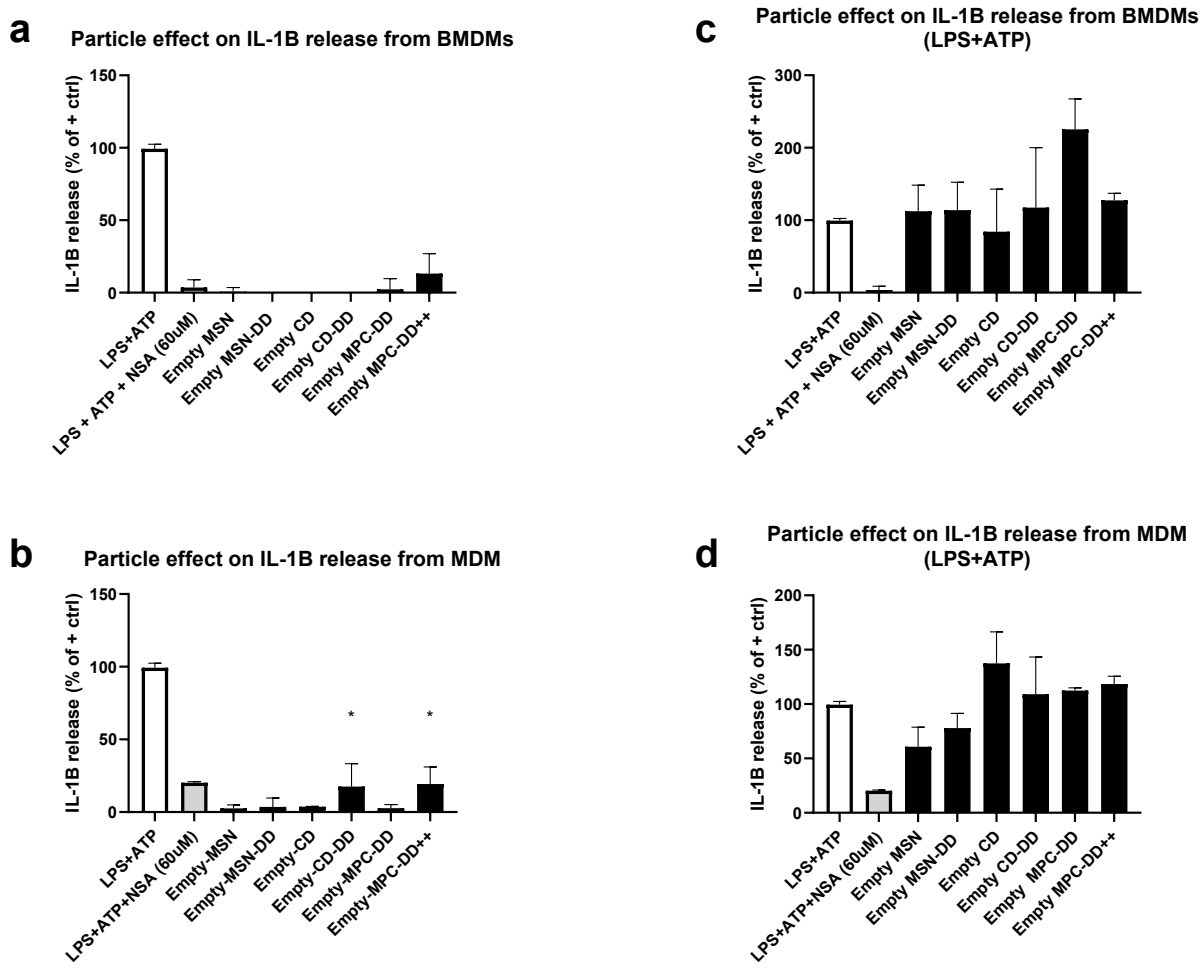

Figure S 5.14: IL-1β release by mouse BMDM (a,c) and human MDM (b,d): effect of unloaded particles on untreated mouse BMDM (a) and untreated human MDM (b). Effect of unloaded particles on activated (LPS+ATP) mouse BMDM (c) and hMDM (d). Exposure time and particle concentration are as in Fig. 9.

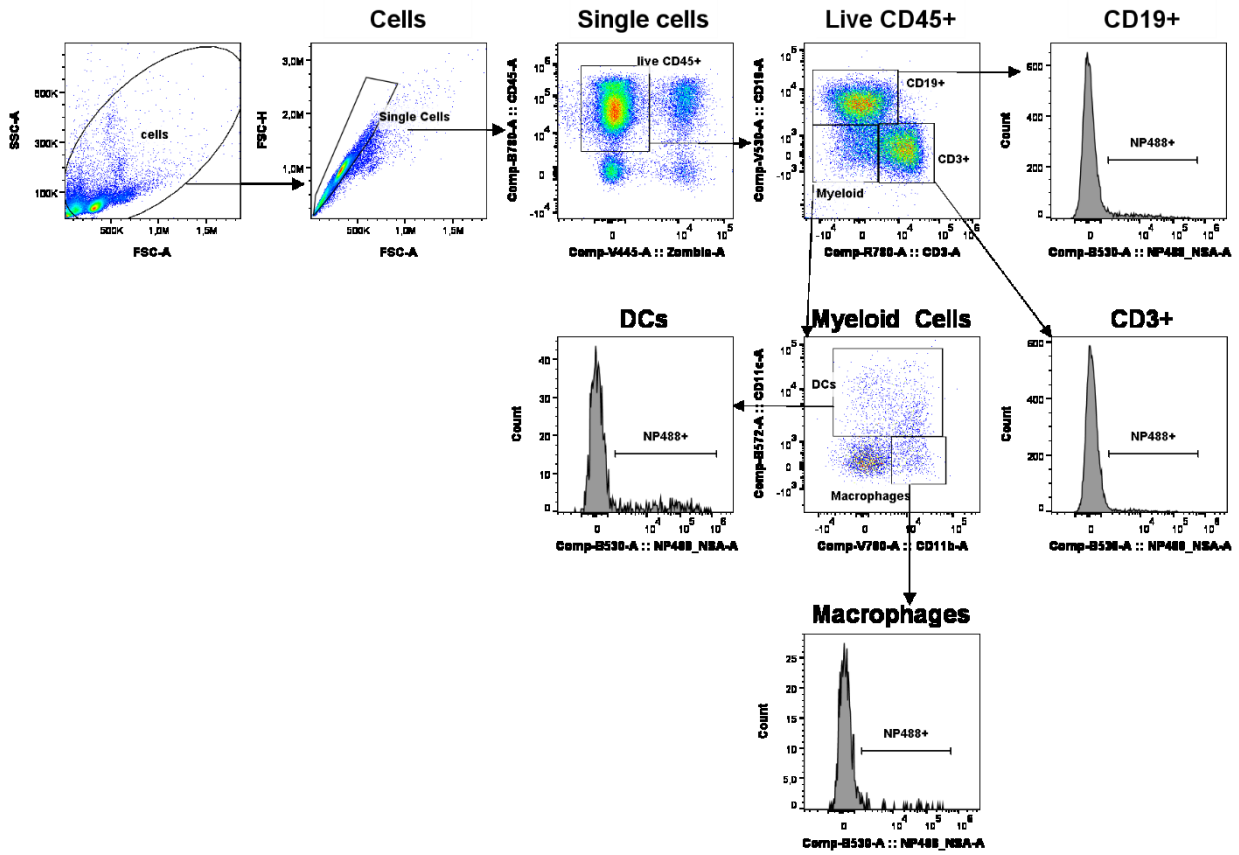

Figure S 5.15: Flow cytometer gating strategy to compare uptake of CD-488, CD-DD-488, MSN-488 and MSN-DD-488 in different subsets of immune cells among murine splenocytes. Splenocytes were incubated for 2, 6 and 24 hours with the particles. After incubation cells were washed with a light acid (NaCl, glycine, pH=3) to wash away cell membrane-bound particles. The following gating strategy was then applied. The first two gates were set to exclude cell debris and doublets. Dead cells were excluded using a viability marker. B-cells ($CD19^+$), T-cells ($CD3^+$), dendritic cells (DCs, $CD11c^+$) and macrophages ($CD11b^+$, $CD11c^-$) were then further examined for the presence of NPs.

CHAPTER 6

Particle-Size-Dependent Delivery of Antitumoral miRNA Using Targeted Mesoporous Silica Nanoparticles

6. Particle-Size-Dependent Delivery of Antitumoral miRNA Using Targeted Mesoporous Silica Nanoparticles

This chapter was published as:

Lisa Haddick, Wei Zhang, Sören Reinhard, Karin Möller, Hanna Engelke, Ernst Wagner, Thomas Bein *Pharmaceutics* **2020**, *12*, 505.

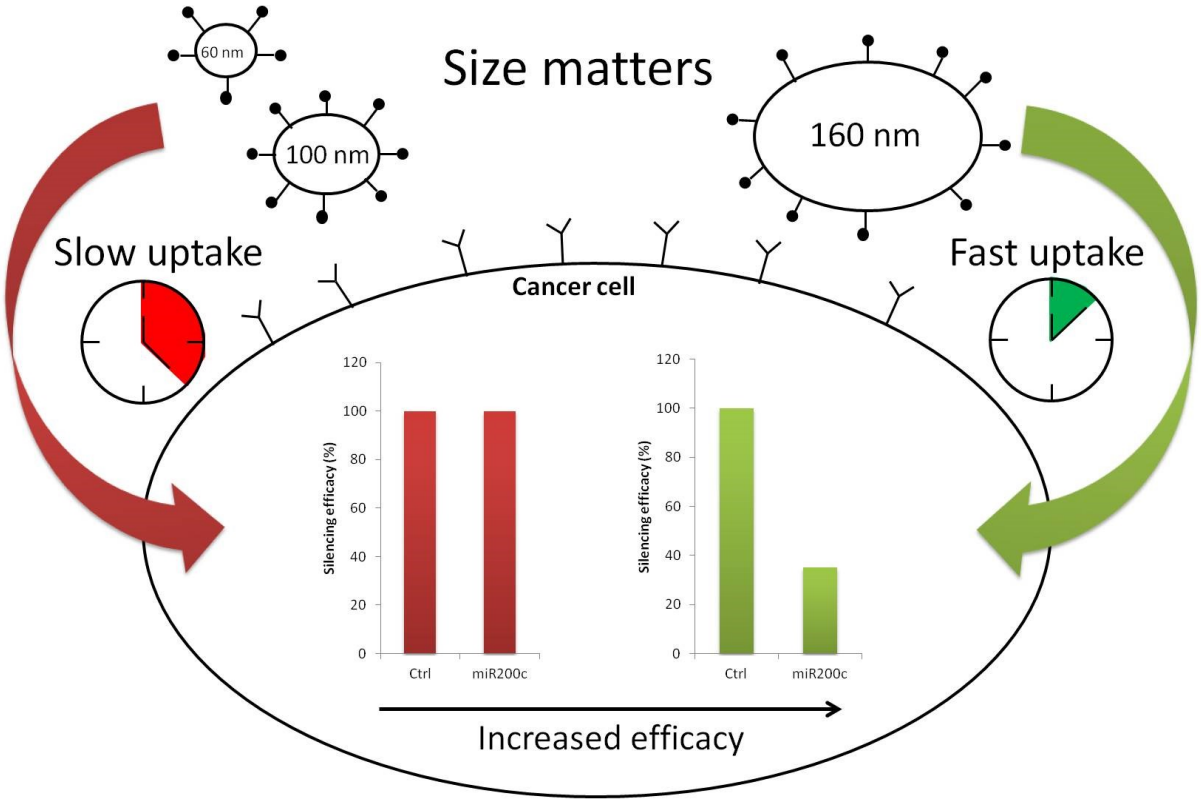

Abstract

Multifunctional core-shell mesoporous silica nanoparticles (MSN) were tailored in size ranging from 60 to 160 nm as delivery agents for antitumoral microRNA (miRNA). The positively charged particle core with a pore diameter of about 5 nm and a stellate pore morphology allowed for an internal, protective adsorption of the fragile miRNA cargo. A negatively charged particle surface enabled the association of a deliberately designed block copolymer with the MSN shell by charge-matching, simultaneously acting as a capping as well as endosomal release agent. Furthermore, the copolymer was functionalized with the peptide ligand GE11 targeting the epidermal growth factor receptor, EGFR. These multifunctional nanoparticles showed an enhanced uptake into EGFR-overexpressing T24 bladder cancer cells through receptor-mediated cellular internalization. A luciferase gene knock-down of up to 65% and additional antitumoral effects such as a decreased cell migration as well as changes in cell cycle were observed. We demonstrate that nanoparticles with a diameter of 160 nm show the fastest cellular internalization after a very short incubation time of 45 min and produce the highest level of gene knock-down.

6.1. Introduction

A novel modality in cancer therapy emerged over the past two decades in the form of gene therapy and in this context, small interfering RNA (siRNA) and micro RNA (miRNA) are promising alternatives to common anti-cancer medications.[1, 2]. Both nucleotide oligomers mediate the process of RNA interference (RNAi) in which cells use these short RNA strands of 19-24 nucleotides to recognize messenger RNA (mRNA) with a complementary sequence, induce their destruction and thus inhibit the translation into proteins. To provide cancer therapy, synthetically produced siRNA and miRNA mimics can be used that target and silence specific oncogenes. Recent studies have identified a number of cancer-related genes as potential targets for RNAi-based therapy[3-5]. One of these tumor suppressor miRNA is miR200c, which targets the proto-oncogene KRAS. It regulates cell differentiation, proliferation and survival[6], the epithelial to mesenchymal transition[7] and suppresses chemoresistance[8].

However, a major challenge for a widespread therapeutic application of RNAi is creating appropriate delivery vehicles to safely and effectively deliver and release siRNA and miRNA into the cytosol of disease-causing cells. Several excellent reviews summarize the requirements for siRNA delivery and comprehensively report on the efficiencies of gene silencing achieved with various delivery materials[9-11].

Some promising results were recently obtained from ongoing clinical trials concerning RNA delivery vehicles and in 2018 Alnylam's Onpattro (Patisiran) has been FDA-approved as the first ever RNAi drug against nerve damage caused by the rare hereditary disease, transthyretin amyloidosis.[12] However, Patisiran is a lipid-based nanocarrier system that does not actively target the cancer tissue, and most of the administered drug accumulates passively in the liver instead. Therefore, robust and specifically targeted carrier systems are needed for an efficient delivery of siRNA and miRNA to prevent a premature degradation of the unstable RNA. For

this purpose, nanoparticles have attracted much attention because they provide a stable, nontoxic, and highly flexible platform.

Mesoporous silica nanoparticles (MSN) are emerging as potential nanocarriers for a variety of anti-cancer cargos including nucleic acids.[13,14] The properties that have rendered them specifically suitable for siRNA and miRNA delivery include a high surface area and pore volume, a controllable biodegradability[15, 16], the tunability of particle size and pore size, their variable morphology and importantly, the possibility to create core-shell particles constructed of spatially separated regions with different surface functionalization.[17,18]

This tunability of MSNs opens the possibility to systematically study the influence of the carrier properties on the gene silencing efficacy. Multiple parameters can affect successful gene silencing using carrier agents, e.g., the adsorption and release kinetics of the nucleic acid in the drug carrier, the dependence of cellular uptake or endosomal escape on nanoparticle size, surface characteristics such as charge and/or the attachments of functional residues, to name a few, but systematic studies addressing these issues are rare.[19]

For the adsorption and release kinetics of nucleic acids using MSNs, the pore size, pore morphology and surface charge are important parameters. High loadings of nucleic acid were achieved by using large pore MSNs with a pore diameter of around 10–20 nm[20] and when pores were modified with cationic functional groups—aminopropyltriethoxysilane (APTES) or polylysine—to create a cationic layer for nucleic acid adsorption.[14, 21] However, some of these systems suffer from poor release kinetics associated with low knockdown efficacies because of either the high affinity of polycations towards nucleic acid or because of a bottleneck-type pore morphology that features smaller pore openings than pore diameters, which both might decrease an efficient release of the highly charged nucleic acid molecules. Based on these findings, our group introduced novel medium-pore MSNs (pore diameter of around 5 nm) with

stellate pore morphology, which were able to adsorb an exceptionally high amount of siRNA of 380 μg mg^{-1} and which enabled a mainly electrostatically driven fast and efficient RNA desorption, resulting in a high silencing efficacy.[21]

Cellular internalization of the nanocarrier is another factor that influences gene silencing efficacy. The relationship between shape and size of MSNs[22-25] or other nanocarriers[26,27] and cellular internalization is important as nanoparticle size may affect the uptake efficiency and kinetics and the internalization mechanism.[28] One of the great advantages of MSNs is that they can be designed to feature different sizes and shapes. For MSNs[22,29] as well as for Au[30], polystyrene[31] and iron oxide nanoparticles[32], a size-dependent uptake in cells was observed with a maximum uptake at a particle diameter of 30–50 nm. However, as size is only one among several parameters controlling cellular uptake of nanoparticles, optimal sizes may vary for different surfaces and different surface functionalizations. Additionally, targeting ligands were shown to improve selective cellular uptake and a better accumulation in tumor tissue.[33,34] The effect of particle size on gene transfection efficiency using silica-based nanoparticles with diameters from 125 to 570 nm as nanocarriers for plasmid DNA was studied by Yu *et al.* Here, the transfection efficiency was found to be a compromise between binding capacity of the nanocarriers and cellular uptake. Smaller particles showed higher cellular uptake but less binding capacity for plasmid DNA. Particles with a diameter of 330 nm showed the best gene transfection efficacy.[35]

Gene silencing mediated by delivery of siRNA and miRNA with MSN nanocarriers is strongly dependent on the escape of siRNA or miRNA from the endosomes into the cytosol. To trigger this reaction, the surface of particles is often decorated with cationic polymers, which are known to support an endosomal escape. Polyethylenimine (PEI) is one well-studied polymer exhibiting good endosomal escape capability when used at high dosage, attributed to a ‘proton

sponge' effect, however, it has a poor toxicity profile.[36] For instance, the group of Gu showed very good knockdown efficacies when PEI was attached to the outside of their particles.[37,38]

A systematic study of the correlation between gene knockdown efficacy and endosomal escape kinetics was performed by Wang *et al.*.[39] They used magnetic MSNs capped with PEI at low concentrations to avoid toxic effects, resulting in poor endosomal escape ability. When endosomal escape was induced by a chloroquine treatment at early transfection times they could still see a high gene silencing efficacy. In contrast, when applied at later stages, a low gene-silencing efficacy was found, presumably because the released RNA was already degraded within the endosome.

Although MSNs have shown great potential as an efficient carrier system for siRNA and miRNA delivery, systematic studies about particle properties and corresponding gene-silencing efficacy remain rare. Herein, we present a systematic investigation of the particle size-dependent delivery of miRNA using core-shell MSNs for gene silencing in T24 cells. A series of MSNs with uniform sizes ranging from 60 to 160 nm with an average pore diameter of around 5-6 nm was used to encapsulate an antitumoral microRNA mimic (miR200c) or a control RNA with a scrambled sequence (Ctrl). The core of these particles was functionalized with APTES to yield a positively charged inner surface to accommodate the negatively charged miRNA, while a thinner surface layer was enriched with mercaptosilane, forming a negatively charged shell to enable binding of the capping agent. This consisted of an amino-acid block-copolymer 454 (see Figure 6.1) to aid endosomal escape and which was further linked via polyethylene glycol (PEG) to the peptide GE11, targeting the epidermal growth factor receptor.[40] This vector is abbreviated as MSN-454-GE11. An alternative construct for the delivery of this miRNA was studied before by Müller *et al.* using RNA-encapsulating polyplexes consisting of the same copolymer 454 functionalized with GE11.[41] Their particles,

featuring a size of 120-150 nm, successfully showed antitumoral effects with two different therapeutic RNAs.

Our series of MSN-454-GE11 particles covers a broad size range but still provides comparable properties for each sample, including surface chemistry, surface charge, pore size and miRNA concentration to enable a conclusive study of the particle-size effect on miRNA delivery. Here, we show that good gene-silencing and antitumoral effects are obtained when miR200c is delivered by the largest MSN-454-GE11 particles in this sequence.

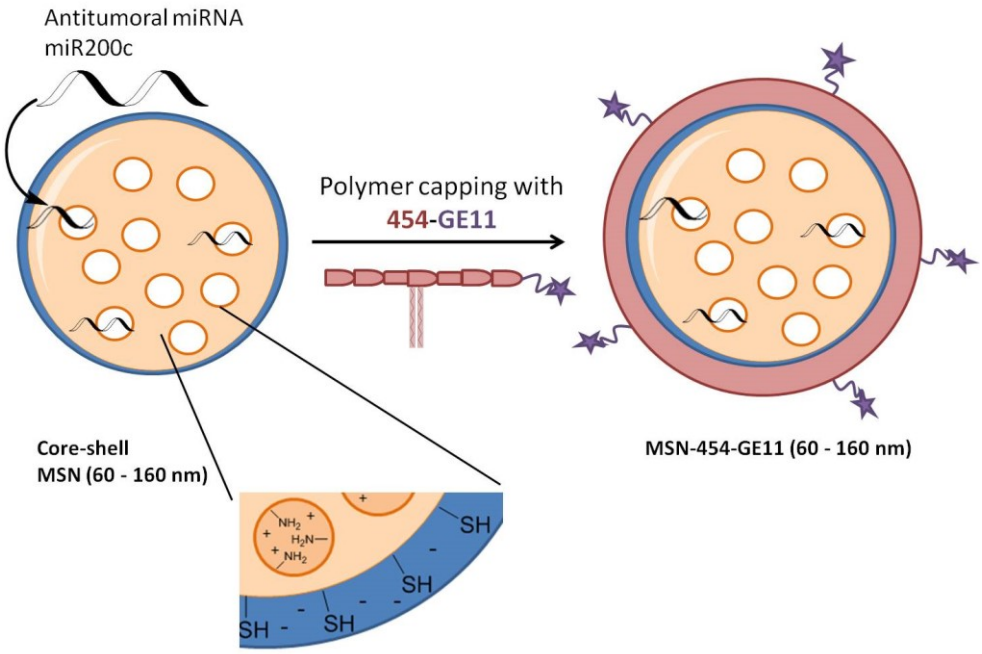

Figure 6.1: Schematic overview of the structure of core-shell mesoporous silica nanoparticles (MSN), the loading of miR200c and the polymer capping resulting in the MSN-454-GE11 vector. The positively charged core in core-shell MSN enables a high loading capacity for miRNA. The mercapto-lined MSN shell associates with a positively charged block copolymer carrying the targeting ligand GE11, thus acting simultaneously as capping, endosomal release and targeting agent.

6.2. Results and Discussion

Particle Synthesis. We synthesized a series of core-shell MSNs with uniform size, ranging from 60 to 160 nm via a delayed co-condensation method.[17] The core of all MSNs was functionalized with 4.5 mol% APTES (with respect to total silica) carrying amino groups in

order to create a positively charged inner void volume capable of encapsulating the negatively charged RNA by electrostatic interaction. The outer surface was functionalized with 2 mol% mercaptopropyl triethoxysilane (MPTES) carrying a thiol functionalization to act as regiospecific linker for external binding of polymer and targeting ligand.

Two slightly different approaches were used to modulate the particle size of MSNs and to prepare a series of MSNs with uniform sizes over a range from 60 to 160 nm. Larger particles with average particle sizes of 160, 130 and 100 nm (MSN160 nm, MSN130 nm and MSN100 nm) were synthesized based on our previous reports using a decreasing amount of the base triethanolamine (TEA) in order to reduce the particle size (experimental details are described in the Materials and Methods section).[43,44,46] Briefly, to prepare the core of our core-shell particles, a preheated solution containing cetyltrimethylammonium chloride (CTAC) as template and triisopropylbenzene (TiPB) as pore-expanding agent was mixed with a preheated solution containing TEA, tetraethoxysilane (TEOS) and APTES at an elevated temperature for 20 min. This was then followed by addition of the ingredients for the surface layer containing TEOS and MPTES. To prepare smaller particles with average particle sizes of 80 and 60 nm (MSN80 nm and MSN60 nm), we applied a slightly different procedure, additionally using F127 as growth inhibitor/pore expanding agent according to published reports.[45] The particle size and core-shell structure were then established as above, again by changing the molar ratio of TEOS:TEA. Hereby, a preheated solution of octadecyltrimethylammonium bromide ($C_{18}Br$) as template was mixed with a second preheated solution of TiPB, F127, TEA, TEOS and APTES, and stirred at 60 °C for 30 min. Afterwards, premixed TEOS and MPTES were added to form the negatively charged shell layer.

Characterization. The particles were characterized using a number of techniques including transmission electron microscopy (TEM), dynamic light scattering (DLS), thermogravimetric analysis (TGA), zeta potential measurements, Raman and IR spectroscopy. The particle size

and the morphology were analyzed with TEM and DLS. All MSN samples show a spherical particle morphology with a disordered, wormlike pore structure, independent of size (Figure 6.2). Figure 6.2a,b shows a size distribution around 160 nm (sample MSN160 nm) for particles obtained with the CTAC synthesis using a molar ratio of TEOS:TEA = 1:10. As the molar ratio of TEOS:TEA was decreased to TEOS:TEA = 1:5 and 1:3, the average particle size decreased to 128 nm (sample MSN130 nm, Figure 6.2c,d) and 100 nm (sample MSN100 nm, Figure 6.2e,f), respectively. Particles obtained by the F127 synthesis show a mean particle size of 80 nm (sample MSN80 nm, TEOS:TEA = 1:5, Figure 6.2g,h). The smallest particles with a mean particle size of 60 nm (sample MSN60 nm, Figure 2i,j) were obtained with F127 and a TEOS:TEA ratio of 1:3. DLS measurements of suspended particles show slightly larger hydrodynamic diameters ranging from 90 to 250 nm (Figure S6.1) but clearly illustrate the same trend of a decreasing particle size with decreasing TEA concentration.

Nitrogen sorption measurements resulted in typical type IV isotherms for all samples, as expected for MSNs (Figure 6.3a). Surface analysis indicates higher surface areas for particles prepared by the CTAC synthesis (samples MSN160 nm, MSN130 nm and MSN100 nm) ranging between 742–960 m^2/g, and shows a similar pore size of about 4.8 nm. Slightly smaller surface areas but larger pore sizes were obtained for particles prepared by the F127 synthesis (MSN80 nm, MSN60 nm; 660–685 m^2/g; pore size 6.0 nm, Figure 6.3b). Table 6.1 summarizes the properties of the particles obtained by the different synthesis methods.

Table 6.1 Synthesis and properties of MSN samples.

Name	**Synthesis Method**	**Diameter TEM [a] [nm]**	**A_{BET} [m^2/g]**	**Pore Volume [b] [cc/g]**	**Pore Size [c] [nm]**
MSN160 nm	CTAC Synthesis; TEOS:TEA = 1:10	159 ± 21	742	0.80	4.8
MSN130 nm	CTAC Synthesis; TEOS:TEA = 1:5	128 ± 30	961	1.06	4.8

MSN100 nm	CTAC Synthesis; TEOS:TEA = 1:3	100 ± 37	811	0.95	4.8
MSN80 nm	F127 Synthesis; TEOS:TEA = 1:5	84 ± 23	685	0.95	6.0
MSN60 nm	F127 Synthesis; TEOS:TEA = 1:3	59 ± 8	660	1.00	6.0

[a] The average particle size was obtained from TEM micrographs by measuring the diameter of around 200 particles of respective samples. [b] The total pore volume was determined at p/p_0 = 0.9 to exclude contributions of textural porosity. [c] Data were acquired from the adsorption branch of the nitrogen isotherm.

The presence of the amino and thiol groups originating from functionalization was verified with Raman and IR spectroscopy as well as with TGA. Representative results for sample MSN160 nm are shown in Figure 6.3c–d, respectively. Raman spectroscopy shows the S–H stretching mode of the thiol groups in the particle shell at 2580 cm^{-1} (Figure 6.3c), while the primary amines from core functionalization are seen at 1630 cm^{-1} with IR spectroscopy (MSN160 nm, black line, Figure 6.3d). TGA confirms the inclusion of organic functional groups by a weight loss of 20% (Figure S6.2). The decomposition of aminopropyl and successively, the mercaptopropyl groups starts at 290 °C.

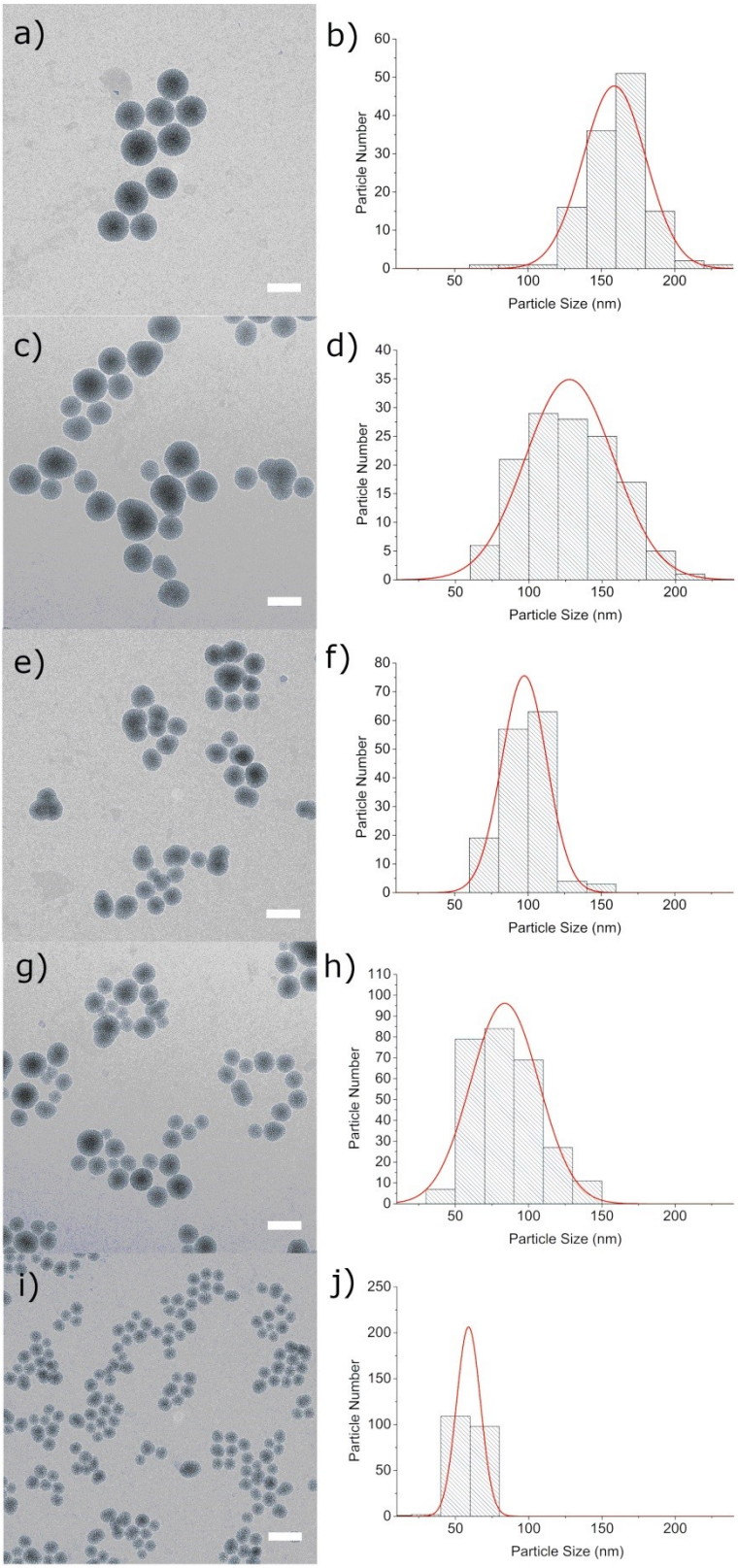

Figure 6.2 TEM micrographs of (a) MSN160 nm, (c) MSN130 nm, (e) MSN100 nm, (g) MSN80 nm, (i) MSN60 nm and corresponding particle size distribution histograms obtained from TEM images (b,d,f,h,j). Scale bar represents 150 nm.

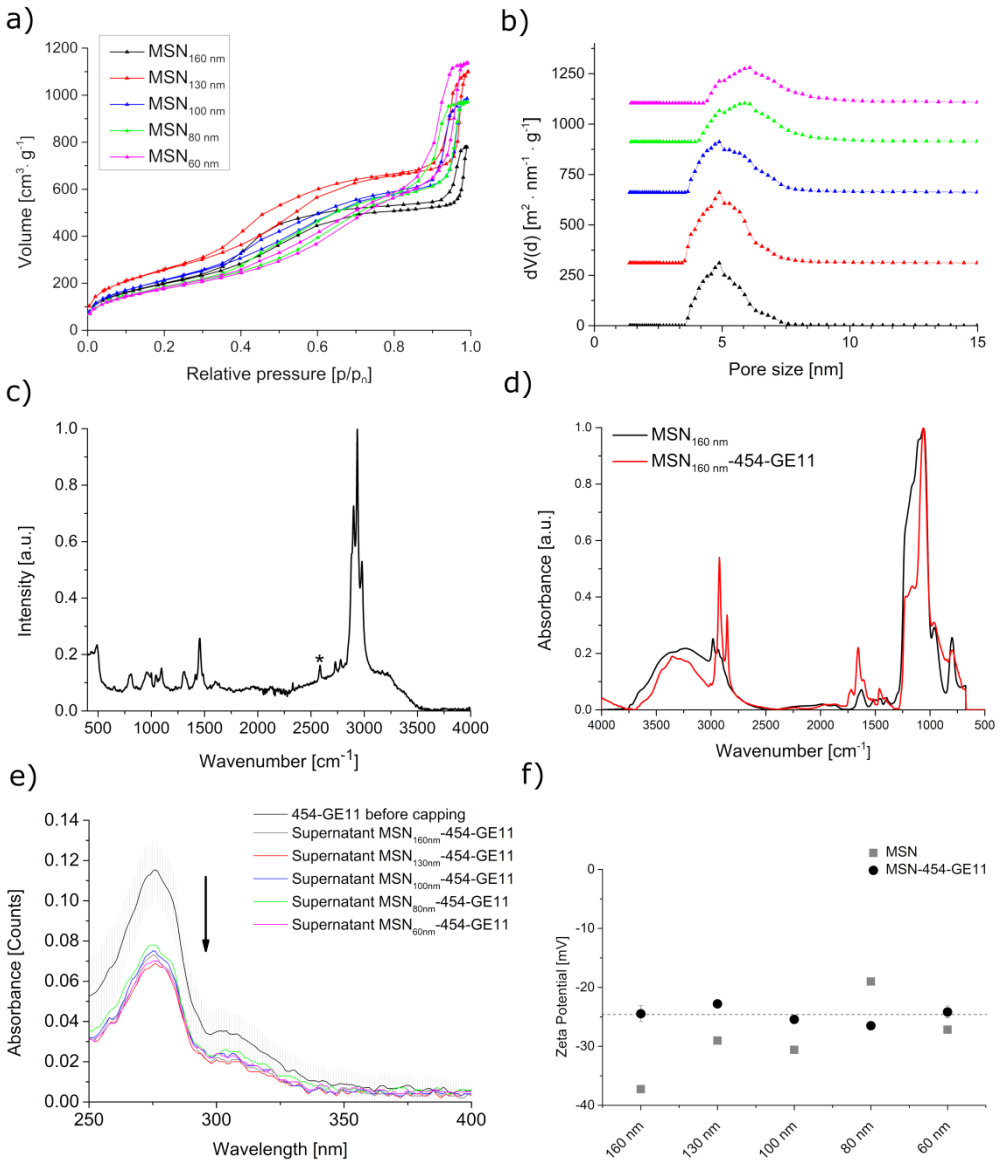

Figure 6.3 Characterization of MSN and MSN-454-GE11. (**a**) Nitrogen sorption isotherms and (**b**) corresponding pore size distributions. For clarity, the pore size distribution curves in panel b are shifted along the y-axis. (**c**) Raman spectrum of MSN160 nm. The signal at 2580 cm^{-1} (indicated by *) indicates the presence of thiol groups. (**d**) IR spectra, (**e**) UV VIS spectra of the capping solution before capping (black line) and the supernatants after capping, and (**f**) zeta potential measurements of MSN and MSN-454-GE11 at pH = 7.3.

Polymer Capping with 454-PEG and 454-GE11 and Targeting The surface of the MSNs was capped with a modularly designed block copolymer 454 to prevent a premature release of the cargo and to enhance endosomal escape for intracellular delivery of miRNA. The structure of the copolymer 454 is shown in Figure S6.3. This T-shaped polymer 454 consists of a hydrophobic domain in the center made of two oleic acids attached to lysine units. Branched off at each side from the center are two succinyl-tetraethyl-pentamine (Stp) units[47], providing

the polymer with a cationic charge. Each end contains a tyrosine trimer coupled to a terminal cysteine unit, potentially allowing additional functionalization. The combination of the central Stp and oleic acid units in 454 is assumed to facilitate interactions with the endosomal membrane, resulting in endosomal destabilization and thus enabling the nucleic acid cytosolic delivery. This block copolymer was successfully used for the formulation of INF-7-polyplex/siRNA vehicles [48] and was further essential for the highly efficient delivery of siRNA using MSNs, reported previously.[21]

An anticancer therapy can potentially be improved by implementing cancer-cell-specific targeting molecules to the external surface of a carrier system. It is well known that EGF receptors (EGFR) are concentrated on many cancer cells. The small peptide GE11 has been used successfully before to specifically address EGFR-expressing cells.[41,49,50] Here, we exploit the mercapto residues of the cysteine groups in the capping polymer 454 for binding GE11 via a PEG linker to study the targeted, particle-size-dependent delivery of the miR200c.

For anchoring GE11 to the cysteine units in the block copolymer, we used a mercapto-reactive maleimide-PEG moiety consisting of 28 ethylene glycol monomer units that was previously linked to the GE11 ligand (Mal-PEG-GE11 reagent). The Mal-PEG-GE11 reagent was then mixed with the 454 block-copolymer (454-GE11). Only 0.1 equivalents (eq.; relative to 454-polymer) of the targeting ligand were used for 454-functionalization to maintain free thiol groups at the end of 454. The latter can potentially undergo a disulfide bridging with the terminal mercapto-groups on the outer surface of the MSNs, thus creating a stable copolymer capping. The attachment of the cationic polymer 454 to the surface is additionally electrostatically favored since zeta potential measurements of our pure MSNs reveal a negative surface charge for all samples at a pH higher than 5.5 (Figure S6.4). To perform the attachment of the premixed 454-GE11 to the surface of MSN, a suspension of MSN at pH 7.3 was mixed with 454-GE11 and the successful capping was confirmed using UV–VIS, IR, and zeta

potential measurements. IR spectroscopy shows a significant increase of the CH stretching vibrations between 2850 and 2930 cm^{-1} and of the C-H bending vibrations of 1460 cm^{-1} as compared to the bare MSN particles (red graph in Figure 6.3d). Furthermore, the MSN-454-GE11 spectrum shows an increase of the N–H bending vibrations at 1650 cm^{-1} and a new signal at 1720 cm^{-1} related to a C=O stretching mode, indicating the multiple amide bonds of the copolymer. UV–VIS measurements were further used to quantify the amount of the 454-GE11 capping agent, which was similar in all samples and ranged from 17 to 20 wt% (Figure 6.3e, calibration curve Figure S5 and capping amount of different samples, Table S6.1).

Figure 6.3f shows the zeta potential measurements of all MSN samples before and after attachment of the 454-GE11 linker (MSN-454-GE11) at pH = 7.3. Besides the size of the nanoparticles, their surface charge is an important parameter for cellular internalization. Our pure MSN samples display a negative surface charge between − 37 and – 20 mV, as expected for mercapto-covered MSNs. The zeta potential of all capped MSN-454-GE11 samples is very comparable and has increased to about −24 mV when measured at pH 7.3. The observed difference before and after capping can be seen as an additional indication for a successful attachment of the targeted copolymer. The polymer capping did not affect the particle size distribution in water for most of the MSN-454-GE11 samples when measured by DLS. Only the sample with a mean particle size of 60 nm showed some moderate agglomeration (Figure S6.6).

Cell Internalization. As documented above, we have now established that our MSN carrier system shows physical properties such as surface area, pore size, zeta potential and capping concentration that are all very comparable, thus, leaving solely the particle size as a distinct variable. First, flow cytometry and confocal fluorescence microscopy data were used to investigate how the targeting ligand concentration as well as particle size might influence the cell internalization of the fully assembled MSN-454-GE11 samples.

Figure 6.4 shows the cellular internalization of the MSNs by T24 cells as examined via flow cytometry after a 45 min incubation time. MSN-454-GE11 samples were labeled with the Atto-633-carboxy fluorescent dye, which was covalently bound to the amino groups in the core of the particles. In order to investigate the best targeting concentration, we mixed different weight equivalents of targeting ligand GE11 with the 454 polymer in the range from 0.1 to 1 eq. before attaching the polymer to the MSN samples. Maleimide-PEG without ligand was used as negative control for polymer capping without targeting ligand (sample MSN-454-PEG). A significant targeting effect can be seen in Figure 6.4a when 0.1 eq. of the targeting ligand was used, while only a minor improvement is observed at higher concentrations.

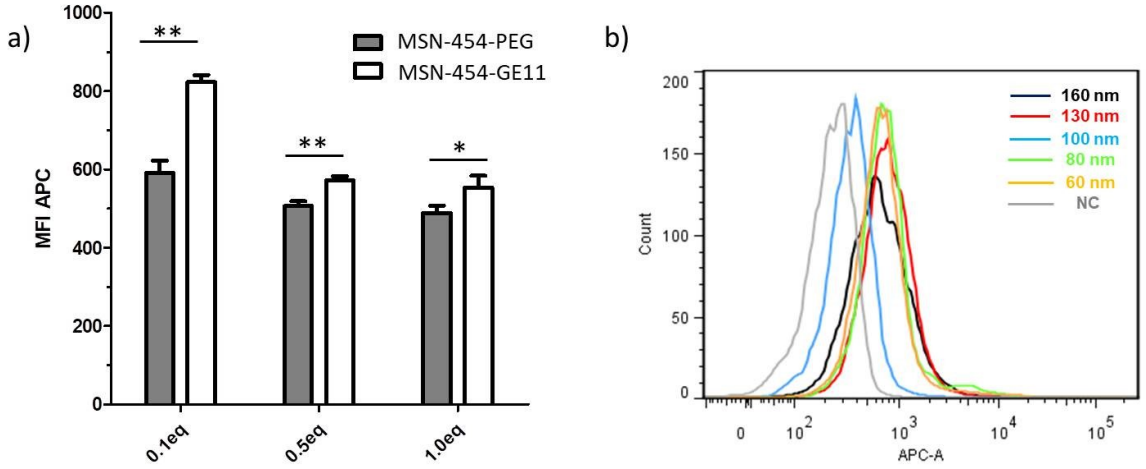

Figure 6.4 Cellular internalization determined by flow cytometry. Cells were incubated for 45 min, washed and analyzed. (a) MSN160 nm-454-PEG was used for passive and MSN160 nm-454-GE11 for receptor-mediated uptake. 454 was functionalized with different equivalents of Mal-PEG (454-PEG) and Mal-PEG-GE11 reagent (454-GE11), respectively, in the range from 0.1 to 1 eq. The mean fluorescence intensity of the Atto-633 signal (MFI APC) represents the amount of internalized nanoparticles. A high MFI corresponds to a large cell uptake of MSN. For statistical analysis, a two-tailed t-test was performed (n = 3, mean ± SD, * $p < 0.05$, ** $p < 0.01$) (b) Histograms of cellular internalization of Atto-633 labeled MSN-454-GE11 after 45 min incubation with particle sizes in the range of 160 nm to 60 nm and negative control (NC). The Atto-633 intensity (APC-A channel) is plotted against the number of events detected ('count'). 'Count' represents cumulative counts of cells with indicated Atto-633 fluorescence after appropriate gating by forward/sideward scatter and pulse width. For statistical analysis, see Figure S6.7.

Figure 6.4b documents the particle-size-dependent association of MSN-454-GE11 to cells as investigated via flow cytometry. Flow cytometry showed a similar degree of cell association for all samples, while a slight trend towards stronger association can be seen for smaller particles (quantification and statistical analysis can be found in SI, Figure S6.7). Since flow cytometry is not able to differentiate internalization from externally adhering particles, we followed this process also with confocal fluorescence microscopy as shown in Figure 6.5 (for enlarged images with additional orthogonal views of each image showing the particle internalization, see Figure S6.8, SI). Images were subsequently analyzed via the digital method `Particle_in_Cell-3D` to quantify the cellular uptake of the differently sized MSN vectors. After imaging cells directly after an incubation time of 45 min, we found that only MSN160 nm-454-GE11 particles had penetrated through the cell membrane and were truly internalized. Other smaller MSN-454-GE11 particles were only attached to the outer cell membrane at this time. In contrast, all particle sizes were internalized after a 6 h incubation time. However, also after this time, MSN160 nm-454-GE11 particles showed the highest number of internalized particles of all samples (Figure S6.9).

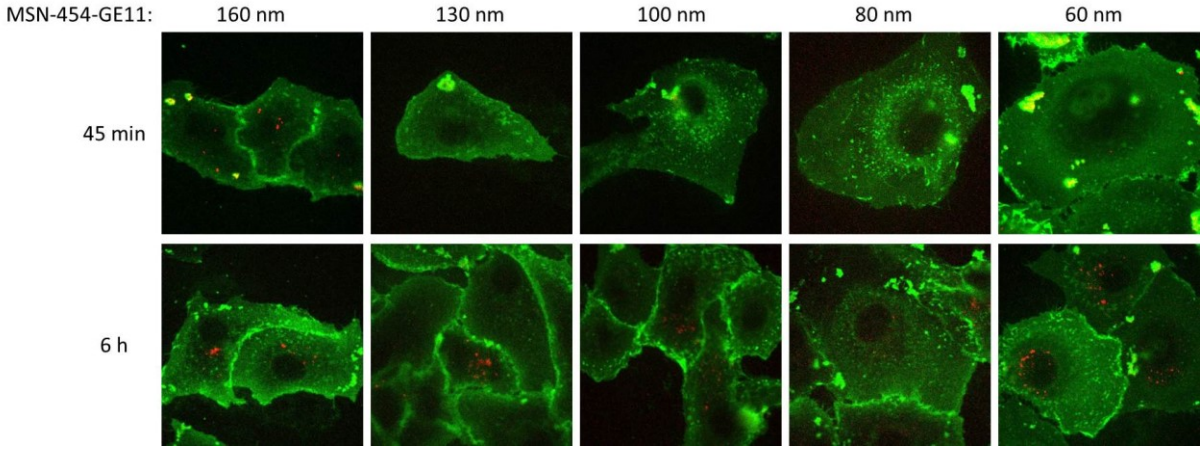

Figure 6.5 Representative confocal fluorescence microscopy images of Atto-633 labeled MSN-454-GE11 (red) with particle sizes in the range of 160 nm to 60 nm after 45 min (upper panel) and 6 h (lower panel) incubation on WGA488-stained T24 cells (green). For a statistical evaluation of particle-size-dependent uptake, see Figure S6.9, SI.

Loading of RNA. Loading of the genetic material into our MSN samples was performed with all samples prior to the attachment of the block copolymer. The adsorption of the miRNA is mainly driven by electrostatic interactions with the cationic, amino-functionalized core of the MSNs. The negatively charged thiol groups at the particle periphery are expected to minimize any external adsorption. For the best results, we performed the RNA adsorption in MES buffer at pH = 5. The MSN particles show a positive zeta potential at this pH due to protonation of the amino groups (zeta potential titration, see Figure S6.4).

Here, aliquots of 50 µg mg^{-1} RNA/MSN were used for loading and the actual uptake was calculated by difference measurements by determining the remaining RNA concentration in the supernatant. All samples were able to adsorb the amount offered, as no residual RNA could be detected in the supernatant after loading times as short as 30 min. The samples were subsequently capped with 454-GE11 to obtain the final MSN-454-GE11 samples used for subsequent experiments. The stable binding of RNA in these samples is reflected in gel shift results, as shown in Figure 6.6a). Only little RNA elution is visible upon applying a voltage of 100 V for 1 h to the gel.

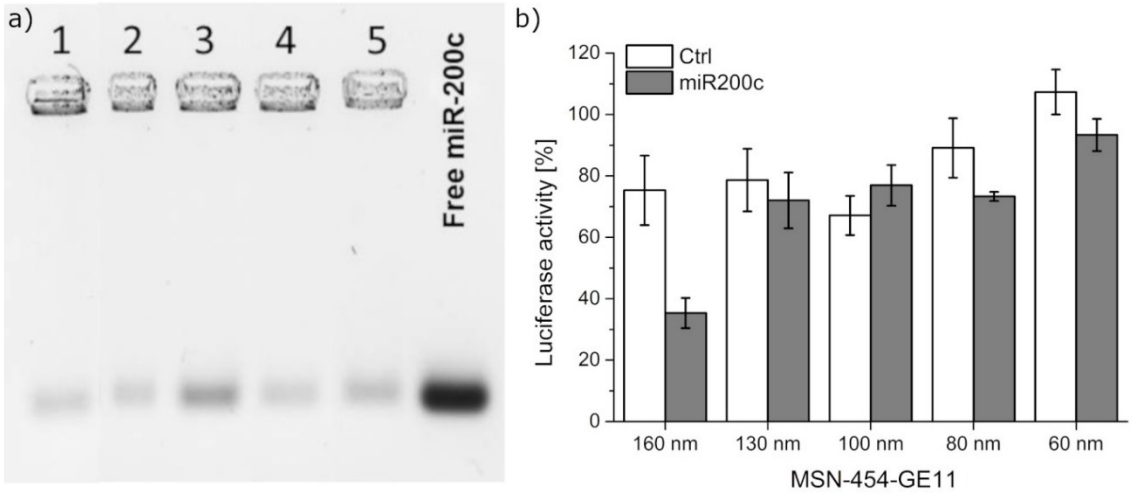

Figure 6.6 (**a**) Gel electrophoresis of samples MSN160 nm-454-GE11 (1), MSN130 nm-454-GE11 (2), MSN100 nm-454-GE11 (3), MSN80 nm-454-GE11 (4), and MSN60 nm-454-GE11 (5). (**b**) Gene silencing of T24/eGFPLuc-200cT cells transfected with MSN-454-GE11 containing either Ctrl (white) or miR200c (grey). After an incubation time of 45 min, cells were washed. At 48 h after transfection, gene-silencing effects were analyzed.

Gene Silencing. As a proof of concept, the gene silencing of the eGFP-luciferase reporter gene was performed using T24/eGFPLuc-200cT cells. This cell line stably expresses the eGFP-luciferase fusion protein, while simultaneously featuring a miR200c target site on the expressed mRNA. Therefore, the gene expression of eGFP-luciferase fusion protein can be blocked by the delivery of miR200c. The luciferase signal was thus used to evaluate the gene-silencing efficacy of miR200c. In order to simulate the dynamic conditions of drug delivery and to avoid a prolonged overexposure of the cells with particles suspended in the medium, we have used extremely short incubation times of 45 min. Cells were subsequently washed by exchanging the medium and the effect of this short exposure was then analyzed after time spans referred to as transfection time in the following. Cells were transfected with MSN and MSN-454-GE11 of different sizes loaded with either a synthetic miR200c mimic or a control siRNA without any target gene (Ctrl, Figure 6.6b). Gene silencing was never observed with the pure MSN samples (missing the 454 polymer construct) loaded with miR200c for silencing (Figure S6.10a). This might be caused by a premature release of the RNA or by endosomal trapping of the MSN samples missing the 454 polymer.

Similarly, none of the smaller sized MSN-454-GE11 samples showed any significant silencing efficacy. In contrast, with the larger 160 nm targeted polymer-capped MSN160 nm-454-GE11 sample, a luciferase gene knockdown of up to 65% was observed. These findings are in good agreement with the confocal fluorescence microscopy images, which showed the fastest internalization for particles with a size of 160 nm.

Flow cytometry data showed an improved cellular internalization of the targeted MSN160 nm-454-GE11 vector in comparison with the non-targeted control MSN-454-PEG when 0.1 eq. of the targeting ligand was used. This targeted vector showed a higher silencing efficacy

compared to the non-targeted control, which is in good agreement with the increased uptake observed via flow cytometry.

As expected, the same sample loaded with just scrambled RNA (Ctrl) did not show a significant unspecific knockdown, thus excluding major toxic effects induced by the carrier system itself. Systematic cell viability studies using an MTT assay also show a good tolerance of the cells towards these samples (Figure S6.11).

These results show that a particle size of about 160 nm in combination with the copolymer 454 enables the fastest cell internalization and also the best transfection efficacy when short incubation times of only 45 min are used. Inhibition experiments addressing specific endocytic pathways were inconclusive with respect to a preferred mechanism for a certain particle size. However, endocytosis was substantially more blocked for the larger particles as compared to the 60 nm particles (see Figure S6.12, SI). Our data also confirm the endosomolytic activity of the 454 polymer since cell adherence/uptake was observed for all pure MSN samples (flow cytometry of pure MSN samples in Figure S6.13), but no transfection occurred without the 454 polymer (see Figure S6.10a). As described above, we further found that only MSN160 nm-454-GE11 showed gene-silencing activity, while all smaller MSN-454-GE11 samples were not active after the short incubation period applied here. Confocal fluorescence microscopy showed that MSN160 nm-454-GE11 particles were already internalized after 45 min, while all other MSN-454-GE11 samples needed much longer incubation times to achieve internalization. Thus, particle internalization of the smaller particles is likely too slow and prevents a larger efficacy.

Recently, miR200c was delivered by some of us using GE11 modified 454 polyplexes with a similar size of 120–150 nm.[41] The gene silencing efficiency achieved in the same T24/eGFPLuc-200cT cells with these polyplexes was around 60%, which is in the same range

as the knockdown efficiency of the MSN-454-GE11 constructs presented here. This comparison suggests that the size of the targeted constructs is a determining feature controlling the knockdown efficiency. As MSN160 nm-454-GE11 constructs were shown to offer the best cellular-uptake behavior and gene-silencing efficiency, they were used for the following cell migration and cell cycle experiments.

Antitumoral Effects. The tumor suppressor miR200c inhibits the epithelial–mesenchymal transition, a process involved in metastasis by enhancing the motility and migration of tumor cells, by targeting ZEB1 and ZEB2. ZEB1 and ZEB2 are transcriptional repressors, which downregulate the marker E-cadherin.[7,51] Furthermore, Kopp *et al.* reported that one of the most prominent oncogenes KRAS is targeted by miR200c, which results in an altered cell cycle of the cancer cells.[6] Notably, they could show that miR200c inhibits cell cycle progression by decreasing the G1-population. We have performed direct investigations of these antitumoral effects through tumor cell migration and cell cycle analysis on two different EGFR overexpressing cell lines, T24 bladder cancer and HeLa cervical cancer cells using miR200c loaded MSN-454-GE11 samples.

Cell migration was studied using a scratch assay, as shown in Figure 6.7. T24 cells and HeLa cells were incubated with MSN-454-GE11 for 4 h (5 µg miR200c/well), then the medium was changed. After additional 24 h, the cell layer was broken by a scratch using a 200 µL Eppendorf pipette tip. The closure of the scratch, which is an indicator for cell migration, was measured at indicated time points. In both cell lines, the scratch was almost completely closed after 48 h when MSN-454-GE11 was loaded with Ctrl-RNA (88% scratch closure for T24 and 82% closure for HeLa cells). In contrast, with MSN-454-GE11 particles loaded with miR200c, a scratch closure of only 48% (for T24) and 53% (for HeLa cells) was observed after this time. Hence, miR200c delivered by MSN-454-GE11 significantly hinders cell migration.

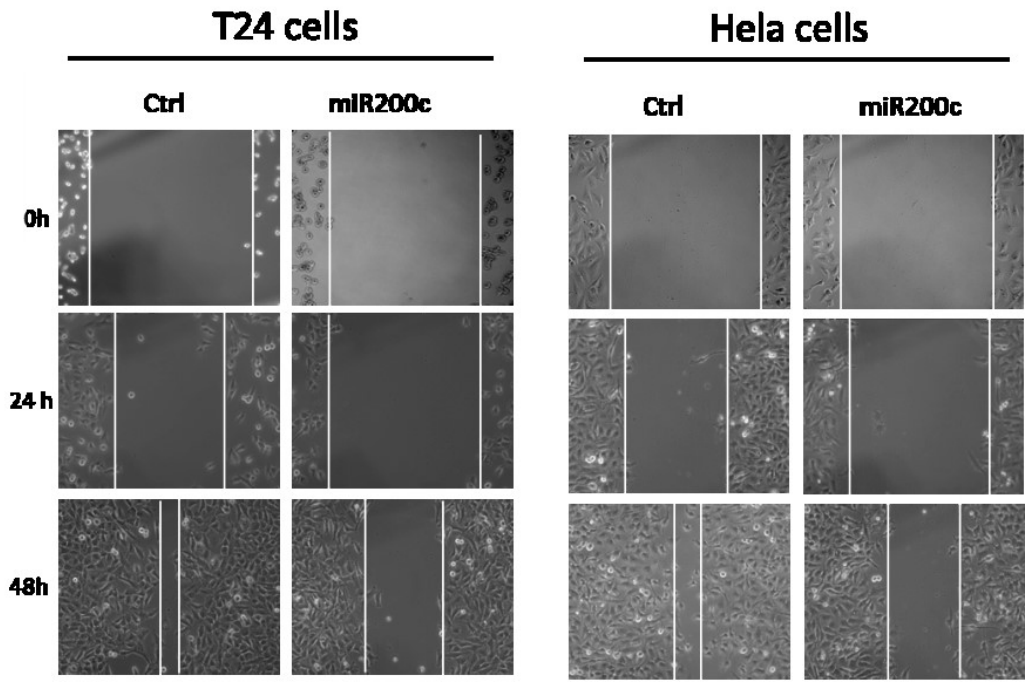

Figure 6.7 Inhibition of tumor cell migration. Images of a scratch assay of T24 and HeLa cells. Cells were treated with MSN160 nm-454-GE11 loaded with miR200c. The cell layer was broken after 24 h through a scratch and the closure was monitored for 48 h.

In addition, the effect of miR200c on the cell cycle was studied. Cells were transfected with MSN-454-GE11 loaded with miR200c or with the control RNA Ctrl and incubated for 4 h (Figure 8). A significant decrease in the number of cells in the G1 phase is observed when exposed to miR200C delivered by MSN, in combination with an increase in the number of cells in the S-phase. Thus, tumor cells transfected with MSN-454-GE11 loaded with miR200c showed the expected decreased migration and changes in the cell cycle.

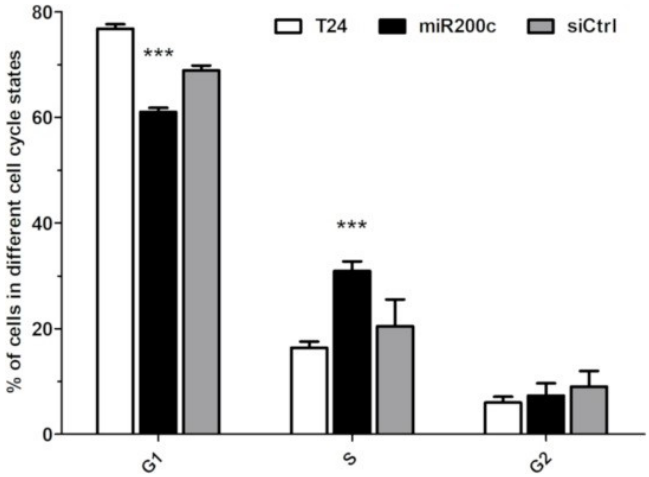

Figure 6.8 Cell cycle analysis via flow cytometry of cell stages G1, S and G2 of T24 cells at 72 h after treatment. For statistical analysis, a two-tailed t-test was performed ($n = 3$, mean ± SD, *** $p < 0.01$).

6.3. Conclusion

In this study, we exploited the tunability of MSNs to synthesize a series of core-shell MSNs with different particle sizes between 60 to 160 nm for studying the size effect of these carriers on antitumoral miRNA delivery. All other properties of the delivery vehicles, including surface area, pore size and zeta potential were kept comparable. The nanoparticles were capped with a positively charged block copolymer 454 equipped with the targeting agent Mal-PEG-GE11. Since gene silencing was only observed after capping the nanocarriers with this 454 polymer, we conclude that it is essential for the endosomal escape by destabilizing the endosomal membrane. It was shown that the targeting ligand GE11 enhances a receptor-mediated uptake. After capping, the MSN-454-GE11 vehicles were used for a systematic investigation of size-dependent gene silencing. While smaller particles did not lead to significant effects, MSN-454-GE11 with a size of 160 nm showed a remarkable gene knockdown efficacy and antitumoral effects such as a decreased migration and changes in cell cycle. Overall, we observed the fastest cellular internalization as well as the best knock-down efficacies with MSN-454-GE11 sized 160 nm. In contrast to FACS results that indicated a particle association with the cells independent of MSN particle size, we found with statistically evaluated image analysis that only the largest particles are truly internalized in the cells after short incubation times. Thus, cell studies as performed here, aiming to simulate dynamic conditions of in vivo drug delivery by washing the incubated cells after a short incubation time, might discriminate against all particles that are not well attached to the cell surface. Fast internalized particles are thus the winner. We hypothesize that due to their size, they expose a larger contact area to the cell membrane and simultaneously a larger number of targeting ligands, which, when spaced just right, allow for a maximum degree of endocytosis. Our study shows that fast cellular internalization is essential for a successful downregulation. In summary, the nanoscale

MSN160 nm-454-GE11 vehicles show the most promising potential for future in vivo biomedical applications.

6.4. Experimental Part

Reagents and Materials. 2-(N-morpholino)ethanesulfonic acid (MES, Sigma-Adrich, Darmstadt, Germany), 3-aminopropyltriethoxysilane (APTES, Sigma-Adrich), 3-mercaptopropyl triethoxysilane (MPTES, >95%, Sigma-Adrich), ammonium fluoride (NH4F, >98% Fluka, Darmstadt, Germany), Atto 633-carboxy dye (Atto-Tec, Siegen, Germany), 4′,6-diamidino-2-phenylindole (DAPI, Thermo Fisher, Schwerte, Germany), block copolymer surfactant (Pluronic F127 (EO106PO70EO106), Sigma-Aldrich), cetyltrimethyl-ammonium chloride (CTAC, 25% in H2O, Sigma-Adrich), N-(3-dimethylaminopropyl)-N′-ethylcarbodiimide hydrochloride (EDC, >97%, Sigma-Adrich), N-hydroxysulfosuccinimide (sulfo-NHS, 98%, Sigma-Adrich), octadecyltrimethylammonium bromide (C18Br, Sigma-Adrich), propidium iodide, tetraethylorthosilicate (TEOS, >98%, Sigma-Aldrich), triethanolamine (TEA, 98%, Fluka), triisopropylbenzene (TiPB, 96%, Sigma-Adrich). Oligomer 454[42] and Mal-PEG-GE11[41] were synthesized as described before. siRNA and miRNA duplexes were purchased from Axolabs GmbH (Kulmbach, Germany):

Control RNA (sense: 5-AuGuAuuGGccuGuAuuAGdTsdT-3′,

antisense: 5′-CuAAuAcAGGCcAAuAcAUdTsdT-3),

miR200c (sense: 5′-UCCAUCAUUACCCGGCAGUAUUA-3,

antisense: 5′-UAAUACUGCCGGGUAAUGAUGGA-3).

Synthesis of MSN-NH2$_{in}$-SH$_{out}$. Two slightly different synthesis methods were used to prepare core-shell functionalized MSN containing 4.5% amino groups in the core and 2% thiol groups on the shell (MSN-NH2in-SHout).

Procedure A: Core-shell MSN particles were prepared by a co-condensation reaction according to our previous reports.[17,43] Early reports from our group showed that a consistent decrease in particle size can be obtained by decreasing the amount of TEA serving as organic base. This

concept was applied for the synthesis of samples MSN160 nm, MSN130 nm and MSN100 nm.[44] A mixture of TEA (14 g, 138 mmol/10 g, 101,2 mmol/4 g, 39,5 mmol, respectively), tetraethylorthosilicate (TEOS, 1.74 mL, 7.84 mmol) and 3-aminopropyltriethoxysilane (APTES, 89 µL, 0.38 mmol) in a polypropylene reactor was heated in an oil bath at 90 °C for 20 min without stirring. A second solution was prepared consisting of water (21.7 mL, 1.21 mol), CTAC (2.71 mL, 1.83 mmol), TiPB (2.97 mL, 12 mmol) and ammonium fluoride (NH4F, 100 mg, 2.7 mmol) and was heated to 60 °C under stirring. The second solution was subsequently added to the first solution under strong stirring. The whole mixture was further stirred at room temperature for 20 min. After this time, four portions of TEOS (4 × 51 µL, 0.92 mmol) were added in three minutes intervals and the solution was stirred for another 30 min. To prepare the shell layer, a premixed solution of TEOS (42 µL, 0.190 mmol) and mercaptopropyl triethoxysilane (MPTES) (42 µL, 0.22 mmol) was added to the whole mixture. The condensation reaction was allowed to continue over night at room temperature.

Procedure B: MSN80 nm and MSN60 nm were prepared using the tri-block copolymer F127 as a particle growth inhibitor/dispersant. The procedure is based on an adapted recipe reported in the literature.[45] First, a mixture of TEA (7 g, 46.8 mmol/4 g, 26.7 mmol, respectively), TiPB (1.5 mL, 6.2 mmol), F127 (100 mg, 8 µmol) TEOS (2 mL, 9 mmol), and APTES (89 µL, 0.38 mmol) was prepared in a polypropylene reactor and heated at 90 °C for 20 min. Separately, NH4F (100 mg, 2.7 mmol) and C18Br (0.35 g, 0.9 mmol) were dissolved in H2O. This solution was heated to 90 °C under static conditions for 30 min and was then added under strong stirring to the first solution at once. The combined solutions were further heated at 60 °C for 30 min. The ingredients for the shell layer, TEOS (42 µL, 0.190 mmol) and MPTES (42 µL, 0.22 mmol), were mixed, preheated to 60 °C and added to the reaction mixture. Heating at 60 °C was continued for 30 min, and then the reaction mixture was allowed to cool down to room temperature under stirring and was continuously stirred overnight.

Template Extraction. Agglomerates were removed from the as- synthesized samples by centrifugation for a short time at low speed (7197 rcf, 5 min). The pellet was discarded and the remaining particles in the supernatant were collected via centrifugation (7197 rcf, 20 min) for template extraction. After centrifugation, the particles were resuspended in a solution containing 2 g ammonium nitrate in 100 mL ethanol and heated for 45 min under reflux (90 °C), cooled and collected by centrifugation (7197 rcf, 20 min). The first reflux treatment was followed by a second extraction step for 45 min under reflux (90 °C) using a solution of 10 mL concentrated hydrochloric acid in 90 mL ethanol. The MSNs were collected by centrifugation for 20 min (7197 rcf) and washed with ethanol (3 × 70 mL). Finally, MSNs were dispersed in 15 mL ethanol and used for further characterization.

Characterization

For transmission electron microscopy (TEM), samples were prepared by drying a diluted ethanolic suspension of MSN on a carbon-coated copper grid at room temperature for several hours. The measurements were performed on a Tecnai G2 20 S-Twin instrument operated at 200 kV with a TVIPS TemCam-F216 camera.

Dynamic light scattering (DLS) and zeta potential measurements were performed with a Malvern Zetasizer Nano instrument equipped with a 4 mW He-Ne-Laser (633 nm). For DLS data, a diluted colloidal suspension of the particles was measured in PMMA cuvettes at 25 °C. For zeta potential measurements, the additional Zetasizer titration system (MPT-2) was used based on diluted NaOH and HCl as titrants. For this purpose, a colloidal suspension of MSNs in water at a concentration of 0.1 mg mL−1 was prepared.

Raman spectroscopy was performed on a Bruker Equinox 55 with FRA-106 Raman attachment with a ND:YAG laser (1064 nm) and a laser power of 100 mW. Infrared spectra of dried sample

powder were recorded on a ThermoScientific Nicolet iN10 IRmicroscope in reflection–absorption mode with a liquid-N2 cooled MCT-A detector.

A Quantachrome Instrument NOVA 4000e was used for nitrogen sorption analysis at −196 °C. Sample outgassing was performed for 12 h at 120 °C and at a vacuum of 13.3 × 10−3 mbar. A quenched solid density functional theory (QSDFT) equilibrium model of N2 on silica at a relative pressure p/p0 = 0.8 was used to calculate the pore size and pore volume, based on the adsorption and desorption branch of the isotherm. A BET model in the range p/p0 = 0.05–0.2 was used to determine the specific surface area.

Thermogravimetric analysis (TGA) of the powder samples (10 mg) was performed on a Netzsch STA 440 C TG/DSC using a heating rate of 10 °C/min up to 900 °C with a stream of synthetic air of about 25 mL·min−1.

siRNA concentrations were determined by UV measurements performed with the Nanodrop 2000c spectrometer (Thermo Scientific).

Loading of Ctrl and miR200c for Gene Silencing. In all experiments, 100 µL Ctrl or miR200c solution (c = 50 ng µL−1) in MES buffer (pH = 5) was added to 100 µg MSN-NH2in-SHout samples, resulting in a final RNA concentration of 50 µg mg−1 of MSN carrier. Samples were vortexed and shaken at 37 °C for 30 min to complete adsorption. Particles were washed via centrifugation and were resuspended in 100 µL HEPES buffer. The supernatant was collected to verify complete adsorption of RNA.

Loading of Fluorescent Dye for Cellular Internalization Studies. A total of 1 mL MSN-NH2in-SHout samples (pH = 5; 1 mg mL−1 MES buffer) was mixed with 2 µL Atto-633 carboxy (2 mg mL−1 in anhydrous DMSO), 10 µL EDC and a catalytic amount of sulfo-NHS. The samples were vortexed and shaken for 4 h, were washed multiple times afterwards with

MES and HEPES buffer (1 mL, respectively) (centrifugation steps: 10 min, 16,900 rcf) and were redispersed in 1 mL MES buffer.

Capping with 454-GE11. For capping of MSN-NH2in-SHout samples, 10 µL Mal-PEG-GE11 reagent (5 mg mL−1 in H2O) was added to 100 µL 454 solution (5 mg mL−1 in H2O) and shaken for 2 h at 37 °C. Then, 454-GE11 was mixed with 1 mL MSN suspension (1 mg mL−1 in HEPES buffer) and again shaken for 2 h at 37 °C. Resulting MSN-454-GE11 samples were centrifuged (16900 rcf, 10 min) and washed with water and HEPES buffer. The samples were redispersed in 2 mL HEPES buffer.

miRNA Binding Assay. For the miRNA binding assay, a 2.5% agarose gel was prepared by dissolving agarose in TBE buffer (Trizma base 10.8 g, boric acid 5.5 g, disodium EDTA 0.75 g, and 1 L of water) and by heating to 100 °C. GelRed® (1:10,000) was added and the agarose gel was cast in the electrophoresis unit. MSN-454-GE11 samples loaded with Ctrl RNA were mixed with 4 µL loading buffer (6 mL glycerol, 1.2 mL of 0.5 M EDTA, 2.8 mL H2O, 0.02 g bromophenol blue) and placed into the gel sample pockets. Electrophoresis was run at 120 V for 90 min.

Cell Culture. HeLa, T24 or T24/eGFPLuc-200cT (authenticated by DSMZ, Braunschweig, Germany) cells, stably expressing an eGFP-luciferase fusion gene under the control of the CMV promoter and with a target site for miR200c, were cultivated in Dulbecco's modified Eagle's medium (DMEM) supplemented with 10% fetal bovine serum (FBS), 100 U mL−1 penicillin and 100 U mL−1 streptomycin.

Cell Viability Determined by MTT Assay. MTT assay was performed in triplicate in 96-well plates. One day prior to transfection, T24 cells were seeded at 3500 cells/well. Before transfection, medium was replaced by 80 µL fresh medium. MSN samples (20 µL) loaded with or without RNA were added at different concentrations in HEPES buffer and incubated for 45

min at 37 °C followed by a medium exchange. Subsequently, cells were returned to the incubator and 48 h after transfection a viability assay was performed. For this, an MTT solution (100 µL/well; 0.5 mg mL^{-1} in DMEM) was added for 2 h. Then, the supernatant was removed and cells were lysed by freezing at –80 °C. DMSO (100 µL) was added and plates were incubated at 37 °C under shaking. Absorption at 590 nm against a reference wavelength of 630 nm was measured using a SpectraFluorTM Plus microplate reader S4 (Tecan, Groeding, Austria). Cell viability was calculated as percentage of absorption compared to wells treated with HEPES buffer.

Cellular Adhesion Determined by Flow Cytometry. T24/eGFPLuc-200cT cells were seeded 24 h before transfection on 24-well plates with a density of 5 × 105 cells per well in 1000 µL growth medium. After 24 h, the medium was replaced by 400 µL fresh medium. A total of 100 µL MSN, MSN-454-PEG and MSN-454-GE11 samples loaded with fluorescent dye (500 µg mL−1 MSN in HEPES buffer) were added and incubated for 45 min at 37 °C. After incubation time, the cells were washed three times with PBS, 500 I.U. heparin to remove particles non-specifically associated to the cell surface and were detached with trypsin/EDTA, taken up in growth medium, centrifuged and resuspended in PBS containing 10% FBS. Cellular internalization of the MSN samples was assayed by flow cytometry at an Atto-633 carboxy fluorescent dye excitation wavelength of 635 nm and detection of emission at 665 nm. Cells were gated by forward/sideward scatter and pulse width for exclusion of doublets. DAPI (4′,6-diamidino-2-phenylindole) was used to discriminate between viable and dead cells. Data were recorded by BD LSRFortessa™ (BD Biosciences, USA) and analyzed by FlowJo® 7.6.5 flow cytometric analysis software. All experiments were performed in triplicate.

Confocal Fluorescence Microscopy. Fluorescence microscopy was performed with a Zeiss Observer SD spinning disk confocal microscope using a Yokogawa CSU-X1 spinning disc unit and an oil objective (63× magnification) and BP 525/50 (WGA488) and LP 690/50 (Atto633)

emission filters. A 488 nm and a 639 nm laser were used for excitation. At 24 h prior to transfection, 3500 T24 cells per well were seeded in 8-well plates in 280 µL growth medium. A total of 20 µL MSN-454-GE11 covalently labeled with Atto-633 carboxy (200 µg mL−1 MSN in HEPES buffer) were added to each well and incubated for 45 min or 6 h, respectively, at 37 °C followed by addition of WGA-488 to the medium for cell membrane staining. Cells were washed with PBS and after addition of 300 µL fresh medium, cells were directly imaged.

The cellular uptake of nanoparticles was quantified using the ImageJ macro "Particle_in_Cell-3D" developed by Adriano A. Torrano and Julia Blechinger, Department of Chemistry and Center for NanoScience (CeNS, University of Munich (LMU), Munich, Germany. http://imagejdocu.tudor.lu/doku.php?id=macro:particle_in_cell-3d)

Luciferase Gene Silencing. In all experiments, siRNA and miRNA delivery was performed in 96-well plates in triplicate. 3500 T24/eGFPLuc-200cT cells per well were seeded 24 h prior to transfection in 100 µL growth medium. Before transfection, medium was replaced with 80 µL fresh growth medium. 20 µL MSN, MSN-454-PEG and MSN-454-GE11 for RNA delivery (500 µg mL−1 MSN in HEPES buffer) were added to each well and incubated for 45 min at 37 °C followed by a medium exchange. Cells were then incubated with 100 µL fresh medium for an additional 48 h following transfection. After this time, cells were treated with 100 µL cell lysis buffer (Promega (Mannheim, Germany)). Luciferase activity in cell lysate (35 µL) was measured using a luciferin-LAR (1 M glycylglycine, 100 mM MgCl2, 500 mM EDTA, DTT, ATP, coenzyme A) buffer solution on a luminometer for 10 s (Centro LB 960 plate reader luminometer, Berthold Technologies, Bad Wildbad, Germany).

Cell Cycle Analysis. At 24 h prior to transfection, 3.5 × 104 T24 cells per well were seeded in a 12-well plate in 1000 µL growth medium and then medium was replaced by 400 µL fresh medium. A total of 100 µL MSN-160 nm-454-GE11 (500 µg mL−1 in HEPES buffer) loaded

with Ctrl RNA or miR200c was added and incubated at 37 °C for 4 h. After a selected incubation time, the medium was replaced with fresh medium and cells were incubated for an additional 72 h. Afterwards, cells were washed with PBS and detached with trypsin/EDTA. Cells were washed with PBS twice and suspended in 100 µL PBS. The cell suspension was added dropwise to 0.9 mL cold 70% ethanol and incubated at 4 °C for 2 h. Then, cell pellets were suspended in 1 mL PBS after centrifugation and incubated for 15 min at room temperature for counting. A total of 1 × 105 cells of each sample was incubated in 300 µL propidium iodide/TritonX-100 containing RNase solution for 15 min at 37 °C. For cell cycle analysis, the cells were analyzed by flow cytometry at an excitation wavelength of 488 nm and detection of emission with a 613/20 bandpass filter. Data were recorded by BD LSRFortessa™ (BD Biosciences, USA) and analyzed by FlowJo® 7.6.5 flow cytometric analysis software. All experiments were performed in triplicate.

Scratch Assay. At 24 h prior to transfection, 1 × 105 T24 and MDA-MB 231 cells per well were seeded in a 6-well plate in 2000 µL of growth medium. The medium was replaced by 800 µL fresh medium and 200 µL MSN160 nm-454-GE11 (500 µg mL−1 in HEPES buffer) loaded with Ctrl RNA or miR200c was added. Cells were incubated with MSN160 nm-454-GE11 for 4 h, then the medium was changed. After 24 h additional incubation time, the cell layer was broken by a scratch using a 200 µL Eppendorf tip. Cells were washed with PBS and microscope (Axiovert 200, Zeiss, Oberkochen, Germany) pictures were taken after 24 h.

6.5. References

1. Elbashir, S.M.; Harborth, J.; Lendeckel, W.; Yalcin, A.; Weber, K.; Tuschl, T. Duplexes of 21-nucleotide RNAs mediate RNA interference in cultured mammalian cells. Nature 2001, 411, 494.
2. McCaffrey, A.P.; Meuse, L.; Pham, T.-T.T.; Conklin, D.S.; Hannon, G.J.; Kay, M.A. RNA interference in adult mice. Nature 2002, 418, 38.
3. Xin, Y.; Huang, M.; Guo, W.W.; Huang, Q.; Zhang, L.z.; Jiang, G. Nano-based delivery of RNAi in cancer therapy. Molecular Cancer 2017, 16, 134.
4. Friedman, R.C.; Farh, K.K.-H.; Burge, C.B.; Bartel, D.P. Most mammalian mRNAs are conserved targets of microRNAs. Genome Research 2009, 19, 92-105.
5. Lee, S.J.; Kim, M.J.; Kwon, I.C.; Roberts, T.M. Delivery strategies and potential targets for siRNA in major cancer types. Advanced Drug Delivery Reviews 2016, 104, 2-15.
6. Kopp, F.; Wagner, E.; Roidl, A. The proto-oncogene KRAS is targeted by mir-200c. Oncotarget 2013, 5, 185-195.
7. Hurteau, G.J.; Carlson, J.A.; Spivack, S.D.; Brock, G.J. Overexpression of the microRNAleads to reduced expression of transcription factor 8 and increased expression of e-cadherin. Cancer Research 2007, 67, 7972-7976.
8. Kopp, F.; Oak, P.S.; Wagner, E.; Roidl, A. miR-200c sensitizes breast cancer cells to doxorubicin treatment by decreasing trkb and bmi1 expression. PLOS ONE 2012, 7, e50469.
9. Kim, H.J.; Kim, A.; Miyata, K.; Kataoka, K. Recent progress in development of siRNA delivery vehicles for cancer therapy. Advanced Drug Delivery Reviews 2016, 104, 61-77.
10. Kim, B.; Park, J.-H.; Sailor, M.J. Rekindling RNAi therapy: Materials design requirements for in vivo siRNA delivery. Advanced Materials 2019, 31, 1903637.
11. Revia, R.A.; Stephen, Z.R.; Zhang, M. Theranostic nanoparticles for RNA-based cancer treatment. Accounts of Chemical Research 2019, 52, 1496-1506.
12. Adams, D.; Gonzalez-Duarte, A.; O'Riordan, W.D.; Yang, C.-C.; Ueda, M.; Kristen, A.V.; Tournev, I.; Schmidt, H.H.; Coelho, T.; Berk, J.L., et al. Patisiran, an RNAi therapeutic, for hereditary transthyretin amyloidosis. New England Journal of Medicine 2018, 379, 11-21.
13. Chen, Y.; Gu, H.; Zhang, D.S.-Z.; Li, F.; Liu, T.; Xia, W. Highly effective inhibition of lung cancer growth and metastasis by systemic delivery of siRNA via multimodal mesoporous silica-based nanocarrier. Biomaterials 2014, 35, 10058-10069.
14. Hartono, S.B.; Gu, W.; Kleitz, F.; Liu, J.; He, L.; Middelberg, A.P.J.; Yu, C.; Lu, G.Q.; Qiao, S.Z. Poly-l-lysine functionalized large pore cubic mesostructured silica nanoparticles as biocompatible carriers for gene delivery. ACS Nano 2012, 6, 2104-2117.
15. Möller, K.; Bein, T. Degradable drug carriers: Vanishing mesoporous silica nanoparticles. Chemistry of Materials 2019, 31, 4364-4378.
16. Braun, K.; Pochert, A.; Beck, M.; Fiedler, R.; Gruber, J.; Lindén, M. Dissolution kinetics of mesoporous silica nanoparticles in different simulated body fluids. Journal of Sol-Gel Science and Technology 2016, 79, 319-327.
17. Kecht, J.; Schlossbauer, A.; Bein, T. Selective functionalization of the outer and inner surfaces in mesoporous silica nanoparticles. Chemistry of Materials 2008, 20, 7207-7214.
18. Möller, K.; Bein, T. Talented mesoporous silica nanoparticles. Chemistry of Materials 2017, 29, 371-388.
19. Wang, J.; Lu, Z.; Wientjes, M.G.; Au, J.L.S. Delivery of siRNA therapeutics: Barriers and carriers. The AAPS journal 2010, 12, 492-503.
20. Gao, F.; Botella, P.; Corma, A.; Blesa, J.; Dong, L. Monodispersed mesoporous silica nanoparticles with very large pores for enhanced adsorption and release of DNA. The Journal of Physical Chemistry B 2009, 113, 1796-1804.
21. Möller, K.; Müller, K.; Engelke, H.; Bräuchle, C.; Wagner, E.; Bein, T. Highly efficient siRNA delivery from core–shell mesoporous silica nanoparticles with multifunctional polymer caps. Nanoscale 2016, 8, 4007-4019.
22. Jin, Y.; Lohstreter, S.; Pierce, D.T.; Parisien, J.; Wu, M.; Hall, C.; Zhao, J.X. Silica nanoparticles with continuously tunable sizes: Synthesis and size effects on cellular contrast imaging. Chemistry of Materials 2008, 20, 4411-4419.
23. Gan, Q.; Dai, D.; Yuan, Y.; Qian, J.; Sha, S.; Shi, J.; Liu, C. Effect of size on the cellular endocytosis and controlled release of mesoporous silica nanoparticles for intracellular delivery. Biomedical Microdevices 2012, 14, 259-270.
24. Huang, X.; Teng, X.; Chen, D.; Tang, F.; He, J. The effect of the shape of mesoporous silica nanoparticles on cellular uptake and cell function. Biomaterials 2010, 31, 438-448.

25. Zhu, J.; Tang, J.; Zhao, L.; Zhou, X.; Wang, Y.; Yu, C. Ultrasmall, well-dispersed, hollow siliceous spheres with enhanced endocytosis properties. Small 2010, 6, 276-282.
26. Chono, S.; Tanino, T.; Seki, T.; Morimoto, K. Uptake characteristics of liposomes by rat alveolar macrophages: Influence of particle size and surface mannose modification. Journal of Pharmacy and Pharmacology 2007, 59, 75-80.
27. Osaki, F.; Kanamori, T.; Sando, S.; Sera, T.; Aoyama, Y. A quantum dot conjugated sugar ball and its cellular uptake. On the size effects of endocytosis in the subviral region. Journal of the American Chemical Society 2004, 126, 6520-6521.
28. Shang, L.; Nienhaus, K.; Nienhaus, G.U. Engineered nanoparticles interacting with cells: Size matters. Journal of Nanobiotechnology 2014, 12, 5.
29. Lu, F.; Wu, S.-H.; Hung, Y.; Mou, C.-Y. Size effect on cell uptake in well-suspended, uniform mesoporous silica nanoparticles. Small 2009, 5, 1408-1413.
30. Chithrani, B.D.; Ghazani, A.A.; Chan, W.C.W. Determining the size and shape dependence of gold nanoparticle uptake into mammalian cells. Nano Letters 2006, 6, 662-668.
31. Varela, J.A.; Bexiga, M.G.; Åberg, C.; Simpson, J.C.; Dawson, K.A. Quantifying size-dependent interactions between fluorescently labeled polystyrene nanoparticles and mammalian cells. Journal of Nanobiotechnology 2012, 10, 39.
32. Huang, J.; Bu, L.; Xie, J.; Chen, K.; Cheng, Z.; Li, X.; Chen, X. Effects of nanoparticle size on cellular uptake and liver mri with polyvinylpyrrolidone-coated iron oxide nanoparticles. ACS Nano 2010, 4, 7151-7160.
33. Goel, S.; Chen, F.; Hong, H.; Valdovinos, H.; Hernandez, R.; Shi, S.; Barnhart, T.; Cai, W. VEGF121 - conjugated mesoporous silica nanoparticle: A tumor targeted drug delivery system. 2014, 6, 21677-21685.
34. Chen, F.; Nayak, T.R.; Goel, S.; Valdovinos, H.F.; Hong, H.; Theuer, C.P.; Barnhart, T.E.; Cai, W. In vivo tumor vasculature targeted pet/nirf imaging with trc105(fab)-conjugated, dual-labeled mesoporous silica nanoparticles. Molecular Pharmaceutics 2014, 11, 4007-4014.
35. Yu, M.; Niu, Y.; Zhang, J.; Zhang, H.; Yang, Y.; Taran, E.; Jambhrunkar, S.; Gu, W.; Thorn, P.; Yu, C. Size-dependent gene delivery of amine-modified silica nanoparticles. Nano Research 2016, 9, 291-305.
36. Nayak, T.R.; Krasteva, L.K.; Cai, W. Multimodality imaging of RNA interference. Current medicinal chemistry 2013, 20, 3664-3675.
37. Li, X.; Chen, Y.; Wang, M.; Ma, Y.; Xia, W.; Gu, H. A mesoporous silica nanoparticle – PEI – fusogenic peptide system for sirna delivery in cancer therapy. Biomaterials 2013, 34, 1391-1401.
38. Chen, Y.; Wang, X.; Liu, T.; Zhang, D.S.-Z.; Wang, Y.; Gu, H.; Di, W. Highly effective antiangiogenesis via magnetic mesoporous silica-based siRNA vehicle targeting the VEGF gene for orthotopic ovarian cancer therapy. International Journal of Nanomedicine 2015, 10, 2579-2594.
39. Wang, M.; Li, X.; Ma, Y.; Gu, H. Endosomal escape kinetics of mesoporous silica-based system for efficient siRNA delivery. International Journal of Pharmaceutics 2013, 448, 51-57.
40. Li, Z.; Zhao, R.; Wu, X.; Sun, Y.; Yao, M.; Li, J.; Xu, Y.; Gu, J. Identification and characterization of a novel peptide ligand of epidermal growth factor receptor for targeted delivery of therapeutics. Faseb j 2005, 19, 1978-1985.
41. Müller, K.; Klein, P.M.; Heissig, P.; Roidl, A.; Wagner, E. EGF receptor targeted lipo-oligocation polyplexes for antitumoral siRNA and miRNA delivery. Nanotechnology 2016, 27, 464001.
42. Troiber, C.; Edinger, D.; Kos, P.; Schreiner, L.; Kläger, R.; Herrmann, A.; Wagner, E. Stabilizing effect of tyrosine trimers on pDNA and siRNA polyplexes. Biomaterials 2013, 34, 1624-1633.
43. Cauda, V.; Schlossbauer, A.; Kecht, J.; Zürner, A.; Bein, T. Multiple core−shell functionalized colloidal mesoporous silica nanoparticles. Journal of the American Chemical Society 2009, 131, 11361-11370.
44. Möller, K.; Kobler, J.; Bein, T. Colloidal suspensions of nanometer-sized mesoporous silica. Advanced Functional Materials 2007, 17, 605-612.
45. Gu, J.; Huang, K.; Zhu, X.; Li, Y.; Wei, J.; Zhao, W.; Liu, C.; Shi, J. Sub-150nm mesoporous silica nanoparticles with tunable pore sizes and well-ordered mesostructure for protein encapsulation. Journal of Colloid and Interface Science 2013, 407, 236-242.
46. Kobler, J.; Möller, K.; Bein, T. Colloidal suspensions of functionalized mesoporous silica nanoparticles. ACS Nano 2008, 2, 791-799.
47. Schaffert, D.; Badgujar, N.; Wagner, E. Novel fmoc-polyamino acids for solid-phase synthesis of defined polyamidoamines. Organic Letters 2011, 13, 1586-1589.
48. Zhang, W.; Muller, K.; Kessel, E.; Reinhard, S.; He, D.; Klein, P.M.; Hohn, M.; Rodl, W.; Kempter, S.; Wagner, E. Targeted siRNA delivery using a lipo-oligoaminoamide nanocore with an influenza peptide and transferrin shell. Advanced Healthcare Materials 2016, 5, 1493-1504.
49. Genta, I.; Chiesa, E.; Colzani, B.; Modena, T.; Conti, B.; Dorati, R. Ge11 peptide as an active targeting agent in antitumor therapy: A minireview. Pharmaceutics 2017, 10, 2.

50. Biscaglia, F.; Rajendran, S.; Conflitti, P.; Benna, C.; Sommaggio, R.; Litti, L.; Mocellin, S.; Bocchinfuso, G.; Rosato, A.; Palleschi, A., et al. Enhanced EGFR targeting activity of plasmonic nanostructures with engineered GE11 peptide. Advanced Healthcare Materials 2017, 6, 1700596.
51. Korpal, M.; Lee, E.S.; Hu, G.; Kang, Y. The miR-200 family inhibits epithelial-mesenchymal transition and cancer cell migration by direct targeting of e-cadherin transcriptional repressors zeb1 and zeb2. Journal of Biological Chemistry 2008, 283, 14910-14914.

6.6. Appendix

DLS Measurements of MSN Samples. The particles obtained via the reported synthesis procedure were characterized using DLS. The different samples show an average hydrodynamic radius between 90 and 250 nm.

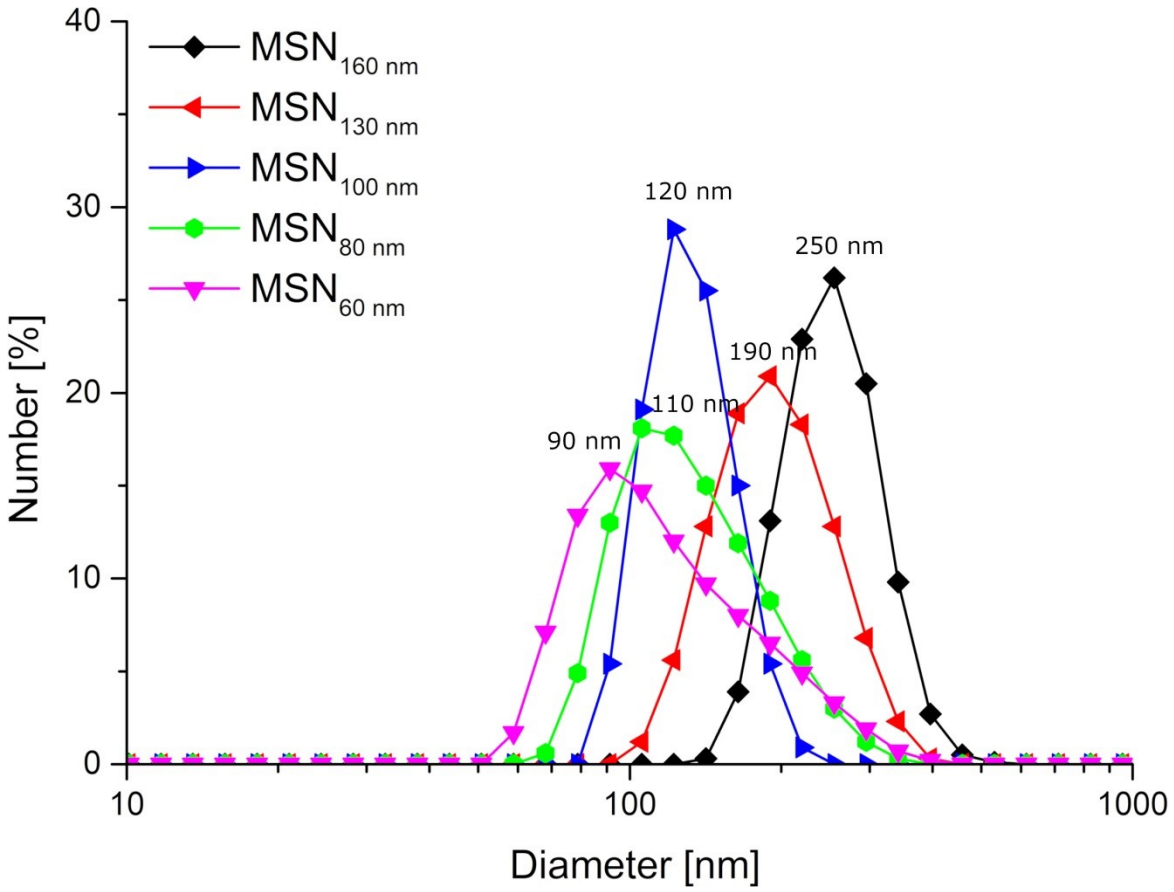

Figure S6.1 DLS measurements of MSN samples in EtOH: MSN_{160nm} (black line), MSN_{130nm} (red line), MSN_{100nm} (blue line), MSN_{80nm} (green line), and MSN_{60nm} (magenta line).

TGA Data of MSN160 nm up to 900 °C

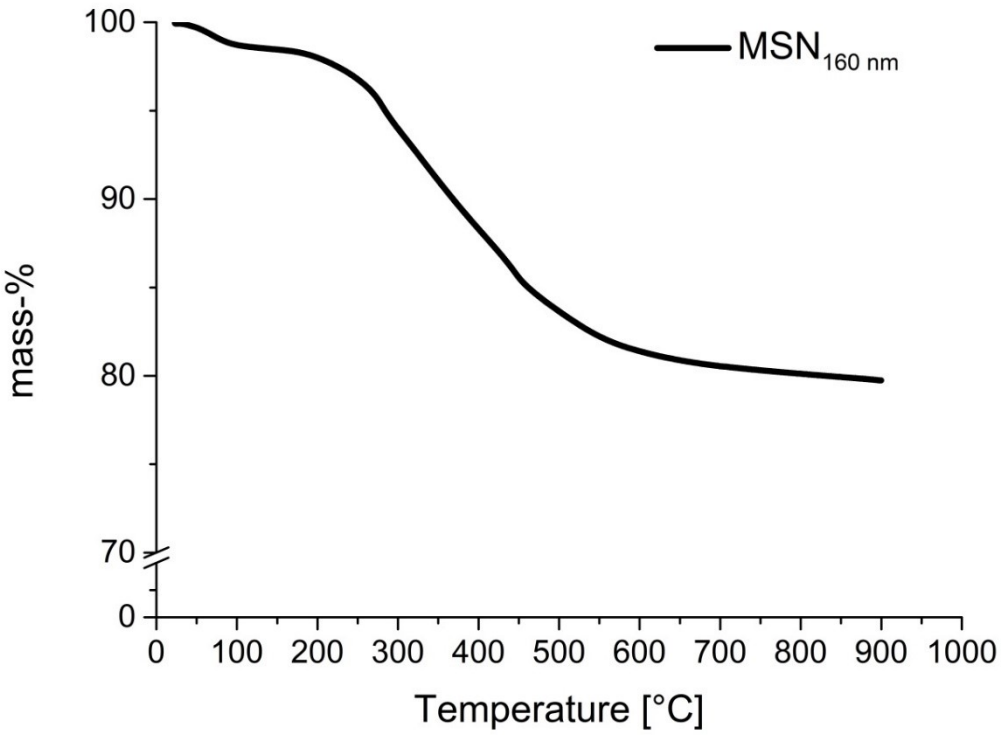

Figure S6.2 TGA curves of sample MSN_{160nm} measured up to 900 °C.

Structure of Copolymer 454

The structure of the copolymer is depicted in Figure S6.3.

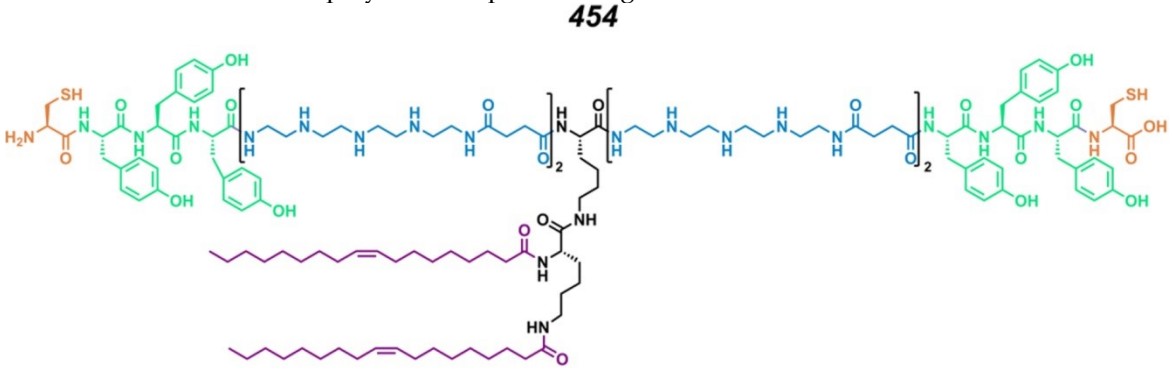

Figure S6.3 Structure of copolymer 454

Zeta Potential of MSN Samples

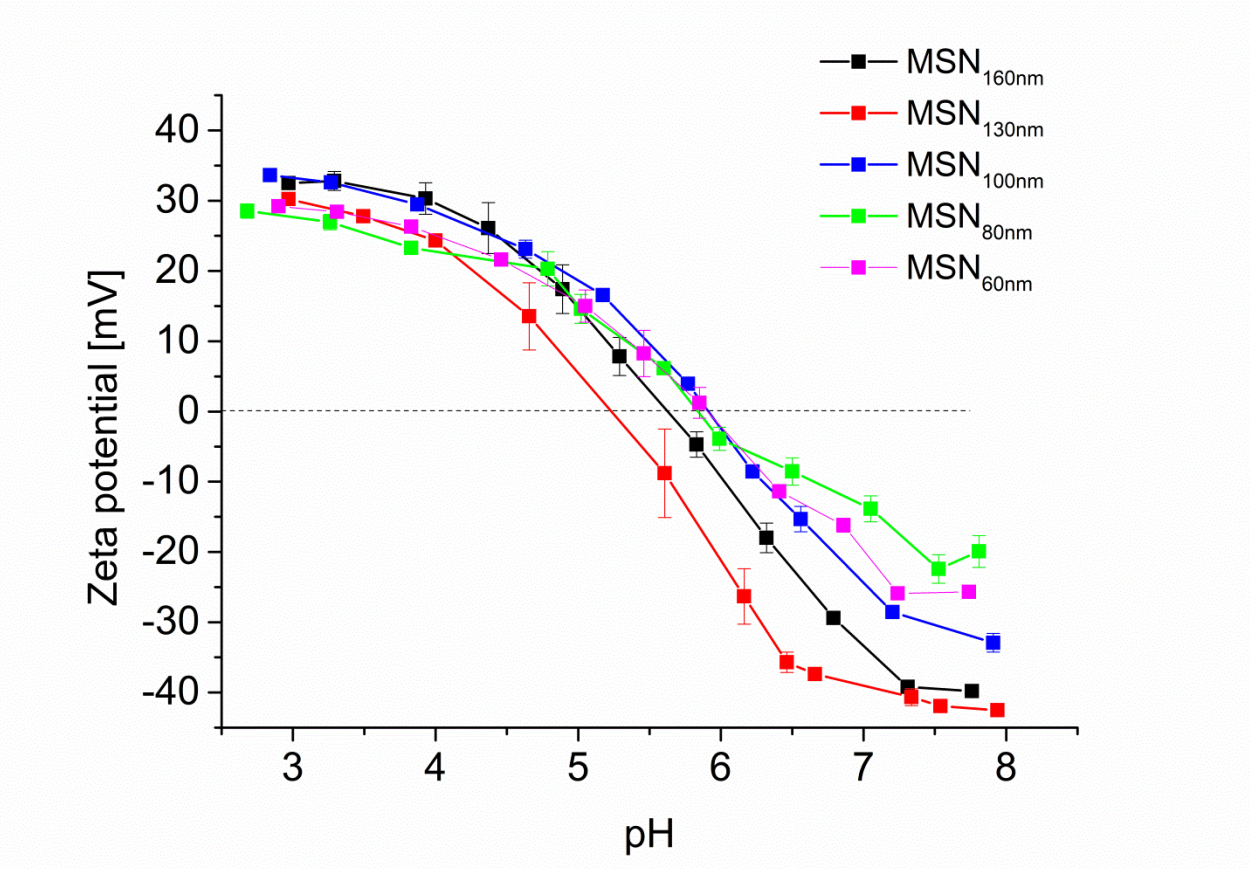

Figure S6.4 Zeta potential titration curves of pure MSN samples: MSN_{160nm} (black line), MSN_{130nm} (red line), MSN_{100nm} (blue line), MSN_{80nm} (green line), and MSN_{60nm} (magenta line).

UV-VIS Measurements for Quantification of Capping Amount of 454-GE11. The amount of the attached 454-GE11 polymer was obtained by difference measurements: increasing concentrations of 454-GE11 in MES buffer were used to obtain a calibration curve and were measured at a spectral maximum of 275 nm. For determining the capping concentration, we added a 454-GE11 solution to a defined amount of MSN in MES buffer. After 2 h, the particles were centrifuged to form a pellet and the unreacted 454-GE11 in the supernatant was determined by UV-VIS spectroscopy. A substantial decrease in absorbance in the coupling

solution was observed for all MSN samples. The particles were capped with 454-GE11 with amounts ranging between around 17–20 wt% (detailed amounts are listed in Table S6.1).

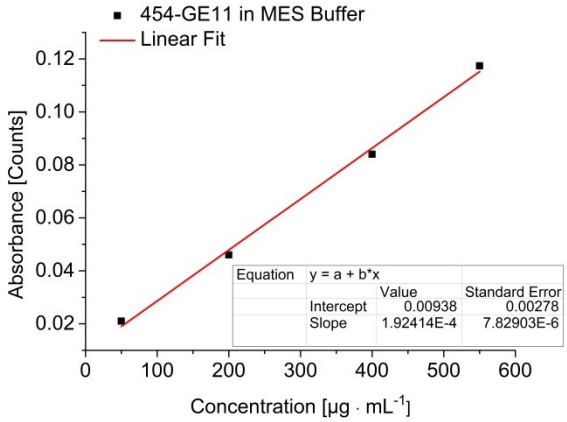

Figure S6.5 454-GE11 calibration curve measured at 275 nm for quantification of the capping concentration.

Table S 6.1 Estimated capping amount of 454-GE11 for different MSN samples.

MSN-454-GE11	Difference Concentration before and after Capping [µg/mL]	Capping Amount wt%
160 nm	230,7	18,7
130 nm	256,7	20,4
100 nm	220,3	18,0
80 nm	204,7	17,0
60 nm	246,3	19,7

Comparison of DLS Measurements of Pure MSN and MSN-454-GE11 Samples of Different Sizes.

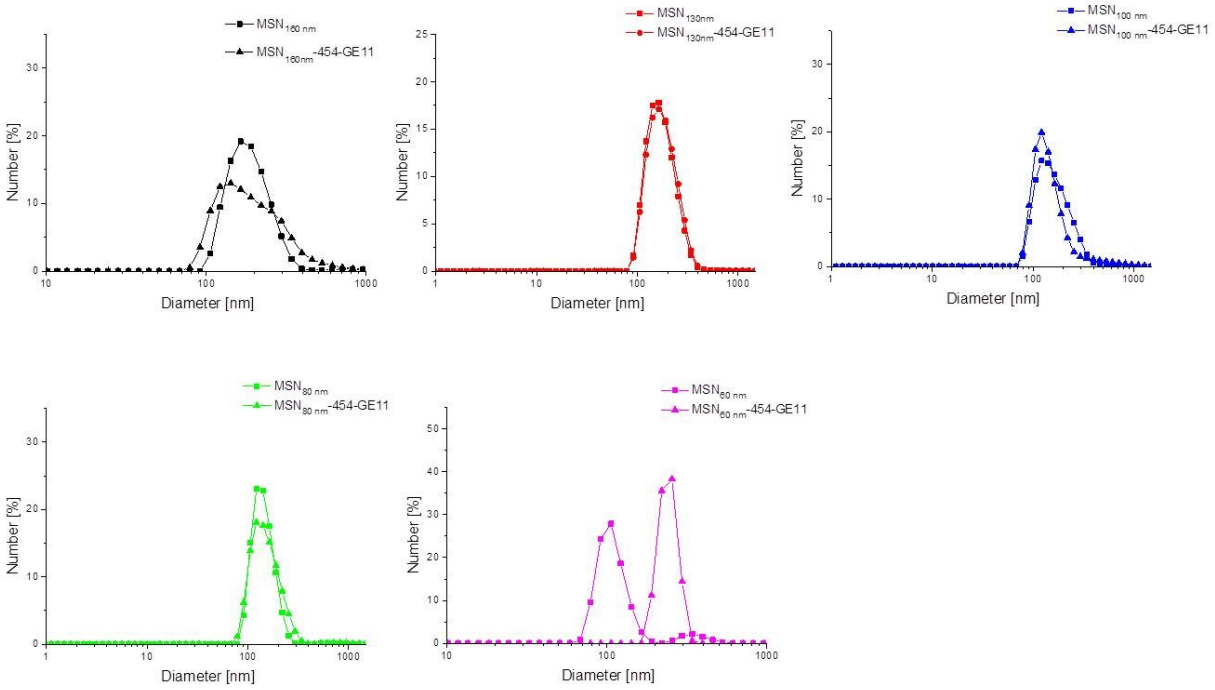

Figure S6.6 DLS measurements of MSN and corresponding MSN-454-GE11 samples in HEPES buffer: MSN_{160nm} (black line), MSN_{130nm} (red line), MSN_{100nm} (blue line), MSN_{80nm} (green line), MSN_{60nm} (magenta line).

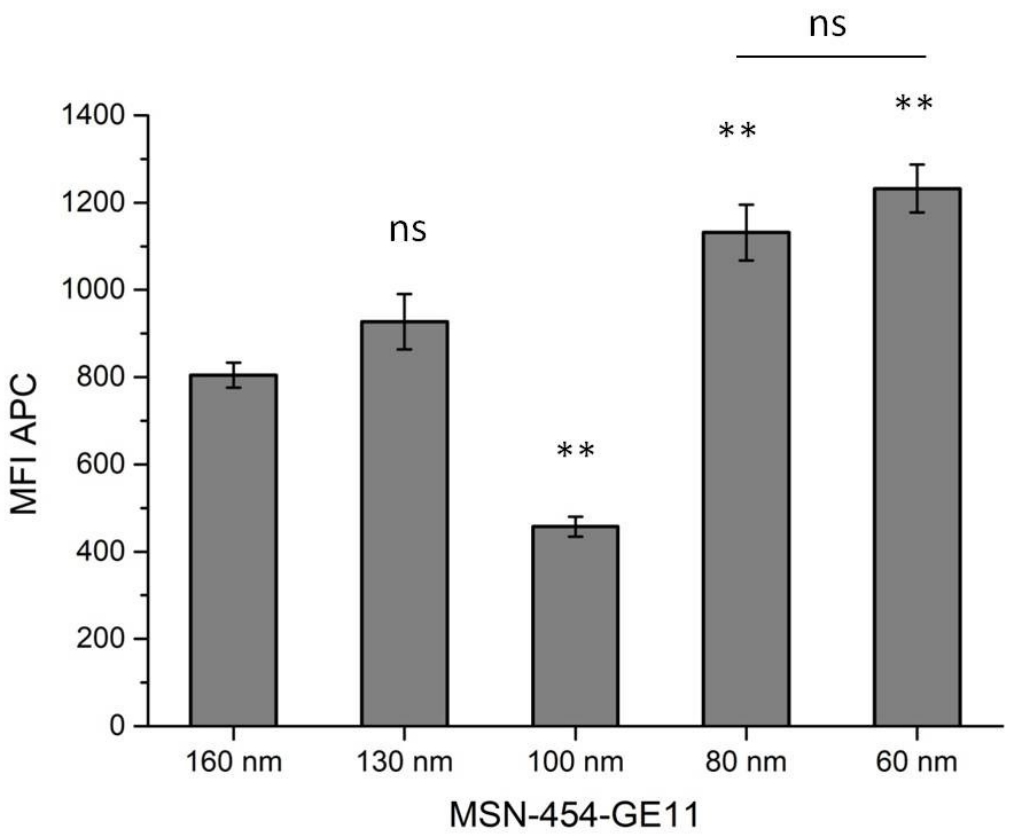

Figure S6.7 Quantification of the FACS data shown in Figure 6.4b in the main text. It shows the cellular internalization of Atto-633 labeled MSN-454-GE11 after 45 min incubation with particle sizes in the range of 160 nm to 60 nm. For statistical analysis a two-tailed t-test was performed (n = 3, mean ± SD, ns (not significant) $p > 0.05$, * $p < 0.05$, ** $p < 0.01$). Statistical significance indications on top of the flow cytometry bars without connecting line show statistical significance between 160 nm sample and other sizes of MSN-454-GE11 samples. Indicated statistical significance with connecting line shows no statistical significance between MSN80 nm-454-GE11 and MSN60 nm-454-GE11.

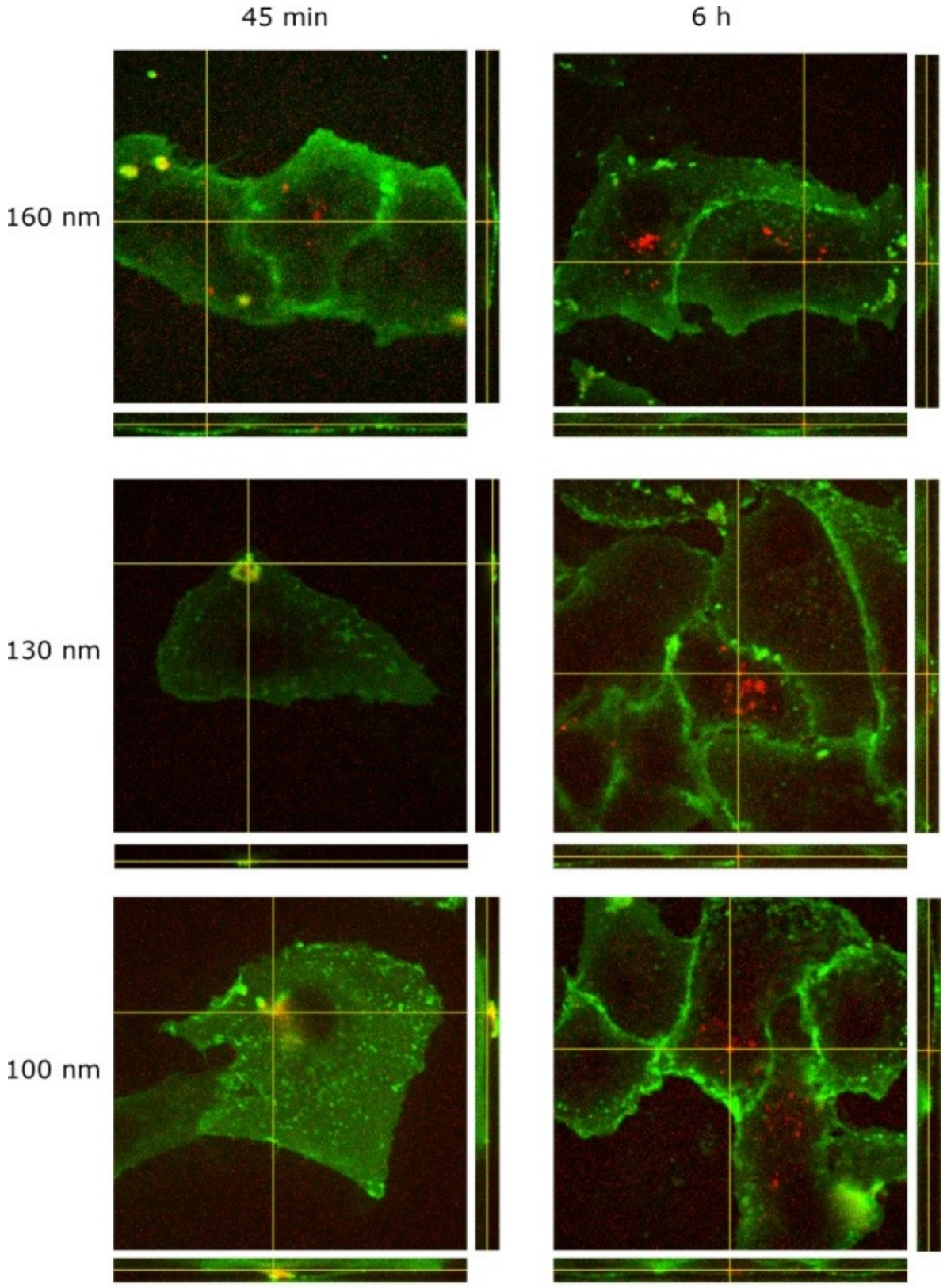
45 min
6 h
160 nm
130 nm
100 nm

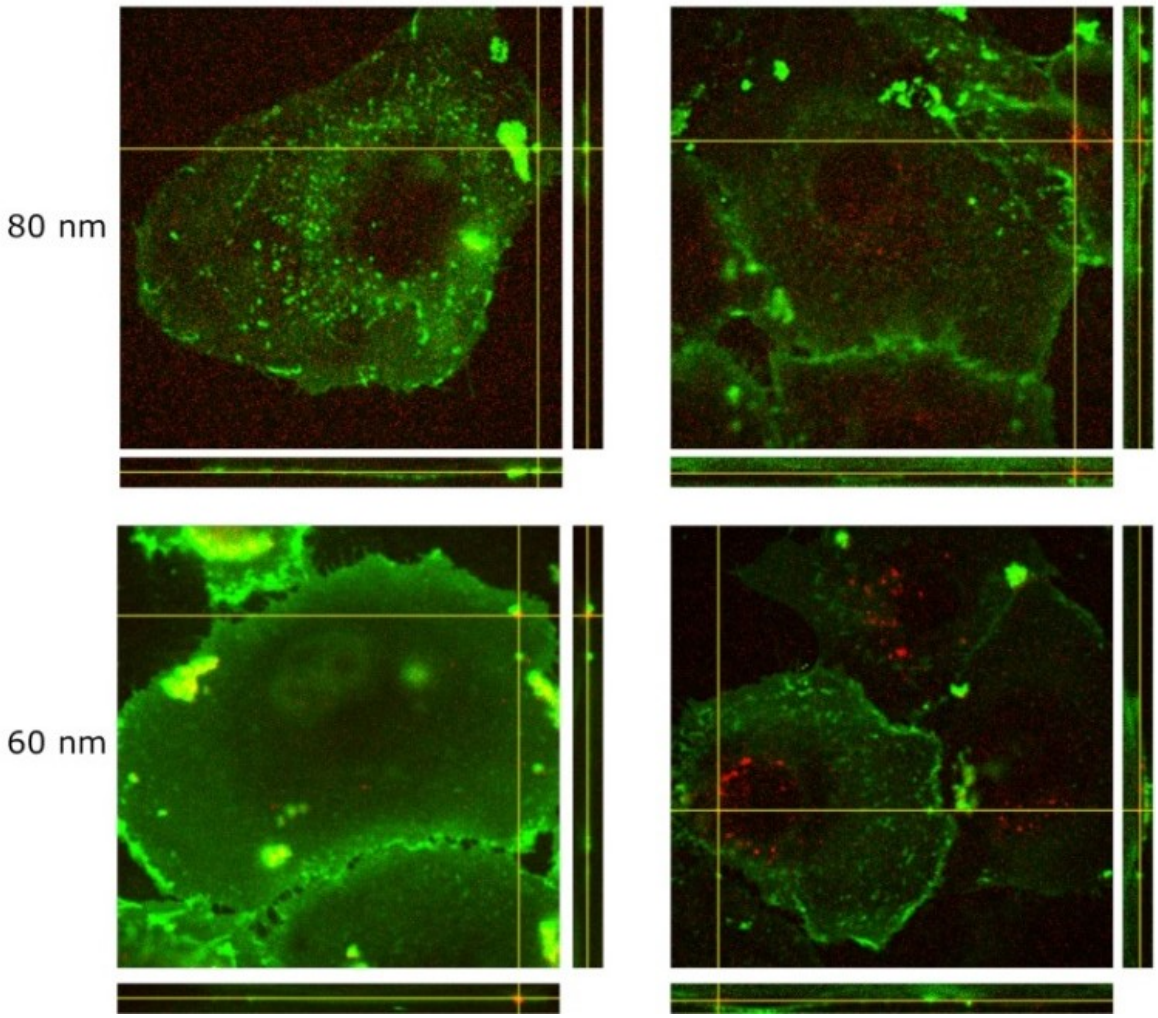

Figure S 6.8**. Enlarged** representative confocal fluorescence microscopy images of Atto-633 labeled MSN-454-GE11 samples (red) with particle sizes in the range of 160 nm to 60 nm after 45 min and 6 h of incubation on WGA488-stained T24 cells (green), respectively. The orthogonal views on the side of each image show the particle internalization.

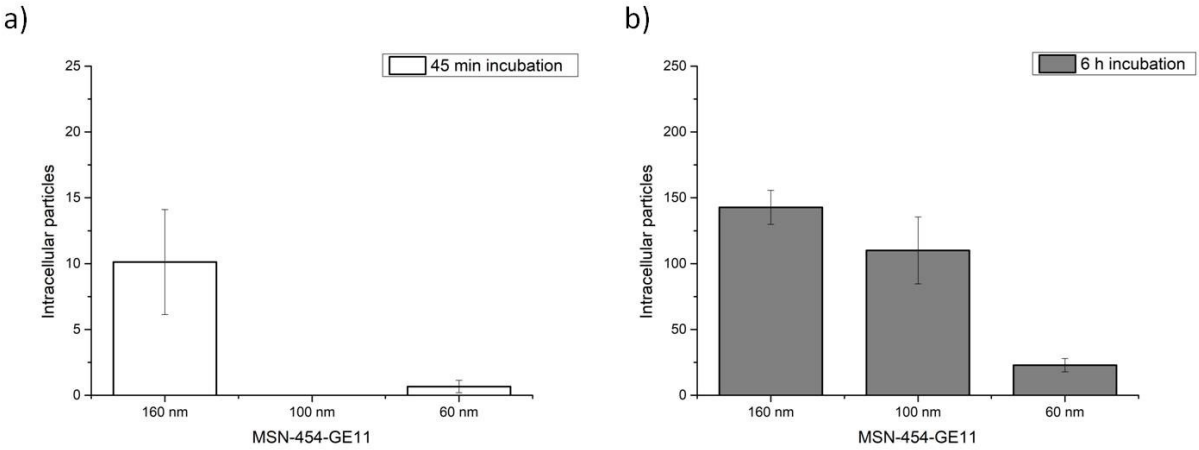

Figure S6.9 Quantification of the cellular uptake of MSN-454-GE11 with 160, 100 and 60 nm particle sizes in T24 cells after a) 45 min and b) 6 h incubation time using Particle_in_Cell-3D as analysis method for confocal fluorescence microscopy images. The histograms represent three independent experiments (n = 21–25).

Gene Silencing of eGFP-Luciferase using Pure MSN Samples without 454-GE11. No silencing efficacy was observed when the gene silencing of the eGFP-luciferase reporter gene was examined using pure MSN samples without the capping/targeting ligand 454-GE11 but loaded with either miR200c or siCtrl RNA (Figure S6.11a). Figure S6.11b shows the comparison of silencing efficacy of the targeted MSN160 nm-454-GE11 sample to a non-targeted control (MSN-454-PEG). The non-targeted MSN show again a lower effectivity, as was anticipated from the flow cytometry results shown in Figure 6.4a.

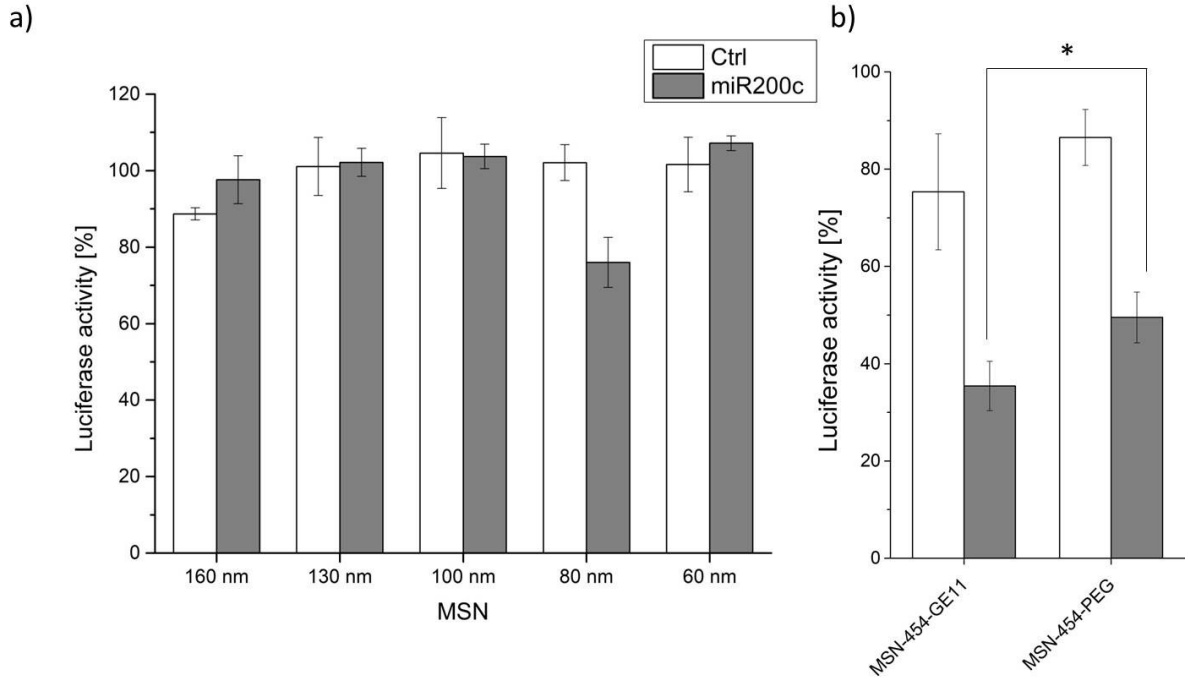

Figure S6.10 Gene-silencing assay using a) pure MSN loaded with miR200c or Ctrl, but without the capping/targeting ligand 454-GE11, b) MSN 160 nm-454-GE11 as a targeted sample in comparison to a non-targeted MSN160 nm-454-PEG sample. For statistical analysis a two-tailed t-test was performed (n = 3, mean ± SD, * $p < 0.05$). All samples were incubated for 45 minutes and transfected for 48 h after medium change.

Cell Viability Assay with siRNA Control

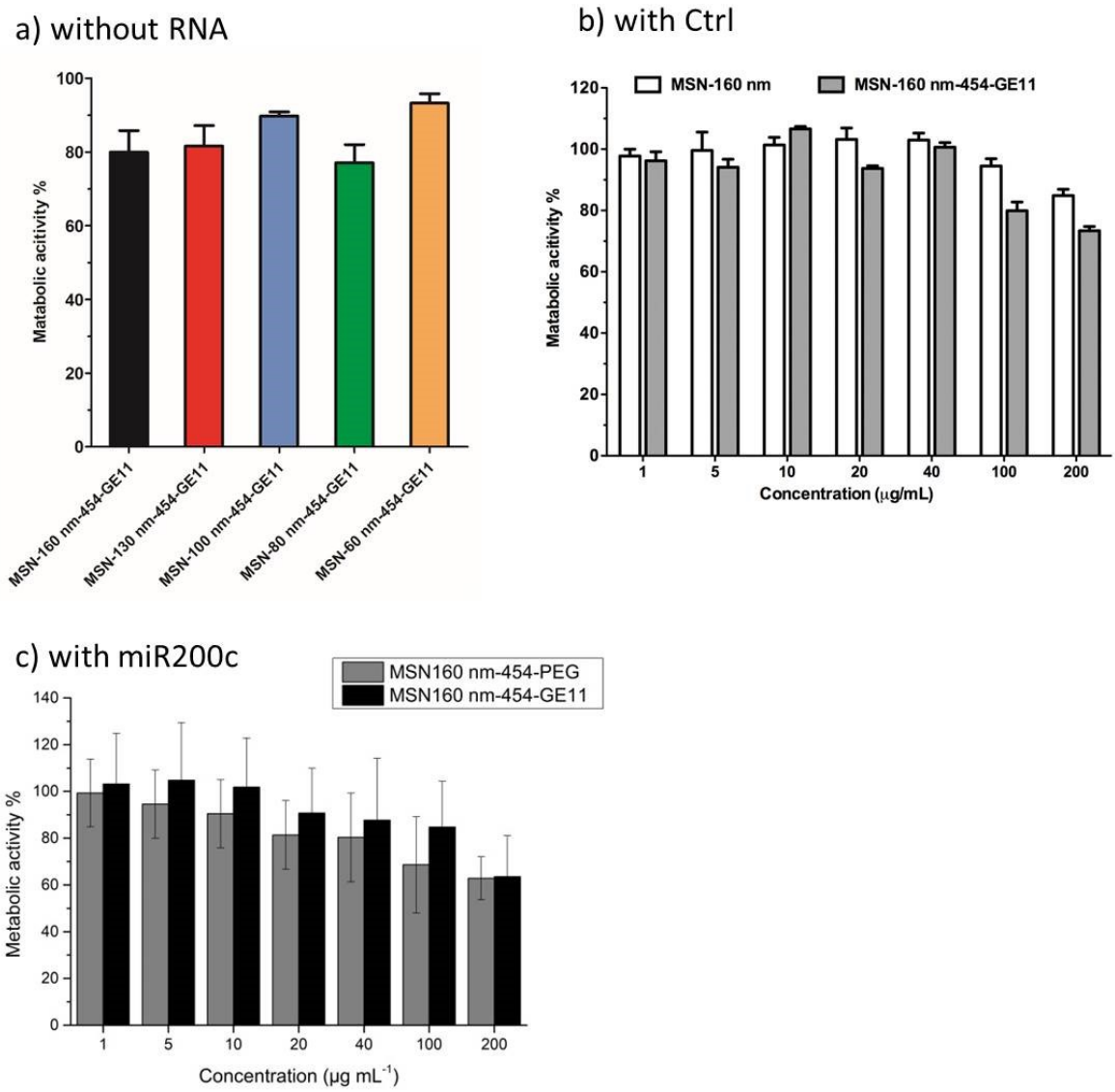

Figure S6.11 MTT cell viability study of MSN-454-GE11 samples on T24 cells after 48 h of incubation (cells were washed once after 45 min). a) MTT cell viability study of MSN-454-GE11 samples with various diameters using a concentration of 100 µg mL^{-1} as applied before in the *in vitro* cell experiments. b) MSN dose-dependent MTT assay with MSN160 nm (white) and MSN 160 nm-454-GE11 (grey) loaded with Ctrl. c) MTT assay of MSN-160 nm-454-GE11 in various concentrations in comparison with non-targeted sample MSN160 nm-454-PEG, both loaded with active miR200c (RNA concentration = 50 µg mg^{-1} of MSN carrier).

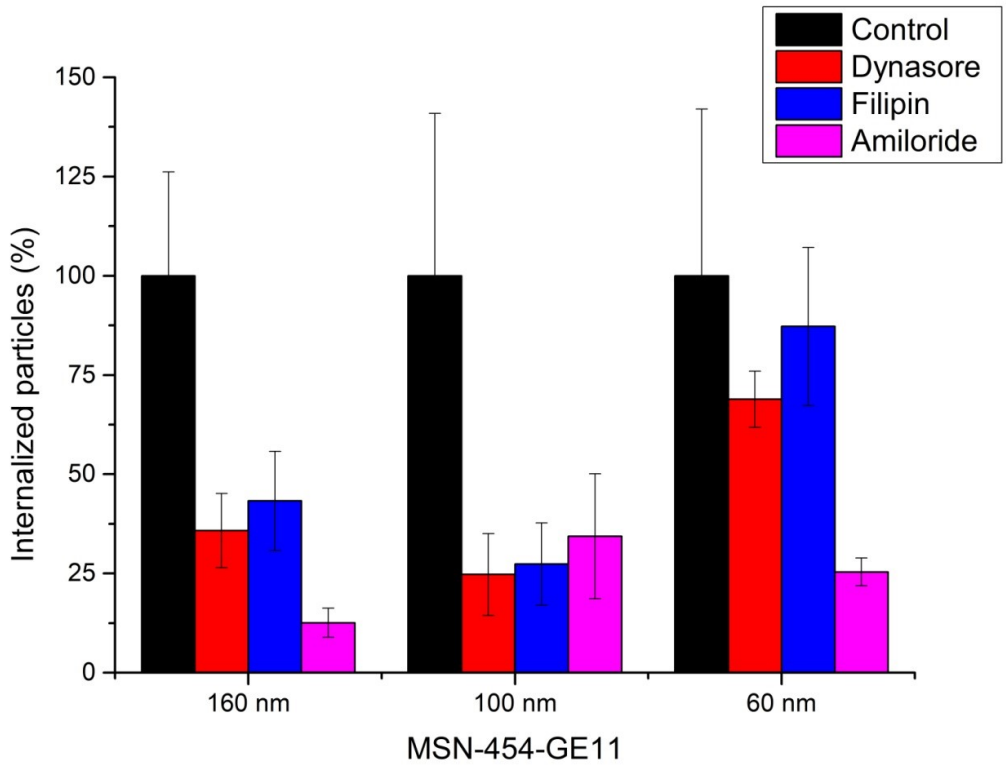

Figure S6.12 Inhibition results using Dynasore, 5-(N-Ethyl-N-isopropyl)amiloride and Filipin to inhibit different endocytosis pathways. We have performed confocal fluorescence microscopy experiments with subsequent image analysis for quantification of internalized particles and find that there are slight differences in uptake pathways. Control: uptake of particles in cells without inhibitor.

Flow cytometry of pure MSN samples

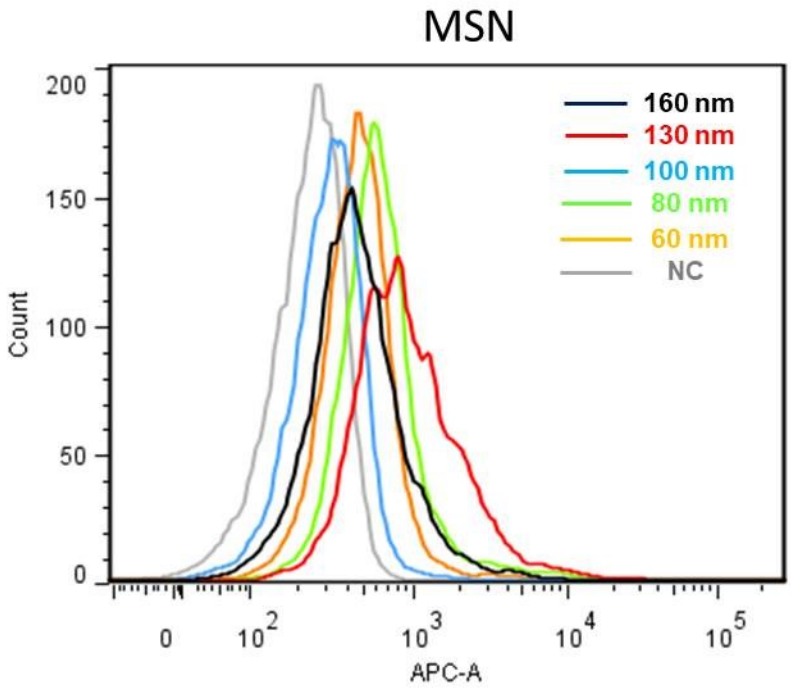

Figure S6.13: Cellular internalization of Atto-633 labeled pure MSN samples (without 454-GE11 polymer capping) with particle sizes in the range of 160 nm to 60 nm.

CHAPTER 7

Conclusion and Outlook

7. Conclusion and Outlook

The focus of this thesis was the development of two new innovative nanoparticle materials and the fine-tuning of MSN as well-established nanosystem platform and their further use in drug delivery applications. We demonstrated their potential as biocompatible drug delivery agents in various fields and additionally compared the influence of particle size and nanocarrier type on delivery efficiencies.

In Chapter 3, colloidal mesoporous magnesium phosphate-citrate nanoparticles (MPCs) were synthesized and investigated for drug delivery applications. The effect of the chelating agent, citric acid, on the properties of these nanoparticles was examined. It was found that the amount of citric acid used in the synthesis process affects the colloidal stability of MPCs and their mesoporosity. The optimized MPCs show all prerequisites for successful drug delivery applications: A high BET surface area of 650 m^2/g was achieved, with a pore size of approximately 5.6 nm, the MPCs degrade in slightly acidic pH, such as that found in the lysosome, and we observed a tight closure and entrapment of drugs for lipid-coated MPCs with only 15% premature release within 12 hours. Furthermore, MPCs showed good biocompatibility *in vitro*, making them a promising and biodegradable platform for drug delivery applications. To assess if this system can principally function as carrier for anti-cancer drugs, methotrexate (MTX) was loaded into MPCs and the loaded nanoparticles were applied to HeLa cells. Compared to free MTX, the effect of the anticancer drug was enhanced nine times when delivered by lipid-coated MPCs. Hence, it was demonstrated that MPCs hold great promise as biocompatible drug carrier, which has to be evaluated in further studies.

The next chapter of this thesis introduces a novel biocompatible drug carrier system which is based on crosslinked β-cyclodextrins (β-CDs). These crosslinked CD nanoparticles are organic, water-dispersible, and small in size (~100 nm in the scanning electron microscope). The nanoparticles consist mainly of β-CD linked by diesters and are stabilized by short PEG

molecules. *In vitro* studies demonstrated that these nanoparticles are well tolerated by HeLa cells, indicating a good biocompatibility. The nanoparticles remain stable at pH 7 but are readily degraded at pH 5, demonstrating their biodegradability and thus allowing for efficient release of cargo molecules with rapid kinetics. This is exemplarily shown by delivery of the model cargo Hoechst dye into HeLa cells. A time-delayed staining of cell nuclei by the membrane-permeable fluorescent Hoechst dye was observed when delivered in comparison to the free dye. In total, these nanoparticles hold great promise for future applications as a biocompatible drug carrier system.

The potential of the two newly developed nanocarriers was investigated in the following chapter of this thesis (Chapter 5). In a comparative study, three different types of nanoparticles were used to deliver necrosulfonamide (NSA) into macrophages. The three types of nanocarrier tested were MSN, crosslinked cyclodextrin nanoparticles (CD-NP) and MPCs. NSA is a potent inhibitor of Gasdermin D (GSDMD)-mediated pyroptotic cell death and inflammatory cytokine (such as IL-1β) release, which occurs in response to inflammatory stimuli in macrophages. Targeting macrophages with an NSA-loaded nanocarrier to inhibit GSDMD-mediated pyroptosis has potential as a therapeutic strategy for the treatment of inflammatory diseases, while at the same time preventing unwanted toxicity of the drug to other cell types. The fast internalization of MSN and CD-NP in a macrophage cell line was established, since these cells are specialized in the uptake of particulate material. After exposure of the nanoparticles to a mixed population of immune cells, a high proportion of macrophages and dendritic cells were positive for CD-NP after 24 h, indicating that porous NP may be an effective manner to target both cells as the main initiators of inflammation. All three empty porous nanoparticles neither showed any effect on the metabolic activity nor the membrane integrity using a macrophage cell line as well as freshly differentiated primary macrophages from mice and human donors, indicating their good biocompatibility. To investigate if unloaded particles already induce an

immune response, proinflammatory cytokine release was measured upon addition of empty nanoparticles with and without activation of GSDMD of macrophages. No significant up- or downregulation of IL-1β, respectively, could be observed after exposure to cargo-free particles, showing that empty nanoparticles could not induce inflammation. In contrast, when the nanocarriers were loaded with NSA, we demonstrated that MSN-NSA as well as CD-NSA were able to inhibit the release of pro-inflammatory cytokines IL-1β in primary macrophages from mice and human sources. CD particles were able to fully prevent the release of IL-1β, similar to the effect of free NSA, while in terms of metabolic activity the particle-loaded NSA was better tolerated by macrophages than the free NSA. In contrast, NSA-loaded MPC particles completely blocked metabolic activity of macrophages even at low NSA concentrations. MPC particles require small amounts of surfactant for loading of NSA, which may have toxic effects on these cells. Thus, with the exception of MPC particles, it was shown that CD-NSA and MSN-NSA have potential as an effective anti-inflammatory agent that can selectively target macrophages and inhibit IL-1β release, which is involved in the inflammatory response. Overall, porous nanoparticles are a promising platform for the development of targeted drug delivery systems for the treatment of inflammatory diseases.

The final part of this thesis focuses on the tailoring of MSN to further establish their potential as multifunctional delivery agents for antitumoral microRNA (miRNA). MSN were modified in size ranging from 60 to 160 nm for studying the influence of the particle size on antitumoral miRNA delivery. All other properties of the delivery vehicles, including surface area, pore size and zeta potential were kept similar. To exploit the potential of these nanoparticles, the interior of MSN was functionalized to allow for the successful loading of RNA molecules through electrostatic adsorption. Exterior functionalization allowed for the capping of MSN with a positively charged block copolymer 454 equipped with a targeting ligand (GE11). Since gene silencing was only observed after capping the nanocarriers with this 454 polymer, we conclude

that it is essential for the endosomal escape by destabilizing the endosomal membrane. It was shown that the targeting ligand GE11 enhances a receptor-mediated uptake. After capping, the MSN-454-GE11 vehicles were used for a systematic investigation of size-dependent gene silencing. The study showed that the size of the MSN nanocarriers had a significant impact on the efficiency of RNA delivery and gene knockdown. Specifically, it was found that MSN-454-GE11 with a size of 160 nm showed the best knockdown efficacy and antitumoral effects, including decreased migration and changes in cell cycle. In contrast, smaller particles did not have significant effects. Following the uptake of MSN-454-GE11 over time into cells using confocal fluorescence microscopy, it was revealed that only the largest particles (160 nm) were truly internalized in cells after a short incubation time. In summary, fast cellular internalization was essential for successful gene knockdown. We hypothesize that this is due to the larger contact area of the particles with the cell membrane and consequently the larger number of targeting ligands interacting with the cell surface. Overall, the potential of MSN nanocarriers was demonstrated for the delivery of antitumoral miRNA and the importance of considering the nanocarriers' size and surface properties for optimal delivery efficiency was highlighted.

In conclusion, we have developed novel synthesis and application strategies for multifunctional nanocarriers. The nanomaterials were applied as carrier systems in cellular delivery investigations for the treatment of cancer as well as inflammatory diseases. Overall, it is hoped that the insights gained in this work regarding nanoparticle-based drug delivery will help to provide more effective and targeted therapies that can improve patient outcomes and quality of life.

CHAPTER 8

Publications and Presentations

8. Publications and Presentations

Publications

1. L. Wehl, K. Muggli, H. Engelke, T. Bein, Crosslinked Cyclodextrin-based Nanoparticles as Drug Delivery Vehicles: Synthesis Strategy and Degradation Studies, *ACS Omega* **2023**, submitted.
2. B. Boersma[§], K. Möller[§], L. Wehl[§], V. Puddinu, A. Huard, S. Fauteux-Daniel, C. Bourquin, G. Palmer, T. Bein, Inhibition of IL-1β release from macrophages targeted with necrosulfonamide-loaded porous nanoparticles**,** *J Control Release* **2022**, *351*, 989-1002**.** [link]
3. L. Wehl[§], C.von Schirnding[§], M. Bayer, O. Zhuzhgova, H. Engelke, T. Bein. Mesoporous Biodegradable Magnesium Phosphate-Citrate Nanocarriers Amplify Methotrexate Anticancer Activity in HeLa Cells, *Bioconjugate Chem.* **2022**, *33*, 566-575**.** [link]
4. C. von Schirnding, I. Giopanou, A. Hermawan, L. Wehl, G. Ntaliarda, B. Illes, S. Datz, F. Geisslinger, K. Bartel, A.-K. Sommer, M. Lianou, V. Weiss, J. Feckl, A. M. Vollmar, C. Braeuchle, G. T. Stathopoulos, E. Wagner, A. Roidl, T. Bein, H. Engelke, Synergistic Combination of Calcium and Citrate in Mesoporous Nanoparticles Targets Pleural Tumors**,** *Chem,* **2021**, *7*, 480-494**.** [link]
5. L. Haddick, W. Zhang, S. Reinhard, K. Moeller, H. Engelke, E. Wagner, T. Bein, Particle-Size-Dependent Delivery of Antitumoral miRNA Using Targeted Mesoporous Silica Nanoparticles, *Pharmaceutics*, **2020**, *12*, 505-525. [link]
6. H.-Y. Chiu, D. Goessl, L. Haddick, H. Engelke, T. Bein, Clickable Multifunctional Large-Pore Mesoporous Silica Nanoparticles as Nanocarriers, *Chem. Mater.* **2018**, 30, 644-654[link]

[§] These authors contributed equally

Presentations

Oral presentations

1. Particle-Size-Dependent Delivery of Antitumoral miRNA Using Targeted Mesoporous Silica Nanoparticles, SFB1032 Adhoc-Workshop 2018, München, Germany.

2. Mesoporous silica nanoparticles as universal drug delivery vehicle
   Center for Nanoscience Seminar Science Rocks! 2018, München, Germany.

3. Particle-Size-Dependent Delivery of Antitumoral miRNA Using Targeted Mesoporous Silica Nanoparticles
   Center for Nanoscience Winter Retreat 2019, Kleinwalsertal, Germany.

Poster presentations

1. Particle-Size-Dependent Delivery of Antitumoral miRNA Using Targeted Mesoporous Silica Nanoparticles;
   Center for NanoScience (CeNS) Workshop 2017, Venice, Italy.

2. Synergistic Combination of Calcium and Citrate in Mesoporous Nanoparticles Targets Pleural Tumors
   16th European Symposium on Controlled Drug Delivery 2018, Egmond aan Zee, Netherlands.

3. Crosslinked Cyclodextrin-based Nanoparticles as Drug Delivery Vehicles: Synthesis Strategy and Degradation Studies
   Nanosystems Initiative Munich Conference "The Future of Nanoscience" 2018, Tutzing, Germany.